The Pennsylvania State University

The Graduate School

Department of Astronomy and Astrophysics

THE X-RAY EVOLUTION OF INFLOWS AND OUTFLOWS IN ACTIVE GALACTIC NUCLEI

A Dissertation in

Astronomy and Astrophysics

by

Cristian Saez

Submitted in Partial Fulfillment
of the Requirements
for the Degree of

Doctor of Philosophy

August 2010

The dissertation of Cristian Saez was reviewed and approved[1] by the following:

Michael Eracleous
Associate Professor of Astronomy and Astrophysics
Co-Chair of Committee

George Chartas
Adjunct Professor of Astronomy and Astrophysics
Assistant Professor of Physics and Astronomy at CofC
Dissertation Adviser
Co-Chair of Committee

Derek Fox
Assistant Professor of Astronomy and Astrophysics

Stephane Coutu
Professor of Physics

Steinn Sigurdsson
Associate Professor of Astronomy and Astrophysics
Chair of Graduate Program

[1]Signatures on file in the Graduate School.

Abstract

The evolution[2] of the space density of AGNs might have spectral counterparts which could be observable in X-rays. The main objective of this thesis is to study the spectral properties of AGNs in X-rays in order to increase our current knowledge of AGN evolution. We are especially interested in high redshift AGNs with $z \gtrsim 1.0$, because the analysis of their spectra may indicate what parameters show evolutionary trends and provide insight as to which physical processes are markers of AGN evolution. The thesis begins with an introduction and review of the scientific topics that are pursued in this study. The core of my research is presented in chapters 2, 3 and 4 of the thesis.

In chapter 2, we present results from a statistical analysis of 173 bright radio-quiet AGNs selected from the *Chandra* Deep Field-North and *Chandra* Deep Field-South surveys (hereafter, CDFs) in the redshift range of $0.1 \lesssim z \lesssim 4$. We find that the X-ray power-law photon index (Γ) of radio-quiet AGNs is correlated with their 2–10 keV rest-frame X-ray luminosity (L_X) at the $> 99.5\%$ confidence level in two redshift bins, $0.3 \lesssim z \lesssim 0.96$, and $1.5 \lesssim z \lesssim 3.3$ and is slightly less significant in the redshift bin $0.96 \lesssim z \lesssim 1.5$. The X-ray spectral slope steepens as the X-ray luminosity increases for AGNs in the luminosity range 10^{42} to 10^{45} erg s^{-1}. Combining our results from the CDFs with those from previous studies in the redshift range $1.5 \lesssim z \lesssim 3.3$, we find that the $\Gamma - L_{\rm X}$ correlation has a null-hypothesis probability of 1.6×10^{-9}. We investigate the redshift evolution of the correlation between the power-law photon index and the hard X-ray luminosity and find that the slope and offset of a linear fit to the correlation change significantly (at the $> 99.9\%$ confidence level) between redshift bins of $0.3 \lesssim z \lesssim 0.96$ and $1.5 \lesssim z \lesssim 3.3$. We explore physical scenarios explaining the origin of this correlation and its possible evolution with redshift in the context of steady corona models focusing on its dependency on variations of the properties of the hot corona with redshift.

In chapter 3, we present results from three *Suzaku* observations of the $z = 3.91$ gravitationally lensed broad absorption line quasar APM 08279+5255. We detect strong and broad absorption at rest-frame energies of $\lesssim 2$ keV (low-energy) and 7–12 keV (high-energy). The detection of these features confirms the results of previous long-exposure (80–90 ks) *Chandra* and *XMM-Newton* observations. The low and high-energy absorption is detected in both the back-illuminated (BI) and front-illuminated (FI) *Suzaku* XIS spectra (with an F-test significance of $\gtrsim$99%). We interpret the low-energy absorption as arising from a low-ionization absorber with $\log (N_{\rm H}/{\rm cm}^{-2}) \sim 23$ and the high-energy absorption as due to lines arising from highly ionized ($2.75 \lesssim \log \xi \lesssim 4.0$; where ξ is the ionization parameter) iron in a near-relativistic outflowing wind. Assuming this interpretation we find that the velocities in the outflow range between $0.1c$ and $0.6c$. We constrain the angle between the outflow direction of the X-ray absorber and our line of sight to be $\lesssim 36^{\rm o}$. We also detect likely variability of the absorption lines (at the

[2]In extragalactic astronomy the reference to the term evolution is interpreted as evolution with cosmological distance, or redshift. Given that the speed of light is finite, the evolution with cosmological distance can also be thought as an evolution with cosmic time.

$\gtrsim$99.9% and $\gtrsim$98% significance levels in the FI and BI spectra, respectively) with a rest-frame time scale of $\sim$1 month. Assuming that the detected high-energy absorption features arise from Fe XXV, we estimate that the fraction of the total bolometric energy injected over the quasar's lifetime into the intergalactic medium in the form of kinetic energy to be $\gtrsim$ 10%.

In chapter 4, we present an expansion of our previous work on the study of X-ray outflows on APM 08279+5255. The main conclusions from our multi-epoch spectral analysis of *Chandra*, *XMM-Newton* and *Suzaku* observations of the z = 3.91 gravitationally lensed broad absorption line (BAL) quasar APM 08279+5255 are: 1) In every observation we confirm the presence of two strong features, one at rest-frame energies between 1–4 keV, and the other between 7–18 keV. 2) The low-energy absorption is interpreted as arising (1–4 keV rest-frame) from a low-ionization absorber with log $(N_{\rm H}/{\rm cm}^{-2}) \sim 23$ and the high-energy absorption (7−18 keV rest-frame) as due to lines arising from highly ionized ($3 \lesssim \log \xi \lesssim 4$; where ξ is the ionization parameter) iron in a near-relativistic outflowing wind. Assuming this interpretation, we find that the velocities on the outflow could get up to $\sim$ 0.7c. We also present results obtained from fits to all the long exposure observations of APM 08279+5255 with a new outflow model. This model is based on CLOUDY[3] simulations of a near-relativistic quasar outflow. From the analysis of this new model we conclude that the wind is likely to get more powerful as the spectra get softer. Our results also suggest that changes in the X-ray and UV portions of the spectral energy distribution (hereafter SED) of the central source could be related to changes in the terminal velocities of the outflows. If this result is confirmed it will imply that radiation pressure is an important mechanism in producing quasar outflows.

In the final chapter of the thesis, we present the conclusions and future work.

[3]CLOUDY is a photoionization code designed to simulate conditions in interstellar matter under a broad range of conditions.

Table of Contents

List of Tables

List of Figures

Acknowledgments

This work is made possible by the help and support (both emotional and financial) of many different people. First I would like to thank the faculty of the Department of Astronomy of Penn State for offering me the possibility of doing my Ph.D. in this lovely place. I would also like to thank my thesis advisor George Chartas for his constant support and mentoring in my formation as an astronomer. I acknowledge him for his pejorative work helping me with all the different drafts and papers that we have done together. I thank also Gordon Garmire for his financial support and unconditionality. I would like to extend special thanks to Niel Brandt for his important role in the research presented in this thesis. I thank also to the committee members (Mike Eracleous, Jane Charlton, Derek Fox, Stephane Coutu and Steinn Sigurdsson) for their helpful discussions and revision of this work. I also thank Jian Wu, Rodrigo Nemmen, Konstantin Getman, and Bret Lehmer for their friendship and helpfulness in solving different technical challenges related to this work.

Finally, I thank my parents for giving me life and constant support, and I especially thank my wife, for her sacrifice in coming to the USA with me, and her constant emotional support, love and partnership that made the whole difference during the time I was a graduate student.

No man ever steps in the same river twice, for it is not the same river and he is not the same man. –Heraclitus

Chapter 1

The X-ray evolution of inflows and outflows in Active Galactic Nuclei.

1.1 What are AGNs and why are they important?

Currently it is commonly accepted within the astronomical community that in the center of every galaxy lies a supermassive black hole (Kormendy & Richstone 1995). When the accretion onto the black hole is large enough that the emitted radiation dominates the luminosity output of the entire galaxy these objects are referred to as active galactic nuclei (hereafter AGNs). AGNs are present in approximately 10% of all galaxies (e.g., Silverman et al. 2008), however, it is thought that all the galaxies that we see today have had periods of strong accretion activity in the past in order to form their supermassive black holes (Soltan 1982). An example of a quiescent (or inactive) black hole is our galaxy and a case of an active black hole is 3C 273, the first quasar ever discovered. A typical way of identifying black hole activity is detecting X-ray emission from the center of a galaxy with a luminosity above $L_{\rm X} \gtrsim 10^{41}$erg s^{-1}. When the optical B-band absolute magnitude of an AGN is greater than $M_B \lesssim -23$ (or $L_B \gtrsim 10^{44}$ erg s^{-1}; Schmidt & Green 1983) it is usually referred to as a quasar. When quasars were discovered in the 50's they were thought to be stars with peculiar spectra, and were therefore named quasi stellar objects (QSOs).

The study of AGNs offers the unique opportunity of learning about the nature of supermassive black holes and their environments. As we will see in §1.2, the study of AGNs also provides crucial information for understanding galaxy formation and evolution.

1.1.1 Key Properties of AGNs

Here we present several important properties and definitions related to AGNs. Many of these will be heavily used in the next sections and chapters.

1.1.1.1 Black-hole mass estimates

The mass of the black hole is often derived from the widths of broad emission lines originating from gas orbiting the central black hole. In general, since broad emission lines of QSOs show velocity broadening of $v \sim 10^4$ km s^{-1}, coming from an emission region with a size of $r \approx 0.01$ pc, the mass of the black hole ($M_{\rm BH}$) can be estimated by:

$$\frac{v^2}{r} = \frac{GM_{\rm BH}}{r^2}, \tag{1.1}$$

from which we obtain $M_{\rm BH} \sim 10^8 M_\odot$. A more precise method of estimating black hole masses is "Reverberation Mapping" in which one observes the response of the broad emission lines to variations of the continua. From these studies the reverberation distance r can be approximated by expressions of the type $r \propto L^\delta$ where $\delta \sim 0.5$ (e.g., Bentz et al. 2009). A recent study (Vestergaard & Peterson 2006) estimates r from reverberation mapping of the Hβ line and derives the black hole mass from the following expression

$$\frac{M_{BH}}{10^6 M_\odot} = 8.3 \left[\frac{\rm FWHM(H_\beta)}{10^3 {\rm km\ s^{-1}}}\right]^2 \left[\frac{\lambda L_\lambda (5100\mathring{A})}{10^{44} {\rm erg\ s^{-1}}}\right]^{0.5}. \quad (1.2)$$

It is important to note that equation (1.2) is not applicable to every broad line AGN, given that the detection of the Hβ line in an optical spectrum is restricted by the "optical observing window"[1]. In view of the latter, other lines such as Mg II and C IV are also used. The C IV line is the most unappealing line to use given that it could contain non-virial components (e.g. disk wind, Shemmer et al. 2008). Note that there are many other ways of estimating black-hole masses, however, most of these methods are limited to close-by galaxies. Examples of additional methods make use of the dynamics of stars, the Keplerian motion of water massers, and the $M_{\rm BH} - \sigma$ relation (see §1.2.1.2).

1.1.1.2 Schwarzschild radius

The Schwarzschild radius (R_S) is the radius at which a test mass (mass m) moving at the speed of light (c) would not be able to escape from the gravitational field of a point mass (mass M). This radius is found by solving the following equation

$$\frac{1}{2}mc^2 - \frac{GMm}{R_{\rm S}} = 0, \quad (1.3)$$

from which we obtain $R_{\rm S} = 2GM/c^2 \sim 3 \times 10^{13} M_8$ cm, where M_8 is the mass of the point mass in units of $10^8 M_\odot$. We note that equation (1.3) is a classical mechanics formula attempting to describe a general relativistic effect. If we use the general relativistic metric for a non-rotating black hole we obtain that $R_{\rm S}$ corresponds to the event horizon, and therefore the simple derivation is valid for the case of a non-rotating black-hole.

1.1.1.3 Eddington luminosity and Eddington ratio

If the luminosity of a radiating source is large enough that its radiation pressure is greater than the gravitational force bounding it then the material surrounding this source will escape. Remembering that the momentum transfered by photons of energy E is $\Delta p = E/c$, the material surrounding a radiating source will be bounded by gravity up to a maximum luminosity given by

[1] The laboratory wavelength of the Hβ line is 4861Å. If we assume that the optical observing window is between (4000-8700)Å then from ground telescopes we can detect the Hβ line up to $z \sim 0.75$. After this limit the line is present in some specific near infrared windows. For example in the J-band, H-band and K-band the Hβ line will be visible in the redshift ranges $\Delta z \sim 1.4 - 1.8$, $\Delta z \sim 2.1 - 2.7$, and $\Delta z \sim 3.2 - 3.9$ respectively.

$$\frac{L \cdot \sigma_T}{4\pi r^2 c} = \frac{G m_p M}{r^2}. \tag{1.4}$$

Where σ_T is the Thompson cross section, m_p is the proton mass, r is a distance from the central source and M is the mass of the central source. The maximum luminosity ($L_{\rm Edd}$) is given by

$$L_{Edd} = \frac{4\pi c G m_p M}{\sigma_T} \sim 3\ 10^4 \frac{M}{M_\odot} L_\odot, \tag{1.5}$$

and it is called the Eddington luminosity. In addition, the ratio of the bolometric luminosity of the source to its Eddington luminosity (i.e., $L_{\rm bol}/L_{\rm Edd}$) is defined as the Eddington ratio.

1.1.1.4 Accretion rate and AGN lifetime

The mass accreted onto a black hole is converted into energy with an efficiency of η which will depend on the metric of the black hole; for a non-rotating black hole $\eta \approx 0.06$ and for a maximally rotating Kerr black hole $\eta \approx 0.32$ (e.g., Thorne 1974).

If we assume that the Eddington ratio is ϵ we have the following equation

$$L_{\rm bol} = \epsilon L_{\rm Edd} = \eta \dot{M}_{\rm Edd} c^2. \tag{1.6}$$

and therefore $\epsilon = \dot{m}$ where $\dot{m}$ is the accretion in units of the Eddington accretion rate, given by

$$\dot{M}_{\rm Edd} = \frac{L_{\rm Edd}}{\eta c^2}. \tag{1.7}$$

Since $L_{\rm Edd}$ is proportional to the mass of the black-hole equation (1.6) has a solution given by (see e.g., Salpeter 1964)

$$M = M_0\ e^{\frac{t}{\tau}} \quad \text{with} \quad \tau = \frac{\eta \sigma_T c}{4\pi G \epsilon m_p} \sim 4.5 \times 10^7 \text{ yrs}. \tag{1.8}$$

In the last step we assumed[2] that $\epsilon \sim 1$ and $\eta \sim 0.1$. The value of τ in equation (1.8) is a rough estimate of the time scale of black-hole growth. This time scale is similar to the estimated duration of AGN activity in N-body simulations of galaxy mergers (e.g., Di Matteo 2005). The value of τ given by equation (1.8) also agrees with the value inferred from surveys of quasar lifetimes (e.g., Yu & Tremaine 2002). [3]

[2]Measured Eddington ratios for high redshift ($z \gtrsim 1$) and massive black holes $M_{\rm BH} \gtrsim 10^8\ M_\odot$ show lognormal distributions peaking at $L_{\rm bol}/L_{\rm Edd} \sim 1/4$ and with dispersions of ≈ 0.3 dex (Kollmeier et al. 2006). Therefore, for the time-scale obtained in equation (1.8), the underlying assumption is that during the periods of black-hole growth the quasars are accreting close to their peak luminosity ($\epsilon \sim 1$) .

[3]An estimate of the lifetime of quasars with black-hole masses greater than a threshold M_* is given by

$$\tau(> M_*) = \frac{\int_{L(M_*)}^{\infty} \int_0^{t_o} \phi(L,t) dL dt}{\int_{M_*}^{\infty} n(M'_*, t_o) dM'_*};$$

1.2 AGN evolution and quasar outflows

This section provides a general overview of important results regarding AGN evolution and quasar winds. We mainly focus on results related to the scientific goals of this thesis. In §1.2.1, we describe the main observational results that motivated this thesis. In §1.2.2 we provide a brief description of observational constraints we obtained from X-ray observations of AGNs that allowed us to better understand AGN evolution. In §1.2.3, we describe plausible models to explain our X-ray observations of AGNs. Finally in §1.2.4, we provide a general description of AGN winds and information about their properties obtained from X-ray and optical observations of their spectral signatures.

1.2.1 Observational Studies of AGN Evolution.

Observations of local and high redshift normal and active galaxies obtained in the last fifty years have resulted in two major discoveries. First, optical and X-ray observations point to a luminosity dependent number density evolution of AGN. Second, it is found that the mass of the supermassive black hole of a galaxy is correlated with the velocity dispersion of the galaxy.

1.2.1.1 Comoving space density evolution of AGN

The evolution of the comoving density of AGNs was discovered with the first optical quasar surveys at the end of the 60's. It was first noticed that the space density of quasars increased by about two orders of magnitude between $z = 0$ and $z = 1$. (Schmidt 1968). Later on, with more sensitive surveys, it was found that the space density of quasars was increasing with redshift, reaching a peak at $z \sim 3$ and then decreasing beyond this redshift (see Figure 1.1).

In X-rays the evolution of AGNs is strongly dependent on their X-ray luminosity. As shown in Figure 1.2, the most X-ray luminous AGNs have a similar comoving space density evolution to that of powerful quasars; however, in AGNs with fainter X-ray luminosities the peak of the comoving density shifts to lower redshifts. This tendency has also been confirmed in optical surveys (Croom et al. 2009) where high luminosity AGNs (magnitude in the g-band $M_g = -28.5$) have peaks in their comoving density at higher redshifts than those of low luminosity ($M_g = -21.5$).

One possible origin of the space density evolution of quasars could be the increase of the Eddington ratio with redshift (e.g., Kauffmann & Haehnelt 2000). Another explanation of the space density evolution could be that on average the mass of high redshift quasars is larger than the mass of lower redshift AGNs. This means that massive black holes were already in place at redshifts near the peak in the space density of quasars

---

where $\phi(L,t)$ is the quasar luminosity function, i.e. the number of quasars with luminosities between L and $L + dL$ and at cosmological time between t and $t + dt$ per comoving volume, and $n(M_*, t_o)$ is the number density of galaxies with masses between M_* and $M_* + dM_*$ at the present time (t_o). Notice that in Yu & Tremaine (2002) the authors assume $M_* = 10^8 M_\odot$, black holes emitting at Eddington luminosities and luminosity function in the B-band. In this same work $n(M'_*, t_o)$ is approximated by counting the number of black holes of mass M_* in nearby galaxies through the use of the $M_{\rm BH} - \sigma$ relation (see §1.2.1.2). The conclusion from Yu & Tremaine (2002) is that the lifetime of quasars is $\tau(> M_*) \sim (3 - 13) \times 10^7$ yrs.

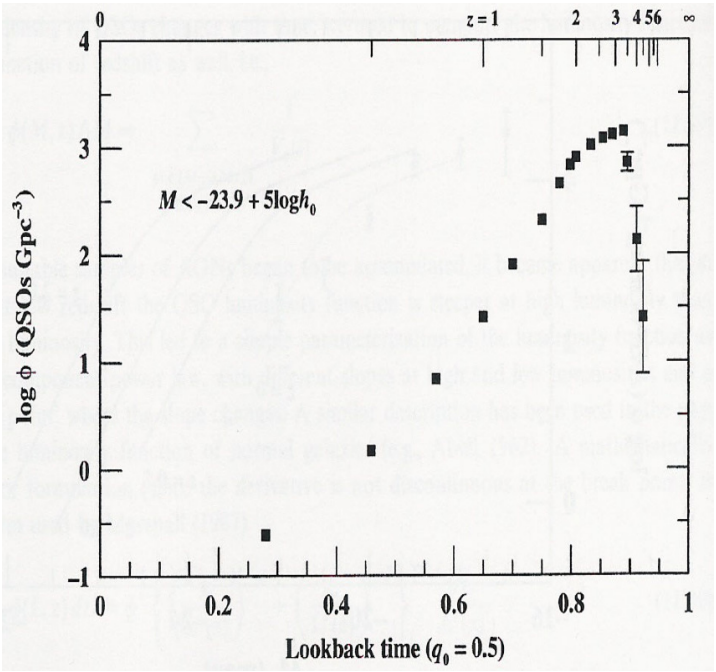

Fig. 1.1 Comoving space density (in Gpc^{-3}) of quasars with $M < -23.9 + 5 \log h$ as a function of look-back time (or redshift), h is the Hubble constant in units of 100 km s^{-1}Mpc^{-1} . The luminosity is presented as a function of the monochromatic magnitude at 1215Å (rest-frame). This is a modified version of Figure 8 from Warren et al. (1994) found in Peterson (1997).

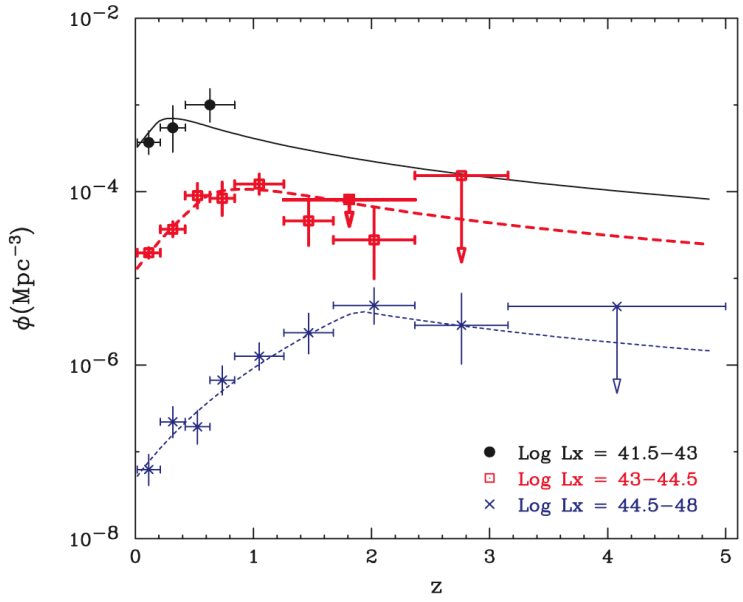

Fig. 1.2 Comoving space density of AGNs (in Mpc^{-3}) as a function of redshift. The sample has been divided in 3 luminosity bins, log $L_{\rm X} = 41.5 - 43$ (circles), log $L_{\rm X} = 43 - 44.5$ (squares) and log $L_{\rm X} = 44.5 - 48$ (stars). The lines are calculated from fits to the data using two smoothly connected power-law functions (from Ueda et al. 2003).

($z \sim 3$), and now at $z = 0$ most of them are dormant. The fact that in the local universe less massive black holes than in the past ($z \gtrsim 1$) are active now is commonly referred to as downsizing. At present, there is substantial evidence in favor of the downsizing scenario. For example, starburst galaxies show downsizing in their stellar masses, i.e., the mean mass of stars in star forming galaxies is smaller in the local universe when compared with the $z \sim 1$ universe (Cowie et al. 1996; Bundy et al. 2006; Cowie & Barger 2008). Additionally, there are several recent observational studies (e.g., Heckman et al. 2004; Barger et al. 2005) that support the downsizing of black-hole masses of AGNs.

1.2.1.2 $M_{\rm BH} - \sigma$ relation.

An intriguing relation has been discovered between the mass of the supermassive black-hole ($M_{\rm BH}$) and the velocity dispersion of the stars in the galaxy's bulge (σ). This $M_{\rm BH} - \sigma$ relation was first discovered in galaxies near the Milky Way (Gebhardt et al. 2000; Ferrarese & Merritt 2000).

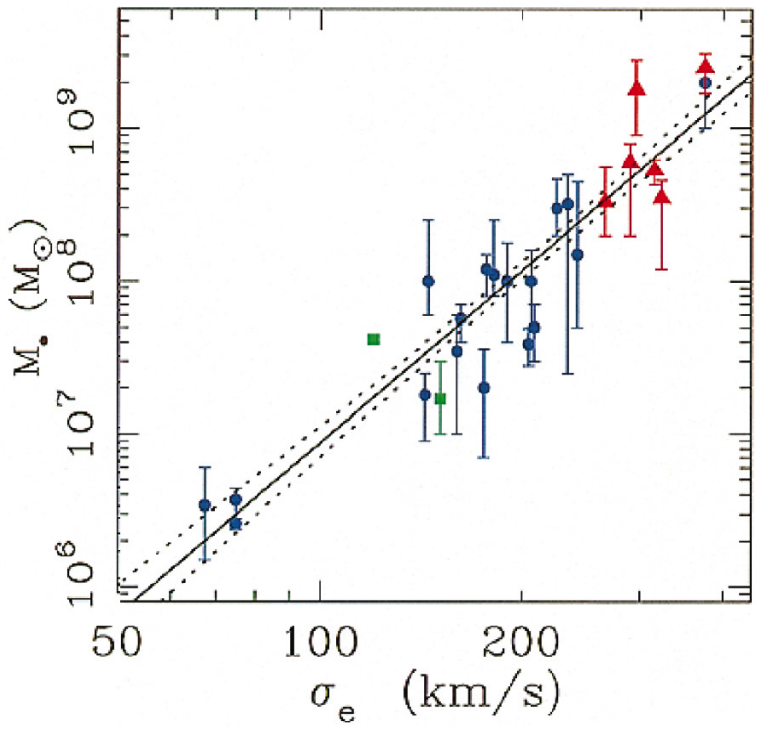

Fig. 1.3 Black hole mass versus luminosity-weighted velocity dispersion, from Gebhardt et al. (2000). The galaxy black hole masses have been estimated from maser detections (squares), gas kinematics (triangles) and stellar kinematics (circles).

As shown in Figure 1.3 (from Gebhardt et al. 2000) $M_{\rm BH}$ increases with σ as a power law given by

$$M_{\rm BH} = 1.2(\pm0.2) \times 10^8 M_\odot \left(\frac{\sigma}{200 \text{ km s}^{-1}} \right)^{3.75(\pm0.3)}. \quad (1.9)$$

This result suggests a possible interchange of energy (or feedback) between the central black hole and its host galaxy. The feedback mechanism has to be powerful and at the same time it must act on time-scales long enough to produce a substantial transport of energy from the black hole to the surrounding galaxy. We note that equation (1.9) can also be used to estimate the masses of black holes in the local universe (see e.g., Heckman et al. 2004).

We conclude that the evolution of the space density of AGNs indicates a period of major black-hole activity at $z \sim 3$. Associated with this enhanced accretion activity it is also expected that some sort of feedback mechanism may have existed between the supermassive black hole and its host galaxy.

1.2.2 X-ray Spectra of AGN

Through the use of observations primarily in the X-ray band this thesis attempts to improve our understanding of AGNs and galaxy evolution. In this section we briefly introduce AGN properties that can be constrained from observations of the X-ray spectra of AGN.

In this work we study the emission of AGNs from the UV to X-rays with particular emphasis in the X-ray band. The currently accepted standard model of AGNs postulates that most of their emission originates from a hot accretion disk that radiates mostly in UV and optical bands (Shields 1977). This disk has a hot atmosphere called the "corona" where most of the 0.2-10 keV observed emission of AGNs is thought to originate from. The fast variability of AGNs in the X-ray band (e.g., Reeves et al. 2002; Brenneman et al. 2007), and studies of microlensed quasars (e.g., Morgan et al. 2008; Chartas 2009b) suggest that the X-ray emission originates very close to the central black-hole, implying that the size of the corona is a few Schwarzschild radii. The mechanism that is thought to produce this X-ray emission in the corona is inverse Compton scattering of the UV photons from the accretion disk by the hot electrons in the corona (e.g., Haardt & Maraschi 1991). The X-ray spectra of AGNs are to first order approximated by a power-law $f_\nu \propto \nu^\alpha$ (flux dependency on frequency ν) or typically plotted as photon counts (S) per unit time per unit area as a function of energy (E), with the power-law expressed as $S \propto E^{-\Gamma}$; where $\Gamma = -\alpha + 1$ is referred to as the photon index. At high energies ($\gtrsim$ 10 keV), the X-ray spectra can contain an additional feature called the Compton hump (see dashed curve of Figure 1.4). The origin of the Compton hump is thought to be reflection of the hard photons of the corona from the surface of the accretion disk (Lightman & White 1988). A significant fraction of X-ray spectra also contain features produced by absorption from the host galaxy and from material intrinsic to the AGN, such as the failed wind (also referred to as the shield). This absorption typically results in the attenuation of the spectra at energies $\lesssim$ 2 keV (see dotted lines of Figure 1.4). The signature of this absorption will depend on the column density (N_H), covering fraction and ionization state of the absorbing medium. Although simple analytic expressions are used to describe absorption for a neutral absorber (e.g, Morrison

& McCammon 1983), for ionized absorbers the formulas are more complex (e.g, Done et al. 1992). Additionally, a detailed analysis of an ionized absorber requires the use of a sophisticated photoionization code. The X-ray spectra also contain signatures of highly ionized intrinsic material which in some cases can be seen as outflowing from the AGN center. These signatures are manifested as absorption lines of highly ionized elements such as iron ions (Chartas et al. 2002; Reeves, O'Brien & Ward 2003; Chartas et al. 2007a). In this work we use the photoionization codes XSTAR (Kallman & Bautista 2001) and CLOUDY (Ferland al. 1998) to study the state of the gas, around a high redshift quasar, which is producing outflow signatures in X-rays. Finally, in every AGN we must consider the absorption originating from our galaxy. This Galactic absorption is well fitted by a neutral absorber and is obtained through the use of tables inferred from Galactic H I surveys (see e.g., Dickey & Lockman 1990).

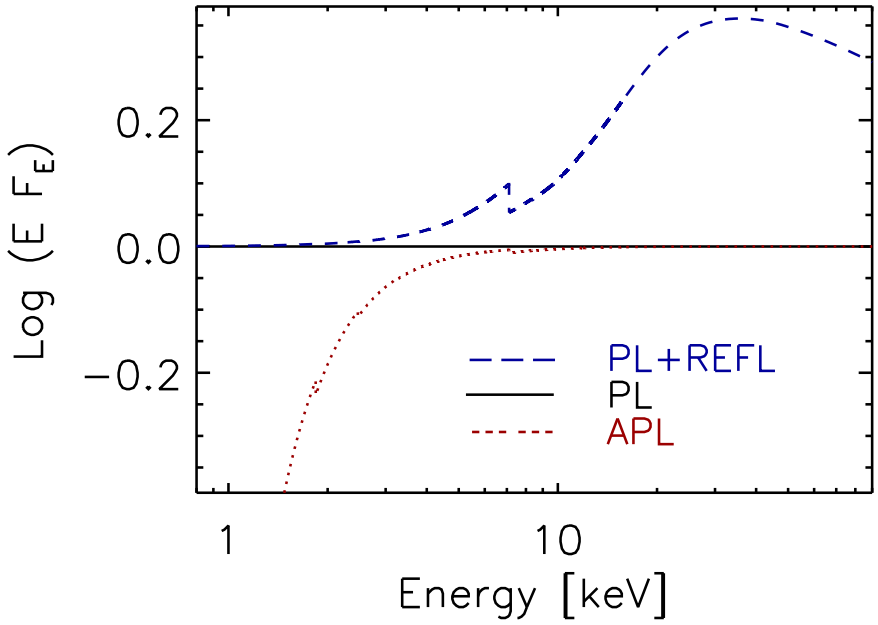

Fig. 1.4 Energy times flux (arbitrary units) as a function of Energy for three typical models of AGN emission. The solid line is a featureless power-law (PL) with $\Gamma = 2$ (or $\alpha = -1$). The dotted line is a absorbed power law ($\Gamma = 2$) with neutral absorption (APL; log $(N_{\rm H}/{\rm cm}^{-2}) = 22$) which corresponds to the XSPEC model WABS*POW. The dashed line corresponds to a power law ($\Gamma = 2$) with a reflection component (PL+REFL) generated with the XSPEC model PEXRAV (Magdziarz & Zdziarski 1995). The parameters used in the PEXRAV model are a reflection-scaling factor of $R = 2.0$, an inclination angle of the reflector of $i = 63^{\circ}$ (PEXRAV default), and a cut-off energy of $E_{\rm cut} = 1000$ keV.

We conclude that from the study of the X-ray spectra of AGNs we can extract information about an AGN's inner regions and the material that surrounds the central engine. Observational studies aimed at tracking the evolution of X-ray spectral parameters such as Γ, $N_{\rm H}$, and $L_{\rm X}$ will allow us to better comprehend the connection between

the corona and disk, the physical properties of the gas surrounding the central engine, and the evolution of the X-ray space density of AGNs.

1.2.3 AGN activation through mergers.

In the last two-decades there has been substantial progress in the field of numerical N-body simulations aimed at explaining AGN evolution. One of the key ingredients of these simulations is galaxy collisions. A main result of these numerical simulations is that after the first galaxies form[4], they start to merge into larger galactic structures. During the process of merging, galaxies radiate strongly due to the accretion of gas onto their centers, and thus become active. Observations of binary AGN SDSS J1254+0846 show how galaxy mergers might be producing AGNs (Green et al. 2010). Interestingly enough, the merger models successfully predict the evolution of the space density of quasars and at the same time the presence of strong winds co-evolving with the stages of galaxy coalescence (e.g., Hopkins et al. 2005a; Di Matteo 2005; Degraf, Di Matteo & Springel 2010).

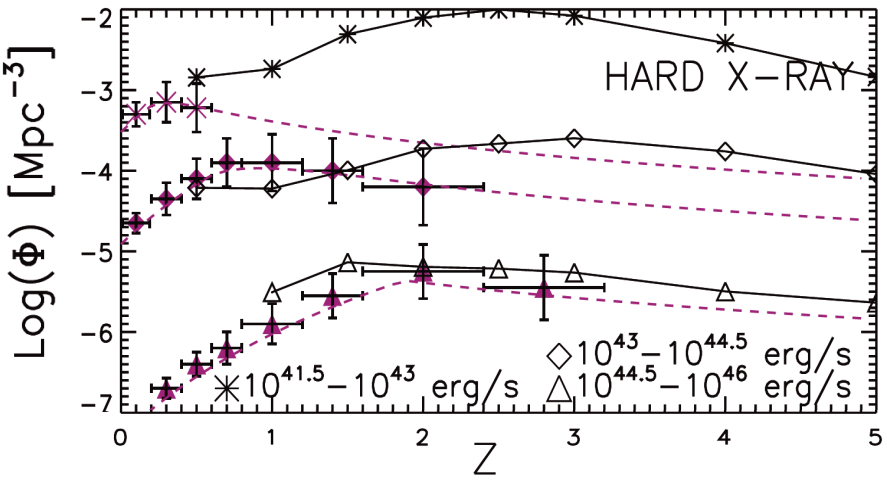

Fig. 1.5 Comoving space density of quasars (in Mpc^{-3}) as a function of redshift. The sample has been divided in 3 luminosity bins, log $L_{\rm X} = 41.5 - 43$ (stars), log $L_{\rm X} = 43 - 44.5$ (rhombs) and log $L_{\rm X} = 44.5 - 48$ (triangles). The dashed lines are calculated from fits to the data using smoothly connected two power-law functions (from Ueda et al. 2003). The continuous lines have been calculated using the N-body simulations of Degraf, Di Matteo & Springel (2010) for black holes with $M > 10^6 M_{\odot}$.

Numerical simulations of galaxy mergers (e.g, Hopkins et al. 2005a; Springel et al. 2005; Di Matteo 2005) have successfully predicted many properties of AGNs and galaxies. Among the most important results obtained from these simulations are the reproduction of the $M_{BH} - \sigma$ relation, and the lifetimes of quasars of $\sim 10^7 - 10^8$ yrs which are in agreement with current estimates from quasar surveys (see e.g., Yu &

[4]The first galaxies were formed around 1 billion years after the big bang ($z \sim 6$)

Tremaine 2002). In the galaxy-galaxy merger simulations of Hopkins et al. (2005a,b) the authors found that quasars have stages of accretion evolving with time. In the first accretion stage quasars have $L_X \sim 10^{41} - 10^{42}$ erg s^{-1} well below the peak observed X-ray quasar luminosity $\sim 5 \cdot 10^{44}$ erg s^{-1}. In this particular stage the AGNs have low column densities ($\log (N_{\rm H}/{\rm cm}^{-2}) \lesssim 22$). In the second accretion stage, quasars reach a luminosity close to their peak ($L_X \sim 10^{44.5}$ erg s^{-1}) and have high column densities ($\log N_{\rm H} \gtrsim 22$) due to the fact that more gas is being channelled into the AGN. Finally in the last stage, also called the "blowout phase", thermal feedback from the growing accretion heats the surrounding gas, driving a strong wind that eventually cuts off the accretion process. In this final stage, it is expected that the merged galaxy will have a low column density.

Galaxy-galaxy merger simulations by Di Matteo (2005) and Springel et al. (2005) in general predict similar phases as those presented by Hopkins et al. (2005a); however in the first two phases star formation is considered. In the early stages of the Di Matteo and Springel et al. simulations, the inflow of mass produced by the merger will promote star formation and once the AGN is ignited an AGN wind will deplete the available gas and inhibit any further star formation. We note that almost every simulation of galaxy mergers predicts a phase where strong outflows are present. The presence of these winds will eventually halt the accretion process and at the same time shut-down star formation in the galaxies (e.g., Granato et al. 2004; Hopkins et al. 2005a; Springel et al. 2005; Di Matteo 2005).

The use of N-body simulations of many galaxies[5] in large volume boxes (length $\sim 40h^{-1}$ Mpc; Di Matteo 2008; Degraf, Di Matteo & Springel 2010) has contributed to the success of these simulations to explain among other things the evolution of the quasar space density. In order to make calculations on a realistic time-scale Degraf, Di Matteo & Springel (2010) performed their simulations using galaxies with a resolution lower than those used for galaxy-galaxy mergers (e.g., Springel et al. 2005; Di Matteo 2005).[6] Despite the success of the Degraf, Di Matteo & Springel (2010) simulations they do not provide an accurate picture of the evolution of the comoving space density of AGNs in different X-ray luminosity bins. As Figure 1.5 shows, the comoving density of the simulated high luminosity AGNs matches the results found by Ueda et al. (2003). However, for the fainter AGN population the simulations predict that the comoving number density peaks at a higher redshift than observed. A possible explanation of this disagreement (as suggested in Degraf, Di Matteo & Springel 2010) would be the coarse resolution used in the simulations in combination with a possible observational bias produced by an unaccounted population of heavily absorbed faint AGNs.

To conclude this section we note that the merger simulations are on the right track of predicting and possibly explaining most of the observational results of AGN evolution. The models incorporated in these simulations include powerful AGN outflows during the merging of galaxies and thus are consistent with a picture in which winds provide a

[5] In the simulations of Di Matteo (2008) and Degraf, Di Matteo & Springel (2010), the total number of particles is $\sim 10^7$, therefore if we assume $\sim 10^4$ particles per galaxy then there are ~ 1000 galaxies in a volume box.

[6] In the Degraf, Di Matteo & Springel (2010) simulations the number of particles assumed for each galaxy is $N_p \sim 10^4$ (Di Matteo 2008); for the galaxy-galaxy collision simulations of Springel et al. (2005) each galaxy has $N_p \sim 10^6$.

feedback mechanism controlling the co-evolution of black-hole activity with their host galaxies. Observations of the energetics and dynamics of these winds are essential in order to evaluate their relevance in the evolution of galaxies. Observations of outflows will also allow us to place better constraints on current models of AGN activation.

1.2.4 AGN winds

In this section I provide a basic description of AGN outflows and focus on ones that have velocities comparable to the speed of light. More details are also provided in the introductions of chapters 3 and 4.

1.2.4.1 Spectral signatures of BAL quasars

Since our study of winds is centered on broad absorption line (BAL) quasars we provide a brief description of their properties in this section. The widths of the absorption lines observed in the UV and optical spectra of BAL quasars are in general larger than 2000 km s^{-1}(Weymann et al. 1991). BAL QSOs are divided into two groups based on the ionization state of the outflowing material. If a BAL QSO contains absorption troughs from only high-ionization species (e.g., C IV, N V and O VI) it is called a HiBAL; if it contains absorption troughs from low-ionization species (e.g., Mg II, Fe II and Al III) it is called a LoBAL.

A parameter commonly used to describe the ratio of the UV to X-ray flux of AGNs is α_{ox} (Tananbaum et al. 1979). This parameter represents the spectral index of a hypothetical power law connecting two points in the spectra, one at 2500 Å and the other at 2 keV, both in the quasar's rest frame i.e.,

$$\alpha_{ox} = \log\frac{F_\nu(2\mathrm{keV})}{F_\nu(2500\text{Å})}/\log\frac{\nu(2\mathrm{keV})}{\nu(2500\text{Å})} = 0.3838\ \log\frac{F_\nu(2\mathrm{keV})}{F_\nu(2500\text{Å})}. \tag{1.10}$$

BAL quasars in general appear to be heavily obscured in X-rays (e.g., Gallimore et al. 2006) and therefore their α_{ox} values (uncorrected for intrinsic absorption) tend to be lower than those of normal unabsorbed AGNs (e.g., Green & Mathur 1996; Gibson et al. 2009). In addition, the equivalent width of the C IV line of BAL quasars is found to be anticorrelated with α_{ox} (Brandt, Laor & Wills 2000), probably indicating that radiative driving in these sources is an important mechanism controlling the dynamics of the UV absorber (see §1.2.4.2). Velocities of the outflowing UV absorbers in BAL quasars range between a few thousand km/s to speeds as great as $\sim 0.2c$ (Rodriguez-Hidalgo et al. 2007) .

The commonly accepted model of BAL quasars posits that all quasars have winds and the reason we observe outflows in only a fraction of them is due to their orientation (Weymann et al. 1991). Numerical simulations of quasar winds suggest that BALs are observable when the line of sight intersects the funnel shaped structures of gas launched from the disk in the vicinities of the black-hole (e.g., Proga et al. 2000; Murray et al. 1995). These simulations indicate that the outflows are near equatorial and that near the black hole lies a shielding gas (Murray et al. 1995) which softens the X-ray spectra. Recent observations also suggest that a fraction of BAL QSOs may contain polar winds

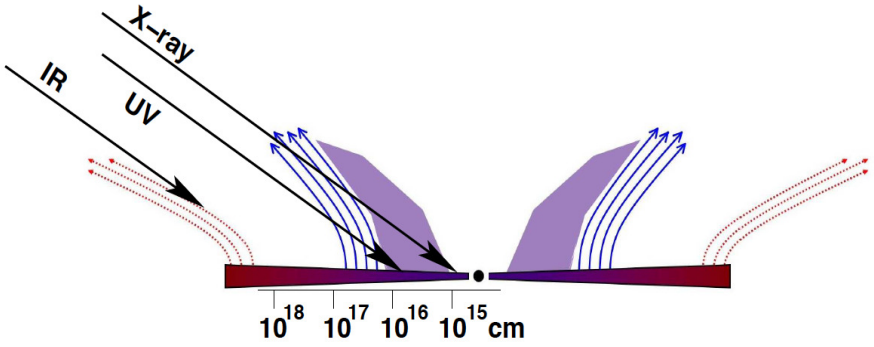

Fig. 1.6 A diagram of the structure of winds in radio-quiet AGNs. The innermost structure corresponds to the shielding gas (shaded area), the solid streamlines represent the UV BAL-wind and the dotted streamlines represent the dusty wind (observable in infrared) (from Gallagher & Everett 2007).

(e.g., Wang et al. 2008). This shielding gas is not expected to cover the line of sight towards the UV emission region (see Figure 1.6). The gas that produces the blueshifted absorption features in the X-ray band probably lies between the shielding gas and the UV outflow region.

The gradient of the velocity in the outflows of BAL quasars is reflected in the broadening of the absorption trough. These funnel shaped structures are expected based on the simulations of (e.g., Proga et al. 2000; Murray et al. 1995) to cover between $(10-20)\%$ of the source in agreement with the observations of the fraction of BAL quasars found (e.g., Hewett & Foltz 2003). The ratios of equivalent widths of the broad emission and absorption features provide estimates of the covering fraction of BAL quasars $\lesssim 20\%$ (Hamann, Korista, & Morris 1993). These estimates suggest not only that these features are very localized but also that winds should be present in the majority of quasars. A review of these models and an illustration showing a plausible wind geometry is presented in Figure 1.7 taken from Elvis 2000.

As a final remark we emphasize that in this thesis we study the X-ray spectral signatures of BAL winds. The large absorption present in BAL quasars and the low resolution of the available X-ray spectra have limited the cases where high S/N detections can be made. In this thesis we concentrate on the $z = 3.91$ gravitationally lensed BAL quasar APM 08279+5255 which has presented clear evidence of a fast and energetic outflow.

1.2.4.2 Driving mechanisms of quasar winds

Plausible driving mechanisms of quasar winds include thermal driving, radiation driving (line and continuum) and magnetic driving. Thermally driven models produce a relatively slow wind at large radii from the black hole. This mechanism occurs when the gas sound speed is greater than the escape velocity, which decreases with radius. Thermal winds do not provide a plausible explanation of the presence of near-relativistic winds. The relatively low disk-temperatures ($T \sim 10^5$ K; UV spectra) surrounding a super-massive black-hole (SBH) suggest the presence of low ionization material over the disk.

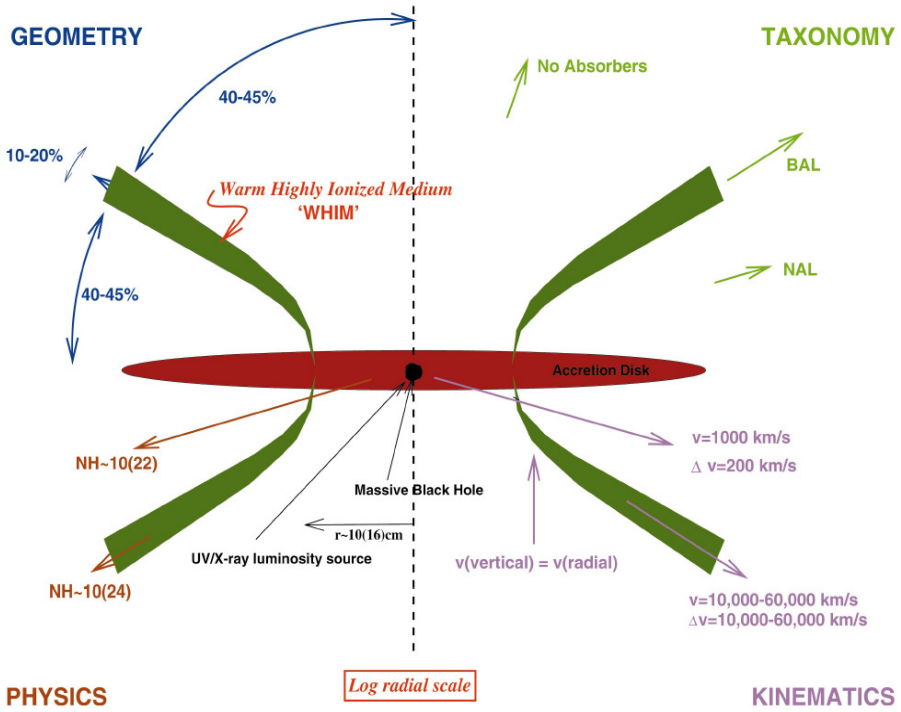

Fig. 1.7 Proposed structure of BAL outflows presented in Elvis (2000). The funnel shaped structures coming from the accretion disk are the ones producing the BAL troughs. These structures have inclination angles of $\sim 45^{\circ}$ and covering fractions between $10 - 20\%$.

Under such conditions, line-driving is a much more effective mechanism than thermal driving to produce a fast wind. A simple formula characterizing radiation-pressure driven winds is the following [7] :

$$v_{\rm wind} = [2GM_{\rm BH}(\frac{\Gamma_{\rm f} L_{\rm bol}}{L_{\rm Edd}} - 1)(\frac{1}{R_{\rm launch}} - \frac{1}{R})]^{1/2} \quad (1.11)$$

Where $\Gamma_{\rm f} = (\sigma_T + \sigma_{abs})/\sigma_T$ is also known as the "force multiplier", $R_{\rm launch}$ is the launching radius, σ_T and σ_{abs} are the Thompson (electron scattering) and the absorption cross-sections, respectively. The absorption cross-section consists of a continuum component, mainly produced by bound-free transitions and a discrete component produced by the bound-bound transitions. In general the force multiplier for a highly ionized material is dominated by the Thompson cross-section which represents the minimum radiation pressure we expect on any wind material. A radiatively-driven wind dominated by Thompson scattering can only be produced in cases where $L_{\rm bol}/L_{\rm Edd} \gtrsim 1$. In less ionized material, $\Gamma_{\rm f}$ is dominated by the absorption cross-section, therefore radiation-driving could become effective for lower values of $L_{\rm bol}/L_{\rm Edd}$ (i.e. $L_{\rm bol}/L_{\rm Edd} \gtrsim 1/\Gamma_f$). Since Γ_f in general depends on the SED of the central source as well as the ionization state of the surrounding gas, observations of a source with a variable SED may test the importance of radiative driving. For example, using equation (1.11) we infer that the terminal velocity of the wind will increase with Γ_f and decrease with $R_{\rm launch}$. The correlation between the equivalent width of the C IV lines and $\alpha_{\rm ox}$ found in BAL quasars (Brandt, Laor & Wills 2000) may be indicating an increase in the maximum velocity of the UV absorber with the softening of the SEDs of the BAL quasars. This $\alpha_{\rm ox} - v_{\rm max}$ dependence provides an argument in favor of radiative driving of the UV absorber. The main reason of the latter is that the SED softening is associated with an increase in soft X-ray absorption which in turn prevents the UV BAL wind from becoming over-ionized, and therefore, it can reach larger velocities (Gallimore et al. 2006). As we show in chapter 4 we also find possible evidence of changes in the SED that produce variations in the maximum velocity of the outflowing X-ray absorbing material in BAL quasar APM 08279+5255.

Several studies have shown that radiation-driving can result in winds with velocities of up to ∼0.1c (e.g., Murray et al. 1995; Proga et al. 2000). Higher velocity winds are usually prevented by this mechanism due to over-ionization of the accelerated wind. We note however, that recent studies (e.g., Chelouche & Netzer 2003; Everett 2005) indicate that with the appropriate shielding, initial density of the wind, AGN SED and $L_{\rm bol}/L_{\rm Edd}$, the efficiency of the outflows can be significantly increased and the wind velocities may approach near-relativistic values. Shielding is very important in producing fast radiative driven winds (e.g., Murray et al. 1995). The main reason for this is that shielding of the outflowing material from X-rays prevents this material from being completely ionized, and consequently favors conditions of radiative driving (i.e., large force multipliers).

[7] This is obtained assuming that the radiation force $F_{rad} = \Gamma_f L_{\rm bol}\sigma_T/(4\pi r^2 c)$ is higher than the gravitational force for an atom $F_{grav} = GMm_p/r^2$; i.e. $m_p dv/dt \approx L\sigma_T/(4\pi r^2 c) - GMm_p/r^2$. The solution of this equation is $v = \sqrt{-2A/r + 2B}$, where $A = GM(\Gamma_f L_{\rm bol}/L_{\rm Edd} - 1)$ and B is a constant to be determined. Imposing that $v(R_{\rm launch}) = 0$ implies $B = A/R_{\rm launch}$.

Numerical simulations of radiatively driven winds by Proga et al. (2000, 2004) have successfully predicted that these winds can be self-shielded from the emitting source and at the same time be accelerated to large velocities. These simulations are two dimensional and make the underlying assumption that the radiative source responsible for the driving is a physically thin and optically thick accretion disk. A central X-ray source is used with the goal of ionizing the media, and therefore, the radiative driving is underestimated. The Proga et al. (2000, 2004) simulations predict winds with maximum speeds $\sim 0.1c$, covering fractions ~ 0.2 and mass outflow rates which are approximately one third of the mass accretion rates. These models also suggest a feedback mechanism between disk winds and the corona (Proga 2005). This feedback is thought to be produced because winds tend to increase the effective thickness of the disk (puffed disk) and thus suppress the corona (quenching of the corona) at the expense of increasing the UV emission. As a consequence, it is expected that the presence of winds will decrease the ratio of the X-ray to UV flux. This result could give an alternative explanation of the $\alpha_{\rm ox} - $ C IV correlation (Brandt, Laor & Wills 2000). The disk-wind simulations of Proga (2005) provide important insights to the possible relationship between disk winds and the X-ray emission of AGNs.

The Magnetorotational Instability is thought to produce viscosity in the accretion disk, and consequently, it may provide a mechanism for the outward transport of angular momentum (Balbus & Hawley 1991). This mechanism, which can be effective in the presence of moderate magnetic fields, is a basic ingredient for the formation of magnetically driven winds. Magnetically driven winds are characterized by strong magnetic fields that co-rotate with the accretion disk. These co-rotating magnetic fields generate an effective way to transmit the angular momentum from the disk to the ionized material surrounding it (Blandford & Payne 1982). These magnetic fields will produce collimated outflows in the polar direction perpendicular to the plane of the accretion disk (Lynden-Bell 1996). We note that MHD (Magneto-Hydro-Dynamic) models can produce fast winds (see e.g., Kato, Mineshige, & Shibata 2004), however, they are not easily testable through observations. A recent study by Fukumura et al. (2010) claims that their MHD model could explain the distribution of absorption as a function of ionization parameter ($d\log N_{\rm H}/d\xi$) in the X-ray spectra of nearby AGNs (Fukumura et al. 2010). The sample used in their analysis contained low redshift ($z \lesssim 0.1$) AGNs with very high signal-to-noise ratio (S/N) spectra. The predictions of Fukumura et al. (2010) are not easily testable in winds similar to the one of APM 08279+5255. For example, in chapters 3 and 4 the observed outflowing material of APM 08279+5255 is found to be highly ionized ($3 \lesssim \log \xi \lesssim 4$), and therefore it is not possible to sample a large enough set of absorption lines at different ionization levels that is necessary to estimate $d\log N_{\rm H}/d\xi$. In general, for fast winds with substantial gradients in velocity, we expect to observe only the strongest absorption lines, which will be found within a narrow range of ionization levels. Additionally, the two dimensional MHD simulations of Fukumura et al. (2010) predict the formation of slow winds (maximum velocities ~ 4000 km s^{-1}) and smooth spatial distributions of density, ionization parameter and velocity. We do not expect such a scenario in the production of faster MHD winds (e.g., Kato, Mineshige, & Shibata 2004) and therefore, the approach of Fukumura et al. (2010) might not be suitable for the study of winds with speeds $\sim 0.1c$.

A possible mechanism to explain fast (with velocities up to few times 0.1c) and energetic AGN winds is the joint action of MHD and radiation-pressure forces (i.e., hybrid models; e.g., Everett 2005), with the contribution of radiation pressure becoming increasingly important in sources with higher $L_{\rm bol}/L_{\rm Edd}$.
The study of AGN-winds is an ongoing field of research. Currently there is no strong observational evidence supporting any particular driving mechanism and there are no wind models that can adequately predict the formation of near-relativistic winds in quasars. X-ray observations of quasars with fast winds will be key in providing insights into the wind driving mechanism and distinguishing between competing models.

1.3 Thesis objectives

The evolution of the space density of AGNs might have spectral counterparts which could be observable in X-rays. The main objective of this thesis is to study the spectral properties of AGNs in X-rays in order to increase our current knowledge of AGN evolution. We are especially interested in high redshift AGNs with $z \gtrsim 1.0$, because the analysis of their spectra may indicate what parameters show evolutionary trends and provide insight as to which physical processes are responsible for AGN evolution. A significant part of my thesis involves the study of quasar winds and how they may be driving quasar evolution.

In this thesis we center on the study of evolution of AGNs using two approaches: The first approach centers on studying the X-ray spectral properties of a big sample of AGNs extended over a broad range of cosmological distances. The particular objective is to study the validity and potential evolution of a correlation between the photon index (Γ) and X-ray luminosity ($L_{\rm X}$) found in a small sample of high redshift ($z \gtrsim 1.5$) gravitationally lensed radio-quiet AGNs by Dai et al. (2004). The results could be very important in understanding the physical properties controlling the emitting corona, its connection to the accretion disk and its possible evolution. In order to track the evolution in terms of the X-ray spectral properties, we need deep exposures with the goal of getting a complete high S/N sample at high redshifts. With this objective in mind, we used the *Chandra* Deep Fields surveys, which are currently the deepest X-ray surveys. The exposure of each one of these surveys is higher than 1 Ms, meaning that the ACIS instrument onboard *Chandra* observed the same field of view for more than ≈ 2 weeks.
The second approach of this thesis centers on a detailed study of the gravitationally lensed BAL quasar APM 08279+5255. This source is at a high redshift ($z = 3.91$), and therefore lies close to the period where AGNs were most active. The activity is manifested in this source through its large luminosity ($L_{\rm bol} > 10^{47}$ erg s^{-1}; e.g., Irwin et al. 1998), high column density and the presence of fast (relativistic) outflows (see e.g., Chartas et al. 2002). The analysis of the X-ray signatures of these strong outflows is important in improving our understanding of galaxy evolution. The study of these outflows will also help us place better constraints on models of AGN activation and formation. Estimates of the amount of energy transported through outflows, allow us to estimate the importance of this feedback mechanism in explaining the co-evolution of the black hole with its host galaxy.

Based on the above, I list the main scientific objectives of this thesis.

1. Study of the spectral evolution of AGNs

   1.1 Study the evolution of the X-ray spectral shape of AGNs (i.e. Γ) with z.

   1.2 Study the evolution of a possible correlation between Γ vs $L_{\rm X}$.

   1.3 Study the possible evolution on AGN accretion rate and corona properties.

2. Study of AGN outflows and how they may affect AGN and galaxy evolution by regulating the growth of the black hole and the formation of the host galaxy.

   2.1 Constrain the properties of AGN outflows through the analysis of X-ray broad absorption lines in quasars; i.e., constrain the kinematics of the winds, the ionization properties of the wind and column densities.

   2.2 Simulate quasar outflows to understand their driving mechanism. Perform CLOUDY simulations to better understand the acceleration mechanism of AGN outflows. The results from these simulations will be compared to observations.

   2.3 Develop sophisticated photoionization models to fit X-ray BALs.

1.4 Outline of the thesis

In this thesis, I present a study of the X-ray properties and evolution of AGNs. Each chapter is by itself self-contained and details on each topic can be found at the beginning of each chapter. In the second chapter we use the CDFs to study the X-ray spectral evolution of a sample of AGNs covering a wide range of cosmological distances ($0.3 \lesssim z \lesssim 3.3$). In the third and fourth chapter we concentrate on the X-ray signatures of winds of the high redshift quasar APM 08279+5255. We note that chapter two centers on objective one of §1.3, and chapters three and four center on objective two of §1.3.

At the time of writing this thesis chapters two and three have been published. The titles of each chapter and references to the journals where chapters two and three were published are listed below.

- Charper 2: "Confirmation of a Correlation Between the X-Ray Luminosity and Spectral Slope of Active Galactic Nuclei in the *Chandra* Deep Fields"; Saez, C., Chartas, G., Brandt, W.N., Lehmer, B.D., Bauer, F.E., Dai, X. & Garmire, G.P. 2008, AJ, 135, 1505.

- Charper 3: "*Suzaku* Observations of Near-Relativistic Outflows in the BAL Quasar APM 08279+5255"; Saez, C., Chartas, G. & Brandt, W.N. 2009, ApJ, 697, 194.

- Charper 4: "A Study of the X-rayed Outflow of APM 08279+5255 through photoionization codes."

Chapter 2

Confirmation of a correlation between the X-ray Luminosity and spectral slope in the Chandra Deep Fields

2.1 Introduction

It is important to extend the study of quasars to high redshifts in order to understand their evolution and environments. A relevant conclusion from modern studies is that the quasar luminosity function evolves positively with redshift, having a comoving space density strongly peaked at $z \approx 2$ (e.g., Schmidt 1968; Boyle et al. 1987; Warren et al. 1994). More recent findings suggest that the evolution of the space density of AGNs is strongly dependent on X-ray luminosity ($L_{\rm X}$), with the peak space density of AGNs moving to higher redshifts for more luminous AGNs (e.g., Ueda et al. 2003; Hasinger et al. 2005).

The X-ray band probes the innermost region of the central engines of AGNs. The study of AGNs in the X-ray band provides important insights about their central engines and the evolution of the AGN luminosity function. In most AGNs, the observed X-ray continuum can be modeled using a power-law of the form $N(E) = N_0(E/E_0)^{-\Gamma}$, where Γ is the photon index. This power-law is attenuated by material in our Galaxy as well as material intrinsic to the host galaxy. Several recent studies have centered on estimating the distribution of intrinsic column densities ($N_{\rm H}$) and the fraction of AGNs having $N_{\rm H} \gtrsim 10^{22}$ cm^{-2}. Recent theoretical studies of AGNs (e.g., Hopkins et al. 2005b) suggest that the distribution of $N_{\rm H}$ is luminosity dependent; this is supported observationally with the detection of an anti-correlation between the obscuration fraction and luminosity (e.g., Steffen et al. 2003; Ueda et al. 2003; La Franca et al. 2005; Akylas et al. 2006). We note, however, recent work by Dwelly & Page (2006) reporting that the obscuration fraction may be independent of luminosity. The dependence of the obscuration fraction on redshift is a controversial issue. Some authors detect an increase of the obscuration fraction with redshift (e.g., La Franca et al. 2005; Treister & Urry 2006; Tozzi et al. 2006), while others do not find any evidence for evolution (e.g., Ueda et al. 2003; Akylas et al. 2006; Dwelly & Page 2006).

A recent mini-survey of relatively high-redshift ($1.5 < z < 4$) gravitationally lensed radio-quiet quasars (RQQs) observed with *Chandra* and *XMM-Newton* (Dai et al. 2004) indicated a possible correlation between the X-ray power-law photon index and X-ray luminosity. This correlation, characterized by an increase of Γ with $L_{\rm X}$, was found for RQQs with 2–10 keV luminosities in the range 10^{43} to 10^{45} erg s^{-1}. Such a correlation is not found in nearby $z \lesssim 0.1$ quasars (e.g., George et al. 2000). Several studies to date of high-redshift quasars do not have large enough sample sizes in the

2–10 keV luminosity range 10^{43} to 10^{45} erg s^{-1} to place any significant constraints on a possible $\Gamma - L_{\rm X}$ correlation (e.g., Reeves & Turner 2000; Page et al. 2005).

One of the concerns with the Dai et al. (2004) analysis was that the limited number of quasars in the sample, combined with the poor signal-to-noise ratio (S/N) available for several of the observations and the relatively large fraction of BAL quasars, may have led to problematic systematic effects. The number of available lensed radio-quiet quasars used by Dai et al. (2004) was limited to a total of 25 sources, of which the brightest 11 had X-ray observations. In order to increase the size of the high-redshift radio-quiet quasar sample, we have compiled a sample of 173 high-redshift AGNs with moderate-to-high S/N spectra available from the *Chandra* Deep-Field-North and *Chandra* Deep-Field-South surveys (CDF-N and CDF-S, respectively; jointly CDFs; Giacconi et al. 2002; Alexander et al. 2003).

The main scientific goal of this work is to constrain better the $\Gamma - L_{\rm X}$ correlation found by Dai et al. (2004). The significant increase in sample size allows us to place tighter constraints on the significance of the correlation. We also test the correlation in narrower redshift bands which will allow us to determine the epoch by which possible changes in the average emission properties of AGNs occurred. Currently, the two deepest X-ray surveys are the CDF-N and CDF-S with ≈2 Ms and ≈1 Ms exposures, respectively. Both surveys cover ≈300 arcmin^2 areas and target different regions of the sky characterized by low Galactic column densities and an absence of bright stars (Giacconi et al. 2002; Alexander et al. 2003). The CDFs pointings have sufficient sensitivity to detect the X-ray emission from AGNs with moderate luminosities ($L_{\rm X} \approx 10^{43} - 10^{44}$ erg s^{-1}) out to $z \approx 2 - 6$.

Radio-quiet AGNs (RQ AGNs) correspond to the majority of active galaxies ($\sim$ 90%) that contain a central active nucleus and show several differences in their spectral properties compared to radio-loud AGNs. Radio-loud AGNs have powerful sub-parsec jet-linked X-ray synchrotron self-Compton (SSC) emission, which introduces an additional component to their spectra. As a consequence RQ AGNs are observed to have, on average, steeper X-ray power-laws than radio-loud AGNs (e.g., Reeves et al. 1997). We therefore have chosen to exclude radio-loud AGNs from this study. Throughout this chapter we adopt a flat Λ-dominated universe with $H_0 = 70$ km s^{-1}Mpc^{-1}, $\Omega_\Lambda = 0.7$, and $\Omega_M = 0.3$. The *Chandra* data were reduced using the CIAO version 3.3 software tools provided by the *Chandra* X-ray Center (CXC), and the spectral analysis was performed using XSPEC version 12.

2.2 Sample selection

Our sources were selected from the CDFs, currently the two deepest X-ray surveys. The on-axis sensitivity limits for the CDF-N are $\approx 2.5{\times}10^{-17}$ erg cm^{-2} s^{-1} (0.5–2.0 keV) and $\approx 1.4 \times 10^{-16}$ erg cm^{-2} s^{-1} (2–8 keV). These limits are around two times more sensitive than those for the CDF-S (Giacconi et al. 2002; Alexander et al. 2003). The CDFs are 50–250 times more sensitive than previous X-ray surveys, detecting ≈ 900 point sources, of which ≈ 600 are AGNs and galaxies with measured redshifts (Giacconi et al. 2002; Alexander et al. 2003; Barger et al. 2003; Zheng et al. 2004).

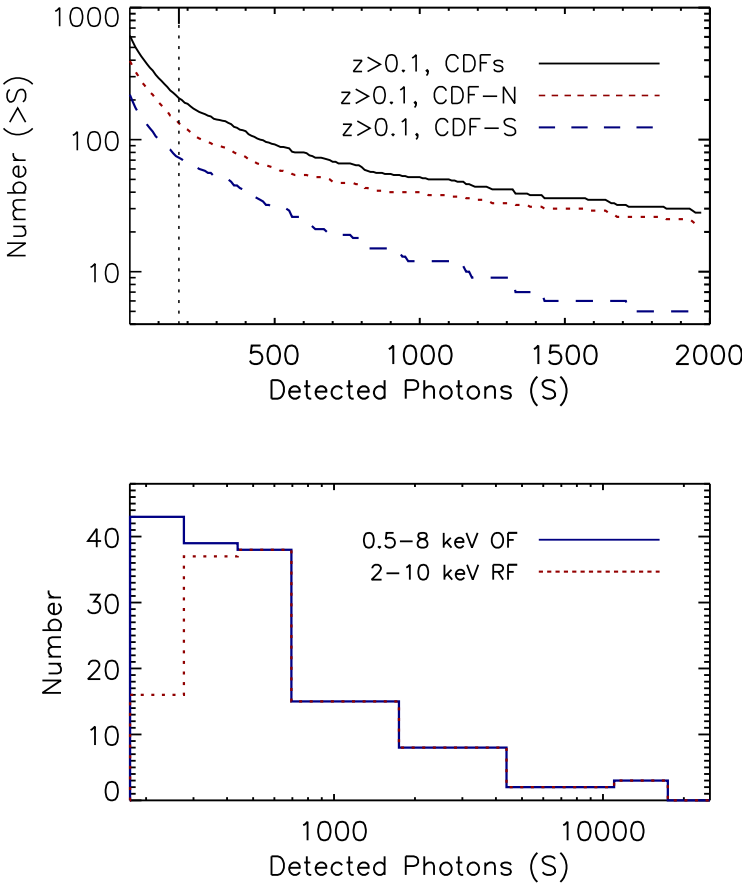

Fig. 2.1 (upper panel) Number of sources with more than S photons (0.5–8 keV observed-frame) versus S. The thick line corresponds to all CDFs sources with measured redshifts of $z \gtrsim 0.1$. The dotted line shows sources of the CDF-N survey with $z \gtrsim 0.1$, and the dashed line shows sources of the CDF-S survey with $z \gtrsim 0.1$. The vertical dotted line corresponds to S=170. Note that the sample used to generate this figure contains AGNs (both RQ and radio-loud AGNs), normal galaxies and starburst galaxies. (lower panel) Number of radio-quiet AGNs with $z \gtrsim 0.1$ vs. the number of photons (S; 0.5–8 keV) in their spectra. The solid line represents sources with fits performed in the 0.5–8 keV observed-frame band and the dotted line represents sources with fits performed in the 2–10 keV rest-frame band.

Spectroscopic and photometric redshifts were gathered from the literature (Croom et al. 2001; Barger et al. 2003; Steidel et al. 2003; Cowie et al. 2004; Mobasher et al. 2004; Szokoly et al. 2004; Wirth et al. 2004; Wolf et al. 2004; Zheng et al. 2004; Alexander et al. 2005; Colbert et al. 2005; Le Fèvre et al. 2005; Vanzella et al. 2006) and vetted to remove redshifts which did not appear to belong to the most-likely optical counterpart to each X-ray source. The latter was assessed by comparing the optical and X-ray images, which were aligned to between 0.12 arcsec and 0.25 arcsec; this notably affected the redshifts from Zheng et al. (2004), where 47 (≈14%) of the redshifts were rejected for being associated with an unlikely optical counterpart. For the ∼40 faint sources still lacking redshift estimates, we used the BPZ code (Bayesian photometric redshift estimation; Benitez 2000) and available photometry (Arnouts et al. 2001; Barger et al. 2003; Giavalisco et al. 2004) to estimate crude redshifts.

The selection criteria for our sample of RQ AGNs are (1) that the sources are radio-quiet (see below), (2) that the redshifts of the sources are greater than 0.1, and (3) that the total number of photons in the full band (0.5–8 keV) is greater than ~ 170 counts ($S \gtrsim 170$) resulting in moderate-to-high S/N spectra. The selection of a cut-off at ~ 170 counts allows an accurate estimate of the photon index, which is not possible for fainter sources (Tozzi et al. 2006). Based on the condition that $S \gtrsim 170$, the on-axis flux limits of our sample in the full band (0.5–8 keV) in the CDF-N and CDF-S surveys are $\approx 1 \times 10^{-15}$ erg cm^{-2} s^{-1} and $\approx 2 \times 10^{-15}$ erg cm^{-2} s^{-1} , respectively.

In Figure 2.1 (upper panel), we show the cumulative distribution for number of X-ray sources having more than S counts (0.5-8 keV) for the CDF-N and CDF-S. The CDFs contain 205 sources with more than 170 counts at $z > 0.1$. Most of these sources are AGNs; however, in the low-redshift regime of our sample $0.1 \lesssim z \lesssim 1.0$ we expect only a small fraction of starburst and "normal" galaxies (Brandt & Hasinger 2005). Following the classification scheme discussed in §4.1.1 of Bauer et al. (2004a), we found two starburst galaxies and one "normal" galaxy, which we remove leaving 202 AGNs in our sample.

Radio-loud AGNs were classified based on a radio-loudness parameter $R \gtrsim 10$ ($R = f_{5\mathrm{GHz}}/f_{\mathrm{B}}$, Wilkes & Elvis 1987). To find these sources, we matched the X-ray positions with radio sources using a matching radius of 2 arcsec. The flux-density at 5 GHz was obtained from the flux-density at 1.4 GHz assuming a power law radio spectrum ($f_\nu \propto \nu^{-\alpha_r}$), where $\alpha_r = 0.8$ is a characteristic radio spectral index of synchrotron radiation[1].

The flux in the B filter was obtained from Barger et al. (2003) for the CDF-N sources and from public-domain tables of the GOODS and COMBO-17 surveys for the CDF-S sources. When searching the radio catalogs[2] provided by Richards (2000) for the CDF-N and Afonso et al. (2006) for the CDF-S, we find that 29 (∼14%) out of the 202

[1] In AGNs values of α_r could be flatter than the adopted $\alpha_r = 0.8$ (e.g., Richards et al. 1998; Muxlow et al. 2005), with measured standard deviations ∼1 (e.g., Wadadekar 2004). We investigated how a flatter α_r may affect our results and find that choosing a value of $\alpha_r = 0.6$, for example, to estimate R will not change our sample of RQ AGNs, whereas, a value of $\alpha_r = 0.4$ will result in the exclusion of only two sources from our sample (1% of the entire sample) in order to satisfy $R \lesssim 10$. We conclude that our sample selection and results of our statistical analysis are not significantly affected by values of the radio spectral index as low as $\alpha_r = 0$.

[2] The radio surveys of Richards (2000) and Afonso et al. (2006) cover the entire CDF-N and CDF-S regions respectively. More details of the CDF-S radio observations are found in Norris et al. (2006).

X-ray detected AGNs were radio-loud. This leaves 173 RQ AGNs which we use for our analysis out of which 111 have spectroscopic redshifts.

2.3 Spectral extraction

The X-ray spectra of the sources of the CDFs analyzed in our study were extracted using the software routine ACIS_EXTRACT v3.94 (hereafter AE; Townsley et al. 2003; Broos et al. 2005), included in the Tools for ACIS Real-time Analysis (TARA; Oct 20, 2005) software package. [3] AE is ideal for extracting and analyzing the spectra of large numbers of point and diffuse sources observed with ACIS over multiple epochs. AE calls procedures from both CIAO (v3.3) and HEASOFT (v6.0.4) and uses calibration files that are part of the CALDB v3.2.1 product provided by the *Chandra* X-ray Center.

The ≈2 Ms CDF-N (≈1 Ms CDF-S) observations comprise 20 (10) event files. The event files were corrected for charge transfer inefficiency, bad columns, bad pixels, and cosmic ray afterglows. The event files were also filtered for time intervals of acceptable aspect solution and background levels. A detailed description of the data reduction procedures is presented in Alexander et al. (2003). Background event files and exposure maps were created by excluding circular regions centered on the detected sources with radii that are a factor of 1.1 times larger than the 99% encircled energy radii of the point spread functions at $\sim$ 1.49 keV. Source extraction regions were constructed to contain 90% of the PSF encircled energy derived from the CXC 1.4967 keV PSF libraries. There were two exceptions to this procedure. First, for sources with greater than 1000 counts in the Alexander et al. (2003) catalog we used extraction regions that contained 99% of the PSF encircled energy. Second, for sources with 90% encircled energy extraction regions that overlapped we reduced the extraction regions to avoid overlap. Local background extraction regions were chosen as annuli centered on the source positions with inner radii equal to that of the source extraction regions and with outer radii selected such that the background region contained at least 100 background counts and had an area at least four times that of the source region.

We note that in the current analysis we made no attempt to correct for possible spectral variability over the few year period[4] respectively of the CDFs. Spectra obtained are therefore time-averaged over the period of the observations.

2.4 Spectral analysis

Two energy bands were used to fit the *Chandra* spectra: the 0.5–8 keV observed-frame and the 2–10 keV rest-frame. To obtain the maximum S/N we utilized the observed-frame energy range of 0.5–8 keV. The lower energy bound was chosen because the *Chandra* effective area is not well calibrated below 0.5 keV, and the upper energy bound was chosen because the S/N decreases greatly above this energy for most of the sources in the sample. One advantage of using the same observed-frame energy range

[3] TARA is available at `http://www.astro.psu.edu/xray/docs/TARA/`

[4] In the CDF-N AGNs the median variability amplitude in the vignetting-corrected 0.5–8 keV observed-frame count rate is ≈ 1.9 (Bauer et al. 2004b).

for every object is that the same systematic instrumental uncertainties apply to every fit. Since most of the detected spectrum is used in the analysis, the S/N is higher than for cases where restricted energy ranges were used.

To test how the $\Gamma - L_{\rm X}$ correlation might be affected by absorption and possible contamination from other emission processes, we also fitted the spectra in the rest-frame energy range of 2–10 keV. This range was selected to avoid possible contamination from soft-excess emission that is often detected in AGNs below rest-frame energies of ~ 1 keV. The selection of the 2–10 keV rest-frame band also aids in reducing the effects of X-ray absorption. For example, assuming a source with a power-law spectrum of $\Gamma = 1.7$, $z = 1$, $N_{\rm H} \sim 10^{22}$ cm^{-2}, and solar abundances the fraction of absorbed photons is 30% in the 0.5–8 keV observed-frame band and 9% in the 2–10 keV rest-frameband. The 2–10 keV rest-frame also minimizes possible contamination from Compton-reflection emission from circumnuclear material that is thought to peak at a rest-frame energy of about 20 keV. In general, 2–10 keV rest-frame spectra have fewer counts than 0.5–8 keV observed-frame spectra. For fits performed in the 2–10 keV rest-frame band, we selected sources with more than 170 counts in this band, leaving a sub-sample of 144 RQ AGNs.

The total number of photon counts per source (S) with energies in the 0.5–8 keV observed-frame band lies in the range 170–13000. In Figure 2.1 (lower panel) we present the number of $z > 0.1$ radio-quiet AGNs in our sample versus the number of photons with energies in the 0.5–8 keV observed-frame band. The solid line applies to sources with spectral fits performed in the 0.5–8 keV observed-frame, and the dotted line applies to sources with spectral fits performed in the 2–10 keV rest-frame. The mean logarithm of S for sources with spectral fits performed in the 0.5–8 keV observed-frame is $\langle \log S \rangle = 2.74$ with a standard deviation of $\sigma \simeq 0.42$. The mean logarithm of S for sources with spectral fits performed in the 2–10 keV rest-frame is $\langle \log S \rangle = 2.83$ with a standard deviation of $\sigma \simeq 0.41$. Based on the fact that our sample contains sources with relatively low counts, we used the C-statistic (Cash 1979) to fit spectra as adopted in a similar study presented in Tozzi et al. (2006). In this study, the authors concluded that the C-statistic is more accurate than the χ^2-statistic in estimating the spectral parameters of AGNs with low-count spectra (~ 100 counts); similar arguments are presented in Nousek & Shue (1989). We also performed spectral fits in the 0.5–8 keV observed-frame band using the χ^2-statistic, with a grouping of 10 counts per bin. The sole purpose of using the χ^2-statistic was to apply the F-test to assess the use of more complex spectral models.

For the CDF-S and CDF-N sources of our sample, we assumed Galactic column densities of 8.8×10^{19} cm^{-2} (Stark et al. 1992) and 1.3×10^{20} cm^{-2} (Lockman 2004), respectively. The spectral analysis was performed using XSPEC version 12. The default spectral model used is a power law (PL; POW) with Galactic absorption (WABS). Additional model components were added to the default model in cases where the F-test showed an improvement in the fit at the $> 95\%$ confidence level (0.5–8 keV observed-frame) when these additional components were used. We refer to models comprising the default model plus additional model components as alternative models. Alternative models included an absorbed-power-law model (APL) at the redshift of the source (WABS ZWABS POW), an ionized-absorbed-power-law model (IAPL) (WABS ABSORI POW), a partial-absorbed-power-law model (PAPL) (WABS ZPCFABS POW) and/or models that included an iron line (PL+EL;APL+EL)(WABS ZGAUSS POW; WABS ZWABS ZGAUSS POW).

Table 2.1. Models used in fitting the spectra of the RQ AGNs of our sample.

Model [a]	Number of sources[b]	% of the whole sample
PL	77	44.5
APL	76	43.9
PAPL	9	5.2
IAPL	4	2.3
PL+EL	4	2.3
APL+EL	3	1.7

[a]PL≡power-law (XSPEC model WABS*POW); APL≡absorbed power-law (XSPEC model WABS*ZWABS*POW); PAPL≡partially absorbed power-law (XSPEC model WABS*ZPCFABS*POW); IAPL ≡ionized absorbed power-law (XSPEC model WABS*ABSORI*POW); PL+EL≡power-law + emission-line (XSPEC model WABS(POW+ZGAUSS)); APL+EL≡absorbed power-law + emission-line (XSPEC model WABS*ZWABS(POW+ZGAUSS)).

[b]The selection criteria for the sample of RQ AGNs of our present study were that the redshifts of the sources were greater than 0.1 and the total number of photons in the full band (0.5–8 keV) was greater than ~ 170.

We also considered models that contained a Compton-reflection component (PEXRAV), but we did not find any improvement in the fits using such models. Our finding, that none of the sources in our sample require a Compton-reflection component, is in agreement with Tozzi et al. (2006) who find that only 14 out of 321 CDF-S sources require Compton-reflection components. We note that none of these 14 sources are part of our sample mostly because they contain less than 170 counts. Even though we do not detect a significant reflection-component in our spectral fits, an unaccounted reflection-component could still be affecting the estimation of Γ (see §2.5.2.6 for details). In Table 2.1, we list the number of sources from our sample (the entire sample contains 173 RQ AGNs) fit with a particular spectral model. From Table 2.1, we notice that based on the F-test there are 92 sources with detected absorption ($\sim$53 % of the whole sample) and 7 cases with detected iron lines ($\sim$4 % of the whole sample). For visualization purposes, in Appendix A.1 we have described χ^2-statistics spectral fits using a PL and APL model for CXOJ123719.86+620955.3. This is an absorbed source with a typical number of photon counts in the 0.5–8 keV observed-frame.

Table 2.2: Properties of our sample of RQ AGNs selected from the Chandra Deep Field Surveys.

Xid[a]	z[b]	Counts[c]	Γ	$N_{\rm H}$[d]	log L_{2-10}	C-stat	dof	type[e]	model[f]
RESULTS BASED ON FITS PERFORMED IN THE 0.5–8 KEV OBSERVED-FRAME.									
CXOJ123521.32+621628.1	$0.559^{\rm sp}$	513.4	$1.51^{+0.17}_{-0.07}$	..	42.79	519.2	510	non-type 1	PL
CXOJ123528.77+621427.8	$0.850^{\rm ph}$	183.2	$1.19^{+0.92}_{-0.42}$	$5.0^{+4.6}_{-2.0}$	43.06	542.0	509	non-type 1	APL
CXOJ123529.45+621822.8	$3.000^{\rm ph}$	205.8	$0.81^{+0.24}_{-0.24}$	..	43.93	516.1	510	non-type 1	PL
CXOJ123535.21+621429.1	$2.240^{\rm ph}$	310.5	$1.64^{+0.32}_{-0.42}$	$2.6^{+1.9}_{-2.6}$	43.80	467.8	509	non-type 1	APL
RESULTS BASED ON FITS PERFORMED IN THE 2–10 KEV REST-FRAME.									
CXOJ123521.32+621628.1	$0.559^{\rm sp}$	320.5	$1.49^{+0.23}_{-0.23}$	..	42.80	386.6	349	non-type 1	PL
CXOJ123535.21+621429.1	$2.240^{\rm ph}$	256.7	$1.89^{+0.70}_{-0.62}$	$3.2^{+3.7}_{-3.2}$	43.81	176.0	165	non-type 1	APL
CXOJ123537.10+621723.6	$2.050^{\rm sp}$	365.7	$1.88^{+0.24}_{-0.23}$	..	43.94	220.0	177	type 1	PL
CXOJ123539.14+621600.3	$2.575^{\rm sp}$	604.0	$1.84^{+0.42}_{-0.40}$	$2.0^{+2.2}_{-2.0}$	44.33	161.0	149	type 1	APL

[a] Xid with RA+DEC coordinates.

[b] Spectroscopic (sp) and photometric (ph) redshifts gathered from the literature (see §2.2).

[c] Counts in the 0.5–8 keV observed-frame.

[d] In units of 10^{22} cm^{-2}.

[e] Based on Bauer et al. (2004a), source classifications from §4.1.1 (http://www.astro.psu.edu/∼niel/hdf/hdf-chandra.html)

[f] PL≡power-law (XSPEC model WABS*POW); APL≡absorbed-power-law (XSPEC model WABS*ZWABS*POW); PAPL≡partially-absorbed-power-law (XSPEC model WABS*ZPCFABS*POW); IAPL ≡ionized-absorbed-power-law (XSPEC model WABS*ABSORI*POW); PL+EL≡power-law + emission-line (XSPEC model WABS(POW+ZGAUSS)); APL+EL≡absorbed-power-law + emission-line (XSPEC model WABS*ZWABS*(POW+ZGAUSS)).

(This table is available in its entirety in a machine-readable form in the online journal. A portion is shown here for guidance regarding its form and content.)

The spectral-fitting results are presented in Table 2.2 for a sample of fits performed in the 0.5–8 keV observed-frame band (173 RQ AGNs), and the fits performed in the 2–10 keV rest-frame band (144 RQ AGNs). In Table 2.2 we provide the photon index Γ (errors at the 90% confidence level), the intrinsic column density $N_{\rm H}$ (errors at the 90% confidence level) in units of 10^{22} cm^{-2}, and the logarithm of the hard X-ray luminosity in the rest-frame 2–10 keV band in units of erg s^{-1}(hereafter referred to as L_{2-10}). Table 2.2 also includes the X-ray identification of the sources based on their RA and DEC positions, the photon counts in the fitted range, the number of degrees of freedom, and the values of the C-statistic. The last two quantities provide an estimate of the quality of the fits.

In Figure 2.2, we show the distributions of 2–10 keV luminosities (upper panel) and redshifts (lower panel) of the sources in our sample with fits performed in the 0.5–8 keV observed-frame band (solid line; 173 RQ AGNs) and the 2–10 keV rest-frame band (dotted line; 144 RQ AGNs). The luminosities of the sources in our sample cover the range $3 \times 10^{41} - 6 \times 10^{44}$ erg s^{-1} where the lower limit is mostly determined by the sensitivity limit of the CDF-N survey, while the upper limit is a statistical consequence of the fact that luminous AGNs ($L_{2-10} \gtrsim 10^{45}$ erg s^{-1}) are less numerous than lower luminosity AGNs (see e.g., Brandt & Hasinger 2005). The mean redshift and mean logarithmic X-ray luminosity of the sources with fits performed in the 0.5–8 keV observed-frame band are $\langle z \rangle \simeq 1.41$ and $\langle \log L_{2-10} \rangle \simeq 43.6$, respectively. The mean redshift and mean logarithmic X-ray luminosity of the sources with fits performed in the 2–10 keV rest-frame band are $\langle z \rangle \simeq 1.38$ and $\langle \log L_{2-10} \rangle \simeq 43.6$, respectively.

In Figure 2.3 (upper panel), we show the distributions of the photon indices of the sources with fits performed in the 0.5–8 keV observed-frame band (solid line) and the 2–10 keV rest-frame band (dotted line). We find the mean photon indices and their standard deviations for fits performed in the 0.5–8 keV observed-frame and 2–10 keV rest-frame bands to be $\langle \Gamma \rangle \simeq 1.60 \pm 0.27$ and $\langle \Gamma \rangle \simeq 1.70 \pm 0.29$, respectively. In Figure 2.3 (lower panel), we show the distributions of the intrinsic column densities of sources with significant absorption (only sources where the F-test indicated significant intrinsic absorption at the >95% confidence level are included in the distributions); sources with fits performed in the 0.5–8 keV observed-frame band are indicated with the solid line (92/173), and sources with fits performed in the 2–10 keV rest-frame band are indicated with the dotted line (82/144). In the two fitted energy ranges, the peak of intrinsic column density distribution is log ($N_{\rm H}$/cm^{-2}) $\sim$ 22.6, and there is a fraction of $\sim$40% sources from the total sample having log ($N_{\rm H}$/cm^{-2}) $>$ 22. We note that there are likely systematic errors on these column density estimates due to unmodeled absorption complexity. These parameter values and distributions are in agreement with those found in Tozzi et al. (2006) and Dwelly & Page (2006).

In Figure 2.4, we present a diagram comparing estimates of Γ obtained from fits performed in the 2–10 keV rest-frame ($\Gamma_{\rm rest}$) and fits in the 0.5–8 keV observed-frame ($\Gamma_{\rm obs}$). The size of each symbol in Figure 2.4 increases with redshift. Deviations from the straight line ($\Gamma_{\rm obs}$=$\Gamma_{\rm rest}$) are most likely statistical in nature, however, a few may be associated with the effects of intrinsic absorption, soft excesses, non-detected spectral lines, and Compton reflection.

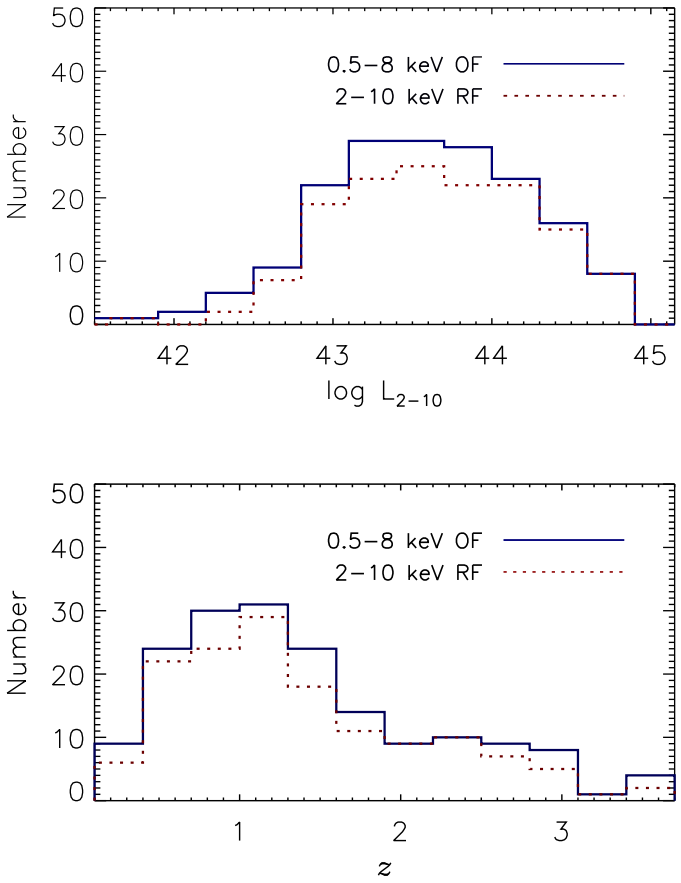

Fig. 2.2 Number of sources vs. luminosity (upper panel) and redshift (lower panel). The solid line represents sources with fits performed in the 0.5–8 keV observed-frame band and the dotted line represents sources with fits performed in the 2–10 keV rest-frame band.

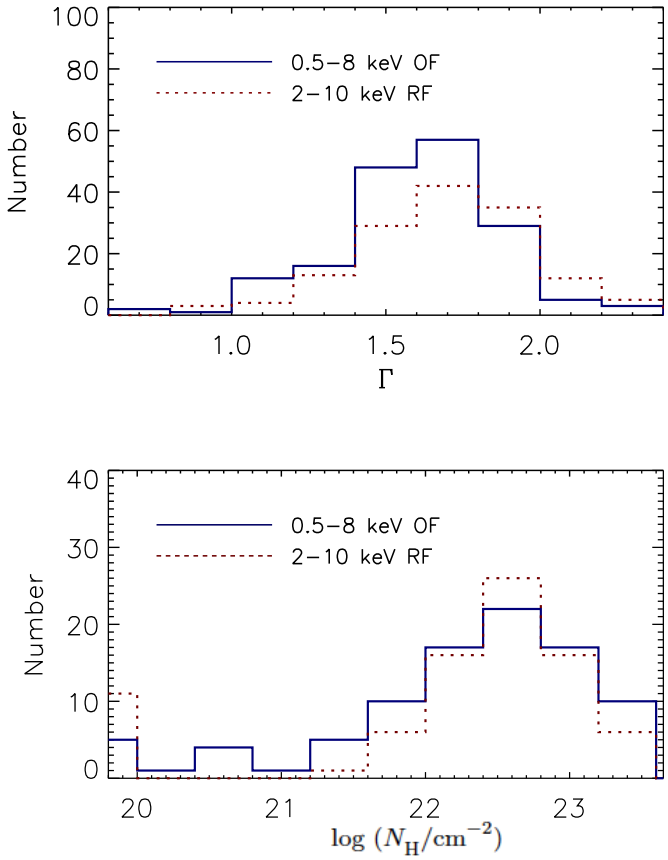

Fig. 2.3 Number of sources vs. photon index (upper panel) and column density (lower panel). In the lower panel we show only the sources with a significant detection of absorption in their spectra. The solid line represents sources with fits performed in the 0.5–8 keV observed-frame band and the dotted line represents sources with fits performed in the 2–10 keV rest-frame band.

In general, the agreement between $\Gamma_{\rm rest}$ and $\Gamma_{\rm obs}$ is good; this is first quantified by a high Pearson linear correlation coefficient ($\sim$0.73) and a very low null hypothesis probability ($\sim 4.8 \times 10^{-25}$). Secondly, this agreement is quantified by testing whether the linear relation between $\Gamma_{\rm rest}$ and $\Gamma_{\rm obs}$ is consistent with $\Gamma_{\rm rest} = \Gamma_{\rm obs}$. To verify the later we performed a χ^2 fit to the data assuming $\Gamma_{\rm rest} = \alpha\Gamma_{\rm obs}$, where α was a free parameter.[5] We considered the errors in both variables $\Gamma_{\rm rest}$ and $\Gamma_{\rm obs}$ when performing the least-squares fit. We obtained $\alpha = 0.996 \pm 0.008$ (error at the 68% confidence level) with $\chi^2 = 99.3$ for 143 degrees of freedom (dof). As a basic check for the luminosity dependence of the linear relation between $\Gamma_{\rm rest}$ and $\Gamma_{\rm obs}$ we performed χ^2 fits of the model $\Gamma_{\rm rest} = \alpha\Gamma_{\rm obs}$ to sources with $\log L_{2-10} \lesssim 43.6$ and sources with $\log L_{2-10} \gtrsim 43.6$. We obtained $\alpha = 0.995 \pm 0.011$ ($\chi^2 = 43.8$; dof=70) for sources with $\log L_{2-10} \lesssim 43.6$ and $\alpha = 0.997 \pm 0.010$ ($\chi^2 = 55.6$; dof=72) for sources with $\log L_{2-10} \gtrsim 43.6$.

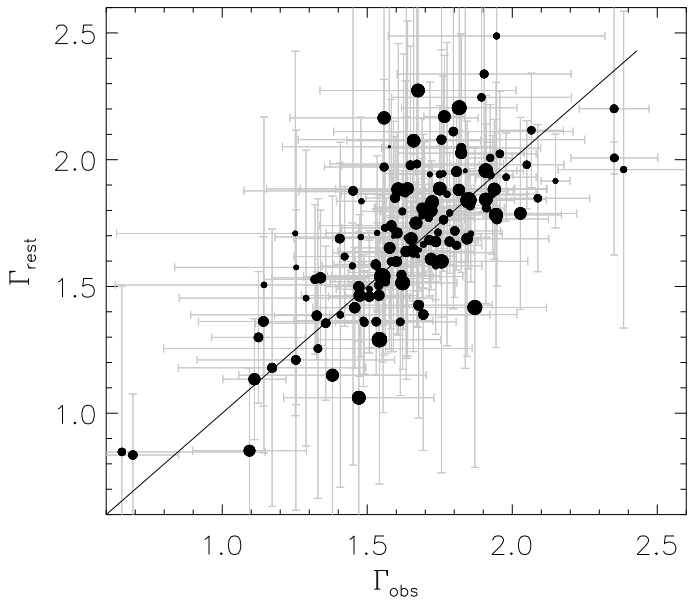

Fig. 2.4 Spectral index for fits performed in the 2–10 keV rest-frame band ($\Gamma_{\rm rest}$) versus spectral index for fits performed in the 0.5–8 keV observed-frame band ($\Gamma_{\rm obs}$). The size of each symbol increases with redshift. The solid line represents the case of $\Gamma_{\rm obs} = \Gamma_{\rm rest}$. Notice that values of $\Gamma_{\rm rest}$ and $\Gamma_{\rm obs}$ can be found in Table 2.2.

[5] A χ^2 fit using the relation y=αx to model some bivariate sample (x_i, y_i) with errors in both variables (σ_{xi}, σ_{yi}) is obtained by minimizing $\chi^2 = \sum_i \frac{(y_i - \alpha x_i)^2}{\sigma_{yi}^2 + \alpha^2 \sigma_{xi}^2}$

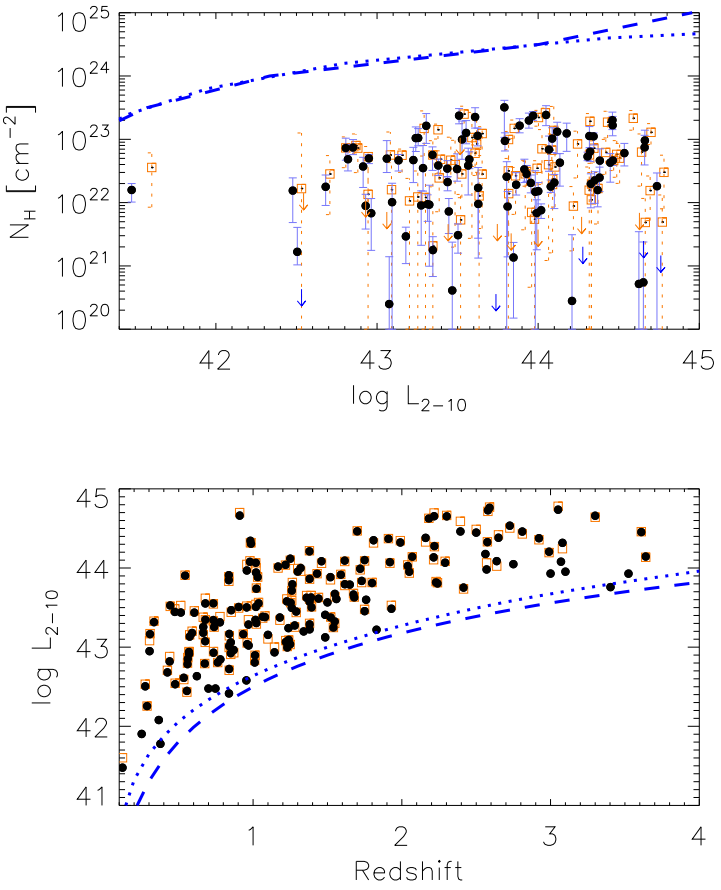

Fig. 2.5 Estimated best-fit column densities versus 2–10 keV luminosities (upper panel), and 2–10 keV luminosities versus redshifts (lower panel) of the $z > 0.1$ RQ AGNs. Filled circles represent sources with fits performed in the 0.5–8 keV observed-frame band and open squares represent sources with fits performed in the 2–10 keV rest-frame band. In the upper panel, the two lines indicate the maximum column density that can be detected for a source with $0.1 \leq z \leq 4.0$, and a total of 170 counts in the 0.5–8 keV observed-frame (dashed) and 2–10 keV rest-frame (dotted). In the lower panel the lines indicate the minimum luminosity required for the detection of a source as a function of redshift. A total of 170 counts in the 0.5–8 keV observed-frame band (dashed) or a total of 170 counts in the 2–10 keV rest-frame band (dotted) is assumed. For the limits shown in this figure it is assumed that the source is detected at the ACIS-I aim-point with an exposure time of ≈2 Ms.

2.5 Results and discussion

2.5.1 Selection Effects.

We begin this section by describing several selection effects that are intrinsic to our sample. Having an exposure of $\approx$ 2 times greater than the CDF-S survey, the CDF-N survey drives the sensitivity limits of our sources, so the following discussion will be focused on this survey.

Figure 2.5 shows the estimated best-fit column density versus the 2–10 keV luminosity (upper panel), and the 2–10 keV luminosity versus redshift (lower panel), for our $z > 0.1$ RQ AGNs. Spectral fits performed in the 0.5–8 keV observed-frame band and 2–10 keV rest-frame band are shown with filled circles and open squares respectively. In the upper panel of Figure 2.5, the dashed line shows the maximum column density that can be found for a source with $0.1 \leq z \leq 4.0$ assuming the source is detected at the ACIS-I aim-point with an exposure time of $\approx$2 Ms (Alexander et al. 2003) and a total of 170 counts in the 0.5–8 keV observed-frame band (dashed line) and 2–10 keV rest-frame band (dotted line). Each point on these curves is obtained by fixing $N_{\rm H}$ and finding the minimum luminosity that can be obtained with $0.1 \leq z \leq 4.0$ assuming a source with $\Gamma = 1.6$, Galactic column density of $1.3{\times}10^{20}{\rm cm}^{-2}$ and 170 counts in each fitted energy range. For low-luminosity sources ($L_{2-10} \lesssim 10^{42}$ erg s^{-1}), the threshold column density is $\approx 10^{24}$ cm^{-2}, which increases by a factor of $\sim$10 for higher luminosity sources ($10^{44} - 10^{45}$ erg s^{-1}). The maximum column density observed at a specific luminosity is set by AGNs with $z = 0.1$ in most of the observed luminosity range; however, for luminous sources ($L_{2-10} \gtrsim 10^{44}$ erg s^{-1}) higher redshift AGNs ($z \sim$ 1–4) establish the limit in N_H because these are less affected by absorption.

In the lower panel of Figure 2.5, the curves indicate the minimum luminosity required for the detection of a source as a function of redshift. We have assumed a source free of intrinsic absorption, positioned at the ACIS-I aim-point with an exposure time of $\approx$2 Ms, $\Gamma = 1.6$, Galactic column density of $1.3{\times}10^{20}{\rm cm}^{-2}$ and with 170 photon counts in the 0.5–8 keV observed-frame (dashed line) or 170 counts in the 2–10 keV rest-frame (dotted line). The threshold luminosity is $\approx 10^{42}$ erg s^{-1} for $z \approx 0.5$ and $\approx 3{\times}10^{43}$ erg s^{-1} for $z \approx 2.5$. The dashed curve in Figure 2.5 is obtained by assuming no intrinsic absorption; however, the presence of $N_{\rm H}$, which might be evolving (e.g., La Franca et al. 2005; Treister & Urry 2006; Tozzi et al. 2006), could be increasing the observed threshold luminosity.

2.5.2 Luminosity and Photon index

One of the goals of this work is to examine a possible correlation between $L_{\rm X}$ and Γ in a sample of RQ AGNs which was previously reported by Dai et al. (2004). To improve on the Dai et al. analysis we significantly increased the sample size using the CDFs, considered a larger redshift range, and used X-ray spectra that contained more than 170 counts in the full band (0.5–8 keV). The results of this analysis are shown in the following sections. For the following analysis we use the X-ray luminosity in the 2–10 keV rest-frame band (L_{2-10}).

Table 2.3. Correlation table of Γ versus $L_{\rm X}$.

Cor. Coeff.	Redshift bin	Fitted Energy Range	Γ vs. L_{2-10} N[a]	r_C	% sign[b]
Spearman	$0.3 \leq z \leq 0.96$	0.5–8 keV observed-frame	53	0.48	>99.9
Kendall	$0.3 \lesssim z \lesssim 0.96$	0.5–8 keV observed-frame	53	0.33	>99.9
Pearson[c]	$0.3 \lesssim z \lesssim 0.96$	0.5–8 keV observed-frame	53	0.42	99.8
Spearman	$0.96 \leq z \leq 1.5$	0.5–8 keV observed-frame	54	0.29	96.7
Kendall	$0.96 \lesssim z \lesssim 1.5$	0.5–8 keV observed-frame	54	0.19	95.9
Pearson[c]	$0.96 \lesssim z \lesssim 1.5$	0.5–8 keV observed-frame	54	0.31	97.5
Spearman	$1.5 \leq z \leq 3.3$	0.5–8 keV observed-frame	57	0.45	>99.9
Kendall	$1.5 \lesssim z \lesssim 3.3$	0.5–8 keV observed-frame	57	0.32	>99.9
Pearson[c]	$1.5 \lesssim z \lesssim 3.3$	0.5–8 keV observed-frame	57	0.43	>99.9
Spearman	$0.3 \leq z \leq 0.96$	2–10 keV rest-frame	44	0.62	>99.9
Kendall	$0.3 \lesssim z \lesssim 0.96$	2–10 keV rest-frame	44	0.42	>99.9
Pearson[c]	$0.3 \lesssim z \lesssim 0.96$	2–10 keV rest-frame	44	0.530	>99.9
Spearman	$0.96 \leq z \leq 1.5$	2–10 keV rest-frame	46	0.22	84.9
Kendall	$0.96 \lesssim z \lesssim 1.5$	2–10 keV rest-frame	46	0.14	83.3
Pearson[c]	$0.96 \lesssim z \lesssim 1.5$	2–10 keV rest-frame	46	0.23	87.8
Spearman	$1.5 \leq z \leq 3.3$	2–10 keV rest-frame	48	0.43	99.8
Kendall	$1.5 \lesssim z \lesssim 3.3$	2–10 keV rest-frame	48	0.31	99.8
Pearson[c]	$1.5 \lesssim z \lesssim 3.3$	2–10 keV rest-frame	48	0.43	99.7

[a]Number of RQ AGNs in each redshift bin.

[b]Percentile significance of the correlation.

[c]Calculated from Γ versus log $L_{\rm X}$.

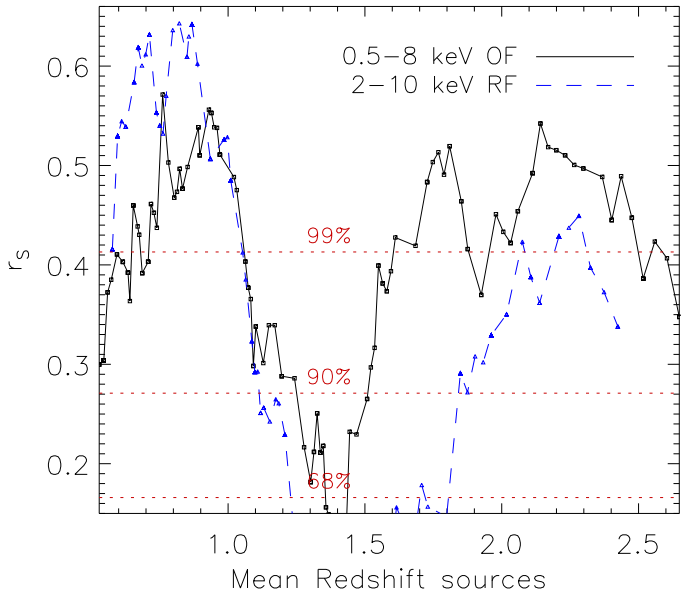

Fig. 2.6 Spearman correlation coefficients of the $\Gamma - L_{2-10}$ relation as a function of the mean redshift within each sub-sample. Each sub-sample contains 38 RQ AGNs. The solid line corresponds to the fits performed in the 0.5–8 keV observed-frame band (Table 2.2). The dashed-line corresponds to the fits performed in the 2–10 keV rest-frame band (Table 2.2). The dotted lines correspond to three different levels of significance (68%, 90% and 99%), assuming 38 independent measurements of Γ vs. L_{2-10}.

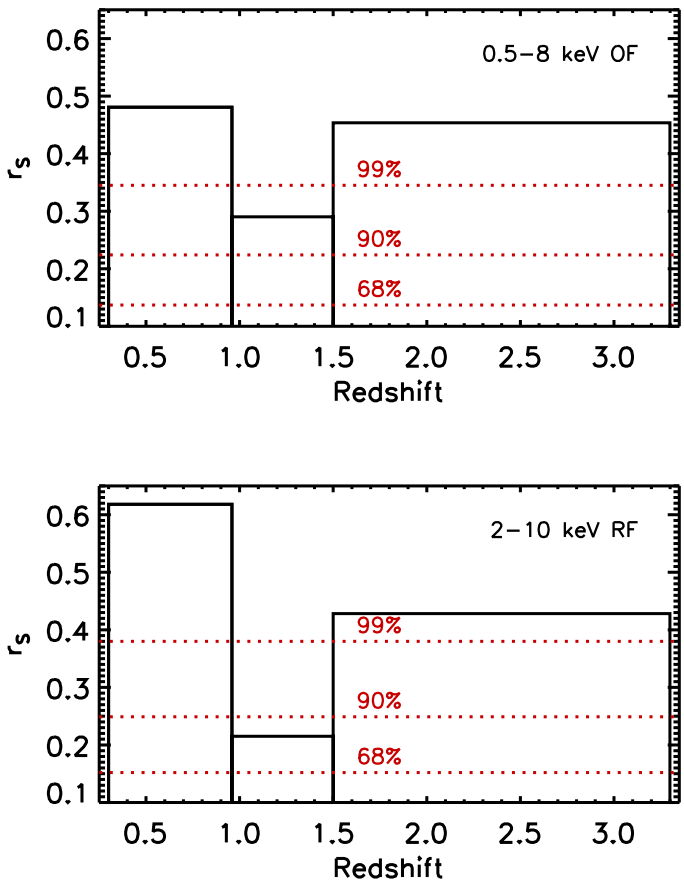

Fig. 2.7 Spearman correlation coefficients of the $\Gamma - L_{2-10}$ relation as a function of redshift for the RQ AGNs within each independent redshift bin. In the upper panel each redshift bin contains ∼55 RQ AGNs and the fits were performed in the 0.5–8 keV observed-frame band (Table 2.2). In the lower panel each redshift bin contains ∼45 RQ AGNs, and the fits were performed in the 2–10 keV rest-frame band (Table 2.2). The dotted lines correspond to three different levels of significance (68%, 90% and 99%); these are obtained assuming 55 sources in the upper panel and 45 sources in the lower panel.

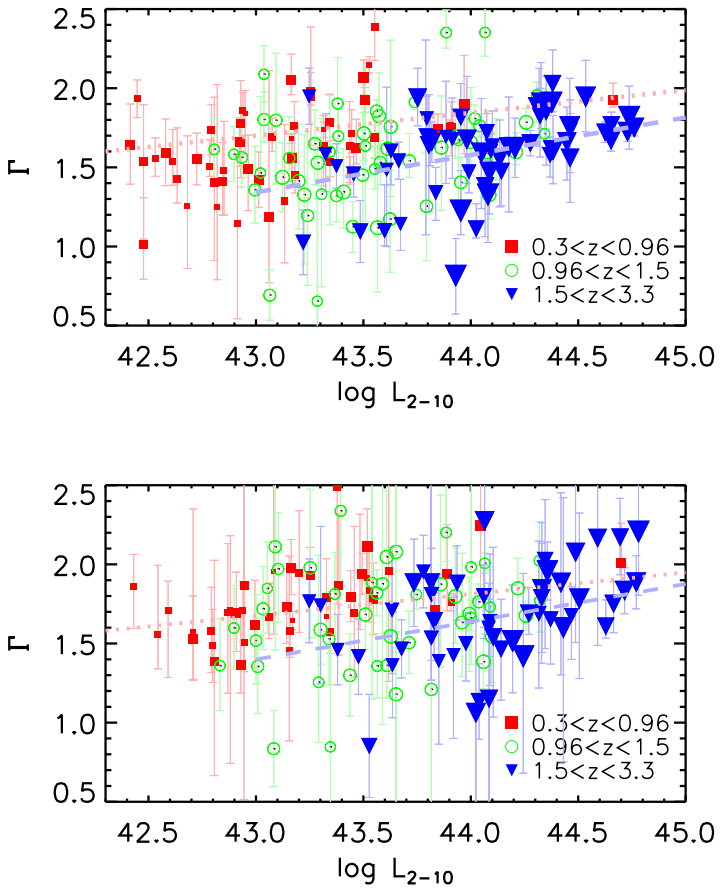

Fig. 2.8 Γ versus 2–10 keV luminosity of radio-quiet AGNs in the redshift range of $0.3 \lesssim z \lesssim 3.3$. In the upper panel we show sources with fits performed in the 0.5–8 keV observed-frame band. In the lower panel we show sources with fits performed in the 2–10 keV rest-frame band. The symbol size increases with redshift. Filled squares are sources with $0.3 \lesssim z \lesssim 0.96$, open circles are sources with $0.96 \lesssim z \lesssim 1.5$, and filled triangles are sources with $1.5 \lesssim z \lesssim 3.3$. The dotted line indicates the least-squares fit to sources having $0.3 \lesssim z \lesssim 0.96$. The dashed line shows the least-squares fit to sources having $1.5 \lesssim z \lesssim 3.3$.

2.5.2.1 Possible evolution of the strength and significance of the $\Gamma - L_{\rm X}$ correlation

As a first approach, we searched for a Γ – $L_{\rm X}$ correlation as a function of redshift selecting sub-samples ordered in redshift. We used sub-samples containing 38 sources for fits performed in the 0.5–8 keV observed-frame band and the 2–10 keV rest-frame band (Table 2.2). We calculated the mean redshift of each sub-sample and computed the Spearman rank correlation coefficient and significance of the correlation between Γ and L_{2-10}. This process was repeated by shifting the sampling window across the entire observed redshift range. Figure 2.6 shows the values of the significance of the correlations and the Spearman correlation coefficients of the $\Gamma - L_{2-10}$ relation as a function of the mean redshift of the sources within each sub-sample, using the best-fit parameters from Table 2.2. The solid line in Figure 2.6 corresponds to sources fitted in the 0.5–8 keV observed-frame band and the dashed line corresponds to those fitted in the 2–10 keV rest-frame band. We notice that the correlation has two significant peaks ($\sim$99%) in both energy bands fitted, one with a mean redshift of ~ 0.7, and the other with a mean redshift of ~ 2.2.

As a second approach, we selected three independent redshift bins covering the redshift range $0.3 < z < 3.3$. The high redshift bin ($1.5 \lesssim z \lesssim 3.3$) was chosen to match the redshift range where Dai et al. (2004) found the $\Gamma - L_{\rm X}$ correlation while the other two redshift bins ($0.3 \lesssim z \lesssim 0.96$ and $0.96 \lesssim z \lesssim 1.5$) were selected to obtain independent redshift bins with comparable numbers of sources within them. Each redshift bin contained ~ 55 sources in the 0.5–8 keV observed-frame band and ~ 45 sources in the 2–10 keV rest-frame band. In Figure 2.7 and Table 2.3 we show the Spearman rank correlation coefficient and the significance of the Spearman correlation coefficient in each bin. The upper panel of Figure 2.7 corresponds to fits performed in the 0.5–8 keV observed-frame and the lower panel to fits performed in the 2–10 keV rest-frame. The height of each bar is the significance of the $\Gamma - L_{2-10}$ Spearman correlation. The correlation for fits performed in the 0.5–8 keV observed-frame is significant for the three redshift bins; however, we find a slight decrease in the strength and significance in the second redshift bin for fits performed in the 2–10 keV rest-frame. The significance of the correlation in the first and third redshift bins is >99.5% for both fitting ranges. A significant expansion of our sample made by incorporating additional deep AGN surveys will be required to confirm the possible decrease of the strength of the correlation in the second redshift bin.

In Figure 2.8, we plot Γ vs. L_{2-10} for sources in each redshift bin of Figure 2.7, for fits performed in the 0.5–8 keV observed-frame (upper panel) and the 2–10 keV rest-frame (lower panel). Sources in our sample with redshifts in the range $0.3 \lesssim z \lesssim 0.96$ have a lower mean luminosity of $\langle \log L_{2-10} \rangle \sim 43.1$ ($\sigma_{\log L_{2-10}} \sim 0.5$) than sources with redshifts in the range $1.5 \lesssim z \lesssim 3.3$ which have a mean luminosity of $\langle \log L_{2-10} \rangle \sim 44.1$ ($\sigma_{\log L_{2-10}} \sim 0.4$). The luminosity distributions for sources in the redshift bins $0.3 \lesssim z \lesssim 0.96$ and $1.5 \lesssim z \lesssim 3.3$ are shown in Figure 2.9. We notice that the peak of the distribution of the sources in the high-redshift bin is significantly higher in luminosity than the peak of the distribution of the sources in the low-redshift bin. This shift in luminosity distributions is mainly a selection effect (see Figure 2.5) combined with the

fact that luminous sources are more numerous at high redshift (Ueda et al. 2003; Hasinger et al. 2005). The Spearman correlation index of the $\Gamma - L_{2-10}$ data for the whole sample (173 RQ AGN) is $\sim$0.24 (99.8% significance) and $\sim$0.16 (94.1% of significance) for the 0.5–8 keV observed-frame and the 2–10 keV rest-frame spectral fits. These correlation coefficients are significantly lower than those found in the $0.3 \lesssim z \lesssim 0.96$ and $1.5 \lesssim z \lesssim 3.3$ redshift bins (see Table 2.3 for more details).

In Table 2.4, we show the results of a test of the $\Gamma - L_{\rm X}$ correlation using only sources with spectroscopic redshifts. We find that the $\Gamma - L_{\rm X}$ correlation of the sub-sample of sources with spectroscopic redshifts is significant in the three redshift bins; however, as indicated in Table 2.4, this sub-sample includes a larger fraction of type 1 AGNs and contains more sources with $\log\,(N_{\rm H}/{\rm cm}^{-2}) \lesssim 22$ than that of the whole sample. In addition, the size of this sub-sample is significantly smaller than the whole sample. We caution that the strengths of the correlations provided by the non-parametric tests used in our analysis of sub-samples containing a small number of sources N with the present uncertainties in the photon indices may be inaccurate since the variance of the Spearman correlation coefficient is $\sigma^2 = \frac{1}{N-1}$. Photometric redshifts are subject to larger errors than spectroscopic ones and for sources with $z > 1$ the error is approximately given by $\Delta z/(1+z) = 0.05$ (e.g., Cohen et al. 2000). In our analysis, the uncertainties in the redshifts will mainly affect the estimation of the X-ray luminosities. For example, a source at $z \sim 2$ will have an uncertainty in the estimated luminosity of $\Delta L_{\rm X}/L_{\rm X} \sim 0.3$. This level of uncertainty will not significantly affect our results since our study involves estimating changes in the photon index over two orders of magnitude in X-ray luminosity.

In the following three sections, we focus on sources in the first bin ($0.3 \lesssim z \lesssim 0.96$) and the third bin ($1.5 \lesssim z \lesssim 3.3$) and test the sensitivity of the $\Gamma - L_{\rm X}$ correlation to the possible presence of intrinsic absorption and Compton reflection in the spectra of the sources.

Table 2.4: Correlation table of Γ versus $L_{\rm X}$ for AGNs with spectroscopic redshifts.

			Γ vs. L_{2-10}			
Fitted Energy Frame	Redshift bin	N^a	r_C [b]	fraction of type 1	% sign [c]	fraction with log ($N_{\rm H}$/cm^{-2}) $\lesssim 22$
0.5–8 keV observed-frame	$0.3 \lesssim z \lesssim 0.96$	46	0.47	99.9	0.37	0.70
2–10 keV rest-frame	$0.3 \lesssim z \lesssim 0.96$	40	0.64	>99.9	0.40	0.68
0.5–8 keV observed-frame	$0.96 \lesssim z \lesssim 1.5$	31	0.40	97.3	0.42	0.71
2–10 keV rest-frame	$0.96 \lesssim z \lesssim 1.5$	26	0.42	96.6	0.50	0.73
0.5–8 keV observed-frame	$1.5 \lesssim z \lesssim 3.3$	26	0.38	94.3	0.62	0.62
2–10 keV rest-frame	$1.5 \lesssim z \lesssim 3.3$	24	0.49	98.5	0.67	0.67

[a] Number of RQ AGNs in each redshift bin.
[b] Spearman correlation coefficient.
[c] Percentile significance of the correlation.

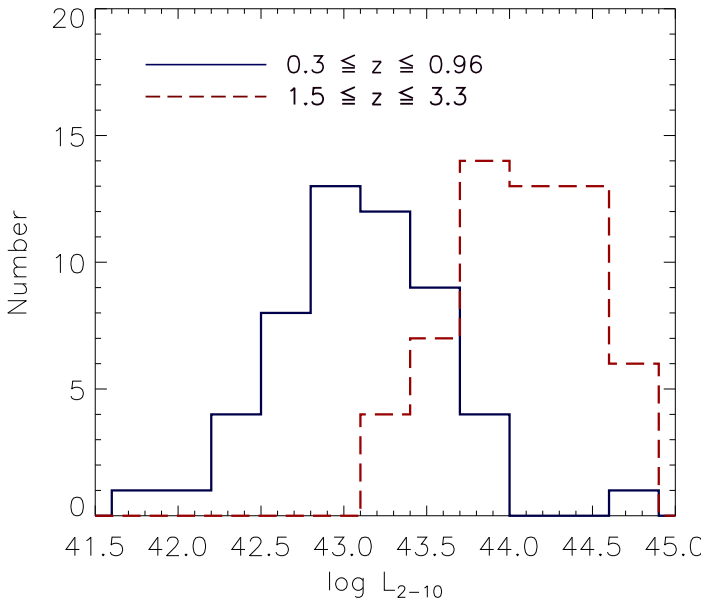

Fig. 2.9 2–10 keV rest-frame luminosity (L_{2-10}) distributions for radio-quiet AGNs with $0.3 \lesssim z \lesssim 1.5$ (thick line) and $1.5 \lesssim z \lesssim 3.3$ (dashed line). The fits are performed in the 0.5–8 keV observed-frame band.

2.5.2.2 Possible evolution of the slope and offset of the $\Gamma - L_{\rm X}$ correlation

In Figure 2.10, we show Γ versus L_{2-10} for sources in the ranges of $0.3 \lesssim z \lesssim 0.96$ (upper panel), and $1.5 \lesssim z \lesssim 3.3$ (lower panel). The values of the X-ray luminosities and spectral indices shown in Figure 2.10 were obtained by fitting the spectra in the observed-frame energy range of 0.5–8 keV (see Table 2.2). We searched for a correlation between Γ and $L_{\rm X}$ by computing the Spearman's and Kendall's correlations (see Table 2.3). We find a strong correlation between Γ and L_{2-10}, at the >99.9% confidence, for sources having $0.3 \lesssim z \lesssim 0.96$ and $1.5 \lesssim z \lesssim 3.3$. We tested for a linear dependence between Γ and $\log L_{\rm X}$ by calculating the Pearson's correlation and find a high significance (>99.8%) for sources within $0.3 \lesssim z \lesssim 0.96$ and $1.5 \lesssim z \lesssim 3.3$ (see Table 2.3). In Table 2.5, we also present results of linear least-squares fits to the $\Gamma - L_{\rm X}$ relation with a model of the form $\Gamma = \alpha \log L_{\rm X} + \beta$. For this test, we assumed that Γ is the dependent variable with errors given at the 68% confidence level. In Table 2.5, we show the best-fit linear fit parameters α and β. We find that the best-fit parameters α and β show a significant change between the redshift bin $0.3 \lesssim z \lesssim 0.96$ and the redshift bins of $0.96 \lesssim z \lesssim 1.5$ and $1.5 \lesssim z \lesssim 3.3$. In particular, for spectral fits performed in the 0.5 – 8 keV observed-frame band we find the following: The slope and offset of the linear fit to the $\Gamma - L_{\rm X}$ correlation in the $0.3 < z < 0.96$ redshift range are, $\alpha = 0.14 \pm 0.02$ and $\beta = -4.5 \pm 0.8$, respectively. The slope and offset of the $\Gamma - L_{\rm X}$ correlation in the $1.5 < z < 0.33$ redshift range are, $\alpha = 0.23 \pm 0.03$, $\beta = -8.7 \pm 1.2$, respectively. Similar result are found for spectral fits performed in the 2–10 keV rest-frame. This change in the linear parameters can also be seen in Figure 2.8.

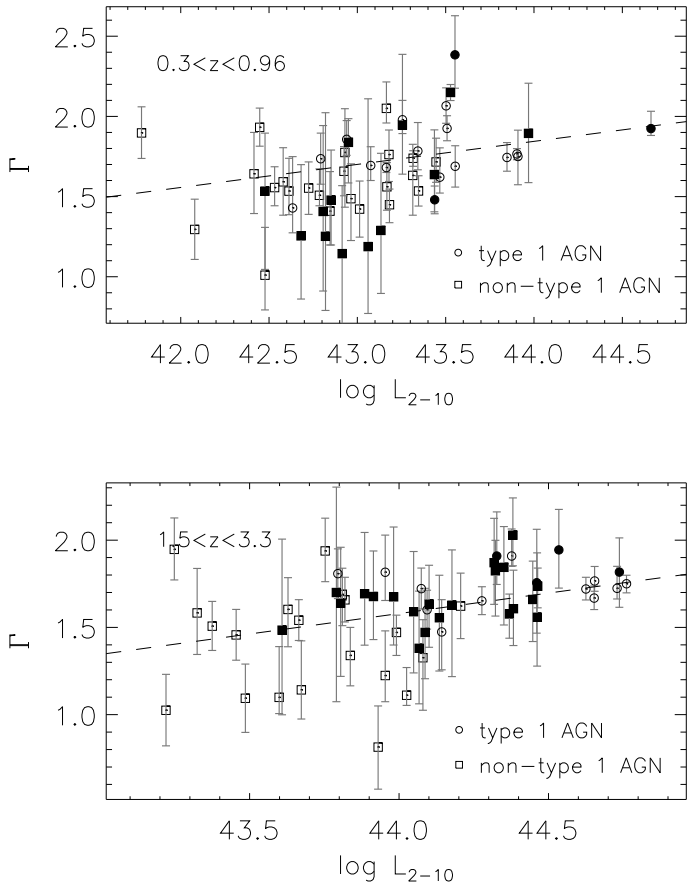

Fig. 2.10 Γ versus 2–10 keV luminosity of radio-quiet AGNs with $0.3 \lesssim z \lesssim 0.96$ (upper panel) and with $1.5 \lesssim z \lesssim 3.3$ (lower panel). The values of the X-ray luminosities and spectral indices were obtained by fitting the spectra in the observed-frame energy range of 0.5–8 keV (see Table 2.2). The dashed lines indicate linear fits to the data using the least-squares method. The open symbols correspond to sources having $\log (N_{\rm H}/{\rm cm}^{-2}) \lesssim 22$, and the filled symbols are sources with $\log (N_{\rm H}/{\rm cm}^{-2}) > 22$. Circles correspond to type 1 AGNs and squares to non-type 1 AGNs.

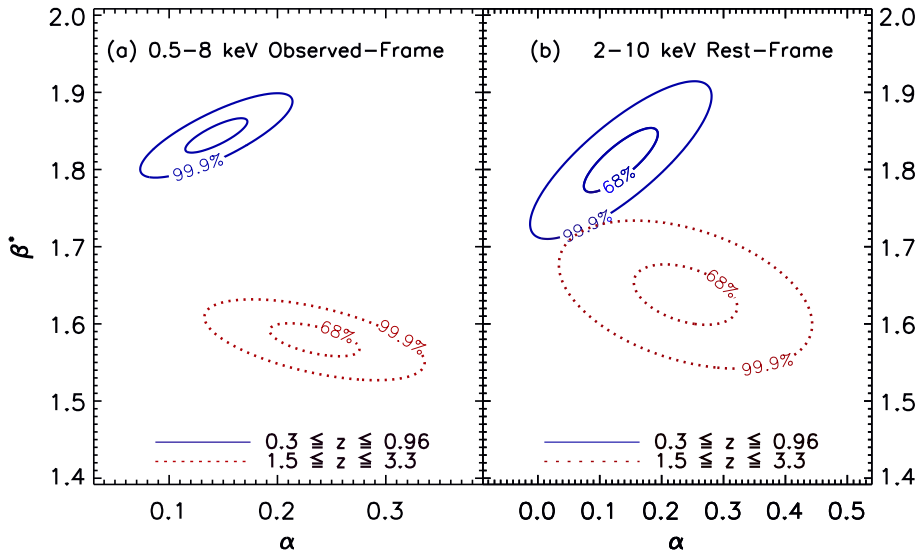

Fig. 2.11 68% and 99.9% confidence contours of the slope α and offset β^* of the $\Gamma - L_{\rm X}$ correlation for AGNs in the $0.3 < z < 0.96$ (solid contours) and $1.5 < z < 3.3$ (dotted contours) redshift ranges. The parameters α and β^* were derived from fits of the linear model $\Gamma = \alpha \log \frac{L_{2-10}}{(10^{44}\ {\rm ergs/s})} + \beta^*$. The fits were performed in the 0.5–8 keV observed-frame band (a) and in the 2–10 keV rest-frame band (b). The confidence contours indicate that the parameters of the linear fit to the $\Gamma - L_{\rm X}$ correlation differ at the $> 99.9\%$ confidence level between the $0.3 < z < 0.96$ and $1.5 < z < 3.3$ redshift ranges.

Table 2.5. Results of linear fits to the Γ vs. $\log L_{2-10}$ relation.

Redshift bin	Fitted energy range	Sample[b]	α [a]	β [a]
$0.3 \lesssim z \lesssim 0.96$	observed-frame 0.5–8 keV	CDFs	0.14 ± 0.02	-4.5 ± 0.8
$0.3 \lesssim z \lesssim 0.96$	rest-frame 2–10 keV	CDFs	0.13 ± 0.04	-4.1 ± 1.7
$0.96 \lesssim z \lesssim 1.5$	observed-frame 0.5–8 keV	CDFs	0.23 ± 0.03	-8.3 ± 1.5
$0.96 \lesssim z \lesssim 1.5$	rest-frame 2–10 keV	CDFs	0.27 ± 0.05	-9.9 ± 2.2
$1.5 \lesssim z \lesssim 3.3$	observed-frame 0.5–8 keV	CDFs	0.23 ± 0.03	-8.7 ± 1.2
$1.5 \lesssim z \lesssim 3.3$	rest-frame 2–10 keV	CDFs	0.24 ± 0.06	-8.9 ± 2.4
$1.5 \lesssim z \lesssim 3.3$	observed-frame 0.5–8 keV	combined	0.27 ± 0.03	-10.3 ± 1.2

[a]The CDFs sample consists of all the sources presented in Table 2.2. The combined sample consists of sources obtained from the independent surveys of Vignali et al. (1999), George et al. (2000), Reeves & Turner (2000), Page et al. (2003) and Dai et al. (2004) combined with the sources of our CDFs sample.

[a]Based on fits of a linear model ($\Gamma = \alpha \log L_{2-10} + \beta$) to the Γ versus $\log L_{2-10}$ relation, using the weighted least-squares method. The errors in Γ at the 68% level are used in the linear fit. L_{2-10} is the 2–10 keV rest-frame luminosity.

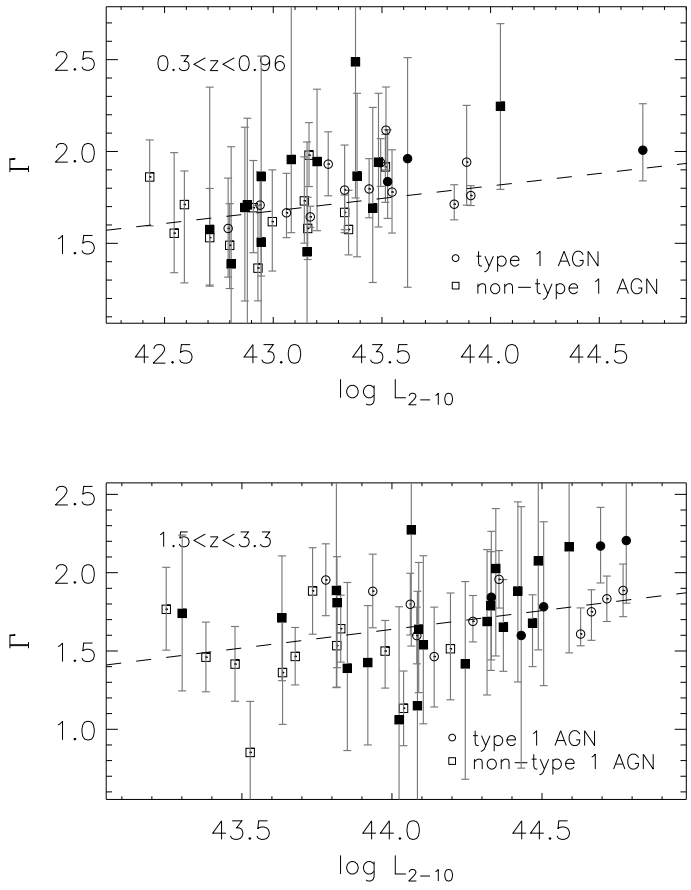

Fig. 2.12 Γ versus 2–10 keV luminosity of radio-quiet AGNs with $0.3 \lesssim z \lesssim 0.96$ (upper panel) and with $1.5 \lesssim z \lesssim 3.3$ (lower panel). The values of the X-ray luminosities and spectral indices were obtained by fitting the spectra in the rest-frame energy range of 2–10 keV (see Table 2.2). The dashed lines indicate linear fits to the data using the least-squares method. The open symbols correspond to sources having $\log (N_{\rm H}/{\rm cm}^{-2}) \lesssim 22$, and the filled symbols are sources with $\log (N_{\rm H}/{\rm cm}^{-2}) > 22$. Circles correspond to type 1 AGNs and squares to non-type 1 AGNs.

In Figure 2.11 we show the 68% and 99.9% confidence contours of α and β^* for AGNs in the $0.3 < z < 0.96$ and $1.5 < z < 0.33$ redshift ranges and for fits performed in the 2–10 keV rest-frame band (Figure 2.11a) and in the 0.5–8 keV observed-frame band (Figure 2.11b). The parameter β^* is obtained from fits of the model $\Gamma = \alpha \log \frac{L_{2-10}}{(10^{44}\ \mathrm{ergs/s})} + \beta^*$. L_{2-10} was re-normalized for the purpose of illustrating better the full range of the contours. The 68% and 99.9% confidence contours levels correspond to $\Delta\chi^2(\alpha, \beta^*)$ values of 2.3 and 13.81, respectively. The confidence contours indicate that the parameters of the linear fit to the $\Gamma - L_{\rm X}$ correlation change at the $> 99.9\%$ confidence level between the $0.3 < z < 0.96$ and $1.5 < z < 0.33$ redshift ranges.

To test the sensitivity and stability of these confidence contours to possible outliers in the data we repeated the confidence contour analysis by excluding data points with significant deviations from the linear fit. In particular, we re-fit the $\Gamma - L_{\rm X}$ correlation and re-calculated the confidence contours after excluding data points that deviated by more than 2σ, 2.5σ and 3σ from the linear fit. In all cases we find that the parameters of the linear fit to the $\Gamma - L_{\rm X}$ correlation change between redshift bins 1 and 3 at the $> 99.9\%$ and $> 98\%$ confidence levels for fits performed in the 0.5–8 keV observed-frame and 2–10 keV rest-frame, respectively.

As discussed in §2.4 to test the influence of possible effects such as Compton reflection, soft excesses, and intrinsic absorption on the Γ – $L_{\rm X}$ correlation, we also fitted the spectra in the 2–10 keV rest-frame, where these effects are expected to be smaller. The results of these spectral fits are presented in Table 2.2. In Figure 2.12, we present Γ versus L_{2-10} for sources in the redshift range of $0.3 \lesssim z \lesssim 0.96$ (upper panel), and in the redshift range of $1.5 \lesssim z \lesssim 3.3$ (lower panel) for spectral fits performed in the 2–10 keV rest-frame band. The results of our correlation analysis applied to the variables Γ and $L_{\rm X}$ are shown in Table 2.3. We find the Spearman, Kendall and Pearson correlation coefficients of Γ vs. L_{2-10} to be significant at the >99.9% and >99.7% confidence levels, for sources within $0.3 \lesssim z \lesssim 0.96$ and $1.5 \lesssim z \lesssim 3.3$ respectively. These results suggest that Compton reflection, soft excesses, and intrinsic absorption are most likely not driving the observed correlation between Γ and $L_{\rm X}$ in the two redshift bins analyzed in this section. In §2.5.2.3 and §2.5.2.6, we provide detailed analyses to show that intrinsic absorption and Compton reflection have negligible contributions to the $\Gamma - L_{\rm X}$ correlation.

2.5.2.3 Dependence of the $\Gamma - L_{\rm X}$ correlation on $N_{\rm H}$

The estimated values of the photon indices used in our correlation analysis depend partially on the assumed spectral models used to fit the AGN spectra. In particular, the default model used in our spectral analysis assumes a simple power law that can be modified by intrinsic absorption. There is some evidence suggesting that the intrinsic column density ($N_{\rm H}$) could be evolving both with X-ray luminosity (e.g, Ueda et al. 2003; Akylas et al. 2006) and redshift (e.g., Akylas et al. 2006; Treister & Urry 2006). At the same time, large values of $N_{\rm H}$ could be producing some dispersion in the estimated values of Γ. In order to analyze the effect of $N_{\rm H}$ in the spectral fitting, we have performed simulations using the software command FAKEIT in XSPEC. We randomly generated 1000 fake spectra for each of five values of $N_{\rm H}$ ($\log(N_{\rm H}/\mathrm{cm}^{-2}) = 21.5$, 22, 22.5, 23 and 23.5).

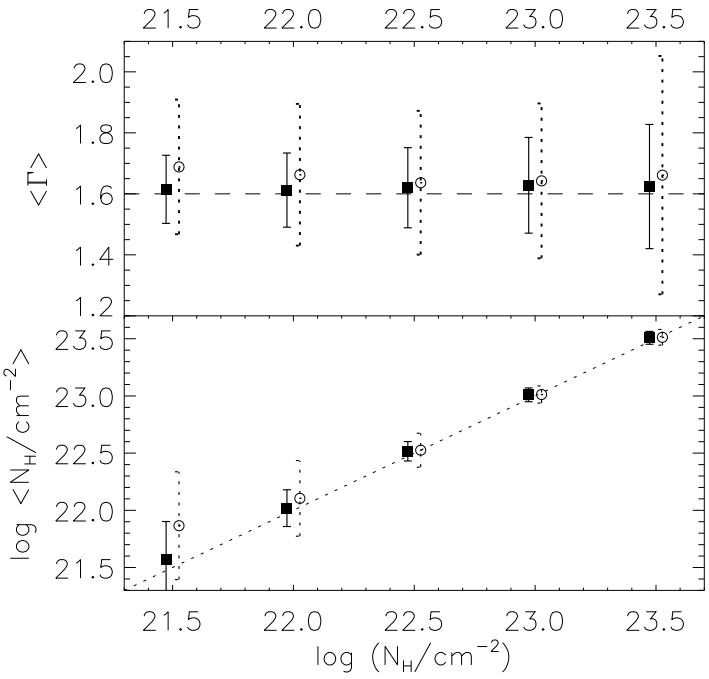

Fig. 2.13 Results from fits performed on 1000 simulated spectra with $S = 550$, $\Gamma = 1.6$, z=1.4 and 5 different values of log ($N_{\rm H}$/cm^{-2}) (21.5, 22, 22.5, 23 and 23.5). The estimated parameters with fits performed in the 0.5–8 keV observed-frame band are shown with filled squares (solid error bars), and the estimated parameters with fits performed in the 2–10 keV rest-frame band are shown with open circles (dashed error bars). A small shift in the value of log $N_{\rm H}$ (horizontal axis) has been introduced for visual purposes. In the upper panel we show $\langle\Gamma\rangle$ vs. log $N_{\rm H}$. In the lower panel we show log$\langle N_{\rm H}\rangle$ vs log $N_{\rm H}$. All error bars represent $\pm$ 1 σ deviations.

Table 2.6. Results of simulations to test the probability of detecting intrinsic absorption through spectral fits.

log ($N_{\rm H}$/cm^{-2})[a]	Percentage of cases[b]
21.5	41.8 %
22.0	74.7 %
22.5	99.1 %
23.0	100.0 %
23.5	99.9 %

[a]For each of the 5 different values of log ($N_{\rm H}$/cm^{-2}) (log ($N_{\rm H}$/cm^{-2})= 21.5, 22, 22.5, 23 and 23.5), we randomly generated 1000 fake spectra assuming sources close to the aim-point of the Chandra ACIS-I CCD, with 550 counts in the 0.5–8 keV band, $\Gamma = 1.6$, and $z = 1.4$.

[b]Percentage of cases out of the 1000 simulated cases where the F-test indicates a significant presence of absorption assuming the input values of column densities listed in the first column.

Each simulated spectrum was created assuming an absorbed power-law (APL) model with 550 counts in the 0.5–8 keV band, $\Gamma = 1.6$, and $z = 1.4$. The simulated sources were considered close to the aim-point of the *Chandra* ACIS-I CCD.[6] The assumed values of the total counts, Γ and z are close to the mean values found in §2.4. We performed fits to the randomly generated spectra using the same APL model, and plot in Figure 2.13 (upper panel) the mean spectral slope (with standard deviation) of the 1000 fits as a function of log $N_{\rm H}$; these fits were performed both in the 0.5–8 keV observed-frame (squares) and the 2–10 keV rest-frame (circles). Based on these results we do not find any significant bias in the estimation of Γ with $N_{\rm H}$. We do, however, find that the standard deviation shows a clear tendency to grow with $N_{\rm H}$ independently of the energy band fit, as seen in Figure 2.13 (upper panel). In Figure 2.13 (lower panel), we see that in general the estimated value of $N_{\rm H}$ is accurate for log ($N_{\rm H}$/cm^{-2}) $\gtrsim 22$; however, for log ($N_{\rm H}$/cm^{-2}) < 22 the column density is slightly overestimated and has a larger dispersion.

Using the same simulations, we estimated the effectiveness of using the F-test at the 95% level of significance to determine the improvement in the fit quality by using an absorbed power-law (APL) model as an alternative to the default power-law (PL) model. Table 2.6 shows that in a simulation of 1000 fake spectra with $S = 550$, $\Gamma = 1.6$, $z = 1.4$ and log ($N_{\rm H}$/cm^{-2}) = 22, the F-test indicates absorption in ∼75% of the spectra. For simulated spectra with log ($N_{\rm H}$/cm^{-2}) = 22.5, the F-test indicates absorption in ∼ 99% of the cases and for log ($N_{\rm H}$/cm^{-2}) > 22.5 the F-test indicates absorption in more

[6]CCD stands for charge-coupled device.

Table 2.7. Correlation table of Γ vs. $L_{\rm X}$ for sub-samples of different absorption.

Redshift bin	Absorption[a]	Fitted energy range	N^b	L_{2-10} vs. Γ $r_C{}^c$	% sign[d]
$0.3 \lesssim z \lesssim 0.96$	$\log(N_{\rm H}/{\rm cm}^{-2}) \lesssim 22.5$	0.5–8 keV observed-frame	40	0.38	98.4
$0.3 \lesssim z \lesssim 0.96$	$\log(N_{\rm H}/{\rm cm}^{-2}) \lesssim 22.0$	0.5–8 keV observed-frame	37	0.38	98.1
$0.3 \lesssim z \lesssim 0.96$	$\log(N_{\rm H}/{\rm cm}^{-2}) \gtrsim 22.0$	0.5–8 keV observed-frame	16	0.66	99.4
$0.3 \lesssim z \lesssim 0.96$	type 1	0.5–8 keV observed-frame	17	0.34	81.6
$0.3 \lesssim z \lesssim 0.96$	$\log(N_{\rm H}/{\rm cm}^{-2}) \lesssim 22.5$	2–10 keV rest-frame	32	0.56	>99.9
$0.3 \lesssim z \lesssim 0.96$	$\log(N_{\rm H}/{\rm cm}^{-2}) \lesssim 22.0$	2–10 keV rest-frame	27	0.56	99.8
$0.3 \lesssim z \lesssim 0.96$	$\log(N_{\rm H}/{\rm cm}^{-2}) \gtrsim 22.0$	2–10 keV rest-frame	17	0.67	99.7
$0.3 \lesssim z \lesssim 0.96$	type 1	2–10 keV rest-frame	16	0.58	98.2
$0.96 \lesssim z \lesssim 1.5$	$\log(N_{\rm H}/{\rm cm}^{-2}) \lesssim 22.5$	0.5–8 keV observed-frame	38	0.27	89.9
$0.96 \lesssim z \lesssim 1.5$	$\log(N_{\rm H}/{\rm cm}^{-2}) \lesssim 22.0$	0.5–8 keV observed-frame	31	0.31	91.6
$0.96 \lesssim z \lesssim 1.5$	$\log(N_{\rm H}/{\rm cm}^{-2}) \gtrsim 22.0$	0.5–8 keV observed-frame	23	0.31	85.4
$0.96 \lesssim z \lesssim 1.5$	type 1	0.5–8 keV observed-frame	17	0.20	49.5
$0.96 \lesssim z \lesssim 1.5$	$\log(N_{\rm H}/{\rm cm}^{-2}) \lesssim 22.5$	2–10 keV rest-frame	33	0.26	85.3
$0.96 \lesssim z \lesssim 1.5$	$\log(N_{\rm H}/{\rm cm}^{-2}) \lesssim 22.0$	2–10 keV rest-frame	27	0.33	91.1
$0.96 \lesssim z \lesssim 1.5$	$\log(N_{\rm H}/{\rm cm}^{-2}) \gtrsim 22.0$	2–10 keV rest-frame	19	-0.18	54.8
$0.96 \lesssim z \lesssim 1.5$	type 1	2–10 keV rest-frame	16	0.15	37.1
$1.5 \lesssim z \lesssim 3.3$	$\log(N_{\rm H}/{\rm cm}^{-2}) \lesssim 22.5$	0.5–8 keV observed-frame	40	0.45	99.7
$1.5 \lesssim z \lesssim 3.3$	$\log(N_{\rm H}/{\rm cm}^{-2}) \lesssim 22.0$	0.5–8 keV observed-frame	32	0.35	95.2
$1.5 \lesssim z \lesssim 3.3$	$\log(N_{\rm H}/{\rm cm}^{-2}) \gtrsim 22.0$	0.5–8 keV observed-frame	25	0.38	94.2
$1.5 \lesssim z \lesssim 3.3$	type 1	0.5–8 keV observed-frame	16	0.12	34.0
$1.5 \lesssim z \lesssim 3.3$	$\log(N_{\rm H}/{\rm cm}^{-2}) \lesssim 22.5$	2–10 keV rest-frame	34	0.45	99.2
$1.5 \lesssim z \lesssim 3.3$	$\log(N_{\rm H}/{\rm cm}^{-2}) \lesssim 22.0$	2–10 keV rest-frame	23	0.42	95.6
$1.5 \lesssim z \lesssim 3.3$	$\log(N_{\rm H}/{\rm cm}^{-2}) \gtrsim 22.0$	2–10 keV rest-frame	23	0.42	96.2
$1.5 \lesssim z \lesssim 3.3$	type 1	2–10 keV rest-frame	16	0.29	72.1

[a]Sub-samples contain RQ AGNs that are either type 1 AGN or have N_H less than a specified value.

[b]Number of RQ AGNs in each sub-sample.

[c]The Spearman correlation coefficient.

[d]The significance of the Spearman correlation coefficient.

than 99.9% of the cases. Based on these simulations, we conclude that the F-test can accurately identify absorption when $\log(N_{\rm H}/{\rm cm}^{-2}) \gtrsim 22$.

Based on our finding that highly-absorbed sources show a greater dispersion of the estimated value of Γ, we tested the sensitivity of the $\Gamma - L_{\rm X}$ correlation for sources having $0.3 \lesssim z \lesssim 0.95$ and $1.5 \lesssim z \lesssim 3.3$ to intrinsic absorption, by removing sources with significant absorption ($\log(N_{\rm H}/{\rm cm}^{-2}) \gtrsim 22.5$). We also tested this correlation for sources having $\log(N_{\rm H}/{\rm cm}^{-2}) < 22$. Finally as a complementary test we analyzed the $\Gamma - L_{\rm X}$ correlation for type 1 AGNs. The results of these three tests are presented in Table 2.7. For sources having $\log(N_{\rm H}/{\rm cm}^{-2}) \lesssim 22.5$ and $\log(N_{\rm H}/{\rm cm}^{-2}) \lesssim 22$ we find in the first and third redshift bins that the Spearman correlation coefficients of Γ versus L_{2-10} are significant at the >95% confidence levels. This result holds for sources with fits performed in both the 0.5–8 keV observed-frame and in the 2–10 keV rest-frame (see Table 2.7). Notice that sources having $\log(N_{\rm H}/{\rm cm}^{-2}) \lesssim 22$ are plotted as empty squares in Figures 2.10 and 2.12.

For type 1 AGNs, we find that the $\Gamma - L_{2-10}$ correlation is significant at the 82% and 12% levels in the first and third redshift bins, respectively, for fits performed in the 0.5–8 keV observed-frame band; the significances are at the 98% and 72% levels, respectively, for fits performed in the 2–10 keV rest-frame band. We briefly investigate possible reasons that may explain the apparent low detection significance of the $\Gamma - L_{2-10}$ relation for the type 1 AGNs of our sample. First we note that the luminosity ranges of the type 1 AGNs of our sample in the first and third redshift bins are $42.6 \lesssim \log L_{2-10} \lesssim 44.7$ and $43.8 \lesssim \log L_{2-10} \lesssim 44.8$. Our sample of type 1 AGNs therefore includes relatively luminous sources in each redshift bin. For sources in the third redshift bin, as we will later see in §2.5.2.7, the values of Γ appear to saturate above $\log L_{2-10} \sim 45$. Therefore, the type 1 AGNs detected in the third redshift bin of our sample are expected to lie on the flat part of the $\Gamma - L_{\rm X}$ relation. We conclude that the apparent low significance of the $\Gamma - L_{2-10}$ relation for the type 1 AGNs of our sample found in the third redshift bin is mainly the result of their relatively large luminosity and the limited number of type 1 AGNs in our sample. Based on the tests presented in this section we confirm that the strong $\Gamma - L_{\rm X}$ correlations that we find in RQ AGNs in the redshift ranges of $0.3 \lesssim z \lesssim 0.95$ and $1.5 \lesssim z \lesssim 3.3$ are not driven by intrinsic absorption.

2.5.2.4 Other Correlations

We searched in the redshift ranges of $0.3 \lesssim z \lesssim 0.95$ and $1.5 \lesssim z \lesssim 3.3$ for possible correlations between the photon index Γ and other physical parameters of our sample of AGNs by computing Spearman rank correlations. The results from this correlation analysis are shown in Table 2.8. In the cases where the intrinsic column densities were $N_{\rm H} \lesssim 10^{20}$ cm^{-2}, we could only obtain upper limits to $N_{\rm H}$, and therefore computed the correlation coefficients using survival analysis (Isobe et al. 1986).

The selection criteria used in this work impose a luminosity limit which is redshift dependent (see Figure 2.5). Furthermore, the co-moving density of luminous AGNs is known to increase with z. These two effects will produce a correlation between $L_{\rm X}$ and z as can be seen in Table 2.8. We do not find any significant correlation between Γ and

Table 2.8. Correlation table of L_{2-10} vs. z, Γ vs. z, $N_{\rm H}$ vs. z, $N_{\rm H}$ vs. L_{2-10} and Γ vs. $N_{\rm H}$.

correlated parameters	N[a]	Redshift bin	Fitted energy Range	$r_{\rm c}$[b]	% sign[c]
L_{2-10} vs z	53	$0.3 \leqslant z \leqslant 0.96$	0.5–8 keV observed-frame	0.26	93.5
Γ vs z	53	$0.3 \lesssim z \lesssim 0.96$	0.5–8 keV observed-frame	0.12	61.4
$N_{\rm H}$ vs z	27	$0.3 \lesssim z \lesssim 0.96$	0.5–8 keV observed-frame	−0.08	30.9
$N_{\rm H}$ vs L_{2-10}	27	$0.3 \lesssim z \lesssim 0.96$	0.5–8 keV observed-frame	0.13	50.7
Γ vs $N_{\rm H}$	27	$0.3 \lesssim z \lesssim 0.96$	0.5–8 keV observed-frame	0.14	53.6
L_{2-10} vs z	44	$0.3 \lesssim z \lesssim 0.96$	2–10 keV rest-frame	0.29	94.4
Γ vs z	44	$0.3 \lesssim z \lesssim 0.96$	2–10 keV rest-frame	0.23	87.4
$N_{\rm H}$ vs z	25	$0.3 \lesssim z \lesssim 0.96$	2–10 keV rest-frame	−0.05	20.6
$N_{\rm H}$ vs L_{2-10}	25	$0.3 \lesssim z \lesssim 0.96$	2–10 keV rest-frame	0.08	30.2
Γ vs $N_{\rm H}$	25	$0.3 \lesssim z \lesssim 0.96$	2–10 keV rest-frame	0.32	88.5
L_{2-10} vs z	54	$0.96 \leqslant z \leqslant 1.5$	0.5–8 keV observed-frame	0.16	75.6
Γ vs z	54	$0.96 \lesssim z \lesssim 1.5$	0.5–8 keV observed-frame	−0.24	91.8
$N_{\rm H}$ vs z	28	$0.96 \lesssim z \lesssim 1.5$	0.5–8 keV observed-frame	−0.33	91.8
$N_{\rm H}$ vs L_{2-10}	28	$0.96 \lesssim z \lesssim 1.5$	0.5–8 keV observed-frame	−0.15	55.4
Γ vs $N_{\rm H}$	28	$0.96 \lesssim z \lesssim 1.5$	0.5–8 keV observed-frame	−0.35	92.7
L_{2-10} vs z	46	$0.96 \lesssim z \lesssim 1.5$	2–10 keV rest-frame	0.17	74.6
Γ vs z	46	$0.96 \lesssim z \lesssim 1.5$	2–10 keV rest-frame	−0.08	41.1
$N_{\rm H}$ vs z	24	$0.96 \lesssim z \lesssim 1.5$	2–10 keV rest-frame	−0.36	91.3
$N_{\rm H}$ vs L_{2-10}	24	$0.96 \lesssim z \lesssim 1.5$	2–10 keV rest-frame	−0.10	36.0
Γ vs $N_{\rm H}$	24	$0.96 \lesssim z \lesssim 1.5$	2–10 keV rest-frame	−0.03	11.8
L_{2-10} vs z	57	$1.5 \lesssim z \lesssim 3.3$	0.5–8 keV observed-frame	0.58	>99.9
Γ vs z	57	$1.5 \lesssim z \lesssim 3.3$	0.5–8 keV observed-frame	0.14	68.4
$N_{\rm H}$ vs z	34	$1.5 \lesssim z \lesssim 3.3$	0.5–8 keV observed-frame	0.13	53.5
$N_{\rm H}$ vs L_{2-10}	34	$1.5 \lesssim z \lesssim 3.3$	0.5–8 keV observed-frame	−0.23	81.8
Γ vs $N_{\rm H}$	34	$1.5 \lesssim z \lesssim 3.3$	0.5–8 keV observed-frame	−0.11	48.3
L_{2-10} vs z	48	$1.5 \lesssim z \lesssim 3.3$	2–10 keV rest-frame	0.65	>99.9
Γ vs z	48	$1.5 \lesssim z \lesssim 3.3$	2–10 keV rest-frame	0.35	98.6
$N_{\rm H}$ vs z	30	$1.5 \lesssim z \lesssim 3.3$	2–10 keV rest-frame	0.34	93.4
$N_{\rm H}$ vs L_{2-10}	30	$1.5 \lesssim z \lesssim 3.3$	2–10 keV rest-frame	−0.02	8.8
Γ vs $N_{\rm H}$	30	$1.5 \lesssim z \lesssim 3.3$	2–10 keV rest-frame	−0.1	40.4

[a]Number of RQ AGNs in each sub-sample.

[b]The Spearman correlation coefficient.

[c]The significance of the Spearman correlation coefficient.

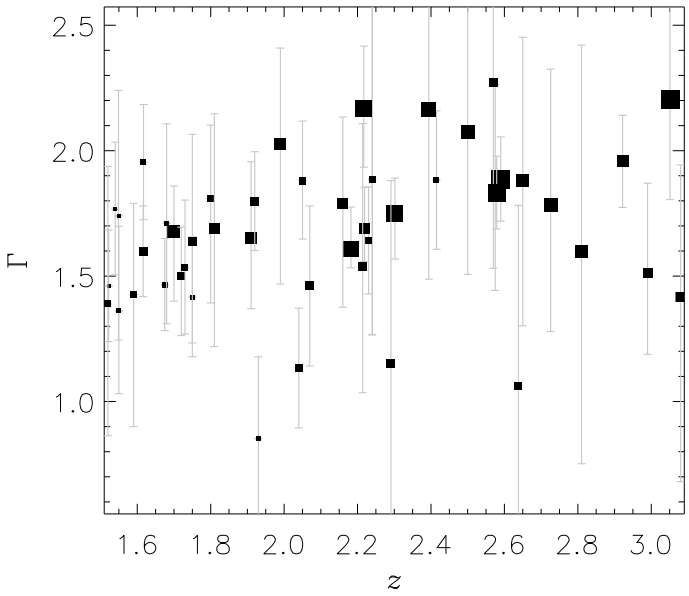

Fig. 2.14 Spectral slope (Γ) versus redshift (z) of radio-quiet AGNs with $1.5 \lesssim z \lesssim 3.3$ with fits performed in the 2–10 keV rest-frame. The size of the symbols increases with L_{2-10}.

$N_{\rm H}$ in any bin. The fact that Γ is not correlated with N_H provides further support that the $\Gamma - L_{\rm X}$ correlation is not driven by N_H.

We also find a weak correlation between $N_{\rm H}$ and z in the redshift range of $1.5 \lesssim z \lesssim 3.3$ for fits in the 2–10 keV rest-frame band. This result may imply that the intrinsic column density evolves, increasing with redshift. Such a result has been reported in several studies (e.g., La Franca et al. 2005; Treister & Urry 2006); however, the evolution of $N_{\rm H}$ with z is still a debatable topic since other authors have not found definitive evidence for the evolution in the "obscuration fraction" (e.g., Ueda et al. 2003; Akylas et al. 2006; Dwelly & Page 2006).

A rather surprising result was the detection of a correlation between Γ and z in the third redshift bin with an apparent significance of 99.6%. A careful analysis indicates that this apparent $\Gamma - z$ correlation is most likely the result of selection effects. This tendency seems to be confirmed in Figure 2.14. This Γ versus z plot indicates that higher luminosity sources tend to group in the upper right area and lower luminosity sources in the lower left area. To test for selection effects, we performed a correlation analysis including sources with luminosities greater than the minimum luminosity of a detectable source at $z \sim 3$. This limit corresponds to $\log L_{2-10} \sim 44$ (see Figure 2.5). We find that the Spearman's correlation probability of the $\Gamma - z$ correlation in the third redshift bin for fits performed in the 2–10 keV rest-frame, decreases to a non-significant level of $\sim 66\%$ when we only include sources with $\log L_{2-10} \gtrsim 44$ (30 RQ AGNs). We note, however, that within the same luminosity range the $\Gamma - L_{2-10}$ correlation is significant at the >99% ($r_C \sim 0.6$) level. Our analysis indicates that the apparent correlation

between Γ and z in the third redshift bin is most likely the result of selection effects. This conclusion is also confirmed in §2.5.2.7.

2.5.2.5 Radio-Quiet AGNs with $0.96 \lesssim z \lesssim 1.5$

In §2.5.2.1, we showed that the $\Gamma - L_{\rm X}$ correlation was not significant for sources having $0.96 \lesssim z \lesssim 1.5$, especially for fits performed in the 2–10 keV rest-frame where we found that the correlation was only significant at the ∼85% confidence level. In this section we investigate the cause of the lower significance of the $\Gamma - L_{\rm X}$ relation for sources having $0.96 \lesssim z \lesssim 1.5$. In Figure 2.15, we show Γ versus L_{2-10} for sources having $0.96 \lesssim z \lesssim 1.5$ with fits performed in the 0.5–8 keV observed-frame (upper panel) and 2–10 keV rest-frame (lower panel). The Γ versus L_{2-10} data points show a larger scatter than what is seen in the other redshift bins consistent with the lower significance found for the $\Gamma - L_{\rm X}$ correlation. In Table 2.7, we present the results of our correlation analysis of the $\Gamma - L_{\rm X}$ data for sub-samples of different intrinsic absorption. We find that sources with $\log (N_{\rm H}/{\rm cm}^{-2}) \gtrsim 22$ and $0.96 \lesssim z \lesssim 1.5$ show no significant correlation between Γ and $L_{\rm X}$, whereas sources with $\log (N_{\rm H}/{\rm cm}^{-2}) \lesssim 22$ and $0.96 \lesssim z \lesssim 1.5$ have a $\Gamma - L_{\rm X}$ correlation that is significant at the >90% confidence level. We conclude that the absorbed sources with $0.96 \lesssim z \lesssim 1.5$ are possibly diluting the correlation significance found in this redshift bin. We caution, however, that the low number of sources per sub-sample used in this analysis combined with the uncertainties in the photon indices may result in inaccurate estimates of the strengths of the correlations.

Our correlation analysis between several other spectral parameters for sources with $0.96 \lesssim z \lesssim 1.5$ is included in Table 2.8. We find an anticorrelation between $N_{\rm H}$ and z at the ∼ 90% confidence level for sources with $0.96 \lesssim z \lesssim 1.5$ and for fits performed in the 0.5–8 keV observed-frame and the 2–10 keV rest-frame bands. Correlations between Γ versus z and Γ versus $N_{\rm H}$ for sources in $0.96 \lesssim z \lesssim 1.5$ are found to be moderately significant for fits performed in the 0.5–8 keV observed-frame band and not significant for fits performed in the 2–10 keV rest-frame band.

2.5.2.6 Dependence of the $\Gamma - L_{\rm X}$ correlation on Compton-reflection

In this section, we address the possibility that the $\Gamma - L_{\rm X}$ correlation found in this work is produced by a change with luminosity of the Compton-reflection component. We note that the Compton-reflection component is difficult to model accurately in low-to-medium S/N X-ray spectra and therefore inaccurate modeling of this component may result in apparent flattening of the X-ray spectra.

Several studies indicate that the equivalent width (EW) of the iron Kα emission line in the X-ray spectra of AGNs is anti-correlated with the 2–10 keV luminosity (e.g., Iwasawa & Taniguchi 1993; Nandra et al. 1997; Page et al. 2004a; Bianchi et al. 2007). This anti-correlation is commonly referred to as the 'X-ray Baldwin effect' and is also known as the 'Iwasawa & Taniguchi effect' . There are several proposed physical explanations in the literature for the X-ray Baldwin effect including (1) a change in the covering factor of a Compton-thick torus with luminosity (e.g., Konigl & Kartje 1994), (2) a luminosity-dependent ionization state of the iron-emitting material (e.g., Nandra

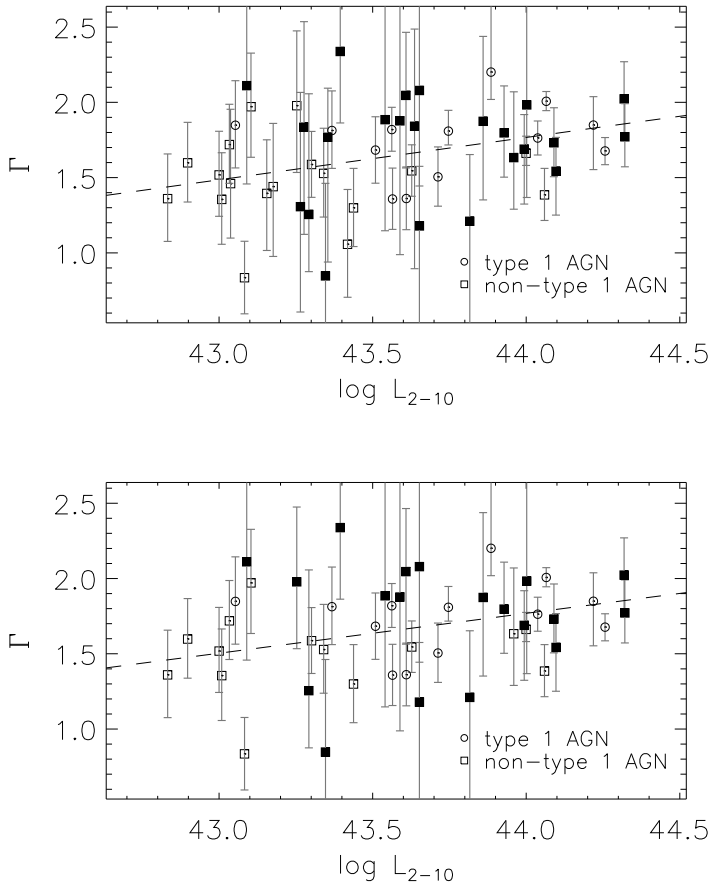

Fig. 2.15 Γ versus 2–10 keV luminosity of radio-quiet AGNs having $0.96 \lesssim z \lesssim 1.5$ with fits performed in the 0.5–8 keV observed-frame band (upper panel) and fits performed in the 2–10 keV rest-frame band (lower panel). The dashed lines indicate linear fits to the data using the least-squares method. The open symbols represent sources having $\log\,(N_{\rm H}/{\rm cm}^{-2}) \lesssim 22$, and the filled symbols represent sources with $\log\,(N_{\rm H}/{\rm cm}^{-2}) > 22$. Circles represent type 1 AGNs and squares non-type 1 AGNs.

et al. 1997), and (3) variability of the continuum AGN emission assuming constant iron-line fluxes (e.g., Jiang et al. 2006). It has also been proposed that the X-ray Baldwin effect is driven mostly by changes in the Eddington luminosity ratio rather than by X-ray luminosity (e.g., Jiang et al. 2006).

Several models of AGN accretion disks assume the iron line and Compton-reflection components originate from X-ray emission reprocessed in the accretion disk and indicate that the strength of the Compton-reflection component increases monotonically with the EW of the iron line (e.g., George & Fabian 1991; Ghisellini et al. 1994), and consequently decreases with $L_{\rm X}$ as well. Therefore, under this premise, these models could possibly explain the $\Gamma - L_{\rm X}$ relation found in this work, since a decrease of the Compton-reflection component with $L_{\rm X}$ could result in an increase in Γ with $L_{\rm X}$ if the Compton-reflection component is not modeled accurately in our spectral analysis.

Bianchi et al. (2007) recently found a strong anti-correlation between the neutral narrow component of the iron Kα emission line and the 2–10 keV luminosity of AGNs. These authors suggest that the neutral narrow iron-line component originates from the molecular torus and the broad iron-line component originates from reprocessing in the accretion disk. The dependencies, however, of the Compton-reflection component with the 2–10 keV luminosity are still unclear (e.g., Nandra et al. 1995; Page et al. 2004b). It is also unclear whether the Compton-reflection component observed in the X-ray spectra of AGNs originates mostly from the torus or the accretion disk. If the neutral narrow iron Kα emission line originates from the torus and the Compton-reflection component from the accretion disk then one cannot simply assume that the Compton-reflection component will follow the X-ray Baldwin effect. Variability studies of individual AGNs such as the Seyfert 1 galaxies NGC 5548 (Chiang et al. 2000) and MCG-6-30-15 (Lee et al. 2000) indicate that the Compton-reflection component increases with X-ray luminosity and the iron line EW and the relative normalization of the Compton-reflection hump are anti-correlated. We note that the Seyfert 1 galaxies in these variability studies were observed to vary over a factor of up to $\approx$3 in luminosity whereas our study includes objects spanning a factor of $\sim$200 in luminosity. It is therefore difficult to extrapolate the results of these variability studies to our work.

Since observationally it is still unclear how the Compton-reflection component depends on X-ray luminosity we have investigated the degree to which Compton-reflection can be driving the $\Gamma - L_{\rm X}$ relation by performing simulations and additional tests upon our data. We first simulated X-ray spectra containing Compton-reflection components with integer reflection scaling factors ranging between $0 \leq R \leq 4$. For each value of the reflection scaling factor (R=0,1,2,3,4); we simulated 1000 spectra using the FAKEIT command in XSPEC. The Compton-reflection components were simulated using the PEXRAV model, assuming sources close to the aimpoint of the ACIS-I CCD, Γ=1.9, log ($N_{\rm H}$/cm^{-2}) = 22, a total number of events per spectrum of S=550, an e-folding cutoff energy of $E_{\rm cut}$=400 keV, and an inclination angle (i) of the reflector equal to 30°. The values of E_{cut} and i were chosen to be close to those generally used to model Seyfert galaxies (e.g., Magdziarz & Zdziarski 1995). Our results are insensitive to any reasonable value of $E_{\rm cut}$ and changing i will mostly affect the overall strength of the reflection component. We performed these simulations assuming redshifts of $z = 0.7$ and $z = 2.2$, which correspond to the mean redshifts of the sources in our sample with

$0.3 \lesssim z \lesssim 0.96$ and $1.5 \lesssim z \lesssim 3.3$. We proceeded in fitting the simulated spectra with absorbed power-law models to estimate the decrease in the fitted values of Γ vs. the strength of the Compton-reflection component. In Figure 2.16 we show the best-fit values of Γ as a function of the reflection scaling factor for sources with redshifts of $z = 0.7$ (upper panel) and $z = 2.2$ (lower panel). In Figure 2.16 we also show the ratio of photons in the full band (0.5–8 keV) that originate from Compton reflection to photons from the direct power-law component ($f_{\rm R}$).

As expected fits performed in the 2–10 keV rest-frame band of the high-z sources are less affected by the Compton-reflection component and show a smaller change of Γ than fits performed in the 0.5–8 keV observed-frame band. Specifically, we find apparent changes of Γ of about 0.7 and 0.3 for fits performed in the 0.5–8 keV observed-frame and 2–10 keV rest-frame bands, respectively, for sources with $1.5 \lesssim z \lesssim 3.3$.

Our simulations indicate that if Compton reflection is producing the observed change in Γ of about 0.5 for sources with $1.5 \lesssim z \lesssim 3.3$ (see lower panel of Figure 2.10), then the mean values of Γ derived from fits performed in the 0.5–8 keV observed-frame band should differ by about 0.2 from the mean values of Γ derived from fits performed in the 2–10 keV rest-frame band. Our observations indicate that this is not the case. For sources in the redshift bins of $0.3 \lesssim z \lesssim 0.96$, $0.96 \lesssim z \lesssim 1.5$ and $1.5 \lesssim z \lesssim 3.3$ the differences between the weighted mean values of Γ ($\langle\Gamma_{rest}\rangle$-$\langle\Gamma_{obs}\rangle$) obtained from fits performed in the 0.5–8 keV observed-frame and 2–10 keV rest-frame band are -0.03 ± 0.02, 0.02 ± 0.02 and 0.01 ± 0.03 (1-σ errors), respectively; the similarity between $\langle\Gamma_{rest}\rangle$ and $\langle\Gamma_{obs}\rangle$ is consistent with the results found in §2.4. According to our simulations, if the $\Gamma - L_{\rm X}$ correlation were produced by the Compton-reflection component then these differences in the weighted mean values of Γ would increase with redshift, reaching values close to 0.2 for sources with $1.5 \lesssim z \lesssim 3.3$.

We also expect that if Compton reflection is driving the observed $\Gamma - L_{\rm X}$ relation then the strength and slope of the correlation for fits performed in the 0.5–8 keV observed-frame band should be significantly stronger and steeper than the strength and slope of the correlation for fits performed in the 2–10 keV rest-frame band, especially for the high-redshift sources. This is not the case. As shown in Table 2.3, the strength of the $\Gamma - L_{\rm X}$ relation in the 0.5–8 keV observed-frame and 2–10 keV rest-frame bands for sources with $1.5 < z < 3.3$ is 0.45 (at the 99.9% confidence level) and 0.43 (at the 99.8% confidence level), respectively. From Table 2.5 the ratio of the slopes of the $\Gamma - L_{\rm X}$ relation for sources with $1.5 < z < 3.3$ is $\alpha_{\rm obs}/\alpha_{\rm rest} = 0.98 \pm 0.25$, where $\alpha_{\rm obs}$ and $\alpha_{\rm rest}$ are the slopes derived from fits performed in the 0.5–8 keV observed-frame and 2–10 keV rest-frame bands, respectively. Based on our simulations the ratio of the slopes of the $\Gamma - L_{\rm X}$ relation for source with $1.5 < z < 3.3$ would be approximately $\alpha_{\rm obs}/\alpha_{\rm rest} \sim 1.5$ if Compton-reflection was driving the correlation.

2.5.2.7 Radio-Quiet AGNs from other surveys with $1.5 \lesssim z \lesssim 3.3$

We also tested the significance of the $\Gamma - L_{\rm X}$ correlation in the redshift range of $1.5 \lesssim z \lesssim 3.3$ by combining results from the independent surveys of Vignali et al. (1999), George et al. (2000), Reeves & Turner (2000), Page et al. (2003), and Dai et al. (2004) with the results obtained from the CDFs. In Figure 2.17, we show Γ versus L_{2-10} for

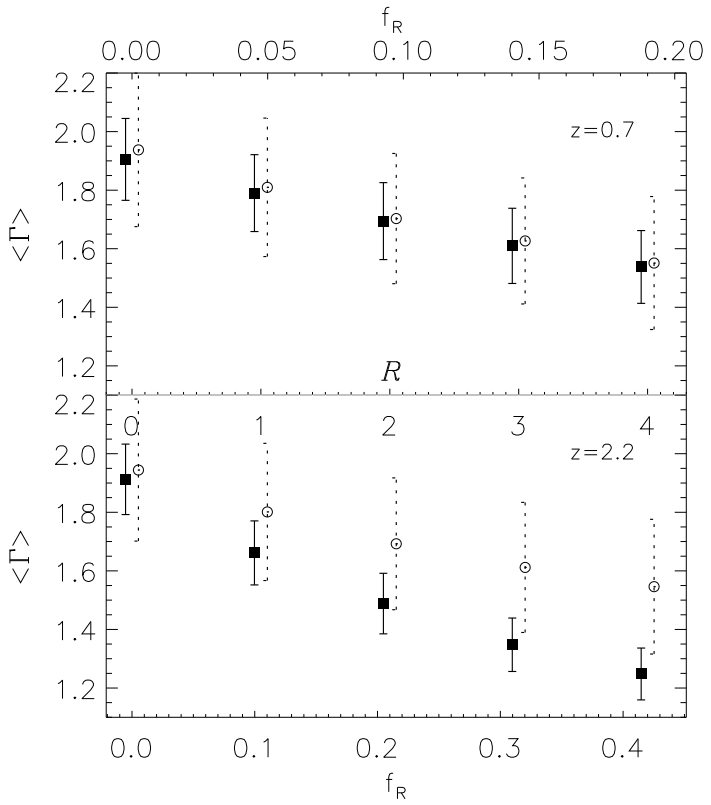

Fig. 2.16 Results from fits performed on 1000 simulated spectra with S=550, Γ=1.9, and 5 different values of the Compton-reflection scaling factor R (R=0,1,2,3,4). The mean of the best-fit values of Γ with fits performed in the 0.5–8 keV observed-frame band are shown with filled squares (solid error bars), and the mean of the best-fit values of Γ with fits performed in the 2–10 keV rest-frame band are shown with open circles (dashed error bars). A small shift in the values of R (horizontal axis) has been introduced for visual purposes. In the upper panel we show $\langle\Gamma\rangle$ vs. R with z=0.7. In the lower panel we show $\langle\Gamma\rangle$ vs. R with z=2.2. On the x-axis we also show the ratio of photons (f_R) in the full band (0.5–8 keV) that originate from Compton reflection to photons that originate from the direct power-law component. All error bars represent $\pm$ 1 σ deviations.

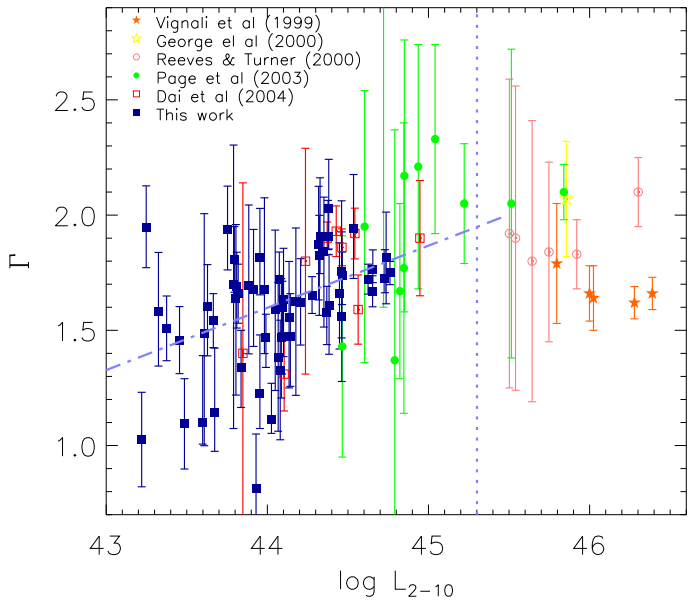

Fig. 2.17 Photon indices of $1.5 \lesssim z \lesssim 3.3$ radio-quiet AGNs obtained from several surveys versus their 2–10 keV luminosities. Open stars are from Vignali et al. (1999), filled stars are from George et al. (2000), filled circles are from Reeves & Turner (2000), open circles are from Page et al. (2003), open squares are from Dai et al. (2004) and filled squares show data from this work. The vertical dashed line corresponds to $L_{2-10} = 2 \times 10^{45}$ erg s^{-1}. The dot-dashed line shows the best-fit linear model over the luminosity range of $10^{43} - 2 \times 10^{45}$ erg s^{-1}.

sources having $1.5 \lesssim z \lesssim 3.3$ combining the results of these surveys with our fits in the 0.5–8 keV observed-frame (Table 2.2). Sources from our survey fill in the low-luminosity range of the combined data $L_{2-10} \sim 10^{43} - 10^{45}$ erg s^{-1}. In this range Γ increases with L_X; however, for $L_{2-10} \gtrsim 10^{45}$erg s^{-1} it appears that this relation begins to saturate.

We find that the Pearson linear correlation coefficient reaches a maximum value for sources with L_{2-10} in the range of $10^{43} - 2 \times 10^{45}$ erg s^{-1}, and the Spearman rank coefficient reaches a maximum value for sources with L_{2-10} in the range of $10^{43} - 8 \times 10^{45}$ erg s^{-1}. There are 76 sources with L_{2-10} in the range of $10^{43} - 2 \times 10^{45}$ erg s^{-1}. The Pearson's correlation coefficient for $\Gamma - L_{\rm X}$ in this luminosity range is $r_p \sim 0.52$ and is significant at the >99.9% confidence level (null hypothesis probability 1.8×10^{-6}). For reference, the values of the parameters of the best-fit model of the form $\Gamma = \alpha \log L_{2-10} + \beta$ can be found in Table 2.5. There are 84 sources with L_{2-10} in the range of $10^{43} - 8 \times 10^{45}$ erg s^{-1}. The Spearman correlation coefficient in this luminosity range is $r_S \sim 0.60$ and is significant at the >99.9% confidence level (null hypothesis probability $\sim 1.6 \times 10^{-9}$). The limits of the optimized ranges are marked in Figure 2.17. Figure 2.17 suggests two different luminosity regimes of the $\Gamma - L_{\rm X}$ relation. In the first regime that covers the luminosity range of $L_{2-10} \sim 10^{43} - 2 \times 10^{45}$ erg s^{-1} we find a linear relation between Γ and $\log L_{2-10}$. In the second regime, where $L_{2-10} \gtrsim 2 \times 10^{45}$ erg s^{-1}, we confirm the finding of Dai et al. (2004) that Γ decreases with L_{2-10}. Specifically, for the 16 sources with $L_{2-10} \gtrsim 2 \times 10^{45}$ erg s^{-1}, we found Γ and $L_{\rm X}$ to be anti-correlated with a Spearman correlation coefficient of $r_S \sim -0.50$ that is significant at the 95.4% confidence level. We also found that for the 84 X-ray luminous sources with L_{2-10} in the range of $10^{43} - 8 \times 10^{45}$ erg s^{-1} Γ and z are not correlated with a Spearman correlation coefficient of ~ 0.09 that is significant at the $\lesssim$60% confidence level.

2.5.2.8 Physical interpretation of the $\Gamma - L_{\rm X}$ relation and its possible evolution

AGN X-ray variability studies have proven very useful for improving our understanding of the physical structures that produce AGN X-ray spectra. Several variability studies of individual AGN have found a positive correlation between Γ and the X-ray luminosity, (e.g., Magdziarz et al. 1998; Zdziarski et al. 2003). However, the slope of the $\Gamma - L_{\rm X}$ correlation found in the studies of individual AGNs appears to be significantly steeper than the Γ versus $L_{\rm X}$ slope found in our current study. For example, Zdziarski et al. (2003) report that a change in $L_{\rm X}$ by a factor of 10 results in an increase in Γ of ~ 0.6. For a similar change in $L_{\rm X}$, we find an increase in Γ of $\sim$ 0.2–0.3 (see Table 2.5).

To explain the $\Gamma - L_{\rm X}$ correlation, we present two steady state corona models proposed by Haardt et al. (1997) and Merloni & Fabian (2001). These coronal models were originally aimed to explain various X-ray variability observations of individual objects and therefore assume a constant black-hole mass. We also introduce a third model (Merloni & Fabian 2002) focused on the relative strength of the corona emission and the accretion rate. The main goal for using this model is to provide a possible connection for the results obtained in our work with the $\Gamma - L_{\rm bol}/L_{\rm Edd}$ correlations found by Wang et al. (2004) and Shemmer et al. (2006). At the end of this section we also comment

on how the $\Gamma - L_{\rm X}$ correlation depends on the optical depth of the hot corona and its evolution with z.

The first model posits that the inner accretion disk is sandwiched by a hot, tenuous and possibly patchy corona (Haardt et al. 1997). The corona is coupled to a cooler optically-thick layer (accretion disk), which provides the seed soft photons that cool the hot layer via inverse Compton scattering. The spectrum of the scattered photons is in general well fitted by a power-law and accounts for a large fraction of the observed X-ray emission in AGNs. This model predicts that Γ increases with the optical depth of the corona τ and it decreases with the temperature of the corona. Moreover, if the corona is dominated by $e^{\pm}$ pairs, the optical depth of the hot phase is determined by the compactness ℓ alone [7], where ℓ is defined as:

$$\ell \equiv \frac{\sigma_T}{m_e c^3}\frac{L_{\rm X}}{R} \approx 10^4 \frac{\mathcal{L}}{r} \tag{2.1}$$

Here $\mathcal{L}$ is the luminosity of the corona in Eddington units, and r is its size in units of Schwarzschild radii. For the case of a pair-dominated corona this first model predicts that Γ will increase with $L_{\rm X}$. In particular, a change in $L_{\rm X}$ of a factor of 10 is predicted to produce a $\Delta\Gamma \sim 0.2$. This predicted variation is consistent with that detected in our sample but slightly lower than that observed in variability studies of individual AGNs. When $\mathcal{L} \gtrsim 0.1\ r$ ($\ell \gtrsim 1000$) the model indicates that τ saturates and does not increase beyond that luminosity (Haardt & Maraschi 1993). The first model therefore predicts a flattening of the $\Gamma - L_{\rm X}$ relation for bright sources as can be seen in Figure 2.17.

The second model originally proposed by Merloni & Fabian (2001) assumes a static patchy corona and is often referred to as the "thundercloud" model. The X-ray spectrum in this model is produced by thermal Comptonization in spherical regions that are raised above the disc at a given height due to magnetic flares in active regions of the corona. The thundercloud model predicts a $\Gamma - L_{\rm X}$ correlation that is consistent with the one we detect in our sample of radio-quiet AGNs in the case where the luminosity of an active region increases with its increasing size at a given height. Larger active regions tend to be more luminous, cooler and produce softer spectra (i.e., Γ increases). If the size of the active region gets too large, then a saturation point is reached and the $\Gamma - L_{\rm X}$ relation becomes flat for luminous sources in agreement with the combined data sample (Figure 2.17). The luminosity of an active region is assumed to scale with its size r via the relation $L(r) \propto r^D$, where D is a free parameter in the model which may be related to the internal structure of the region and/or radial dependence of the energy generation in the accretion disk. Any change in D will directly affect the slope of the $\Gamma - L_{\rm X}$ relation, making this model more flexible to explain both our $\Gamma - L_{\rm X}$ correlation in high redshift AGNs and those found in variability studies of individual AGN (Zdziarski et al. 2003).

Under the assumption that the correlation is produced by sources of similar black-hole masses, it seems natural that changes in X-ray luminosity may result from changes in the Eddington ratio $\epsilon = \dot{m}$, where $\dot{m}$ is the accretion rate in units of $\dot{M}_{\rm Edd} = \frac{L_{\rm Edd}}{\eta c^2}$ (η is the accretion efficiency). Specifically, assuming $L_{\rm X}$ increases with $L_{\rm bol}$ (see equation 21 of Marconi et al. 2004) and since $L_{\rm bol} = \epsilon L_{\rm Edd}$ we expect, for sources with similar

[7] $e^{\pm}$ pair production becomes important for $\ell \gtrsim 10$ (e.g., see page 51 of Peterson 1997)

mass, an increase in ϵ to result in an increase in $L_{\rm X}$. A more detailed analysis is provided in Merloni & Fabian (2002) in the case of a coronal-outflow dominated accretion disk model. Under the assumption that the total power released from the accretion disk-corona system is $L_{\rm bol} \equiv \epsilon L_{\rm Edd}$, a fraction f will be released in the corona $L_{\rm X} \approx f \cdot L_{\rm bol}$. Assuming that magnetohydrodynamic turbulence is the main source of angular momentum transport, Merloni & Fabian (2002) concluded that the relationship between f and ϵ can be approximately modeled as a power-law $f \propto \epsilon^{-\delta}$ with $\delta \sim 0.4$. This relation is mostly independent of the mass of the black hole $M_{\rm BH}$ (Wang et al. 2004). Assuming that $M_{\rm BH}$ is kept constant then $L_{\rm X} \propto \epsilon^{1-\delta}$, and therefore $L_{\rm X}$ increases with ϵ. Using these relations in combination with a steady corona model like the ones already described in this section, while assuming that τ increases with ϵ, Merloni & Fabian (2002) concluded that the corona gets cooler and Γ increases with ϵ. This could give a plausible explanation for the correlation between $\Gamma - L_{\rm bol}/L_{\rm Edd}$ found by Shemmer et al. (2006). Based on the above, and assuming similar black-hole masses, variations in the Eddington ratio could also explain the correlation found in our work since the coronal-outflow dominated accretion disk model predicts that Γ increases with $L_{\rm X}$.

An alternative explanation is that the $\Gamma - L_{\rm X}$ correlation is driven by variations in the black-hole masses of the sources and ϵ is constant, which is in agreement with the predictions of semi-analytic models by Kauffmann & Haehnelt (2000). It is possible that the correlation could be produced in this case if the optical depth of the corona τ increases with the mass of the black hole $M_{\rm BH}$. This is equivalent to assuming that ℓ increases with $M_{\rm BH}$ in the model of Haardt et al. (1997) for an $e^{\pm}$ dominated corona. Since $\mathcal{L} \propto M_{\rm BH}$, the previous assumption is valid if we assume that the size of the corona is kept approximately constant as $M_{\rm BH}$ increases (see equation (2.1)). Under this assumption, both steady corona models (Haardt et al. 1997; Merloni & Fabian 2001) analyzed here will reproduce the $\Gamma - L_{\rm X}$ relation.

The possible evolution of the slope and offset of the $\Gamma - L_{\rm X}$ correlation found in this study of RQ AGNs can be explained by an evolution of the properties of the hot corona. Specifically, the slope of the $\Gamma - L_{\rm X}$ correlation depends on the optical depth and compactness parameter of the corona in the model of Haardt et al. (1997) and the optical depth of the active regions in the thundercloud model by Merloni & Fabian (2001). If AGNs within a certain redshift range contain hot coronae of similar properties we expect them to show a significant correlation between Γ and $L_{\rm X}$ in this redshift range. One explanation of the possible evolution of the slope and offset of the $\Gamma - L_{\rm X}$ correlation is that the mean properties of the hot coronae of AGN evolve resulting in a detectable change in the slope and offset of the $\Gamma - L_{\rm X}$ correlation between AGNs at $z \sim 2.2$ and $z \sim 0.7$. One possible explanation for the slight decrease in the strength of the Γ and $L_{\rm X}$ correlation in the second redshift bin is that this redshift interval includes AGNs with a large range of coronal properties leading to a weaker correlation between Γ and $L_{\rm X}$. We note that the possible decrease in the significance of the Γ and $L_{\rm X}$ correlation in the second redshift bin needs to be confirmed with a larger sample of RQ AGN.

2.6 Conclusions

In this chapter we have selected a sample of radio-quiet AGNs (173) from the CDF surveys with moderate-to-high S/N, and have found strong evidence of a correlation between the X-ray spectral parameters Γ and $L_{\rm X}$. We found that the slope and offset of a linear fit to the $\Gamma - L_{\rm X}$ correlation possibly evolves for sources with $z \gtrsim 0.1$. Analyzing this relation in three different redshift bins that contain a similar number of sources ($\sim$50) we conclude that this correlation is highly significant in two redshift bins, $0.3 \lesssim z \lesssim 0.96$, and $1.5 \lesssim z \lesssim 3.3$ and slightly less significant in the redshift bin $0.96 \lesssim z \lesssim 1.5$. We note that the possible weakness of this correlation for sources with $0.96 \lesssim z \lesssim 1.5$ appears to be driven by the absorbed sources in this redshift range. The $\Gamma - L_{\rm X}$ correlations in $0.3 \lesssim z \lesssim 0.96$ and $1.5 \lesssim z \lesssim 3.3$ are significant at the >99.9% confidence level for fits performed in the 0.5–8 keV observed-frame and at the >99.5% confidence level in the 2–10 keV rest-frame.

The fact that this correlation is also present when we estimate the luminosities in the 2–10 keV rest-frame, and also holds for sources with low column densities, suggests that this correlation is not artificially driven by any unmodeled complexity in the intrinsic absorption ($N_{\rm H}$). We performed several tests to investigate whether the $\Gamma - L_{\rm X}$ correlation found in this study is produced by a change with luminosity of the Compton-reflection component. We found that the strengths and slopes of the $\Gamma - L_{\rm X}$ correlation are similar for fits performed in the 0.5–8 keV observed-frame and 2–10 keV rest-frame bands. Our analysis indicates that the strengths and slopes would be significantly different if the correlation was driven by a Compton-reflection component. The difference between the observed weighted mean values of Γ obtained from fits performed in the 0.5–8 keV observed-frame and 2–10 keV rest-frame bands is less than 0.03. Our simulations indicate that if an un-modeled Compton-reflection component was producing the observed correlation a difference of Γ of about 0.2 would be expected. We conclude that a Compton-reflection component is unlikely to be driving the $\Gamma - L_{\rm X}$ correlation found in this study.

This correlation applies to sources with two different luminosity populations; one with $\log L_{2-10} \sim 43.1 \pm 0.5$ ($0.3 \lesssim z \lesssim 0.96$), and the other with $\log L_{2-10} \sim 44.1 \pm 0.4$ ($1.5 \lesssim z \lesssim 3.3$) (see Figure 2.9), indicating different populations of AGNs. The $\Gamma - L_{\rm X}$ relation results in a softening of the X-ray spectra as the luminosity of the AGNs increases.

The $\Gamma - L_{\rm X}$ correlation found in the redshift range of $1.5 \lesssim z \lesssim 3.3$ is of special interest because it confirms a previous independent study of RQQ at $z \gtrsim 1.5$ (Dai et al. 2004). Combining data from Dai et al. (2004) and other surveys (Vignali et al. 1999; George et al. 2000; Reeves & Turner 2000; Page et al. 2003), cited in Dai et al. (2004), we find that the $\Gamma - L_{\rm X}$ correlation becomes even more significant in the luminosity range of $L_{2-10} \sim 10^{43} - 8 \times 10^{45}$erg s^{-1} with a Spearman correlation coefficient of $r_S \sim 0.6$ significant at the >99.9% confidence level (null hypothesis probability $\sim 1.6 \times 10^{-9}$).

We presented two steady-corona models (Haardt et al. 1997; Merloni & Fabian 2001) that can explain both the $\Gamma - L_{\rm X}$ correlation found in this work and the saturation observed in the L_{2-10} vs. Γ relation using the surveys analyzed in §2.5.2.7. Based on these models, we proposed two different interpretations to explain the $\Gamma - L_{\rm X}$ correlation

and its possible evolution with z. The first interpretation posits that this relation is driven by changes in the Eddington ratio ($\epsilon = L_{\rm bol}/L_{\rm edd}$) for a population of AGNs of similar mass. The second interpretation posits that the $\Gamma - L_{\rm X}$ relation is driven by changes in the mass of the AGNs. The present analysis does not allow us to infer which of these two scenarios is primarily responsible for driving the $\Gamma - L_{\rm X}$ correlation; however, future measurements of the black-hole masses for several AGNs in our sample will allow us to resolve this issue.

To explain the detected possible evolution of the slope and offset of the linear fit to the $\Gamma - L_{\rm X}$ correlation we have proposed a simple model that posits that the mean properties of the hot coronae of AGN at $z \sim 2.2$ differ significantly from those of AGN at $z \sim 0.7$. This model also assumes that within each redshift bin the optical depths of the hot coronae of the AGNs are similar.

We note that the detected change of the $\Gamma - L_{\rm X}$ correlation found in our study applies to RQ AGNs detected in the CDFs, which are two representative and normal fields. Further X-ray spectral studies of deep *Chandra* fields will test if the detected change of the $\Gamma - L_{\rm X}$ correlation also applies to wider fields of view. Expanding the sample will also test the correlation in narrower redshift bands and thus better constrain the epoch at which possible changes in the average emission properties of AGNs occurred.

Chapter 3

Suzaku observations of near-relativistic outflows in the BAL quasar APM 08279+5255

3.1 Introduction

Recent observations of nearby galaxies indicate the presence of a $M_{\rm BH}$–σ relation (e.g., Ferrarese & Merritt 2000; Gebhardt et al. 2000), where $M_{\rm BH}$ is the mass of the central black hole and σ is the velocity dispersion of the stars in the bulge of the host galaxy. The presence of a $M_{\rm BH}$–σ relation suggests that a feedback mechanism exists regulating the co-evolution between the massive black hole at the center of a galaxy and the formation of its bulge. A possible mechanism of feedback is quasar outflows. Recent theoretical models demonstrate that quasar feedback can serve as a fundamental ingredient in structure formation and galaxy mergers (e.g., Granato et al. 2004; Hopkins et al. 2005a,b; Springel et al. 2005). Quasar outflows could possibly provide an important source of feedback during the growth of the super-massive black-holes (SMBHs) in galactic bulges (e.g., Fabian 1999). Another possible mechanism of feedback may be linked to powerful jets apparently driven by magnetohydrodynamic forces. As observations indicate, these powerful jets are predominantly present in radio-loud (RL) AGNs,[1] which tend to be found in massive galaxies and dense environments (e.g., Best et al. 2005). The importance of jets as a feedback mechanism has been demonstrated with recent *Chandra* observations of cavities in clusters of galaxies and giant elliptical galaxies (e.g., McNamara & Nulsen 2007, and references therein). The injection of power into the Intergalactic Medium (IGM) by radio jets is a promising feedback mechanism that may explain the suppression of cooling flows in the centers of clusters of galaxies (e.g., Fabian et al. 2000; McNamara et al. 2000; Schindler et al. 2001; Heinz et al. 2002). It is not clear, however, if radio jets also contribute to the feedback process in field galaxies, especially ones in the redshift range of $z = 1 - 3$ where the number density of galaxy mergers is thought to peak. Most clusters of galaxies are not formed until $z \approx 1$ as inferred from observations (e.g., Hilton et al. 2007) and as predicted in theories that consider a low-density ($\Omega_m \approx 0.3$) Universe (e.g., Bahcall & Fan 1998; Younger et al. 2005). In addition, the fraction of radio-loud AGNs (RLF) appears to evolve with redshift (e.g., Peacock et al. 1986; Schneider et al. 1992; Jiang et al. 2007) and luminosity (e.g., La Franca et al. 1994; Jiang et al. 2007). In particular, the RLF tends to increase with luminosity and decrease with redshift. For example, for luminous AGNs ($M_{2500} = -26$; where M_{2500} is the absolute magnitude at rest-frame 2500Å) it is

[1] Radio-quiet (RQ) AGNs in general do not contain large (i.e. kpc) scale collimated jets, although pc-scale jets have been found in some RQ AGNs (e.g., Blundell et al. 1996). Also a fraction (∼40%) of radio-quiet AGNs could have kpc radio-structures possibly indicating the presence of an "aborted jet" (Gallimore et al. 2006).

expected that the RLF declines from 24.3% to 4.1% as the redshift increases from 0.5 to 3 (Jiang et al. 2007). [2]

Quasar outflows present a promising mechanism of feedback in high-redshift quasars and possibly in both radio-quiet and radio-loud AGNs. Powerful winds are observed in Broad Absorption Line (BAL) quasars, which show deep and broad absorption features from highly ionized ultraviolet (UV) transitions. BAL quasars are also commonly detected to be X-ray weak as a result of high intrinsic absorption column densities ($N_{\rm H}$) typically in the range of (1–50)$\times 10^{22}$ cm^{-2} (e.g., Gallagher et al. 2002, 2006). We note, however, that a recent survey of BAL quasars obtained from the cross correlation of SDSS and 2XMM catalogs by Giustini et al. (2008) finds no or lower than typical intrinsic X-ray neutral absorption than that found in optically selected BAL quasar samples. In the orientation-based BAL model (e.g., Weymann et al. 1991) quasar winds exist in most quasars; however, because of the relatively small opening angles of these outflows only a fraction of radio-quiet quasars have detectable BAL features in their UV and/or optical spectra. Models based on numerical simulations and observations suggest that the winds of BAL quasars are nearly equatorial (e.g., Murray et al. 1995; Elvis 2000; Proga et al. 2000); however, there are a few observed cases of BAL quasars with outflowing absorbers in the polar direction (e.g., Zhou et al. 2006). Recent studies indicate that BAL quasars comprise ∼15–40% of the quasar population (e.g., Chartas 2000; Hewett & Foltz 2003; Gibson et al. 2008; Dai et al. 2008).

Our current understanding of AGN physics suggests that the most likely mechanisms to explain the origin of outflows in AGNs are thermal driving, radiation driving (line and continuum), and magnetic driving. Thermal driving will produce slow winds (with speeds similar to the sound speed) at large radii ($\sim 10^4 R_S$; where $R_S = 2GM/c^2$ is the Schwarzchild radius) and with a relatively small mass-loss rate ($\sim 0.1 M_\odot {\rm yr}^{-1}$) (e.g., Begelman et al. 1983; Krolik et al. 1986). Therefore, in AGNs thermal driving is not expected to produce fast and massive winds and consequently it is likely not a major contributor to feedback. Given the typical low temperatures of AGN accretion disks ($T \sim 10^5$ K) and the large gas densities at the base of winds we expect that initially the absorbing material will have a relatively low ionization parameter. For such conditions radiation-driving can lead to significant acceleration of the absorber. Magnetic driving could also be present in strong AGN winds, through the action of MHD (magnetohydrodynamic) forces (e.g., Everett 2005). In general, we expect MHD and radiation-pressure forces to act jointly with the contribution of radiation pressure becoming increasingly important in sources with higher $L_{\rm bol}/L_{\rm Edd}$ (e.g., Everett 2005, 2007). Dust in the outflow could also boost the radiation pressure depending on the spectral energy distribution (SED) and column density of the material surrounding the AGN (Laor & Brandt 2002; Fabian et al. 2008). At the moment, evidence for the presence of near-relativistic outflows in AGN is accumulating (e.g., Chartas et al. 2002; Reeves, O'Brien & Ward 2003; Pounds et al. 2003; Dadina & Cappi 2004; Chartas et al. 2007a; Zheng & Wang

[2] As in Jiang et al. (2007) the RLF can be written in the form of $\log[{\rm RLF}/(1-{\rm RLF})] = b_0 + b_{\rm z}\log(1+z) + b_{\rm M}(M_{2500}+26)$, where M_{2500} is the absolute magnitude at rest-frame 2500 Å, $b_0 \sim -0.13$, $b_{\rm z} \sim 2.05$, and $b_{\rm M} \sim 0.18$.

2008)[3] ; however, there is no satisfactory model that can produce outflows with the near-relativistic velocities observed (e.g., Murray et al. 1995; Proga et al. 2000; Everett 2005). We note that recent studies (e.g., Chelouche & Netzer 2003; Everett 2005) indicate that with the appropriate shielding, initial density of the wind, AGN SED and $L_{\rm bol}/L_{\rm Edd}$, the efficiency of the outflows can be significantly increased and the outflow velocities may approach near-relativistic values.

Due to their high intrinsic absorption, many BAL quasars appear as faint X-ray sources (e.g., Green & Mathur 1996; Gallagher et al. 1999). Partly because of this faintness, it is difficult to detect BALs in X-ray spectra, and as a consequence, there are only a few cases where X-ray BALs have been detected in gravitationally lensed BAL quasars where the magnification effect results in increased signal-to-noise ratio spectra. Observations in X-rays of the BAL quasar APM 08279+5255, the mini-BAL quasar PG 1115+080, and perhaps the low-ionization BAL quasar H 1413−117 have suggested the presence of near-relativistic outflows of X-ray absorbing material in these objects (Chartas et al. 2002, 2003, 2007a,b). The reported variability of the high-energy absorption features is over rest-frame time-scales of 1.8 weeks in APM 08279+5255 (significant detection of variability) and 6 days in PG 1115+080 (marginal detection of variability). The analysis of these high-redshift quasars implied that outflows should have a significant impact in shaping the evolution of their host galaxies and in regulating the growth of the central black hole. These observations are particularly important because they allow us to probe quasar winds at times close to the peak of the comoving number density of luminous quasars.

In this chapter we describe the analysis of three recent *Suzaku* observations of the lensed BAL quasar APM 08279+5255. A ∼100 ks observation of APM 08279+5255 was performed starting on 2006 October 12 (OBS1), a ∼100 ks observation was performed starting on 2006 November 01 (OBS2), and a ∼120 ks observation was performed starting on 2007 March 24 (OBS3).

Unless stated otherwise, throughout this chapter we use CGS units, the errors listed are at the 1-σ level, and we adopt a flat Λ-dominated universe with $H_0 = 70$ km s^{-1} Mpc^{-1}, $\Omega_\Lambda = 0.7$, and $\Omega_M = 0.3$.

3.2 Data analysis

For the reduction and analysis of our observations we used the *Suzaku* software version 7, which is included in HEASOFT version 6.4. To analyze data from the X-ray Imaging Spectrometer (XIS) and the Hard X-ray Detector (HXD) we used calibration files that are part of the *Suzaku* CALDB database released on 2008 April 01. [4]

[3] A recent paper by Vaughan & Uttley (2008) suggests that some of the claimed near-relativistic outflows, especially in cases with narrow absorption lines, are detected at moderate significance levels and may be spurious. We note, however, that the statistical significance of the blushifted broad X-ray absorption features detected in APM 08279+5255 and PG 1115+080 is not disputed.

[4] CALDB version 20080401.

Table 3.1: Log of observations of APM 08279+5255.

Date	OBS ID[a]	Telescope	Instrument	Exposure	Net exp	Net counts[b]	f_{2-10}[c]
2002-02-24	Cha02[d]	*Chandra*	ACIS BI	88.8 ks	...	5723±76	4.3
2002-04-28	Has02[d]	*XMM-Newton*	EPIC pn	100.2 ks	...	12928±136	4.0
2006-10-12	701057010	*Suzaku*	XIS FI	102.3 ks	71.3 ks	7760±88	4.2±0.4
2006-10-12	701057010	*Suzaku*	XIS BI	102.3 ks	71.3 ks	3046±55	3.5±0.5
2006-11-01	701057020	*Suzaku*	XIS FI	102.3 ks	67.9 ks	7121±84	3.8±0.3
2006-11-01	701057020	*Suzaku*	XIS BI	102.3 ks	67.9 ks	2855±78	3.5±0.4
2007-03-24	701057030	*Suzaku*	XIS FI	117.1 ks	86.4 ks	6059±104	4.0±0.3
2007-03-24	701057030	*Suzaku*	XIS BI	117.1 ks	86.4 ks	3833±88	3.9±0.3

[a]Throughout this chapter we identify the *Suzaku* observations 701057010 as OBS1, 701057020 as OBS2, and 701057030 as OBS3.

[b]These counts are obtained in the 0.6–9 keV observed-frame band and in the 0.4–7 keV observed-frame band for the FI and BI chips, respectively. In each *Suzaku* observation, ≈25% of the FI counts and ≈28% of the BI counts are background.

[c]The fluxes (in units of 10^{-13}ergs cm^{-2} s^{-1}) in the 2–10 keV observed-frame band are obtained using the best-fit absorbed power-law model (model 2; §3.3) in our *Suzaku* observations. The fluxes measured in the BI chips are on average less than those in the FI chips. This is due to a higher half-power-diameter (HPD) of the XIS1 instrument, compared to the HPDs of the XIS0, XIS2, and XIS3 instruments.

[d]In this table we identify as Cha02 the 88.8 ks observation of APM 08279+5255 performed with *Chandra* in 2002 and analyzed in detail in Chartas et al. (2002). We also identify as Has02 the 100.2 ks observation of APM 08279+5255 performed with *XMM-Newton* in 2002 and analyzed in detail in Hasinger et al. (2002).

3.2.1 XIS data analysis

Our data reduction followed the procedures recommended by the *Suzaku* team for Spaced-Row Charge Injection (SCI) data. The data reduction was performed on the event files of each XIS instrument (XIS 0, 1, 2, and 3), and began with recalculating the PI[5] values of the unfiltered event files using the XISPI routine. Once the event files were reprocessed, we used the XSELECT software to apply the standard screening criteria (see the *Suzaku* ABC guide[6]) and obtain "cleaned" event files. The data-screening criteria include selecting events corresponding to ASCA grades 0, 2, 3, 4, and 6, Earth elevation angles greater than 5° (ELV>5), Earth day-time elevation angles greater than 20° (DYE_ELV>20), exclusion of passages through or close to the South Atlantic Anomaly (SAA), and cut-off rigidity[7] criteria of > 6 GeV/c (COR>6). As a final step in screening the data we removed hot-flickering pixels through the use of the SISCLEAN routine in XSELECT. The total exposure time of each XIS chip decreased by ≈20% after the above screening criteria were applied. Using the clean event files we extracted events in a circular region centered on the source with a radius of 150 pixels ($2.5'$). Background events were extracted in an annulus centered on the source with an inner radius of ∼230 pixels ($3.8'$) and an outer radius of ∼430 pixels ($7.1'$). Our selected background region excludes APM 08279+5255 and the calibration sources located near the corners of the CCDs. The response matrix files (RMFs) and ancillary response files (ARFs) were generated using the XISRMFGEN and XISSIMARFGEN routines which include the correction for the hydrocarbon contamination[8] on the optical blocking filter.

For the front-illuminated (FI) XIS chips (XIS 0, 2, 3) we considered events with energies lying in the range 0.6–10 keV, while for the back-illuminated (BI) XIS 1 chip we considered events with energies lying in the range 0.4–8 keV. Due to calibration uncertainties near the CCD Si K absorption edge at 1.84 keV, events with energies lying in the range 1.7–1.95 keV were ignored in the analysis of all four XIS chips. In order to assess systematic uncertainties in the response files, we fitted the Ni Kα (7.470 keV) calibration line of each instrument. We found similar positive shifts in the inferred energies of the calibration lines of each XIS chip ranging from 10 to 20 eV. These shifts in energy were not large enough to cause any significant impact on our analysis, and therefore we did not attempt to correct them. The net source count rate for each XIS chip and each observation was ≈0.04 counts s^{-1}, with a background of ≈30 % of the source rate. The spectra obtained on the FI chips were combined using the routine ADDSPEC (in HEASOFT FTOOLS) in order to increase their signal-to-noise ratio. In Table 3.1 we have included information relevant to the XIS data analysis. Specifically, this table lists the observation ID, exposure time, net exposure time (after the screening process), net

[5]Each event has a measured "Pulse Height Amplitude" (PHA). A calculated "PHA Invariant" (PI) value is obtained using the PHA in combination with the instrumental calibration and gain drift. For the XIS, the PI column name is "PI", which takes values from 0 to 4095. The PI vs. energy relationship is the following: E[eV] = 3.95 × PI[channel].

[6]http://heasarc.gsfc.nasa.gov/docs/suzaku/analysis/abc/

[7]Cut-off rigidity (COR) is a local measure of the ability of the geomagnetic field to repel cosmic rays. Specifically, it is the minimum momentum (in units of GeV/c) with which a cosmic-ray particle can penetrate as far as the satellite orbit.

[8]The XISSIMARFGEN routine incorporates the XISCONTAMICALC routine which is used to correct the observation for the XIS optical blocking filter (OBF) contamination. The absorption due to these contaminants depends on the X-ray energy, time, detector ID and location on the detector.

counts (for the FI and BI chips) and flux in the 2–10 keV observed-frame (for the FI and BI chips) using the best-fitted absorbed power-law model (model 2; §3.3). We also have included in Table 3.1 information from two previous deep X-ray observations of APM 08279+5255. These observations correspond to an 88.8 ks *Chandra* exposure (see Chartas et al. 2002) and to a 100.2 ks *XMM-Newton* exposure (see Hasinger et al. 2002). The counts collected by the XIS FI chips for each of our observations are comparable to those obtained in the *Chandra* observation.

3.2.2 HXD data analysis

Similarly to the XIS case the clean event files were obtained from the unfiltered event files following the instructions in the *Suzaku* ABC guide. The screening criteria are similar to those applied to the XIS instruments, specifically, we used ELV>5°, DYE_ELV>20°, exclusion of passages close to the SAA, and COR>6 (units of $\left[\frac{\mathrm{GeV}}{c}\right]$). The HXD-PIN spectrum was extracted from the cleaned events file described above. We extracted the source spectra from the clean files using XSELECT. In order to estimate non X-ray background (NXB) events, we used version 2 of a time-dependent instrumental background event file (referred to as the PIN background event file) which was provided by the *Suzaku* team. The PIN background event file was generated with a count rate that is ten times larger than the real instrumental PIN background. Therefore, we increased the effective exposure time of our observed PIN background spectra by a factor of ten. The exposure time was corrected for dead time using the HXDDTCOR task, leaving an effective exposure time of ∼90% of the original exposure time. The effective exposure time of each observation, together with the count rates (10–40 keV) of the source and NXB are presented in Table 3.2. The NXB does not include the contribution from cosmic X-ray background (CXB). Therefore the CXB counts (see Table 3.2) have been estimated from a fake spectrum generated using the FAKEIT command of XSPEC with the following model (e.g., Boldt 1987):

$$\frac{CXB(E)}{9.412\times10^{-3}} = e^{-\frac{E}{40\mathrm{keV}}}\left(\frac{E}{1\mathrm{keV}}\right)^{-1.29}\mathrm{cm}^{-2}\mathrm{s}^{-1}\mathrm{sr}^{-1}\mathrm{keV}^{-1}. \quad (3.1)$$

The response file used to fit the PIN spectra was obtained from the *Suzaku* CALDB calibration files. The HXD spectral analysis was performed in the 10–40 keV energy range.

3.3 Spectral analysis

In this section we fit the *Suzaku* spectra of APM 08279+5255 with a variety of models using the software tool XSPEC version 12. We also fit the spectra with more realistic models based on the photoionization code XSTAR. In all spectral models we assume a Galactic column density of $4.1\times10^{20}\mathrm{cm}^{-2}$ (Kalberla et al. 2005). Most of this section concentrates on the analysis of the XIS spectra; however, in the last part (§3.3.2) we present results from the spectral analysis of the PIN spectra of APM 08279+5255.

Table 3.2. Log of PIN HXD *Suzaku* observations of APM 08279+5255.

Epoch	Net exposure	10–40 keV count rate (10^{-2}cts s^{-1}) source	NXB	CXB[a]
OBS1	88 ks	49.75±0.24	48.17±0.07	2.30±0.05
OBS2	89 ks	50.37±0.24	46.05±0.07	2.39±0.05
OBS3	103 ks	47.07±0.21	44.12±0.06	2.29±0.05

[a]The CXB counts have been estimated from a fake spectrum generated using the FAKEIT command of XSPEC with the model given in equation (3.1).

3.3.1 XIS spectral fits.

3.3.1.1 XSPEC spectral fits.

Each observation of APM 08279+5255 provides spectra obtained with the single BI chip (XIS1) and the FI chips (XIS 0, 2, and 3). Since the responses of the FI chips are similar we co-added the FI spectra from each observation. We note that there is no XIS 2 spectrum of APM 08279+5255 for our third epoch (OBS3) due to the failure of the XIS2 chip.[9] To fit the spectra using χ^2 statistics we grouped each XIS spectrum with a sufficient number of counts. The minimum number of counts per bin was also chosen to maximize the signal-to-noise ratio in each bin without losing the features in the spectra and to keep a similar number of spectral bins in each spectrum (≈70). The minimum number of counts per bin chosen for the BI chip was 40 for epochs OBS1 and OBS2 and 50 for epoch OBS3. The grouping for the FI chips was 100 counts per bin for epochs OBS1 and OBS2 and 80 counts per bin for epoch OBS3. Note that for epoch OBS3 we have made the bins broader in the BI spectra due to the longer exposure and have made the bins narrower in the FI spectra to compensate for the loss of XIS2.

[9]On 2006 November 9, about 2/3 of the imaging area of XIS2 became suddenly unusable (http://heasarc.gsfc.nasa.gov/docs/suzaku/news/xis2.html).

Table 3.3: Results from spectral fits to the three *Suzaku* observations of APM 08279+5255.

		FI SPECTRUM[b]			BI SPECTRUM[b]		
Model[a]	Parameter	Values OBS 1	Values OBS 2	Values OBS 3	Values OBS 1	Values OBS 2	Values OBS 3
1.....	Γ	$1.70^{+0.02}_{-0.02}$	$1.75^{+0.03}_{-0.03}$	$1.77^{+0.03}_{-0.03}$	$1.67^{+0.04}_{-0.04}$	$1.58^{+0.05}_{-0.05}$	$1.61^{+0.04}_{-0.04}$
	χ^2/ν	118.3/73	125.8/66	99.1/71	114.0/71	140.8/66	100.6/71
	$P(\chi^2/\nu)$	6×10^{-4}	1×10^{-5}	0.02	9×10^{-4}	2×10^{-7}	0.01
2.....	Γ	$1.89^{+0.04}_{-0.03}$	$1.98^{+0.04}_{-0.04}$	$1.88^{+0.05}_{-0.05}$	$1.96^{+0.07}_{-0.07}$	$1.93^{+0.07}_{-0.07}$	$1.92^{+0.06}_{-0.06}$
	log $(N_{\rm H}/{\rm cm}^{-2})$	$22.83^{+0.09}_{-0.10}$	$22.92^{+0.09}_{-0.10}$	$22.66^{+0.15}_{-0.20}$	$22.74^{+0.09}_{-0.09}$	$22.78^{+0.09}_{-0.10}$	$22.75^{+0.09}_{-0.09}$
	χ^2/ν	90.5/72	87.9/65	91.0/70	86.7/70	101.3/65	59.0/70
	$P(\chi^2/\nu)$	0.07	0.03	0.05	0.59	3×10^{-3}	0.82
3.....	Γ	$1.90^{+0.04}_{-0.05}$	$1.99^{+0.05}_{-0.05}$	$1.90^{+0.05}_{-0.05}$	$1.97^{+0.07}_{-0.07}$	$1.94^{+0.08}_{-0.08}$	$1.94^{+0.07}_{-0.07}$
	log $(N_{\rm H}/{\rm cm}^{-2})$	$22.92^{+0.08}_{-0.07}$	$22.99^{+0.07}_{-0.09}$	$22.80^{+0.13}_{-0.15}$	$22.79^{+0.11}_{-0.11}$	$22.87^{+0.16}_{-0.12}$	$22.93^{+0.08}_{-0.15}$
	log ξ	<0.18	<0.11	<0.75	<0.22	<0.68	<0.98
	χ^2/ν	86.0/71	83.2/64	87.6/69	84.4/70	99.7/64	56.6/69
	$P(\chi^2/\nu)$	0.11	0.05	0.06	0.12	3×10^{-3}	0.86
4.....	Γ	$1.90^{+0.07}_{-0.07}$	$2.00^{+0.07}_{-0.08}$	$1.91^{+0.09}_{-0.09}$	$1.96^{+0.08}_{-0.09}$	$1.92^{+0.09}_{-0.08}$	$1.91^{+0.06}_{-0.06}$
	log $(N_{\rm H}/{\rm cm}^{-2})$	$22.85^{+0.18}_{-0.10}$	$23.01^{+0.20}_{-0.15}$	$22.71^{+0.22}_{-0.16}$	$22.75^{+0.11}_{-0.10}$	$22.79^{+0.12}_{-0.10}$	$22.75^{+0.12}_{-0.07}$
	CF	$0.95^{+0.05}_{-0.32}$	$0.89^{+0.11}_{-0.22}$	$0.92^{+0.08}_{-0.26}$	$0.95^{+0.05}_{-0.11}$	$0.94^{+0.06}_{-0.08}$	$0.93^{+0.07}_{-0.08}$
	χ^2/ν	86.9/71	85.6/64	88.9/69	85.4/70	100.9/64	57.9/69
	$P(\chi^2/\nu)$	0.10	0.04	0.05	0.10	2×10^{-3}	0.82

Continued on Next Page...

Table 3.3 – Continued

Model[a]	Parameter	FI SPECTRUM[b] Values OBS 1	FI SPECTRUM[b] Values OBS 2	FI SPECTRUM[b] Values OBS 3	BI SPECTRUM[b] Values OBS 1	BI SPECTRUM[b] Values OBS 2	BI SPECTRUM[b] Values OBS 3
5.....	Γ	$1.95^{+0.04}_{-0.04}$	$1.98^{+0.04}_{-0.04}$	$1.91^{+0.05}_{-0.03}$	$1.95^{+0.06}_{-0.06}$	$1.91^{+0.07}_{-0.07}$	$1.92^{+0.06}_{-0.06}$
	log ($N_{\rm H}$/cm^{-2})	$22.95^{+0.06}_{-0.07}$	$22.98^{+0.08}_{-0.08}$	$22.82^{+0.10}_{-0.13}$	$22.80^{+0.08}_{-0.07}$	$22.83^{+0.08}_{-0.09}$	$22.80^{+0.07}_{-0.06}$
	$E_{\rm notch}$[keV]	$9.59^{+0.17}_{-0.15}$	$9.75^{+0.25}_{-0.24}$	$9.40^{+0.29}_{-0.20}$	$9.81^{+0.26}_{-0.25}$	$10.41^{+0.56}_{-0.61}$	$9.96^{+0.39}_{-0.42}$
	W$_{\rm notch}$[keV]	$3.98^{+0.35}_{-0.32}$	$3.86^{+0.47}_{-0.53}$	$4.03^{+0.44}_{-0.39}$	$4.71^{+0.88}_{-0.93}$	$5.01^{+0.91}_{-0.96}$	$4.52^{+0.93}_{-0.88}$
	f$_{\rm notch}$[keV]	$0.20^{+0.04}_{-0.05}$	$0.18^{+0.05}_{-0.05}$	$0.17^{+0.05}_{-0.04}$	$0.26^{+0.05}_{-0.05}$	$0.21^{+0.05}_{-0.06}$	$0.18^{+0.05}_{-0.05}$
	EW$_{\rm notch}$[keV][c]	0.80 ± 0.21	0.70 ± 0.22	0.69 ± 0.21	1.22 ± 0.33	1.05 ± 0.36	0.81 ± 0.28
	χ^2/ν	62.3/69	70.6/62	74.2/67	58.1/67	90.8/62	48.1/67
	$P(\chi^2/\nu)$	0.70	0.21	0.26	0.77	0.01	0.96
6.....	Γ	$1.93^{+0.04}_{-0.04}$	$2.00^{+0.03}_{-0.04}$	$1.93^{+0.05}_{-0.05}$	$1.94^{+0.07}_{-0.07}$	$1.88^{+0.07}_{-0.07}$	$1.90^{+0.06}_{-0.06}$
	log ($N_{\rm H}$/cm^{-2})	$22.94^{+0.07}_{-0.08}$	$23.00^{+0.06}_{-0.08}$	$22.82^{+0.11}_{-0.13}$	$22.80^{+0.08}_{-0.08}$	$22.81^{+0.08}_{-0.09}$	$22.79^{+0.07}_{-0.08}$
	$E_{\rm zedge}$[keV]	$7.71^{+0.15}_{-0.14}$	$8.06^{+0.17}_{-0.29}$	$7.48^{+0.12}_{-0.13}$	$7.47^{+0.13}_{-0.13}$	$8.32^{+0.52}_{-0.33}$	$7.74^{+0.20}_{-0.23}$
	$\tau_{\rm zedge}$	$0.32^{+0.07}_{-0.07}$	$0.30^{+0.08}_{-0.08}$	$0.31^{+0.08}_{-0.08}$	$0.56^{+0.18}_{-0.19}$	$0.46^{+0.17}_{-0.18}$	$0.41^{+0.13}_{-0.12}$
	EW$_{\rm zedge}$[c]	1.19 ± 0.28	1.12 ± 0.28	1.09 ± 0.26	1.86 ± 0.59	1.54 ± 0.64	1.42 ± 0.42
	χ^2/ν	67.1/70	71.1/63	74.3/68	64.3/68	91.0/63	46.1/68
	$P(\chi^2/\nu)$	0.58	0.23	0.28	0.60	0.01	0.98

Continued on Next Page...

Table 3.3 – Continued

Model[a]	Parameter	FI SPECTRUM[b] Values OBS 1	FI SPECTRUM[b] Values OBS 2	FI SPECTRUM[b] Values OBS 3	BI SPECTRUM[b] Values OBS 1	BI SPECTRUM[b] Values OBS 2	BI SPECTRUM[b] Values OBS 3
7.....	Γ	$1.94^{+0.04}_{-0.04}$	$2.02^{+0.03}_{-0.03}$	$1.94^{+0.05}_{-0.05}$	$1.95^{+0.07}_{-0.06}$	$1.91^{+0.06}_{-0.06}$	$1.92^{+0.05}_{-0.06}$
	log ($N_{\rm H}$/cm^{-2})	$22.94^{+0.08}_{-0.08}$	$22.99^{+0.07}_{-0.04}$	$22.81^{+0.10}_{-0.13}$	$22.81^{+0.08}_{-0.08}$	$22.79^{+0.10}_{-0.10}$	$22.80^{+0.07}_{-0.06}$
	$E_{\rm abs1}$[keV]	$8.10^{+0.11}_{-0.12}$	$8.62^{+0.26}_{-0.18}$	$7.83^{+0.10}_{-0.09}$	$7.86^{+0.20}_{-0.13}$	$9.26^{+0.14}_{-0.26}$	$8.27^{+0.32}_{-0.36}$
	$\sigma_{\rm abs1}$[keV]	$0.29^{+0.15}_{-0.17}$	$0.37^{+0.20}_{-0.18}$	<0.32	<0.48	<0.52	<0.74
	EW$_{\rm abs1}$[keV][c]	$0.22^{+0.08}_{-0.06}$	$0.25^{+0.10}_{-0.12}$	$0.21^{+0.09}_{-0.11}$	$0.23^{+0.09}_{-0.10}$	$0.34^{+0.22}_{-0.20}$	$0.39^{+0.15}_{-0.12}$
	$E_{\rm abs2}$[keV]	$10.60^{+0.25}_{-0.28}$	$10.85^{+0.24}_{-0.24}$	$10.26^{+0.38}_{-0.37}$	$10.53^{+0.29}_{-0.30}$	$11.32^{+0.63}_{-0.80}$	$10.98^{+0.46}_{-0.48}$
	$\sigma_{\rm abs2}$[keV]	$0.78^{+0.21}_{-0.22}$	$0.36^{+0.21}_{-0.16}$	$0.72^{+0.52}_{-0.33}$	$0.97^{+0.54}_{-0.52}$	<0.92	$0.71^{+0.39}_{-0.36}$
	EW$_{\rm abs2}$[keV][c]	$0.49^{+0.25}_{-0.24}$	$0.27^{+0.16}_{-0.18}$	$0.46^{+0.17}_{-0.16}$	$1.12^{+0.36}_{-0.38}$	<0.98	$0.58^{+0.20}_{-0.26}$
	χ^2/ν	58.0/66	66.4/59	68.8/64	54.0/64	79.8/59	43.8/64
	$P(\chi^2/\nu)$	0.75	0.24	0.32	0.81	0.04	0.97

[a]Model 1 is a power-law with Galactic absorption (PL; XSPEC model WABS*POW); Model 2 is a power-law with Galactic absorption and intrinsic absorption (APL; XSPEC model WABS*ZWABS*POW); Model 3 is a power-law with Galactic absorption and ionized-absorption (IAPL; XSPEC model WABS*ABSORI*POW); Model 4 is power-law with Galactic absorption and partially covered absorption (PAPL; XSPEC model WABS*ZPCFABS*POW); Model 5 is a power-law with Galactic absorption, intrinsic absorption, and a notch absorber (APL+No; XSPEC model WABS*ZWABS*NOTCH*POW); Model 6 is a power-law with Galactic absorption, intrinsic absorption, and an absorption edge (APL+Ed; XSPEC model WABS*ZWABS*ZEDGE*POW); Model 7 is a power-law with Galactic absorption, intrinsic absorption, and two absorption lines (APL+2AL; XSPEC model WABS*ZWABS*[POW+ZGAUSS+ZGAUSS]).

[b]The spectra fitted are the added (ftools ADDSPEC) spectra of the FI chips (XIS0, XIS2 and XIS3). For OBS 2 the XIS2 CCD was not operational, and only the XIS0 and XIS3 spectra were added for this observation. The BI spectra are taken with the XIS1 chip.

[c]EW stands for equivalent width, which is defined as $EW = \int \frac{F_c - F_E}{F_c} dE$, where F_c is the continuum flux and F_E is the flux in the absorber.

We fit the spectra of APM 08279+5255 with the following models: 1) power-law (PL; XSPEC model WABS*POW) , 2) absorbed power-law (APL; XSPEC model WABS*ZWABS*POW), 3) ionized-absorbed power-law (IAPL; XSPEC model WABS*ABSORI*POW), 4) partially covered absorbed power-law (PAPL; XSPEC model WABS*ZPCFABS*POW), 5) absorbed power-law with a notch (APL+No; XSPEC model WABS*ZWABS*NOTCH*POW), 6) absorbed power-law with an absorption edge (APL+Ed; XSPEC model WABS*ZWABS*ZEDGE*POW), and 7) absorbed power-law with two absorption lines (APL+2AL[10]; XSPEC model WABS*ZWABS*[POW+ZGAUSS+ZGAUSS]).

The results of the FI and BI fits with the models described are listed in Table 3.3. The error bars of the fitted parameters are given at the 68% level ($\Delta\chi^2 = 1$). For models 2 to 7 we assume an intrinsic absorber with a redshift of 3.91 (Downes et al. 1999). The fits using a power-law model (model 1) are not acceptable in a statistical sense. We next fit the spectra of APM 08279+5255 with the absorbed power-law model (model 2; Table 3.3) assuming an intrinsic absorber. The F-test indicates that fits with model 2 result in a significant improvement at the $\gtrsim$99% and $\gtrsim$99.9% confidence levels in the FI and BI spectra, respectively, compared to fits using model 1. Fits with model 2 indicate significant intrinsic absorption in APM 08279+5255 with a column density of $\log\,(N_{\rm H}/{\rm cm}^{-2}) \approx 23$. We also fit the spectra of APM 08279+5255 with more complex models that included an ionized and partially covered absorber (models 3 and 4), however, these fits do not result in a significant improvement (F-test significance <95%) compared to the simpler model 2.

Fits to the spectra of APM 08279+5255 with models (models 5–7) that account for the absorption found between 7–12 keV in the rest-frame result in significant improvements (the F-test indicates improvements at $\gtrsim$99.9% and $\gtrsim$99% confidence in the FI and BI spectra, respectively) compared to fits with models that do not include this high-energy absorption. We note that the absorption feature at 7–12 keV in the rest-frame corresponds to a significant detection following the criteria described in §3 of Vaughan & Uttley (2008). Specifically, we find the ratio of the total equivalent width[11] of the absorption features to their uncertainty to be $EW/\sigma_{EW} \gtrsim 3$ in every observation (see models 5–7 in Table 3.3).

To illustrate the presence of the high-energy absorption features, we fit the spectra from observed-frame energies of 3.6–10 keV with a power-law model and extrapolate this model to the energy ranges not fit (see Figure 3.1). The lower panels in Figure 3.1 show the residuals (difference between the measured counts and model) between the best-fit power-law model and the FI and BI data, respectively. The best-fit values of the photon indices in all observations with this model are consistent with $\Gamma = 2$ at the 1-σ level. For the purpose of comparing the absorption residuals between epochs the photon indices for all observations are set to $\Gamma = 2.0$. From these fits we notice that the residuals show an absorption feature centered near a rest-frame energy of ∼8 keV and a possible second

[10]We note that if we replace the APL+2AL model by the XSPEC absorption-line multiplicative model WABS*ZWABS*GABS*GABS(POW), we obtain similar results for the fitted energies and equivalent widths of the absorption features found at energies 7–12 keV in the rest-frame. All the results described in this chapter using the APL+2AL can be reproduced using this multiplicative model.

[11]The equivalent width (EW) is defined as $EW = \int \frac{F_c - F_E}{F_c} dE$, where F_c is the continuum flux and F_E is the flux in the absorber.

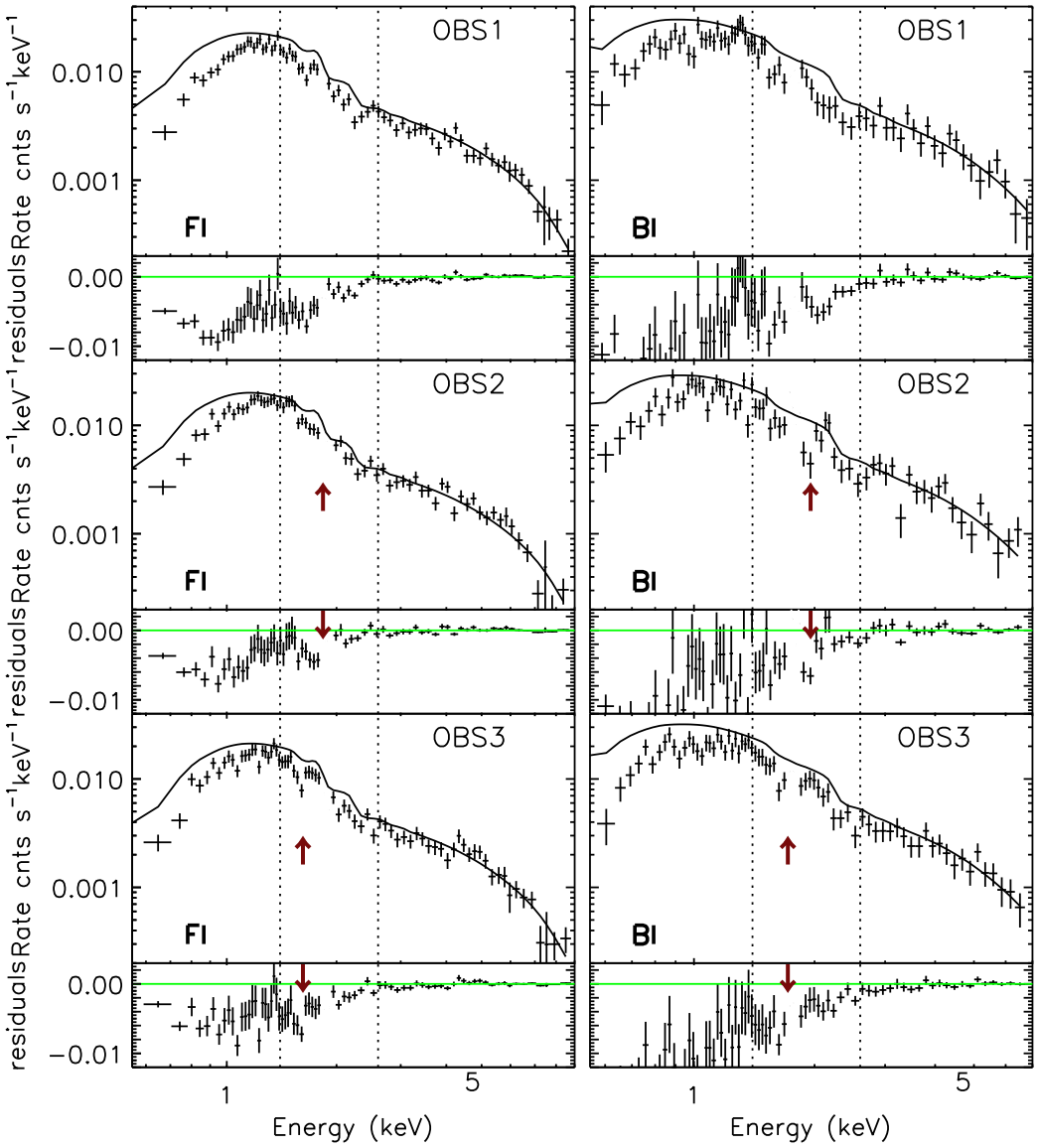

Fig. 3.1 *Suzaku* FI (left panel) and BI (right panel) spectra of the combined images of APM 08279+5255 for the three observations (OBS 1, 2, and 3), fit with Galactic absorption and a power-law model to events with observed-frame energies above 3.6 keV and then extrapolated to lower energies. In the lower panel of each observation, we show the residuals of the fit with 1-σ error bars. High-energy absorption features are detected within the 7–12 keV range (dotted lines). We have marked with an arrow the best-fitted energies of the first absorption feature of model 7 for epochs OBS2 and OBS3. For the FI spectra the grouping in OBS1 and OBS2 is 100 counts per bin, and in OBS 3 it is 80 counts per bin. For the BI spectra the grouping in OBS1 and OBS2 is 40 counts per bin, and in OBS3 it is 50 counts per bin.

absorption feature near a rest-frame energy of ∼10 keV. We fit the high-energy absorption features with the models listed in Table 3.3. From these fits we found that adding to the APL model an absorption edge (APL+Ed) or two absorption lines (APL+2AL) improves the fits at the $\gtrsim$99% confidence level in the two sets of spectra (FI and BI) and in each observation. The F-test indicates that we cannot distinguish between the (APL+Ed) and (APL+2AL) models for fits performed to the spectra of APM 08279+5255 in epochs OBS2 and OBS3, since both models fit equally well the 7–12 keV rest-frame absorption during these epochs. [12] However, fits to the FI and BI spectra of epoch OBS1 using the APL+2AL model provide a significant improvement at the 95% and 98% confidence levels, respectively, compared to fits that use the APL+Ed model. It is important to note that the APL+2AL model was clearly favored over the APL+Ed model in a previous 88.8 ks *Chandra* observation (Chartas et al. 2002). Fits to the spectra in epoch OBS1 with a model that includes an absorption notch (see Table 3.3) also provide a significant improvement compared to ones using the APL+Ed model. These F-test improvements are at the ∼98% and ∼99% levels of significance in the FI and BI spectra, respectively. We note, however, that when we compare the quality of the spectral fits that use the APL+Ed model with fits that use either the APL+2AL or APL+notch models, the F-test may not be a reliable tool. The reason for the non-reliability of the F-test is that we are not comparing nested models (see Protassov et al. 2002 for details). In order to check the reliability of the F-test for these cases, we performed Monte Carlo simulations of 10,000 fake spectra (using the FAKEIT command of XSPEC) assuming an APL+Ed model. In these simulations, the energy and optical depth of the absorption edge are assumed to be normally distributed around their fitted values for epoch OBS1 (see model 6 of Table 3.3), with a standard deviation given by the error bars of the fits. All other parameters of the APL+Ed model were set to their best-fitted values (epoch OBS1 and model 6 of Table 3.3). The results of our Monte Carlo analysis are presented in Table 3.4. In each simulation we have fitted the data with the null model (APL+Ed) and the alternative model (either APL+2AL or APL+notch). We then calculated the value of the F-statistic between the null model and the alternative model. In Table 3.4 we show that the p-value, which represents the fraction of simulated cases with values of the F-statistic higher than the actual value obtained from our real data, is similar to the null probability of the F-test. We therefore conclude that our F-test values are reliable and are approximately representative of the improvement of the alternative model (either APL+2AL or APL+notch) with respect to the null model (APL+Ed).

The results of the spectral fits shown in Table 3.3 indicate a change (greater than 1-σ) of the energies of the best-fit values of the first absorption line (abs1; model 7), and in the absorption-edge energy ($E_{\rm Edge}$; model 6) between epochs OBS2 and OBS3 in both the FI and BI spectra. This change is also suggested by the residuals in Figure 3.1, where we have marked with an arrow the best-fitted energies of the first absorption feature of model 7 for epochs OBS2 and OBS3. The shift in the energy of the first absorption line is indicative of possible variability of the outflow. This change can be

[12] We only find marginal improvements in fits to the spectra of APM 08279+5255 taken in epochs OBS2 and OBS3 using model 7 (APL+2AL) compared to fits using model 6 (APL+Ed). Specifically, in epoch OBS2 these improvements are at the 61% and 91% significance levels in the FI and BI, and in epoch OBS3 they are at the 68% and 50% significance levels.

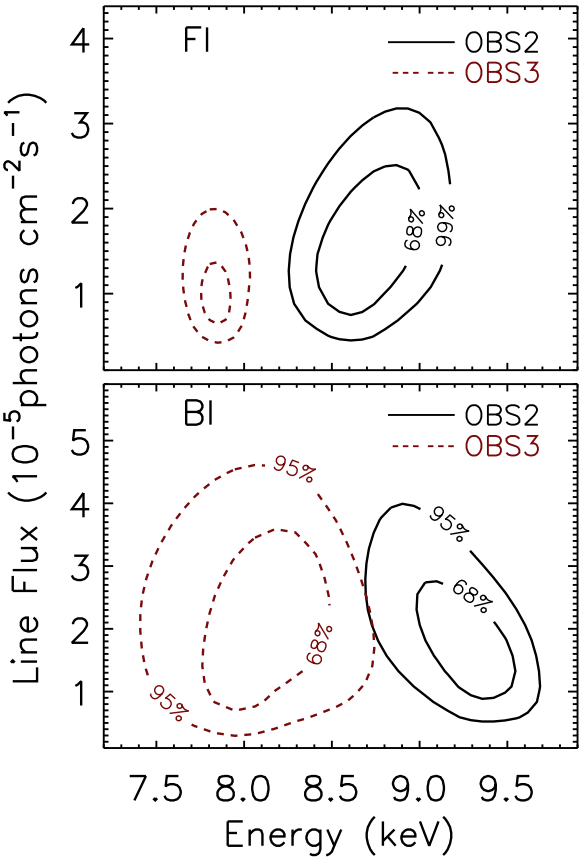

Fig. 3.2 Confidence contours of absorption-line fluxes versus absorption-line energies of the absorption line at rest-frame energies $\sim$ 8 keV (model 7, Table 3.3). The upper and lower panel contours correspond to fits performed to the FI and BI spectra, respectively. The contour plots are at the 68% and 99% level of significance in the upper panel and at the 68% and 95% level of significance in the lower panel. Solid and dotted lines are contours for epochs OBS2 and OBS3, respectively.

Table 3.4. Estimates of the improvement of fits to the spectra of APM 08279+5255 using alternative models to the APL+Edge model.

Alternative model	Spectrum[a]	F-statistic/null probability[b]	p[c]
APL+2AL	FI	2.59 / 4.4×10^{-2}	5.2×10^{-2}
APL+2AL	BI	3.05 / 2.3×10^{-2}	3.1×10^{-2}
APL+notch	FI	5.32 / 2.4×10^{-2}	6.8×10^{-2}
APL+notch	BI	7.15 / 0.9×10^{-2}	3.9×10^{-2}

[a]The XIS FI and BI spectra of APM 08279+5255 considered in this comparison are taken from epoch OBS1.

[b]The value on the left of the slash is the F-statistic and is given by $F = \frac{\chi^2_{\nu_1} - \chi^2_{\nu_1}}{\Delta\nu} / \frac{\chi^2_{\nu_2}}{\nu_2}$. The value on the right of the slash represents the probability of exceeding the F-statistic based on the F-test.

[c]The p-value represents the probability of exceeding the F-statistic based on our Monte Carlo simulations. The value of the F-statistic is obtained by comparing the null model (APL+Edge) with the alternative model listed in the first column for fits performed to the spectra of APM 08279+5255 obtained in epoch OBS1.

seen more clearly in Figure 3.2 where we show the χ^2 confidence contours of the best-fit energies of the first absorption line (line at $\sim$ 8 keV rest-frame in the APL + 2AL model) versus its line-flux normalization in epoch OBS2 (solid line) and in epoch OBS3 (dotted line).[13] In the upper and lower panels of Figure 3.2, we show the χ^2 confidence contours of the FI and the BI spectra, respectively. The confidence contours touch at the $\sim$99% level of significance for the FI spectra and at the $\sim$95% level of significance for the BI spectra. The probabilities that the flux-energy parameters of the first absorption line (model 7; Table 3.3) are the same between OBS2 and OBS3 (null probabilities) are $\lesssim 1 \times 10^{-4}$ and $\lesssim 2.5 \times 10^{-3}$ in the FI spectra and BI spectra, respectively.[14] To take into account possible sampling effects caused by the number of trials used in our variability analysis we multiply the null probabilities by six. This factor corresponds to the number of absorption lines (two) times the number of observations (three). We conclude that the variability of the first absorption line is significant at the $\gtrsim$99.9% and $\gtrsim$98% levels in the FI and BI spectra, respectively. We also note in Figure 3.2 that the slight differences ($<$ 68% significance) between the FI and BI confidence contours

[13]We note that for the FI spectra of APM 08279+5255 during epoch OBS2, the first absorption feature (abs1) falls near the Si K edge where events with energies lying in the range 1.7–1.95 keV were ignored in the analysis. Although the loss of these data points adds a larger statistical error to the best-fitted parameters of abs1, it does not significantly affect the analysis. Specifically, this error in the best-fitted energies is less than the value of $\sigma_{\rm abs1}$ and more likely close to $\frac{\sigma_{abs1}}{2} \sim 0.2$ keV (see Table 3.3).

[14]The square of the probabilities of being outside the confidence contours that barely touch (see Figure 3.2) is an upper limit to the null probabilities.

may possibly be associated with differences in the responses, variations in the signal-to-noise ratios of the two detectors, and statistical noise. Notice that the equivalent width increases with the flux of the line, therefore, Figure 3.2 can be re-plotted as contour plots of equivalent width versus energy (see Appendix B.1).

3.3.1.2 XSTAR spectral fits.

The spectral analysis presented in §3.3.1.1 indicates that the intrinsic X-ray absorbing medium of APM 08279+5255 is complex and contains absorbers with different properties (see models 5–7 in Table 3.3). We identified a low-ionization absorber with a column density of $\log (N_{\rm H}/{\rm cm}^{-2}) \sim 23$ and an ionization parameter of $\log \xi \lesssim 0$ (see models[15] 2–4 in Table 3.3). This low-ionization absorber is required to model the absorption detected below ∼2 keV (observed-frame). An additional complex absorber is required to fit the broad absorption features with rest-frame energies between 7–12 keV. Given the range of energies and variability of the broad absorption features, we interpret this absorption as a blend of highly ionized ($2.75 \lesssim \log \xi \lesssim 4$) iron absorption lines blueshifted by an outflow. This explanation is consistent with recent models that attempt to simulate X-ray BALs in quasars (e.g., Schurch & Done 2007). To test this interpretation we next employ more complex, but more realistic, models to fit the APM 08279+5255 spectra.

As a first attempt we fit the low and high-energy absorption of APM 08279+5255 in epoch OBS1 with a model that includes a power-law (with Galactic absorption) and one warm absorber (model XSTAR1, Table 3.5). The warm-absorber model is calculated using the XSTAR code (see, e.g., Kallman & Bautista 2001; Kallman et al. 1996). XSTAR calculates the physical conditions and absorption-emission spectra of photoionized gases with variable abundances. In the current analysis we use a recent implementation of the XSTAR code called WARMABS that can be used as a model within XSPEC. For the WARMABS model we assume turbulent velocities $v_{\rm turb} = 1,000$ km s^{-1} (default velocity of the model).[16] For the fits we assumed solar abundances, a redshift of 3.91 for the warm absorber, and we left the column density and ionization parameter of the warm absorber free to vary in the fit. We note that spectral fits using model XSTAR1 attempt to fit both the low and high-energy absorption of APM 08279+5255 with a single warm absorber.

To constrain the iron abundance ($a_{\rm Fe}$), we allowed this parameter to vary in the spectral fits in the model XSTAR2. The only difference between models XSTAR1 and XSTAR2 is that $a_{\rm Fe}$ is fixed in model XSTAR1 and free to vary in model XSTAR2. We find that allowing $a_{\rm Fe}$ to vary in our spectral fits does not lead to a significant improvement in the fits, and the best-fit values of $a_{\rm Fe}$ in fits with model XSTAR2 are consistent with no iron over-abundance. Our results do not confirm an apparent iron over-abundance ($a_{\rm Fe} > 2$) claimed by Hasinger et al. (2002) and Ramírez (2008) based on their analyses of previous observations of APM 08279+5255.

[15] The spectral fits did not show an improvement using a warm-absorber model; however the $\lesssim$4 keV absorption was not well constrained since the *Suzaku* spectra start at rest-frame energies of $E \sim 2$ keV.

[16] Since a warm absorber with $\log \xi \sim 1.0$ is expected to have a temperature of $\lesssim 10^6$ K (e.g., Chelouche & Netzer 2003), we do not expect a thermal broadening higher than 100 km s^{-1}.

Table 3.5: Results from spectral fits using XSTAR to epochs OBS1, OBS2 and OBS3 of APM 08279+5255.

XSPEC Model[a]	Parameter	OBS1		OBS2		OBS3	
		Values FI	Values BI	Values FI	Values BI	Values FI	Values BI
XSTAR1.....	Γ	1.96±0.04	1.99±0.05	2.00±0.05	1.96±0.07	1.97±0.05	1.95±0.06
	log ($N_{\rm H}$/cm^{-2})	23.35±0.08	23.19±0.10	23.30±0.09	23.28±0.12	23.25±0.09	23.26±0.08
	log ξ	1.02±0.52	0.45±0.36	0.99±0.52	1.76±0.62	1.05±0.75	1.51±0.66
	χ^2/ν	69.1/71	70.7/69	82.0/64	92.7/64	73.8/69	48.2/69
	$P(\chi^2/\nu)^c$	0.54	0.42	0.06	0.01	0.32	0.97
XSTAR2.....	Γ	1.94±0.05	2.00±0.07	2.01±0.05	1.95±0.07	1.97±0.05	1.95±0.06
	log ($N_{\rm H}$/cm^{-2})	23.30±0.09	23.18±0.10	23.40±0.08	23.24±0.12	23.25±0.09	23.26±0.08
	log ξ	1.09±0.51	0.54±0.42	1.28±0.65	1.70±0.78	1.05±0.75	1.51±0.66
	$a_{\rm Fe}$	1.1±0.3	1.8±0.5	0.6±0.2	1.2±0.5	1.0±0.3	1.0±0.4
	χ^2/ν	68.7/70	65.2/68	77.1/63	92.5/63	73.8/68	48.2/68
	$P(\chi^2/\nu)^c$	0.52	0.57	0.11	0.01	0.29	0.97
XSTAR3.....	Γ	1.97±0.05	1.96±0.08	2.02±0.05	1.95±0.07	1.96±0.05	1.92±0.06
	log ($N_{\rm Habs1}$/cm^{-2})	23.31±0.09	23.17±0.18	23.40±0.08	23.28±0.10	23.21±0.09	23.14±0.09
	log $\xi_{\rm abs1}$	1.17±0.55	0.50±0.36	1.26±0.47	1.28±0.25	0.78±0.46	1.31±0.49
	$a_{\rm Fe}$	0.8±0.2	1.5±0.7	0.6±0.3	1.2±0.6	1.1±0.3	1.3±0.5
	$z_{\rm abs1}$	3.91	3.91	3.91	3.91	3.91	3.91
	log ($N_{\rm Habs2}$/cm^{-2})	23.07±0.31	23.36±0.26	22.79±0.36	22.87±0.41	22.91±0.35	23.21±0.39
	log $\xi_{\rm abs2}$	3.7±0.4	3.6±0.5	3.5±0.3	3.8±0.5	3.5±0.4	3.7±0.5
	$z_{\rm abs2}$	2.06±0.05	2.18±0.08	1.98±0.07	1.79±0.12	2.19±0.13	2.07±0.10
	χ^2/ν	58.0/67	54.9/65	73.6/60	89.8/60	70.2/65	43.6/65
	$P(\chi^2/\nu)^c$	0.77	0.81	0.11	8×10^{-3}	0.31	0.98

Continued on Next Page...

Table 3.5 – Continued

XSPEC Model[a]	Parameter	OBS1		OBS2		OBS3	
		Values FI	Values BI	Values FI	Values BI	Values FI	Values BI
XSTAR4.....	Γ	1.94±0.06	1.95±0.07	2.01±0.05	1.92±0.07	1.93±0.05	1.91±0.07
	log ($N_{\rm Habs1}$/cm^{-2})	22.86±0.16	23.01±0.26	22.93±0.31	23.16±0.36	22.82±0.21	23.02±0.28
	log $\xi_{\rm abs1}$	3.8±0.3	3.5±0.2	3.6±0.2	3.8±0.5	3.1±0.3	3.3±0.3
	$z_{\rm abs1}$	3.08±0.10	3.22±0.12	2.78±0.08	2.57±0.12	3.24±0.06	3.12±0.08
	$(\frac{v_{\rm abs1}}{c})^b$	(0.19±0.02)	(0.16±0.03)	(0.27±0.02)	(0.32±0.03)	(0.15±0.01)	(0.18±0.02)
	log ($N_{\rm Habs2}$/cm^{-2})	23.38±0.15	23.43±0.22	22.91±0.35	23.09±0.39	23.10±0.38	23.07±0.41
	log $\xi_{\rm abs2}$	3.6±0.5	3.4±0.2	3.4±0.3	3.7±0.6	3.5±0.3	3.6±0.6
	$z_{\rm abs2}$	2.10±0.06	2.17±0.08	1.97±0.09	1.78±0.13	2.18±0.12	2.05±0.10
	$(\frac{v_{\rm abs1}}{c})^b$	(0.45±0.02)	(0.43±0.02)	(0.48±0.02)	(0.53±0.03)	(0.42±0.03)	(0.46±0.03)
	χ^2/ν	56.3/66	55.1/64	65.1/59	80.0/59	67.1/64	43.4/64
	$P(\chi^2/\nu)^c$	0.80	0.78	0.27	0.04	0.37	0.98

[a]XSTAR1≡ XSPEC model WARMABS*POW; XSTAR2≡ XSPEC model WARMABS*POW (FeA variable); XSTAR3≡ XSPEC model WARMABS*WARMABS*POW; XSTAR4≡ XSPEC model WABS*ZWABS*WARMABS*WARMABS*POW.

[b] $\frac{v_{\rm abs1}}{c}$ and $\frac{v_{\rm abs2}}{c}$ corresponds to the estimated outflow velocities. They are calculated from equation 3.2 based on the redshift of the absorbers of model XSTAR4. They are not parameters of the spectral fit.

[c]Probability that χ^2/ν is greater than the value obtained.

We next assumed the spectral model XSTAR3 consisting of a power-law, one stationary ionized absorber with a turbulent velocity of $v_{\rm turb} = 1,000$ km s^{-1} and a second outflowing ionized absorber with a turbulent velocity of $v_{\rm turb} = 10,000$ km s^{-1} (the maximum value allowed by the model[17]). We allowed the ionization parameters of both ionized absorbers and the redshift of the second ionized absorber to vary in the fit (model XSTAR3; Table 3.5). We find that the best fitted redshift of the second warm absorber is $z \sim 2$ in both the FI and BI spectra. The F-test indicates an improvement in the fits of OBS1 with model XSTAR3, that assumes two ionized absorbers, compared to fits with models XSTAR1 and XSTAR2, that assume a single ionized absorber, at the $\gtrsim$99.5% of significance level in the FI and BI spectra. We conclude that a single warm-absorber model cannot accurately fit both the low and high-energy absorption in APM 08279+5255.

We finally assumed the spectral model XSTAR4 consisting of an absorbed power-law and two outflowing ionized absorbers. We assumed turbulent velocities of $v_{\rm turb} = 10,000$ km s^{-1} for the first and second outflowing ionized absorber (model XSTAR4; Table 3.5). The main difference between models XSTAR3 and XSTAR4 is that the redshift of the first warm-absorber is fixed in model XSTAR3 to the systemic redshift of the quasar and free to vary in model XSTAR4 and that model XSTAR4 includes a neutral absorber. For fits using model XSTAR4, we allow the redshifts, column densities, and ionization parameters of the absorbers to vary. The χ^2 values for these fits are similar to those found for model 7 (see Table 3.5 and 3.3). We find on average best-fit redshifts of $z_{\rm abs1} \sim 3$ ($v_{\rm abs1} \sim 0.2c$) and $z_{\rm abs2} \sim 2$ ($v_{\rm abs1} \sim 0.5c$), and column densities of log $N_{\rm H,abs1} \sim 23.0$ and log $N_{\rm H,abs2} \sim 23.2$, where $abs1$ and $abs2$ correspond to the two warm absorbers. We confirm the results of model 7, by finding a significant change in the best-fitted redshift of the first warm-absorber component in model XSTAR4 between epochs OBS2 and OBS3 (see Table 3.5). Even though the two warm-absorber model results in acceptable fits, the best-fit parameters should only be considered as basic estimates of the wind properties since the kinematic and ionization structure of the outflow are likely to be more complicated. Our spectral fitting results of models that include ionized absorbers (see Table 3.5) indicate that both models XSTAR3 and XSTAR4 provide acceptable fits to the spectra of APM 08279+5255 for epochs OBS1 and OBS3, however, model XSTAR4 provides a better fit to the data for epoch OBS2 than model XSTAR3. The F-test indicates that in epoch OBS2, spectral fits using model XSTAR4 provide an improvement over fits using model XSTAR3 at the $\sim$ 99% level of significance in the FI and BI spectra.

3.3.2 PIN spectral analysis.

We also examined the spectrum of APM 08279+5255 in the 10–40 keV energy band using the PIN-HXD data. Unfortunately, no signal from the source above the

[17]The high-enengy absorption features modeled with Gaussian absorption lines in model 7 could be the result of one or more highly ionized absorbers. The Doppler broadening velocities of each absorption line component of model 7 are $\sim \frac{\sigma_{\rm absi}}{E_{\rm absi}}$ (where i=1,2 indicates the component). From Table 3.3 these Doppler broadening velocities are at first order comparable to the assumed values of $v_{\rm turb}$.

background in the NXB was found. The background-subtracted source spectrum [18] was found to be within 5% of the non-X-ray background (NXB) spectrum provided by the *Suzaku* team (e.g., Mizuno et al. 2007). We arrive at a similar conclusion from the count rates presented in Table 3.2. The non-detection with the PIN provides an upper limit on the flux density at 20 keV of APM 08279+5255 of $\sim 10^{-3}$photons s^{-1} keV^{-1}. This limit is consistent with an extrapolation of the XIS spectrum.

3.4 Discussion

The X-ray spectrum of APM 08279+5255 is known to contain absorption features at rest-frame energies above 7 keV (Chartas et al. 2002; Hasinger et al. 2002). These features have been interpreted in the past in two different ways. The first interpretation by Chartas et al. (2002) was based primarily on the analysis of the 2002 *Chandra* observation of APM 08279+5255 and posits that the absorption features are due to highly blueshifted Fe XXV Kα and/or Fe XXVI Kα absorption lines. An *XMM-Newton* observation of APM 08279+5255 performed 1.8 weeks (proper-time) after the *Chandra* observation showed significantly different high-energy absorption structure which was interpreted by Chartas et al. (2003) to imply variability of the absorption features over timescales of the order of weeks. The second interpretation by Hasinger et al. (2002) is based on the 2002 *XMM-Newton* observation of APM 08279+5255 and proposes that the high-energy absorption feature arises from an iron absorption edge produced by a metal enriched (Fe/O $\approx$ 2–5 Fe/O$|_{\odot}$) ionized absorber. One important conclusion from section 3.3.1.2 is that the absorption feature found at 7–12 keV rest-frame can be fitted with two highly ionized blue-shifted warm absorbers that do not require super-solar metallicities. We note that Hasinger et al. (2002) and Ramírez (2008) had claimed iron over-abundance ($a_{\rm Fe}$>2) based on their analyses of previous observations of APM 08279+5255. In support of the two-component "iron-blend-outflow" scenario we mention that the two absorption-line model and the notch model (models 7 and 5; Table 3.3) provide significantly better fits to the absorption feature between 7–12 keV rest-frame than an absorption-edge model in epoch OBS1 (see §3.3). We also note that, in the 2002 ∼90 ks *Chandra* observation analyzed in Chartas et al. (2002), the model containing two absorption lines successfully fits the 7–12 keV rest-frame feature whereas an absorption-edge model did not provide an acceptable fit. The absorption described either by two absorption lines or a notch, may crudely represent absorption through an outflow with a large velocity gradient along the flow. Variability of the kinematic and ionization state of the outflow may explain why, depending on the observation, these absorption features could be modelled by either a notch, absorption lines, or an edge (see figure 4 of Schurch & Done 2007). We conclude that a time-variable outflow provides a plausible explanation for all the past X-ray observations of the absorption features of APM 08279+5255 (Chartas et al. 2002; Hasinger et al. 2002) including those analyzed here. In §3.4.1 we provide plausible explanations for the observed variability of the high-energy absorption. In §3.4.2 we use the results of our spectral analysis to place constraints on the kinematics of the outflow

[18] The background-subtracted source spectrum is obtained by subtracting the non-X-ray-background and an estimate of the X-ray background from the total detected PIN spectrum

and in §3.4.3 we provide estimates of the mass-outflow rate and efficiency of the outflow of APM 08279+5255.

3.4.1 Origin of the variability of the high-energy absorption feature.

Assuming the first interpretation of the origin of the high-energy absorption features in APM 08279+5255 the observed shift in the energy of the first absorption line between epochs OBS2 and OBS3 is likely due to a change in the outflow velocity of the absorber. Two alternative explanations of the shift are a change in the direction of the outflow (with respect to the line of sight) and a variation in the ionization parameter of the absorber. A change in the direction of the outflow is expected to show a shift in energy of both components of model 7 (Table 3.3). We only find variability in one component (abs1, see §3.3); however this picture could still be valid if each outflow component is driven independently. A change in the ionization parameter seems to be a less probable scenario. We checked this by fitting the spectra of epochs OBS2 and OBS3 simultaneously with model XSTAR4, keeping the redshift of abs1 as the only common parameter between the fits. In the case where a change in the ionization parameter produced the detected variability of the first absorption line abs1, we expect that the fits to the spectra of epochs OBS2 and OBS3 will not be improved by allowing the redshift of abs1 to vary independently in these fits. For the simultaneous fit to the spectra of epochs OBS2 and OBS3, where the redshift of abs1 was kept a common parameter, we find $z_{\rm abs1}({\rm FI}) = 3.11 \pm 0.04$, $z_{\rm abs1}({\rm BI}) = 3.04 \pm 0.06$, $\chi^2_{\rm FI}/\nu = 138.1/124$ and $\chi^2_{\rm BI}/\nu = 136.3/124$. In the case where we fit the spectra of epochs OBS2 and OBS3 independently using model XSTAR4 (see Table 3.5) we find $\chi^2_{\rm FI}/\nu = 132.2/123$ and $\chi^2_{\rm BI}/\nu = 123.4/123$.[19] The improvement based on the F-test of fitting the spectra of epochs OBS2 and OBS3 independently, compared to keeping a common redshift of abs1, is at the $\sim$99% and >99.9% level of significance in the FI and BI spectra. We conclude that the variability of the energy of the first absorption line abs1 is likely not driven by changes in the ionization parameter of abs1. *Suzaku* cannot resolve the images of APM 08279+5255, however, the time-delay between the two brightest images A and B of APM 08279+5255 is estimated to be of the order of a few hours (e.g., Munoz et al. 2001), much shorter than the observed variability of the high-energy absorption feature. We therefore do not expect the combined X-ray spectrum of all images of APM 08279+5255 to differ from that of the individual images within the time-delay.

3.4.2 Constraints on the kinematics of the outflow.

Under the premise of the outflow interpretation to explain the absorption at rest-frame 7–12 keV we expect a continuous distribution of outflow velocities. This range of velocities leads to the Doppler shift of the energies of the resonance absorption lines. The absorption-line rest-frame energies $E_{\rm lab}$ will thus be shifted to the observed energies $E_{\rm obs}$ according to

[19] These values are obtained by summing the χ^2 and degrees of freedom of epochs OBS2 and OBS3 in Table 3.5.

Table 3.6. The minimum and maximum energies and velocities of the high-energy absorption features in APM 08279+5255.

Model[a]	OBS	Instrument	$E_{\rm min}$ [keV]	$E_{\rm max}$ [keV]	$v_{\rm min}$ [c]	$v_{\rm max}$ [c]
5.....	1	XIS FI	7.60±0.24	11.58±0.24	0.13±0.03	0.52±0.02
7.....	1	XIS FI	7.52±0.36	12.16±0.52	0.12±0.05	0.56±0.04
5.....	2	XIS FI	7.82±0.37	11.68±0.37	0.16±0.05	0.52±0.03
7.....	2	XIS FI	7.88±0.48	11.57±0.51	0.17±0.06	0.51±0.04
5.....	3	XIS FI	7.38±0.34	11.42±0.34	0.10±0.05	0.50±0.03
7.....	3	XIS FI	7.51±0.32	11.70±1.06	0.12±0.05	0.52±0.08
5.....	1	XIS BI	7.46±0.53	12.17±0.53	0.11±0.08	0.56±0.04
7.....	1	XIS BI	7.24±0.51	12.47±1.12	0.08±0.07	0.58±0.08
5.....	2	XIS BI	7.91±0.78	12.92±0.78	0.18±0.10	0.61±0.05
7.....	2	XIS BI	8.74±0.58	12.24±1.16	0.28±0.07	0.56±0.08
5.....	3	XIS BI	7.70±0.63	12.22±0.63	0.15±0.09	0.56±0.04
7.....	3	XIS BI	7.53±0.82	12.40±0.92	0.12±0.11	0.57±0.06
7.....	Cha02[b]	ACIS BI	7.95±0.11	10.28±0.22	0.18±0.01	0.40±0.02
7.....	Has02[b]	EPIC pn	6.95±0.44	15.00±1.06	<0.10	0.72±0.05

[a]Model used to estimate $E_{\rm min}$ and $E_{\rm max}$. Model 5 (see Table 3.3) is a power-law with Galactic absorption, intrinsic absorption, and a notch absorber; Model 7 (see Table 3.3) is a power-law with Galactic absorption, intrinsic absorption, and two absorption lines.

[b]In this Table we identify as Cha02 the 88.8 ks observation of APM 08279+5255 performed with *Chandra* in 2002 and analyzed in detail in Chartas et al. (2002). We also identify as Has02 the 100.2 ks observation of APM 08279+5255 performed with *XMM-Newton* in 2002 and analyzed in detail in Hasinger et al. (2002).

$$E_{lab}/E_{obs} = \gamma(1 - \beta cos\theta), \tag{3.2}$$

where γ is the Lorentz factor, θ is the angle between the wind and our line of sight (l.o.s), and $\beta = v/c$.

The minimum and maximum projected velocities ($v_{\rm min}$, $v_{\rm max}$) of the outflow are estimated from the minimum and maximum energy ranges ($E_{\rm min}, E_{\rm max}$) of the high-energy absorption features in APM 08279+5255. We obtained $E_{\rm min}$ and $E_{\rm max}$ from our spectral fits assuming first the two absorption-line (APL+2AL) model and second assuming the notch (APL+No) model. Specifically, based on the best-fit values of the APL+2AL model (model 7; Table 3.3), we obtain $E_{\rm min} = E_{\rm abs1} - 2\sigma_{\rm abs1}$ and $E_{\rm max} = E_{\rm abs2} + 2\sigma_{\rm abs2}$. From the best-fit values of the APL+No model (model 5; Table 3.3) we have $E_{\rm min} = E_{\rm notch} - W_{\rm notch}/2$ and $E_{\rm max} = E_{\rm notch} + W_{\rm notch}/2$. The values of $E_{\rm min}$ and $E_{\rm max}$ are presented in Table 3.6. In this table the values of $E_{\rm min}$ and $E_{\rm max}$ are shown separately for the FI and BI spectra and for the two different models used to obtain them (model 7≡APL+2AL; model 5 ≡APL+No).

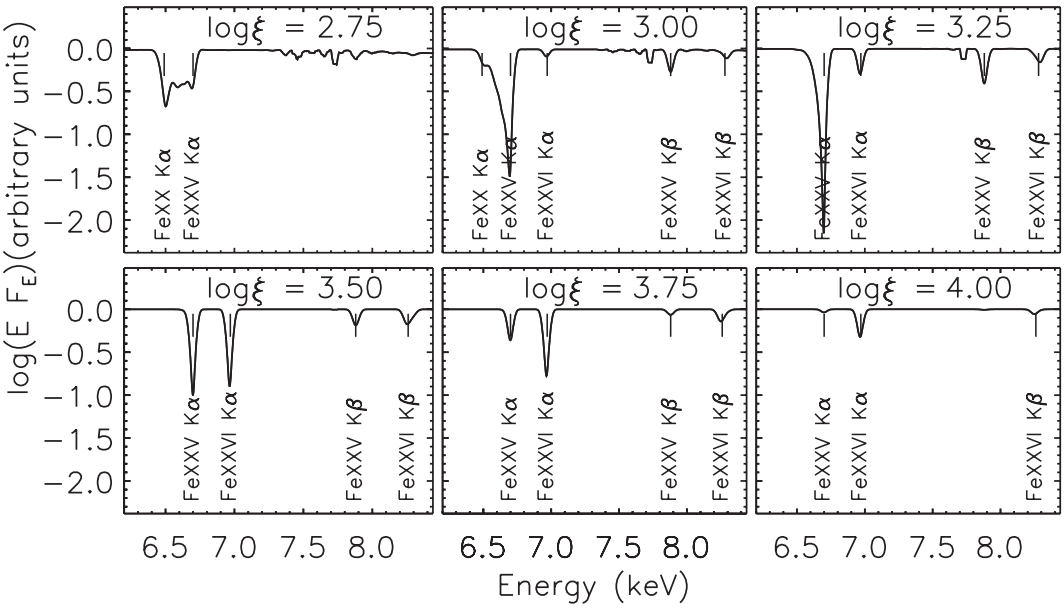

Fig. 3.3 Simulated 6–8 keV absorbed spectra (log (E $F_{\rm E}$)) assuming an incident power-law spectrum with a photon index of $\Gamma = 2$. The ionized absorber is modeled with the XSTAR model WARMABS assuming a column density of log ($N_{\rm H}/{\rm cm}^{-2}$) = 23, solar abundances, $v_{\rm turb}$ = 1000 km s^{-1}, and the following six values of the ionization parameter log ξ=2.75, 3.00, 3.25, 3.50, 3.75, and 4.0, respectively. Some of the main absorption lines in this range of ionization states have been marked in the figure. Among them Fe XX Kα ($2s^2 2p^3 - 1s2s^2 2p^4$; 6.50 keV), Fe XXV Kα ($1s^2 - 1s2p$; 6.70 keV), Fe XXV Kβ ($1s^2 - 1s3p$; 7.89 keV), Fe XXVI Kα ($1s - 2p$; 6.97 keV), Fe XXVI Kβ ($1s - 3p$; 8.27 keV).

The relative strengths of the iron resonance absorption lines will depend on the ionization state of the outflowing medium. To demonstrate this effect in a basic way we

have performed several simulations using the warm-absorber model (WARMABS) of XSTAR. In Figure 3.3 we show a simulated absorbed spectrum in the 6–8 keV rest-frame energy range for an absorbing medium with solar composition, $\log(N_{\rm H}/{\rm cm}^{-2}) = 23$, and having six different values of the ionization parameter ($2.75 \lesssim \log \xi \lesssim 4.0$). The two strongest iron lines for this highly ionized absorbing medium have rest (or laboratory) energies of 6.70 keV (Fe XXV Kα; $1s^2 - 1s2p$) and 6.97 keV (Fe XXVI Kα $1s - 2p$). In general the Fe XXV Kα line will be stronger than the Fe XXVI Kα line for a medium with $2.75 \lesssim \log \xi \lesssim 4.0$. Therefore the absorption at the lower end of the 7–12 keV rest-frame range is most likely associated with the Fe XXV Kα line. Based on our interpretation of the high-energy absorption features we estimate $v_{\rm min}$ assuming that the absorption at the low end of the X-ray BAL is due to a line arising from highly blueshifted Fe XXV Kα ($E_{\rm lab} = 6.7$ keV). On the other hand to estimate $v_{\rm max}$ we make the conservative assumption that the absorption at the high end of the X-ray BAL is due to a line arising from highly blueshifted Fe XXVI Kα ($E_{\rm lab} = 6.97$ keV). The estimated values of $v_{\rm min}$ and $v_{\rm max}$ obtained through the procedure outlined above are presented in Table 3.6. These velocities are obtained using equation (3.2) assuming that our line-of-sight makes an angle of $\theta = 20^{\rm o}$ with the velocity of the outflow (Chartas et al. 2007a). A change of 10° in θ will introduce a variation of $\lesssim$10% in our estimates of the velocities. The velocities of the outflow range between $0.1c$ and $0.6c$. The mean value of $E_{\rm max}$ from all CCDs and observations is 12.04±0.22 keV corresponding to a mean value of $v_{\rm max} = 0.55\pm0.02c$. This maximum value of the outflow velocity constrains the angle between the outflow direction and our line of sight to be $< 36^{\rm o}$.[20] This relatively small angle is consistent with outflow models that posit that BAL quasars are viewed through collimated outflows.

As argued in Chartas et al. (2002, 2003, 2007a) we are likely observing the X-ray absorbers as they are accelerated near their launching radii. We use the following equation to describe the basic dynamics of a radiation-driven outflow (e.g., equation 1 of Chartas et al. 2002):

$$v_{\rm wind} = [(\,\Gamma_{\rm f}\frac{L_{\rm UV}}{L_{\rm Edd}} - 1\,)(\,\frac{1}{R_{\rm launch}} - \frac{1}{R}\,)]^{1/2} \tag{3.3}$$

where $v_{\rm wind}$ is the outflow velocity in units of c, Γ_f is the force multiplier, $L_{\rm Edd}$ is the Eddington luminosity, $R_{\rm launch}$ is the radius (units of R_S) at which the wind is launched from the disk, and R is the distance (units of R_S) from the central source. The expression for the dynamics of the outflow can be simplified by defining $\Omega_f = \sqrt{\Gamma_{\rm f}\frac{L_{\rm UV}}{L_{\rm Edd}} - 1}$.

In Figure 3.4 we plot wind velocity versus radius (left panel) and wind velocity versus time (right panel) for an outflow launched at radii of $3R_S$ (solid lines) and $15R_S$ (dashed lines). In Figure 3.4 the units of velocity, distance, and time are $\Omega_f c$, R_S, and $R_S/(\Omega_f c)$, respectively. Assuming $L_{\rm UV} \sim 0.2L_{\rm bol}$ (Irwin et al. 1998), $L_{\rm bol}/L_{\rm Edd} \sim 0.2$ and $\Gamma_f \sim 100$ (e.g., Arav et al. 1994; Laor & Brandt 2002), we have $\Omega_f \sim 1.7$. $L_{\rm bol}/L_{\rm Edd} \sim 0.2$ is obtained using the $L_{\rm bol}/L_{\rm Edd}$ vs. Γ correlation found in RQ quasars (e.g., Wang et al. 2004; Shemmer et al. 2006, 2008) for $\Gamma \sim 1.9$. Therefore with $L_{\rm bol} =$

[20] The Doppler-shift formula (equation 3.2) predicts that given a fixed ratio of $E_{\rm lab}/E_{\rm obs} \equiv R_{\rm lo}$ the maximum angle between our line of sight and the wind direction is given by $\theta_{\rm max} = \cos^{-1}(\sqrt{1 - R_{lo}^2})$.

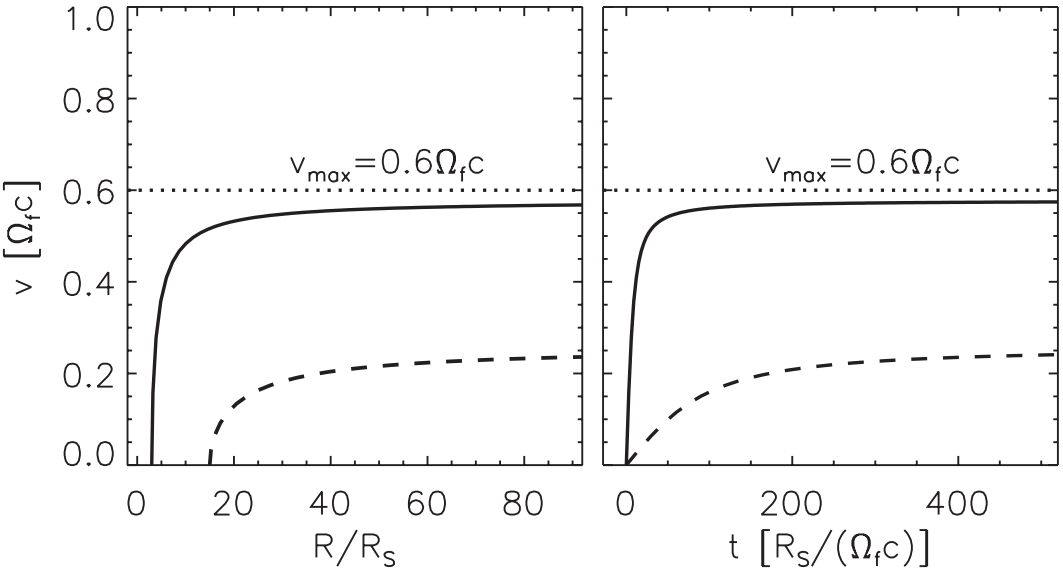

Fig. 3.4 Wind velocity (in units of $\Omega_f c$) plotted as a function of radius from the central source (left panel) and as a function of time (right panel) for a radiation-pressure driven wind. Notice that the radius is in units of the Schwarzschild radius ($R_S = \frac{2GM}{c^2}$) and the time is in units of $\tau = \frac{R_S}{\Omega_f c}$. The wind velocities are calculated for $R_{\rm launch} = 3R_S$ and $R_{\rm launch} = 15R_S$, respectively.

$7\times10^{15}\mu_L^{-1}L_\odot$ (Irwin et al. 1998; Riechers et al. 2009)[21] $M_{\rm BH} \sim 10^{12}M_\odot\mu_L^{-1}$, where $\mu_L \sim$ 100 (Egami al. 2000)[22] is the lens magnification factor. Equation 3.3 could be modified using a reliable SED describing the central source, adding relativistic corrections, and calculating the force multiplier at every point of the trajectory of the outflow. We stress, however, that our simplified approach is sufficient to provide first order approximations to the launching radius and the time scales involved in the dynamics of the outflow. Equation 3.3 can be written as $R_{\rm launch}/R_S = \Omega_f^2(c/v_\infty)^2$; therefore for $\Omega_f \sim 1.7$ we obtain $R_{\rm launch} \sim 3(c/v_\infty)^2 R_S$. The latter expression can be used to obtain first order approximations of the launching radius given the velocity of the outflow.

Assuming a radiation-driven wind, it is expected that the time required to accelerate the outflow to fractions of c is of the order of $10\frac{R_S}{c}$ (see Figure 3.4). For the black-hole mass of APM 08279+5255 of $M_{\rm BH} \approx 10^{10}M_\odot$ we estimate that the time to accelerate an absorber to near-relativistic velocities is ∼weeks (rest-frame). We have reported in this work probable variability of the high-energy absorption features over a time-scale of ∼1 month (rest-frame). This short time-scale variability is consistent with the expected variability timescale of a radiation-driven wind.

[21] We note that an estimation of $L_{\rm bol}$ based on the optical and UV spectra should be more precise than an extrapolation of $L_{\rm bol}$ based on X-ray luminosities as it is done in Ramírez (2008).

[22] See, however, Riechers et al. (2009) that find a magnification of $\mu_L \sim 4$. Riechers et al. (2009) also use the observed width of the C IV line to obtain a black-hole mass of $M_{\rm BH} \sim 10^{11}\mu_L^{-1}M_\odot$

3.4.3 Constraints on mass-outflow rate and efficiency of the outflow.

Based on our estimated values of the outflow velocities, column densities, and launching radii we present constraints on the mass-outflow rates and outflow efficiency associated with the outflowing X-ray absorbers of APM 08279+5255. The efficiency is defined as the ratio of the rate of kinetic energy injected into the ISM and IGM by the outflow to the quasar's bolometric luminosity, i.e.,

$$\epsilon_K = \frac{1}{2}\frac{\dot{M}v^2}{L_{bol}}, \text{ where } \dot{M} = 4\pi R^2 \rho v f_c = 4\pi f_c \frac{R^2}{\Delta R} N_{\rm H} m_p v, \tag{3.4}$$

where f_c is the covering fraction, $N_{\rm H}$ is the column density, R is the radius, and ΔR is the thickness of the absorber. To estimate the efficiency we use the two absorption-line model (APL+2AL; model 7 of Table 3.3). We calculate the bulk velocities of each outflow component based on the energies of the absorption lines in model 7 and through the use of equation (3.2) with $E_{\rm lab}$=6.7 keV and $\theta = 20^{\circ}$. As in Chartas et al. (2002, 2003) we interpret the high-energy absorption features as being due to highly ionized Fe (Fe XXV Kα) in a gas with solar abundances, and we estimate log $N_{\rm H}$ using a curve-of-growth analysis. In Table 3.7 we present the outflow velocities, $v_{\rm abs}$, the column densities, log $N_{\rm H}$, the mass-outflow rates, $\dot{M}$, and the outflow efficiencies, ϵ_K, of the two modeled absorbers of the outflow. We note that the values of the column densities and velocities in Table 3.7 are consistent with those found using the photoionization code XSTAR (see Table 3.5).[23]

To obtain error bars for ϵ_K and $\dot{M}$ we performed a Monte Carlo simulation, assuming a uniform distribution of the parameters f_c, R and $R/\Delta R$ around the expected values of these parameters, and a normal distribution for log $N_{\rm H}$ (described by the parameters in Table 3.7). Specifically, we assume a covering factor lying in the range $f_c = 0.1 - 0.3$, based on the observed fraction of BAL quasars (e.g., Hewett & Foltz 2003) and a fraction $R/\Delta R$ ranging from 1 to 10 based on current theoretical models of quasar outflows (e.g., Proga et al. 2000). Note that in Table 3.7 we also include the outflow parameters of the ∼90 ks *Chandra* observation of APM 08279+5255 performed in 2002 (Chartas et al. 2002). Based on our estimated maximum outflow velocities ($v_{\rm max} \sim 0.6c$) we expect that R will be similar to $R_{\rm launch}$ and range between $3R_S$ and $15R_S$ (see Figure 3.4). We note that this is a conservative assumption since larger values of R will result in larger mass-outflow rates and larger efficiencies. Additionally, the short variability time-scales (∼weeks) are also consistent with a launching radius of a few times R_S. Variability in APM 08279+5255 over time-scales ∼weeks has been previously reported (Chartas et al. 2003) based on the differences of the high-energy absorption features detected in the *Chandra* and *XMM-Newton* observations. Our current analysis of the *Suzaku* observations of APM 08279+5255 allows us to compare absorption features observed with the same instruments; therefore, it avoids any possible systematic uncertainties due to differences in the responses of the instruments.

[23]The velocities obtained in Table 3.5 assume the redshifts of the absorbers in model XSTAR4 are due to the relativistic Doppler effect (see equation 3.2).

Table 3.7: Projected maximum outflow velocities, mass-outflow rates and efficiencies of outflows in APM 08279+5255 [a].

OBS	Instr.	$v_{\rm abs1}$ $[c]$	$\log(N_{\rm Habs1}/{\rm cm}^{-2})$	$\dot{M}_{\rm abs1}/1000$ $[M_\odot \mu_L^{-1} {\rm yr}^{-1}]$	$\epsilon_{\rm Kabs1}$	$v_{\rm abs2}$ $[c]$	$\log(N_{\rm Habs2}/{\rm cm}^{-2})$	$\dot{M}_{\rm abs2}/1000$ $[M_\odot \mu_L^{-1} {\rm yr}^{-1}]$	$\epsilon_{\rm Kabs2}$
1	XIS FI	$0.20^{+0.01}_{-0.02}$	22.84±0.19	$0.5^{+0.5}_{-0.3}$	$0.02^{+0.02}_{-0.01}$	$0.47^{+0.02}_{-0.03}$	23.07±0.27	$2.1^{+2.4}_{-1.5}$	$0.5^{+0.6}_{-0.4}$
2	XIS FI	$0.27^{+0.03}_{-0.02}$	22.86±0.25	$0.7^{+0.8}_{-0.5}$	$0.05^{+0.06}_{-0.04}$	$0.49^{+0.02}_{-0.02}$	22.81±0.39	$1.5^{+2.1}_{-1.2}$	$0.4^{+0.5}_{-0.3}$
3	XIS FI	$0.17^{+0.01}_{-0.01}$	22.87±0.28	$0.5^{+0.6}_{-0.4}$	$0.01^{+0.02}_{-0.01}$	$0.44^{+0.04}_{-0.04}$	23.05±0.19	$1.7^{+1.7}_{-1.1}$	$0.3^{+0.4}_{-0.2}$
1	XIS BI	$0.17^{+0.03}_{-0.02}$	22.89±0.24	$0.5^{+0.5}_{-0.3}$	$0.01^{+0.02}_{-0.01}$	$0.46^{+0.03}_{-0.03}$	23.48±0.20	$4.8^{+4.9}_{-3.3}$	$1.1^{+1.1}_{-0.7}$
2	XIS BI	$0.34^{+0.02}_{-0.03}$	23.01±0.36	$1.5^{+2.0}_{-1.2}$	$0.19^{+0.25}_{-0.15}$	$0.53^{+0.05}_{-0.07}$	23.09±0.36	$2.8^{+3.8}_{-2.2}$	$0.8^{+1.1}_{-0.7}$
3	XIS BI	$0.22^{+0.04}_{-0.05}$	23.10±0.21	$1.0^{+1.0}_{-0.7}$	$0.05^{+0.05}_{-0.03}$	$0.50^{+0.04}_{-0.04}$	23.14±0.24	$2.5^{+2.7}_{-1.8}$	$0.7^{+0.7}_{-0.5}$
Ch02	ACIS BI	$0.20^{+0.01}_{-0.01}$	22.99±0.11	$0.6^{+0.6}_{-0.4}$	$0.03^{+0.02}_{-0.02}$	$0.40^{+0.01}_{-0.01}$	23.07±0.12	$1.5^{+1.4}_{-1.0}$	$0.3^{+0.2}_{-0.2}$
Has02	EPIC pn	$0.21^{+0.03}_{-0.03}$	23.10±0.36	$1.2^{+1.6}_{-0.9}$	$0.10^{+0.14}_{-0.08}$	$0.50^{+0.06}_{-0.07}$	23.36±0.30	$4.5^{+5.4}_{-3.3}$	$1.2^{+1.4}_{-0.9}$

[a]The estimated values of the outflow properties were based on fits that assumed an absorbed power-law model with two absorption lines. The values of $\dot{M}$ and ϵ_K are obtained by equation (3.4) assuming $M_{\rm BH} \sim 10^{12} \mu_L^{-1} M_\odot$ (see §3.4.2) and $L_{\rm bol} = 7 \times 10^{15} \mu_L^{-1} L_\odot$ (Irwin et al. 1998; Riechers et al. 2009).

Our results indicate that the average fraction of the total bolometric luminosity of APM 08279+5255 injected into the IGM in the form of kinetic energy is $\epsilon_K = 0.7 \pm 0.3$. From the results of Table 3.7 we also obtain the average mass-outflow rate of $\dot{M} = (3.3 \pm 0.9) \times 10^3 \mu_L^{-1} M_\odot \mathrm{yr}^{-1}$. On the other hand the mass-accretion rate is $\dot{M}_{\rm acc} = \frac{L}{\eta c^2} \sim 4.8 \times 10^3 \mu_L^{-1} M_\odot \mathrm{yr}^{-1}$ (assuming $\eta \approx 0.1$ and $L_{\rm bol} = 7 \times 10^{15} \mu_L^{-1} L_\odot$). Therefore the mass-outflow rate is comparable to the accretion rate. In the context of recent models of structure formation (e.g., Granato et al. 2004; Springel et al. 2005), our estimated values of ϵ_K in APM 08279+5255 suggest that these outflows should be an important source of feedback in their host galaxies and also play an important role in regulating the growth of the central black hole.

To obtain an independent estimate of the mass-outflow rate $\dot{M}$, we derive nR^2 based on the definition of $\xi = L/(nR^2)$. Assuming $\log \xi \sim 3.5$ (e.g., model XSTAR4, Table 3.5) and an ionizing luminosity similar to the X-ray luminosity $L_{\rm X} \sim 4 \times 10^{46} \mu_L^{-1} \mathrm{erg\ s}^{-1}$, we obtain $nR^2 \sim 1 \times 10^{43} \mu_L^{-1}\ \mathrm{cm}^{-1}$. Therefore assuming an overall velocity of the outflow $\sim 0.45c$ we find $\dot{M} \sim 9 \times 10^3 \mu_L^{-1} M_\odot \mathrm{yr}^{-1}$. The value of $\dot{M}$ derived from the best-fit ionization parameter is comparable (within a factor of three) to the value found for the second absorber abs2 in Table 3.7, where we have estimated the location of the absorber from variability arguments. We caution, however, that the estimation of the mass-outflow rate from the ionization parameter assumes a spherical outflow illuminated by a point source. However, since we expect that the X-ray absorber is located a few R_S from the X-ray source the point source approximation may not be accurate in this case.

3.5 Conclusions

Our analysis of three long *Suzaku* observations of the BAL quasar APM 08279+5255 indicates strong and broad absorption at rest-frame energies of $\lesssim$2 keV (low-energy) and 7–12 keV (high-energy). Based on the F-test the low-energy absorption is significant at the $\gtrsim$99% and $\gtrsim$99.9% levels in the front-illuminated (FI) and back-illuminated (BI) *Suzaku* XIS spectra, respectively. The high-energy absorption is significant at $\gtrsim$99.9% (FI spectrum) and at $\gtrsim$99% (BI spectrum) confidence, respectively. The medium producing the low-energy absorption is a nearly neutral absorber with a column density $\log (N_{\rm H}/\mathrm{cm}^{-2}) \sim 23$. The medium producing the high-energy absorption appears to be outflowing from the central source at near-relativistic velocities and with large ionization parameters ($2.75 \lesssim \log \xi \lesssim 4.0$), consistent with results obtained from a previous *Chandra* observation of this object (Chartas et al. 2002). Simulations of highly ionized near-relativistic winds performed by Schurch & Done (2007) indicate that the resulting X-ray broad absorption profile may have the apparent shape of an absorption edge, a notch, or a combination of absorption lines depending on the assumed dynamics and degree of ionization of the outflowing absorbers.

Our observations of the 7–12 keV rest-frame features are well described by a two component absorber model. We find that in epoch OBS1, spectral fits with the two component absorption-line model (APL + 2AL) are significantly better (>95% confidence level) than fits with absorption-edge models (APL + Ed). We note that spectral

fits with models that included ionized absorbers with free iron abundances (models XSTAR2 and XSTAR3 in Table 3.5) are consistent with no iron over-abundance in all *Suzaku* observations of APM 08279+5255.

Our interpretation, of a near-relativistic outflowing absorbing medium in a high ionization state ($2.75 \lesssim \log \xi \lesssim 4$), is consistent with our analysis of all the past X-ray observations of APM 08279+5255. Our spectral analysis indicates that the outflow velocities of the highly ionized absorbers detected in the three *Suzaku* observations range between $0.1c$ and $0.6c$. The maximum detected projected outflow velocity of $\sim 0.6c$ constrains the angle between our line of sight and the wind direction to be $\lesssim 36^{\rm o}$. We find possible variability of the high-energy absorption lines between epochs OBS2 and OBS3 at the $\sim$99.9% and $\sim$98% significance levels in the FI and BI spectra, respectively. Our spectral analysis indicates that the variability is likely due to a change in the outflow velocity of the absorber. The short time-scale ($\sim$month in the rest-frame) of this variability is probably indicating that this absorber is strongly accelerated. This short time-scale variability combined with the high ionization of the absorbing material imply that the absorbers are launched from distances $\lesssim 10 R_S$ from the central source.

Assuming our interpretation that the absorption lines detected at rest-frame energies of 7–12 keV are due to Fe XXV, we estimate that a significant fraction (0.7 ± 0.3) of the total bolometric energy over the quasar's lifetime is injected into the intergalactic medium of APM 08279+5255 in the form of kinetic energy with a mass-outflow rate of $\dot{M} = (3.3 \pm 0.9) \times 10^3 \mu_L^{-1} M_\odot {\rm yr}^{-1}$.

Chapter 4

A Study of the X-rayed outflow of APM 08279+5255 through photoionization codes

4.1 Introduction

Recent observations of nearby galaxies indicate the presence of a $M_{\rm BH}-\sigma$ relation (e.g., Ferrarese & Merritt 2000), where $M_{\rm BH}$ is the mass of the central black hole and σ is the velocity dispersion of the stars in the bulge of the host galaxy. The existence of a $M_{\rm BH}-\sigma$ relation suggests that a feedback mechanism exists regulating the co-evolution between the massive black hole at the center of a galaxy and the formation of its bulge. A possible mechanism of feedback is quasar outflows. Recent theoretical models demonstrate that quasar feedback can serve as a fundamental ingredient in structure formation and galaxy mergers and predict the existence of outflows coevolving with the different stages of merging (e.g., Hopkins et al. 2005a,b; Di Matteo 2005; Springel et al. 2005). Galaxy merger simulations can reproduce the observed space density evolution of quasars, the $M_{\rm BH}-\sigma$ relation, and the observationally inferred lifetime scales of AGNs (Hopkins et al. 2006; Di Matteo 2005; Springel et al. 2005; Degraf, Di Matteo & Springel 2010). These powerful AGN outflows are also predicted to exist in semi-analytical models of AGNs in spherical haloes (Granato et al. 2004).

Fast and powerful AGN jets and winds can be formed mainly by two mechanisms: (1) magnetic driving and (2) radiative driving. Magnetically driven jets are thought to be responsible for the production of bubbles and cavities in galaxy clusters. The sources of these jets are found to be radio-loud (RL) AGNs located in the central giant elliptical galaxies (see McNamara & Nulsen 2007, and references therein). Although there is compelling evidence for the existence of jets in RL AGNs (see e.g., Bridle & Perley 1984, and references therein), the presence of jets or magnetically-driven winds in radio quiet AGNs is still debated. The mechanism driving winds in the majority of AGNs therefore is currently uncertain since the majority of AGN are radio quiet.[1] It is important to note, however, that a recent study claims observational evidence of magnetically-driven winds in high signal-to-noise ratio (S/N) spectra of nearby AGNs (Fukumura et al. 2010). Specifically, Fukumura et al. (2010) find that a MHD model can explain the distribution of absorption as a function of ionization parameter ($d\log N_{\rm H}/d\xi$) in the X-ray spectra of five nearby AGNs (mostly Seyfert 1 galaxies at $z\lesssim 0.1$). In is not clear if this result can be extended to high redshift sources or sources with relativistic winds where we expect strong and likely discontinuous gradients of velocity and therefore we do not expect to find smooth dlog $N_{\rm H}/d\xi$ distributions.

[1] RL AGNs represent between 10-20% of the whole AGN population (e.g., Ivezić, et al. 2002; Jiang et al. 2007)

At moderate to high Eddington ratios ($L/L_{\rm Edd} \gtrsim 0.2$), which may be common in high redshift sources $z \gtrsim 2$ (Kollmeier et al. 2006), we expect that radiative driving becomes more important than magnetic driving (Everett 2005). Recent observations of the high redshift ($z \approx 2$) ultraluminous infrared galaxy (ULIRG) SMM J1237+6203 suggest a large-scale powerful wind in this object driven by AGN radiation (Alexander et al. 2010). These observations are suggestive that in high redshift AGNs ($z \gtrsim 2$) radiatively driven winds may be more common than the jets found in radio galaxies. Radiative driving is also the favorite mechanism for explaining the formation of outflows observed in the UV from BAL quasars. Evidence of the later is found in the correlation between changes in the velocity of the outflow (C IV equivalent width) as a function of variations in the soft to hard spectral slope $\alpha_{\rm ox}$ (Brandt, Laor & Wills 2000). The outflows observed in the UV from BAL quasars usually have moderate velocities ($\lesssim 0.1c$), however, there have been reported cases with velocities of $\sim 0.2c$ (Rodriguez-Hidalgo et al. 2007). Observations (Hamann et al. 2008) of the quasar J105400.40+034801.2 imply wind velocities of $\sim 0.8c$ based on measurements of the C IV line. We note, however, that even though this source reveals blue-shifted broadenings $\gtrsim 4000$ km s^{-1} in C IV lines, it is not considered a BAL quasar in the strict sense of the definition (i.e. Weymann et al. 1991).[2] Several of the low S/N cases have led to spurious detections (see Vaughan & Uttley 2008, and references therein). A handful of moderate S/N X-ray spectra of BAL and mini-BAL quasars have been obtained that show strong signatures of fast winds (e.g., Chartas et al. 2002, 2007a,b, 2009a). The velocities of the outflowing X-ray absorbing material in some cases are found to be ($\gtrsim 0.7c$) indicating a different dynamical state than the observed outflow in the UV band. The fast variability and high ionization state of the winds observed in the X-rays could also be indicating that these X-ray outflows are originating closer to the central source than the outflows observed in the UV.

Recently (Saez, Chartas & Brandt 2009; Chartas et al. 2009a) we presented observational evidence for the presence of a powerful outflow in BAL quasar APM 08279+5255 based on the analysis of the X-ray spectra of this object. APM 08279+5255 is a high redshift quasar which is unusually bright due to gravitational lensing, providing the exceptional opportunity to study it with high-quality spectral data. Our conclusions from these studies were that the outflow was accelerated to relativistic speeds, and was releasing kinetic energy at a rate comparable to the bolometric luminosity of this source. The latter indicated that this outflow can release an important fraction of the energy produced by black-hole accretion into the surrounding galaxy. In our study of APM 08279+5255 we also found evidence that the outflow could be radiatively accelerated by the central source. In the next section we present the main conclusions extracted from recent studies that focused on long X-ray observations (∼100 ks) of APM 08279+5255 performed with *Chandra*, *XMM-Newton*, and *Suzaku*. We also expand on the previous studies in two directions. First we describe how the use of photoionization models may help us better constrain the physical properties of the outflowing X-ray absorbing gas. Second we discuss how the SED of the central source may influence the dynamics of the outflow.

[2]The commonly used definition of BAL quasar (i.e. Weymann et al. 1991) does not consider outflow velocities $> 25,000$ km s^{-1}. BAL winds have also been found in the X-ray band (Chartas et al. 2002, 2007b), however, the X-ray faintness of BAL quasars (Gallimore et al. 2006) has limited the number of cases with observed X-ray BALs to a few.

4.2 The fast outflow of APM 08279+5255

This section contains information extracted from past studies of APM 08279+5255. In §4.2.1, we concentrate on general information that is relevant to understanding the origin of the fast outflow of X-ray absorbing material observed in this object. In (§4.2.2), we describe the most important results extracted from eight deep X-ray observations of APM 08279+5255.

4.2.1 Properties of the fast outflow of APM 08279+5255

APM 08279+5255 is a gravitationally lensed BAL quasar at redshift z=3.911 (Downes et al. 1999). Its bolometric luminosity estimated as $L_{\rm bol} = 7 \times 10^{15} \mu_L^{-1} L_\odot$ (μ_L is the lens amplification factor; Irwin et al. 1998; Riechers et al. 2009) makes this source one of the most luminous in the universe[3], despite the value of the lens amplification factor. The presence of high-ionization BAL features produced in C IV, O VI, N V and Ly α transitions indicates that it is a high ionization BAL quasar (HiBAL). The C IV BAL of APM 08279+5255 contains multiple absorption troughs with widths ranging between 2000 km s^{-1} and 2500 km s^{-1}. The maximum observed outflow velocity of the C IV absorption is $v_{\rm max(CIV)} \sim 0.04c$ relative to the source systemic redshift of $z = 3.911$ (Srianand & Petitjean 2000).

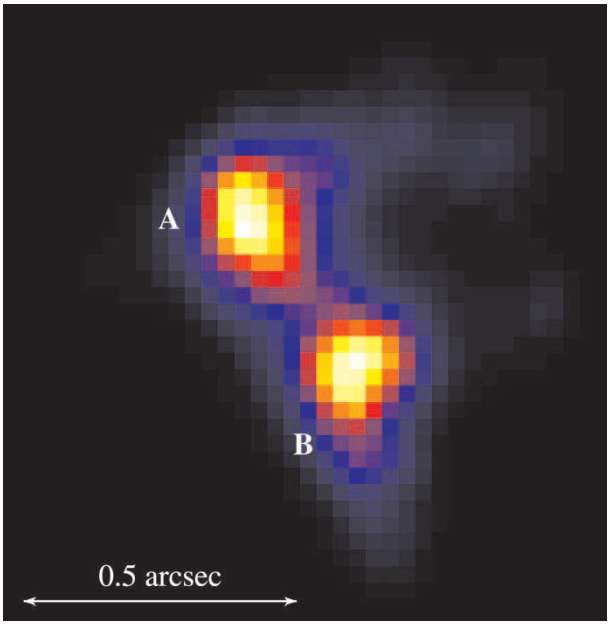

Fig. 4.1 Deconvolved image of the 2002 February 24 Chandra observation of APM 08279+5255. North is up, and east is to the left. From Chartas et al. (2002).

[3] As a reference the most luminous quasars in the SDSS have $L_{\rm bol} \sim 10^{14} L_\odot$ (e.g., Gangully et al 2007).

Gravitational lensing of APM 08279+5255 produces three images with the two brightest ones separated by ~ 0.5" (see Figure 4.1). The time-delay between images A and B of APM 08279+5255 is estimated to be of the order of a few hours (e.g., Munoz et al. 2001). The Eddington ratio of APM 08279+5255 can be estimated from an assumed value of $\Gamma \sim 2$ (where Γ is the X-ray photon index), which is close to the mean value estimated from observations (Saez, Chartas & Brandt 2009; Chartas et al. 2009a), and using the $L_{\rm bol}/L_{\rm Edd}$ vs. Γ correlation found in RQ quasars (e.g., Wang et al. 2004; Shemmer et al. 2006, 2008). The $L_{\rm bol}/L_{\rm Edd}$ vs. Γ correlation for APM 08279+5255 implies $L_{\rm bol}/L_{\rm Edd} \sim 0.2$, and therefore $M_{\rm BH} \sim 10^{12}\mu_L^{-1}M_{\odot}$. A second independent method of estimating the Eddington ratio through the use of the observed width of the C IV line indicates a black-hole mass of $M_{\rm BH} \sim 10^{11}\mu_L^{-1}M_{\odot}$ (see e.g., Riechers et al. 2009). The Eddington ratio derived using the second method is $L_{\rm bol}/L_{\rm Edd} \sim 2$, implying the source is accreting at a super-Eddington rate. However caution must be taken with this result because the estimates of $M_{\rm BH}$ based on C IV emission-line widths is subject to a lot of systematic uncertainties (i.e., it contains non-virial components such as the disk wind that can contribute to the broadening, e.g., Shemmer et al. 2008). There are also conflicting reported estimates of the magnification parameter (μ_L). Optical observations indicate $\mu_L \sim 100$ (e.g, Egami al. 2000), while observations of CO emission yield $\mu_L \sim 4$ (e.g., Riechers et al. 2009). In this work we try, as far as possible, to present our results as a function of the magnification factor, however when this is not possible a value of $\mu_L = 100$ is assumed (as in, Egami al. 2000). The absorption corrected optical to X-ray power-law slope[4], of APM 08279+5255 is [5] $\alpha_{\rm ox} \sim -1.8$ (e.g., Dai et al. 2004).

The relatively soft SED of APM 08279+5255 combined with its relatively large Eddington ratio provide ideal conditions for the production of radiatively driven winds (see e.g., Everett 2005, and §4.4).

4.2.2 Results from eight deep X-ray observations of APM 08279+5255

This section summarizes results from 2 *Chandra*, 3 *XMM-Newton* and 3 *Suzaku* observations of APM 08279+5255 (8 in total; see Table 4.1 for details). The data reduction of the *Chandra* and *XMM-Newton* observations is described in Chartas et al. (2009a) and the reduction of the *Suzaku* observations in Saez, Chartas & Brandt (2009). Note that from here on when we refer to a particular observation we will use the same names defined in Saez, Chartas & Brandt (2009) and Chartas et al. (2009a). Therefore the three *Suzaku* observations are referred to as OBS1, OBS2 and OBS3, the three *XMM-Newton* observations are referred to as Epoch 2, Epoch 3 and Epoch 4 and the two *Chandra* observations are referred to as Epoch 1 and Epoch 5 (see Table 4.1 for details).

[4] $\alpha_{\rm ox}$ is defined as the slope of a hypothetical power law extending between 2500Å and 2 keV in the AGN rest frame, i.e. $\alpha_{\rm ox} = \log\frac{F_\nu(2keV)}{F_\nu(2500\mathring{A})}/\log\frac{\nu(2keV)}{\nu(2500\mathring{A})} = 0.3838\,\log\frac{F_\nu(2keV)}{F_\nu(2500\mathring{A})}$

[5] The $\alpha_{\rm ox} - l_{\rm UV}$ relation described in (Strateva et al. 2005; Steffen et al. 2006) predicts that $\alpha_{\rm ox} = (-0.137 \pm 0.008)\,\log l_{2500\mathring{A}} + (2.638 \pm 0.240)$. Using Irwin et al. (1998) work we estimate that $\log l_{2500\mathring{A}} \sim 31.7$ ($\mu_L \sim 100$) and therefore we obtain $\alpha_{\rm ox} = -1.7 \pm 0.3$ in accordance with Dai et al. (2004) value.

Table 4.1: Log of observations of APM 08279+5255.

Date[a]	OBS ID	Telescope	Instrument	Exposure	Net exp	Net counts[b]	f_{2-10}[c]
2002-02-24 (Epoch1)	2979	*Chandra*	ACIS BI	91.9 ks	88.8 ks	5,627±75	4.3±0.1
2002-04-28 (Epoch2)	0092800201	*XMM-Newton*	EPIC pn	102.9 ks	83.5 ks	12,820±139	4.1±0.1
2006-10-12 (OBS1)	701057010	*Suzaku*	XIS FI	102.3 ks	71.3 ks	6,071±90	4.2±0.3
2006-10-12 (OBS1)	701057010	*Suzaku*	XIS BI	102.3 ks	71.3 ks	2,325±64	3.8±0.3
2006-11-01 (OBS2)	701057020	*Suzaku*	XIS FI	102.3 ks	67.9 ks	5498±87	3.8±0.3
2006-11-01 (OBS2)	701057020	*Suzaku*	XIS BI	102.3 ks	67.9 ks	2,181±62	3.7±0.3
2007-03-24 (OBS3)	701057030	*Suzaku*	XIS FI	117.1 ks	86.4 ks	4750±80	4.0±0.3
2007-03-24 (OBS3)	701057030	*Suzaku*	XIS BI	117.1 ks	86.4 ks	2,918±71	4.0±0.3
2007-10-06 (Epoch3)	0502220201	*XMM-Newton*	EPIC pn	89.6 ks	56.4 ks	11,400±114	3.9±0.1
2007-10-22 (Epoch4)	0502220301	*XMM-Newton*	EPIC pn	90.5 ks	60.4 ks	16,698±133	5.0±0.1
2008-01-14 (Epoch5)	7684	*Chandra*	ACIS BI	91.7 ks	88.06 ks	6,938±83	4.5±0.2

[a] The date is also described by the term in parentheses.

[b] Background-subtracted source counts including events with energies within the 0.2–10 keV band. See §2 of Chartas et al. (2009a) and §2 of Saez, Chartas & Brandt (2009) for details on source and background extraction regions used for measuring N_{sc}.

[c] The fluxes (in units of 10^{-13}ergs cm^{-2} s^{-1}) in the 2–10 keV observed-frame band are obtained using the best-fit absorbed power law model. The details of these fits are presented in Table 3 of Saez, Chartas & Brandt (2009) and in Table 2 of Chartas et al. (2009a).

Our analysis of the X-ray observations of the BAL quasar APM 08279+5255 indicates strong and broad absorption at rest-frame energies of 1–4 keV (low-energy) and 7–18 keV (high-energy). The medium producing the low-energy absorption is a nearly neutral absorber with a column density of $\log(N_{\rm H}/{\rm cm}^{-2}) \sim 23$. However, since APM 08279+5255 is at a high redshift of $z = 3.91$ it is difficult to constrain the ionization state of the low-energy absorber. The absorption signatures of this complex low energy absorber are shifted outside the range of the observed X-ray band (typically between 0.3-10 keV). The high-energy absorption features are easily detected in the 8 deep X-ray observations of APM 08279+5255. In every case these features satisfy ${\rm EW}/\sigma_{\rm EW} \gtrsim 3$ (see, Saez, Chartas & Brandt 2009; Chartas et al. 2009a)[6], and therefore they satisfy realistic limits for significant detections (Vaughan & Uttley 2008).

Chartas el al. 2002 have interpreted the high-energy X-ray BALs as being produced by absorption of highly ionized iron such as Fe XXV Kα ($1s^2 - 1s2p$; 6.70 keV) and/or Fe XXVI ($1s-2p$; 6.97 keV) launched very near an ionizing compact central source. Evidence to support this interpretation is the significant variability in the strength and energy of the X-ray BALs over short time-scales present in many of the observations. This variability is found to be as short as $\sim$ 3 days rest-frame in the *Chandra* and *XMM-Newton* observations, and $\sim$ month in the *Suzaku* observations. This fast variability presents a strong argument in favor of a wind that originates from a distance of a few times the Schwarzschild radius[7].

In the *Suzaku* observations the variability of the high energy absorber is present at energies close to 7 keV rest-frame. On the other hand the *Chandra* and *XMM-Newton* observations show variability of the high-energy absorption profiles at both: low energies (i.e. rest-frame energies $\sim$ 7 keV) and high energies (i.e. rest-frame energies $\gtrsim$ 9 keV). A time-variable outflow provides a plausible explanation for the changes in shape on the absorption features in past X-ray observations of APM 08279+5255 (Chartas et al. 2002; Hasinger et al. 2002). An even stronger case is presented in Chartas et al. (2009a) and Saez, Chartas & Brandt (2009), where it can be seen clearly that in some cases the appearance of the high-energy absorption feature can take the shape of a notch, an edge or two absorption lines. Our spectral analysis of the 8 deep observations also indicates variability of the parameters defining the high energy attenuation which is likely due to a change in the outflow velocity of the absorber (Saez, Chartas & Brandt 2009; Chartas et al. 2009a). The short time-scale ($\sim$week in the rest-frame) of the variability combined with the high ionization of the absorbing material which is moving at relativistic speeds imply that the absorbers are launched from distances $\lesssim 10\ R_S$ from the central source (see e.g §4 of Saez, Chartas & Brandt 2009). The short time-scale of this variability in the *Suzaku* (Saez, Chartas & Brandt 2009) and *XMM-Newton* (Chartas et al. 2009a) observations also indicates that this absorber should be strongly

[6]EW is the equivalent width obtained using the best fitted model of the high energy absorption feature. The equivalent width (EW) is defined as $EW = \int \frac{F_c - F_E}{F_c} dE$, where F_c is the continuum flux and F_E is the flux in the absorber.

[7]The time-scale of the flux variability provides an indication of the size of the emission region. The size of this region should be approximately the time scale of the variability times the speed of light. Variability over a period of a $\sim$week implies an emission region of size $\sim 6R_S$. In the last expression we estimated the Schwarzschild radius (R_S) of APM 08279+5255 using $M_{\rm BH} \sim 10^{10} M_\odot$ (obtained assuming $\mu_L \sim 100$; see §4.2.1). Possible flux variability caused by the time-delay between the images is shorter than R_S/c.

accelerated. The covering fraction of these winds should be low $\lesssim 20\%$ based on the absence of emission features from the outflowing ionized gas (see e.g. Chartas et al. 2009a).

Table 4.2. The minimum and maximum energies and velocities of the high-energy absorption features in APM 08279+5255[a].

OBS	Instrument	$E_{\rm min}$ [keV]	$E_{\rm max}$ [keV]	$v_{\rm min}$ [c]	$v_{\rm max}$ [c]	Γ
1	XIS FI	7.52±0.36	12.16±0.52	0.11±0.05	0.53±0.03	1.94±0.04
2	XIS FI	7.88±0.48	11.57±0.51	0.16±0.06	0.50±0.03	2.02±0.03
3	XIS FI	7.51±0.32	11.70±1.06	0.11±0.04	0.51±0.07	1.94±0.05
1	XIS BI	7.24±0.51	12.47±1.12	0.08±0.07	0.55±0.06	1.95±0.07
2	XIS BI	8.74±0.58	12.24±1.16	0.26±0.06	0.54±0.07	1.91±0.06
3	XIS BI	7.53±0.82	12.40±0.92	0.12±0.11	0.54±0.05	1.92±0.05
1	ACIS S3	8.05±0.11	10.64±0.19	0.18±0.01	0.43±0.01	1.74±0.03
2	EPIC pn	7.54±0.42	15.04±0.97	0.12±0.06	0.67±0.04	1.89±0.03
3	EPIC pn	6.42±0.48	17.94±1.81	< 0.03	0.76±0.04	2.03±0.04
4	EPIC pn	6.94±0.20	16.31±0.90	0.04±0.03	0.71±0.03	2.11±0.02
5	ACIS S3	7.36±0.30	15.35±1.13	0.09±0.04	0.68±0.04	1.94±0.04

[a]The model used to estimate $E_{\rm min}$ and $E_{\rm max}$ is a power-law with Galactic absorption, intrinsic absorption, and two absorption lines (APL+2AL). The fits of this model are presented in Table 3 of Saez, Chartas & Brandt (2009) and in Table 2 of Chartas et al. (2009a).

The minimum and maximum projected velocities ($v_{\rm min}, v_{\rm max}$) of the outflow are estimated from the minimum and maximum energy ranges ($E_{\rm min}, E_{\rm max}$) of the high-energy absorption features in APM 08279+5255. We obtained $E_{\rm min}$ and $E_{\rm max}$ from our spectral fits assuming first the two absorption-line (APL+2AL) model. Specifically, based on the best-fit values of an absorbed power law model with two absorption lines (from Table 3 of Saez, Chartas & Brandt 2009 and Table 2 of Chartas et al. 2009), we obtain $E_{\rm min} = E_{\rm abs1} - 2\sigma_{\rm abs1}$ and $E_{\rm max} = E_{\rm abs2} + 2\sigma_{\rm abs2}$. As in Chartas et al. (2009a), we estimate the line of sight projected velocities $v_{\rm min}$ and $v_{\rm max}$ assuming the absorption arises from highly blueshifted Fe xxv Kα ($E_{\rm lab} = 6.7$ keV). In Table 4.2 we show the values obtained for $E_{\rm min}$, $E_{\rm max}$, $v_{\rm min}$ and $v_{\rm max}$. In this table we also add a column with the fitted values of Γ (based on the APL+2AL model). Using $E_{\rm max} \sim 18$ keV (the maximum observed value), we constrain the maximum angle[8] between our line of sight and the wind direction to be less than 22°.

As we indicated in Chartas et al. (2009a) (and from Table 4.2) there is a hint that changes in the photon index (Γ) may be positively correlated with the changes of the

[8]The Doppler-shift formula predicts that given a fixed ratio of $E_{\rm lab}/E_{\rm obs} \equiv R_{\rm lo}$ (where $E_{\rm lab}$ and $E_{\rm obs}$ is the energy of the absorption line in the rest-frame and observed-frame respectively) the maximum angle between our line of sight and the wind direction is given by $\theta_{\rm max} = \cos^{-1}(\sqrt{1 - R_{lo}^2})$.

maximum velocity of the outflow ($v_{\rm max}$). This possible trend between Γ versus $v_{\rm max}$ is shown in Figure 10 of Chartas et al. (2009a). In §4.3 we recalculate the velocities found in Table 4.2 with a model based on CLOUDY simulations of a near-relativistic outflow. In §4.4 we provide an interpretation of the possible trend between maximum outflow velocity and Γ.

4.3 Photoionization models of near-relativistic outflows

4.3.1 Motivation

From the X-ray analysis of our 8 observations of APM 08279+5255 (see, Saez, Chartas & Brandt 2009; Chartas et al. 2009a, for more details), and past observations of this object and PG 1115+080 (e.g., Chartas et al. 2007a), it became clear that a more sophisticated spectral model was needed to fit the X-ray BALs. Currently there are no proper tools available in the spectral fitting package XSPEC to model absorption profiles resulting from near-relativistic outflows. In Saez, Chartas & Brandt (2009) we used photoionization models created from the photoionization code XSTAR (see, e.g., Kallman & Bautista 2001) to fit the broad absorption feature found between 7−18 keV rest-frame in APM 08279. This spectral analysis did not include relativistic corrections, and does not contain a realistic model of the outflow. In this section we describe new software code that we have developed that provides a more realistic description of radially accelerated near-relativistic outflows. Our main goal is to better constrain important parameters describing near-relativistic outflows; among these are, the velocity profile, the ionization parameter and the column density of the observed X-ray wind.

4.3.2 Description of the code

Our quasar outflow code is based on a multilayer approach which mimics the absorption and scattering through a near-relativistic outflow using the photoionization code CLOUDY (Ferland al. 1998). An existing quasar outflow code called XSCORT developed by Schurch & Done 2007 follows a similar approach and is based on the photoionization code XSTAR.

In our quasar outflow code we use CLOUDY simulations to approximate the absorption signature produced by an outflowing medium that is radiatively accelerated from a central source. We describe the outflowing medium with a set of absorption layers with specific velocity profile and ionization states. The details of the approximations and assumptions used in our quasar outflow model are described in the following paragraphs.

4.3.2.1 The case of one absorption layer

We approximate the attenuation through the outflowing ionized gas as the absorption through a series of layers of different velocities and ionization states. We begin by calculating the output absorption profile assuming the wind is made up of a single layer and then generalize our model by dividing the outflowing wind into multiple layers. We assume the layer is at a distance R from the continuum source, has a thickness $\Delta R \ll R$, a density n, and is moving at a velocity v away from it. We further assume

that spectral energy distribution of the source is a power-law ($L_\nu \propto \nu^\alpha$) with spectral index $\alpha = -1.0$. From here on, unless mentioned otherwise, this is the SED that we will assume in our simulations. The ionization parameter (Tarter, Tucker & Salpeter 1969, see Appendix C.1) measured in the absorption layer's rest-frame is

$$\xi = \frac{4\pi F'_I}{n'} \tag{4.1}$$

where primed quantities n' ($n' = \gamma n$) and F'_I refer to the density and the incident ionizing flux in the layer's rest-frame, respectively. Non primed parameters are assumed to be in the rest-frame of the luminous source. Using the fact that I_ν/ν^3 is a Lorentz invariant, the incident ionization flux in a layer's rest-frame is given by[9]

$$F'_I = \gamma^4 (1 - v/c)^4 F_I. \tag{4.2}$$

The column density (in any reference frame[10]) of the layer is given by $N_{\rm H} = n\Delta r$. The incident flux on a layer is calculated between 1 Ry to 1000 Ry in the rest-frame of the moving layer.[11] From the incident flux in the rest-frame of the layer and from the use of equation (4.1) we calculate the ionization state of this layer. We next input the derived ionization state and column density of the layer into the photoionization code CLOUDY to obtain the output spectrum of the layer in its rest-frame and transform it to the rest-frame of the luminous source.

4.3.2.2 A model to describe X-ray absorption profiles.

The X-ray spectra that we have obtained from observations of several BAL quasars do not show any emission lines associated with the X-ray BALs (Chartas et al. 2009a). This is expected since BAL quasar outflows in general are expected to have relatively small covering fractions (Hewett & Foltz 2003). Therefore, we will concentrate on absorption-dominated outflows neglecting emission features in our model. For our CLOUDY code, we will assume an approximately constant ionization parameter in the outflow.

We assume that the region of the outflow that contributes to the observed Fe XXV and/or Fe XXVI absorption is localized in a relatively thin multilayer of thickness ΔR at a distance R from the black hole. Even though the ionization parameter is expected to fall off with distance along the flow as $1/R^2$ it remains relatively constant within the

[9] Since $F_\nu \propto I_\nu$, $\nu/\nu' = D$; where $D = \gamma^{-1}(1 - v/c)^{-1}$ and $I_\nu = I_{\nu'}\nu^3/\nu'^3 = I_{\nu'}D^3$. Therefore $F'_I = \int_{\nu'_0}^{\nu'_1} F_{\nu'} d\nu' = D^{-4}\int_{\nu_0}^{\nu_1} F_\nu d\nu$, where $\nu'_0 = 1$ Ry and $\nu'_1 = 1000$ Ry; $\nu_{0,1} = D\nu'_{0,1}$. Conversely, to calculate the incident flux in the layer's rest-frame, we integrate the flux in the luminous source rest-frame, and multiply by a factor of D^{-4}. Notice that if the flux is a power law, i.e. $F_\nu = a\nu^\alpha$, then $F'_I = aD^{-4}\ln(\nu'_1/\nu'_0)$ if $\alpha = -1$, and $F'_I = aD^{\alpha-3}(\nu'^{\alpha+1}_1 - \nu'^{\alpha+1}_0)/(\alpha+1)$ if $\alpha \neq -1$. Therefore in the case that the SED is a power-law, the ionizing flux in the rest-frame of the absorbing layer can be found by integrating the flux in the luminous source rest-frame between 1 Ry and 1000 Ry, and then multiply by $D^{\alpha-3}$ where α is the spectral index.

[10] $N_{\rm H} = n\Delta r = (n\gamma)(\Delta r/\gamma) = n'\Delta r'$

[11] The Rydberg is a unit of energy defined in terms of the ground-state energy of an electron for the hydrogen atom, $1Ry \approx 13.6eV$.

multilayer since $\Delta R \ll R$.[12] To compensate for changes in flux across the multilayer due to relativistic effects (e.g., beaming effects) we adjust the density n_i of each layer such that the ionization parameter remains constant with the multilayer ΔR. In the case that the region of the outflow that we are modeling is not physically thin, our approach will still be valid as long as the ionization parameter along this region does not change appreciably.

From equation (4.1) the ionization parameter of each layer is $\xi = 4\pi F'_{\rm I,i}/n'_i$; where $F'_{I,i}$ is the incident flux in the rest-frame of layer i estimated from the flux coming from layer $i-1$ after taking into account relativistic effects. In our calculations we vary the density in order to keep the ionization parameter approximately constant along the simulated outflow. The density of each layer, is determined from an a priori defined velocity profile $v(r)$. In our multilayer approach, the density of each layer is $n_i \propto \gamma_i^3(1-v_i/c)^4$ for $i = 0, 1..(N_l - 1)$, were N_l is the number of layers. We note that the assumed density profile adjusts the ionization parameter so that it does not vary across the multilayer due to relativistic effects. However, the ionization parameter will still decrease between $0.02 - 0.40$ dex mainly due to attenuation (see §4.3.2.3). For our case we concentrate on simulated outflows with $\log \xi \gtrsim 3$. As long as each layer[13] used in our calculations has a column density of $\log (\Delta N_{{\rm H}i}/{\rm cm}^{-2}) \lesssim 23$ it can be assumed to be almost transparent (or thin) to radiation (see Appendix C.2). As we describe in §4.3.2.3 the assumption of optically thin layers will allow us to more greatly reduce the time needed to compute the absorption signature of the multilayered outflow.
In this work we assume that the outflow velocity profile will have a p-type form given by

$$v(\hat{N}_{\rm H}) = v_{\rm min} + (v_{\rm max} - v_{\rm min})(\hat{N}_{\rm H}/N_{\rm H})^p, \tag{4.3}$$

where $N_{\rm H}$ is the total column density of the simulated wind ($0 < \hat{N}_{\rm H} < N_{\rm H}$). We note that given the assumptions described here, and the moderate S/N of the absorption profile in X-ray, we do not expect to obtain significant constraints on the acceleration mechanism of the outflow by using this profile.

4.3.2.3 Passing a continuum spectrum from one absorbing layer to the next

When passing the continuum spectrum from one layer (i-1) to the next (i) we first transform the source rest-frame spectrum coming from layer i-1 to the rest-frame of layer i. In the rest-frame of layer i we remove absorption and add emission (in cases where we do consider emission) to the incident spectrum given the column density and ionization parameter of the layer. The column density of layer i is obtained from the velocity profile, and its ionization parameter is calculated from the input spectrum in its

[12] In our simulations we assume that the ionization luminosity is $L_I = 10^{44}$ erg s^{-1}, therefore for a layer with $\log \xi = 3.0$, $n = 10^{12}$ cm^{-3} (initial density assumed in our runs, see §4.3.2.4), and $\log (N_{\rm H}/{\rm cm}^{-2}) = 23$, we will typically have that the ratio of thickness to distance of the layer is $\Delta R/R \approx 0.001$ and consequently $\Delta\xi \approx -2$. This means that the ionization parameter with typical value of $\log \xi \sim 3$ varies through the outflow ~ 0.001 dex due to the radial dependency.

[13] We use ≈ 100 layers to generate the absorption profile of a simulated wind, therefore each layer has a column density of $\log \Delta N_{{\rm H}i} \lesssim 22$.

rest-frame. Finally we transform the output spectrum coming from layer i back to the source rest-frame.

Since the density of each layer is chosen to correct the attenuation of the flux due to relativistic effects, the ionization parameter will mostly decrease due to the absorption of the outflow across the layer. The decrease of the ionization through the multilayered outflow due to absorption will be greater in winds that are less ionized and with higher column densities. For example, a wind with $\log (N_{\rm H}/{\rm cm}^{-2}) = 22.75$ with initial ionization parameter of $\log \xi_i = 3.25$ will have a final ionization parameter of $\log \xi_f \sim 3.21$, however for $\log (N_{\rm H}/{\rm cm}^{-2}) = 22.75$ and $\log \xi_i = 3.75$ the final ionization parameter is $\log \xi_f \sim 3.73$. Additionally a wind with $\log (N_{\rm H}/{\rm cm}^{-2}) = 23.75$ and $\log \xi_i = 3.25$ will have $\log \xi_f \sim 2.84$, however if $\log (N_{\rm H}/{\rm cm}^{-2}) = 23.75$ and $\log \xi_i = 3.75$ then $\log \xi_f \sim 3.53$.

After correcting the spectrum incident on layer i for the effects of relativistic beaming, we estimate the absorption and emission from layer i using simulations performed with the photoionization code CLOUDY. These CLOUDY simulations are implemented using the unabsorbed source spectrum (power-law with $\alpha = -1$ in our case) and various values of the ionization parameter. The main advantage of this approximation is a dramatic shortening in the time it takes to obtain a profile. This speed-up is possible because the photoionization runs at each layer use a library of preexisting CLOUDY runs (see next paragraph for details). If the flux emitted by the source is a power-law, the flux received by a moving layer is also a power-law with the same spectral index as the source as long as the SED is not significantly attenuated in an energy dependent way. In addition, if each layer of the multilayered media is approximately optically thin then the state of the gas depends primarily on the ionization parameter and secondarily on the SED (Tarter, Tucker & Salpeter 1969). This dependence indicates that our approach is at first order a good approximation as long as the SED along the multilayered outflow does not differ appreciably from the incident SED at the first layer. However, for low ionization states ($\log \xi < 3$) and large total column densities ($\log (N_{\rm H}/{\rm cm}^{-2}) \gtrsim 23.5$), the SED along the multilayered outflow will deviate appreciably from the initial incident SED, and therefore, our approximation breaks down.

In order to avoid invoking CLOUDY too many times (~ 100) to simulate the signature of the multilayered absorber, we created a library of spectra to speed-up our calculations. This library contains a set of simulated transmitted spectra through absorbers having a range of ionization parameters between $1.8 - 4.1$ dex ($\log \xi$ steps of 0.01 dex), column density of $\log (N_{\rm H}/{\rm cm}^{-2}) = 19$, density of $n_{\rm H} = 10^{12}$ cm^{-3} and an input SED that has the form of a power law ($L_\nu \propto \nu^\alpha$) in the energy range between $1 - 10^4$ Rys with spectral index $\alpha = -1$. The value of the density of the absorber ($n_{\rm H} = 10^{12}$ cm^{-3}) is chosen to be close to the value of the density predicted by 2-d numerical simulations of radiative winds by Proga et al. (2000, 2004). The simulations used to construct this library (from here on referred to as library runs), as well as all the simulated profiles described in the next sections, are calculated using standard solar metallicities. We primarily used CLOUDY to perform the photoionization calculations but we also compared our results with those generated by the photoionization code XSTAR.

In order to reduce the number of realizations in our library, we performed these runs assuming a specific turbulent velocity of $v_{\rm turb} = 1500$ km s^{-1}. Our choice of a

specific turbulent velocity requires that the relative speed $\Delta v_i'$ between layers i and $i+1$ to be the same for every layer in the simulations of multilayered outflows[14] (i.e. $\Delta v_i' = \Delta v'$; see Appendix C.3). In our simulations we use a finite number of layers to describe the outflow, each layer having a slightly different velocity following the adopted velocity profile. In our simulations the distribution of the velocity differences between adjacent layers is assumed to be uniform and to extend between 0 and a maximum velocity difference of $\Delta v'$. The velocity difference of $\Delta v'$ is kept lower than $v_{\rm turb}\sqrt{12}$; where $v_{\rm turb} = 1500$ km s^{-1} is the assumed turbulent velocity (see Schurch & Done 2007). By selecting a turbulent velocity we set a lower limit on the number of layers used in simulating a BAL spectrum.[15] The simulations making up our library are all performed using the same column density ($\log(N_{\rm H}/{\rm cm}^{-2}) = 19$). Consequently, the opacity of a layer i (i.e., the layer's rest-frame absorption) is calculated by first obtaining the opacity from the library at the ionization state of the layer, and second, by scaling the opacity obtained (from the library) to the column density of the layer[16]. This approximation is justified given that in the range of densities of our simulations ($8 \lesssim \log n_{\rm H} \lesssim 12$) the dependency of the opacity on n_H is negligible, and therefore, the opacity of a layer i can be found from the library just by knowing its ionization state and column density. Emission spectra may also be obtained from our library runs, however for our study we mostly concentrated on the absorption spectra. We focus on the absorption spectra since the main goal of our study is to fit the spectral signatures produced by winds with low covering fractions in which emission is not important.

4.3.2.4 Testing our relativistic outflow code

We first generate the absorption profiles for a linearly accelerated outflow with $v_{\rm min} = 0$, $v_{\rm max} = 0.3c$ ($v \propto N_{\rm H}$), $N_{\rm H} = 3\times10^{23}$ cm^{-2}, initial density $n_0 = 10^{12}$ cm^{-3}, and values of $\log\xi = 2.75$, 3.00, 3.25, 3.50, 3.75 and 4.00. These profiles have been generated to compare the results of our code with those presented in Schurch & Done (2007). In order to make a fair comparison with the results of Schurch & Done (2007), we use a library of XSTAR runs using a power-law model with $\alpha = -1.4$. This library of XSTAR runs, has the same characteristics as the CLOUDY library described in §4.3.2.3. Our simulated X-ray absorption profiles are very similar to the ones computed by Schurch & Done 2007 under the assumption of a multilayer outflow with spherical symmetry (see Appendix C.4).

We generate a second run of simulations based on our results presented in §4.2.2. For this purpose, we simulate absorption profiles with $v_{\rm min} = 0.1c$, $v_{\rm max} = 0.7c$, $n_0 = 10^{12}$ cm^{-3}, $\log(N_{\rm H}/{\rm cm}^{-2}) = 23.75$, and three values of the ionization parameter $\log\xi = 3.0, 3.5, 4.0$. The outflow parameters have been chosen approximately in accordance to the estimated values based on one of the *XMM-Newton* observations of APM 08279+5255

[14] The relative velocities of two adjacent layers according to special relativity is $\Delta v_i' = (v_{i+1} - v_i)/(1 - v_i v_{i+1}/c^2)$.

[15] For example if the velocity profile has $v_{\rm min} = 0$ and $v_{\rm max} = 0.7c$ we require that the number of layers $N_l > (v_{\rm max} - v_{\rm min})/(\sqrt{1}2v_{\rm turb})$, i.e. with $v_{\rm turb} = 1500$ km s^{-1}, the minimum number of layers that we can use for this case is forty.

[16] For thin layers, the opacity of a layer (τ_2) can be obtained by scaling the opacity of a different layer (τ_1) by the ratio of the column densities of the two layers (i.e. $\tau_2 = \tau_1 N_{\rm H2}/N_{\rm H1}$).

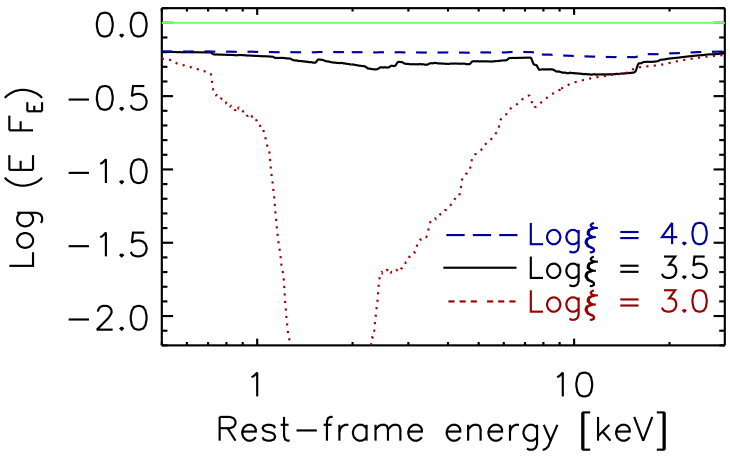

Fig. 4.2 X-ray spectra derived from multilayered CLOUDY simulations of near-relativistic outflows. The assumed input spectrum is a power-law with $\Gamma = 2.0$. The outflow has been accelerated between $0.1c - 0.7c$ using a p-type velocity profile with $p = 1.0$. The total column density of the outflow is $\log\,(N_{\rm H}/{\rm cm}^{-2}) = 23.75$. We have calculated the output spectra for 3 different values of the ionization parameter, $\log\,\xi = 3.0$, 3.5 and 4.0.

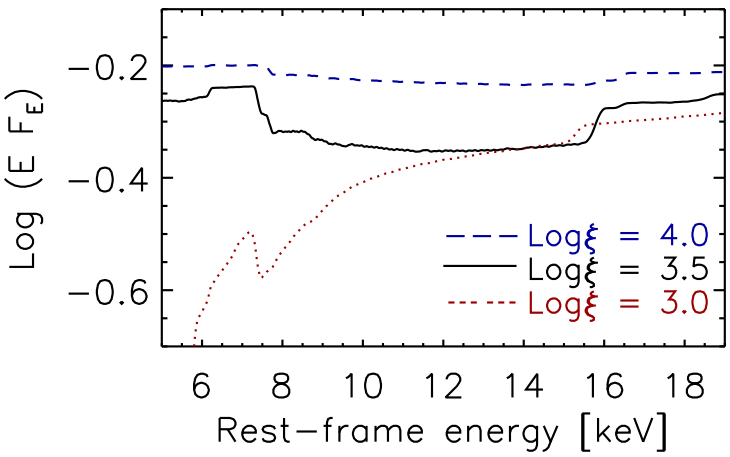

Fig. 4.3 X-ray spectra derived from multilayered CLOUDY simulations of near-relativistic outflows. This is a zooming of Figure 4.2 in the region where we find iron absorption. The assumed input spectrum is a power-law with $\Gamma = 2.0$. The outflow has been accelerated between $0.1c-0.7c$ using a p-type velocity profile with p=1.0. The total column density of the outflow is $\log\,(N_{\rm H}/{\rm cm}^{-2}) = 23.75$. We have calculated the output spectra for 3 different values of the ionization parameter, $\log\,\xi = 3.0$, 3.5 and 4.0.

(Epoch 3 from Chartas et al. 2009a). To generate notch-type absorption profiles we chose $p = 1$ for these simulations. The resulting profiles are presented in Figure 4.2. In Figure 4.3 we zoom in on the iron blend feature which shows up at energies between 7.5−16.5 keV. The resonance absorption lines responsible for the features are mainly Fe XXV Kα ($1s^2 - 1s2p$; 6.70 keV) and Fe XXVI Kα ($1s - 2p$; 6.97 keV). From Figures 4.2 and 4.3 it is clear that the strength of the iron blend feature is larger for $\log \xi = 3.5$. The strength of this feature is large for ionization parameters in the range of $3 \lesssim \log \xi \lesssim 4$, since at lower ionization levels the abundance of highly ionized iron atoms (e.g., Fe XXV and Fe XXVI) is too small to produce any appreciable feature in the spectra. At $\log \xi \gtrsim 4$ the atoms in the gas become stripped of almost all their electrons, and therefore, the resulting spectra contain very few bound-bound and bound-free absorption features. When $\log \xi \lesssim 3$ there is substantial absorption present at energies $\lesssim 2$ keV rest-frame. As a consequence, in a heavily absorbed source like APM 08279+5255, the low-energy ($\lesssim$ 2 keV) absorbed component of the spectrum, possibly due to non-outflowing material, will overlap with the absorbed component produced by the wind (e.g., Saez, Chartas & Brandt 2009; Chartas et al. 2009a). However, the high-energy absorption iron trough (above ~ 7 keV) is not contaminated by absorption lines from non-outflowing material, and consequently, it provides a clean signature of the outflowing material.

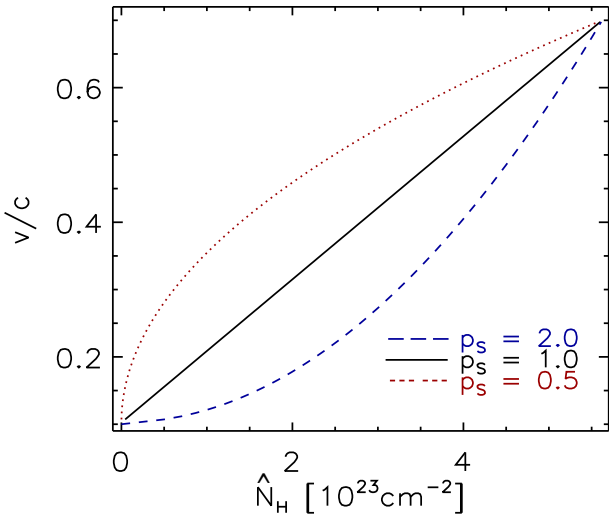

Fig. 4.4 Outflow velocity as a function of column density through the outflow for 3 different values of the the exponent of the p-type velocity profile (see equation 4.3), $p = 0.5$ (dotted line), 1.0 (solid line) and 2.0 (dashed line). We assumed the outflow has a launch velocity of 0.1 c, a terminal velocity of 0.7 c and a total column density of $\log (N_{\rm H}/{\rm cm}^{-2}) = 23.75$.

The absorption profiles described in §4.2.2 contain a diversity of shapes, sometimes resembling notches, edges or two absorption lines. Given the variety of shapes of the absorption profiles we attempted to emulate these different shapes by generating simulations of outflows with $v_{\rm min} = 0.1c$ and $v_{\rm max} = 0.7c$, $\log (N_{\rm H}/{\rm cm}^{-2}) = 23.75$, $\log \xi = 3.5$ and three values of p, $p = 0.5, 1$ and 2. The output spectra of the resulting

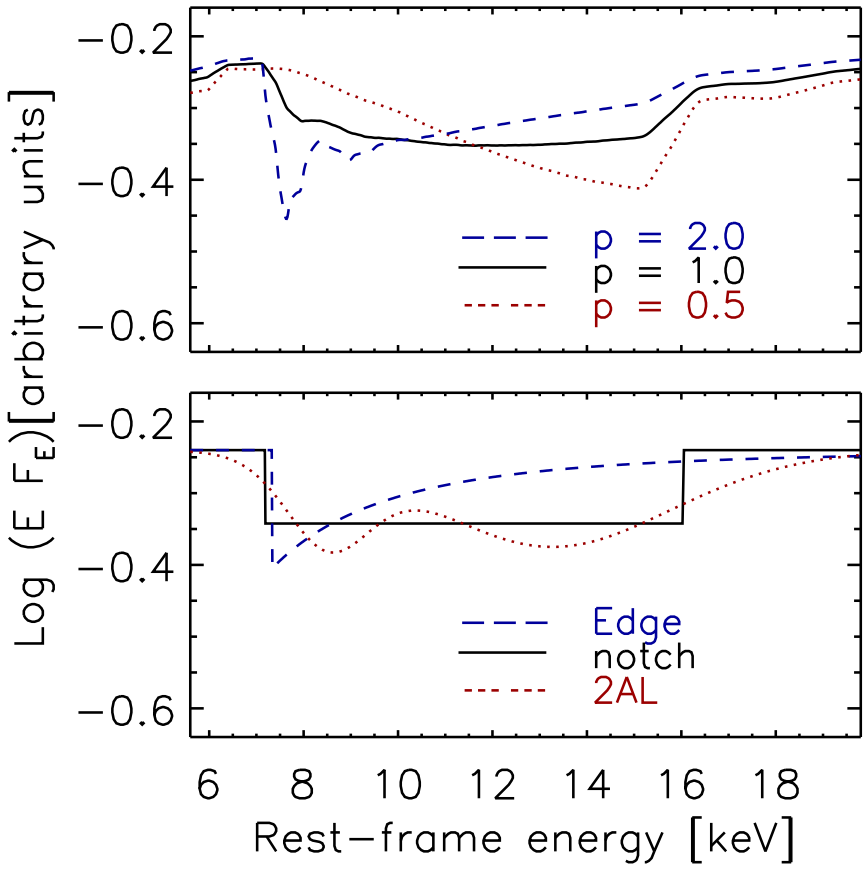

Fig. 4.5 **Upper panel:** X-ray spectra produced from multilayered CLOUDY simulations of near-relativistic outflows. The assumed input spectrum is a power-law with $\Gamma = 2.0$ (solid line). The outflow has been accelerated between $0.1c-0.7c$ using an exponent of the velocity profile with p=1.0. The total column density of the outflow is log $(N_{\rm H}/{\rm cm}^{-2}) = 23.75$. We have calculated the output spectra for 3 different values of the exponent p, $p = 0.5$ (dotted line), 1.0 (solid line) and 2.0 (dashed line). **Lower panel:** X-ray spectra resulting from the best fitted models used in Chartas et al. (2009a) to fit the high energy absorption of APM 08279+5255 in Epoch 3. The solid line is for the notch model, the dotted line corresponds to the two absorption line model and the dashed line is for the absorption edge model.

velocity profiles (see Figure 4.4) are presented in Figure 4.5. In the lower panel of this figure we also show as a reference three observed spectra from Epoch 3. The three different models used to fit these spectra are a notch, an edge and a two absorption line model (see Table 2 from Chartas et al. 2009a).

4.3.3 Fits to the observed spectra of APM 08279+5255 using our quasar outflow model

In this section we present results from fits to spectra obtained from *XMM-Newton*, *Chandra* and *Suzaku* observations of APM 08279+5255 using our thin multilayered outflow model. We created XSPEC table models[17] from a large number of simulated quasar absorption spectra produced from running our multilayered model over a large range of parameter space of the outflow parameters. Specifically, the parameter space of our simulations covered five important properties of the multilayered outflow model: minimum velocity of the outflowing gas $v_{\rm min}$, maximum velocity $v_{\rm max}$, ionization parameter ξ, total column density $N_{\rm H}$ and the value p which defines the outflow velocity profile (see equation 4.3). For our simulations we assume (unless mentioned otherwise) an initial density of the outflowing gas in the multilayer of $n_0 = 10^{12}$ cm^{-3}. We note that our results are not sensitive to the assumed initial density of the outflowing gas. A change of the density by up to two orders of magnitudes from our assumed value does not result in any significant variation of our results.

4.3.3.1 XSPEC table models for quasar outflows

In order to fit the variety of absorption spectra of APM 08279+5255 we generated three different types of XSPEC table models that mainly differ in the parameter space of the outflow properties that are covered.

The first table model (WINDFULL.TAB) assumes the presence of only one outflowing component. We define as component i of an outflow a multilayer absorber at a distance $R_{\rm i}$ from the black hole, with a thickness $\Delta R_{\rm i}$ ($\Delta R_{\rm i}/R_{\rm i} \ll 1$), a velocity gradient of Δv_i across it, a column density of $N_{\rm H}$, and an ionization parameter of log ξ_i. We produced the table model WINDFULL.TAB by simulating transmitted spectra through a range of outflows with minimum velocities ($v_{\rm min}$) in the range of 0.0−0.3c (a simulation for every 0.02c interval), with maximum velocities ($v_{\rm max}$) in the range of 0.3−0.9c (step intervals of 0.04c), log ($N_{\rm H}$/cm^{-2}) in the range 22−24 (step intervals of 0.25 dex), log ξ in the range 2.8−4.0 (step intervals of 0.2 dex), and the index p having values of 0.5, 1.0, 2.0 and 5.0.

In several observations, the X-ray BALs produced by highly ionized iron lines (above 7 keV rest-frame) appear to consist of two broad absorption components. The component covering low energies ($\lesssim$ 9 keV rest-frame) is referred to as slow and the one covering larger energies ($\gtrsim$ 10 keV rest-frame) is referred to as fast. Typical models used to fit the fast component contain a number of gaussian lines (Chartas et al. 2002, 2007a,

[17] A table model consist of a file that contains an N-dimensional grid of model spectra with each point on the grid having been calculated for particular values of the N parameters in the model. XSPEC will interpolate on the grid to get the spectrum for the parameter values required at that point in the fit.

2009a; Saez, Chartas & Brandt 2009). We created the table model WINDVSLOW.TAB to fit the slow component and the table model WINDVFAST.TAB to fit the fast component. Since table models WINDVSLOW.TAB and WINDVFAST.TAB are used to fit a relative small portion of the spectra we fix the velocity profile parameter to $p = 1.0$. Each component of the outflow has a velocity gradient Δv with a minimum ($v_{\rm min}$) and maximum velocity ($v_{\rm max}$) that satisfy $v_{\rm max} = v_{\rm min} + \Delta v$. By fitting these table models to the spectra we constrain the minimum and maximum projected velocities of each component. Table model windvslow.tab is generated with Δv having values in the range 0.02-0.42c (step intervals of 0.04c) and the parameters ($v_{\rm min}$), log $N_{\rm H}$ and log ξ cover the same range and values as those used for producing table model WINDFULL.TAB. Table model windvfast.tab is generated with Δv having values in the range 0.04-0.80c (step intervals of 0.04c for $\Delta v < 0.24c$ and step intervals of 0.08c for $\Delta v \geq 0.24c$) and the parameters ($v_{\rm max}$), log $N_{\rm H}$ and log ξ cover the same range and values as those used for producing table model WINDFULL.TAB.

4.3.3.2 Results from fits to X-ray spectra of APM 08279+5255

We fit the X-ray spectra of APM 08279+5255 using two different models. These two models assume a source spectrum consisting of a power-law attenuated by Galactic absorption (XSPEC model WABS). We assumed a Galactic column density of $4.1 \times 10^{20}{\rm cm}^{-2}$ (Kalberla et al. 2005). The first model (MODEL1) contains an intrinsic neutral absorber (XSPEC model ZWABS) to describe the absorption in the low energy range of 1−4 keV rest-frame and an outflowing ionized absorber (XSPEC table model WINDFULL.TAB) to account for the X-ray BALs. In XSPEC notation MODEL1 is written as: WABS*ZWABS*MTABLE{WINDFULL.TAB}*POW. The second model (MODEL2) contains an intrinsic neutral absorber (XSPEC model ZWABS) to describe the absorption in the low energy range of 1−4 keV rest-frame and a two component outflowing ionized absorber (XSPEC table models WINDVSLOW.TAB and WINDVFAST.TAB) to account for the X-ray BALs. In XSPEC notation MODEL1 is written as:
WABS*ZWABS*MTABLE{WINDVSLOW.TAB}*MTABLE{WINDVFAST.TAB}*POW.

Table 4.3: Results from spectral fits to the three *Suzaku* observations of APM 08279+5255.

		FI SPECTRUM[b]			BI SPECTRUM[b]		
Model[a]	Parameter	Values OBS1	Values OBS2	Values OBS3	Values OBS1	Values OBS2	Values OBS3
MODEL1...	Γ	$1.96^{+0.04}_{-0.05}$	$2.03^{+0.06}_{-0.05}$	$1.95^{+0.06}_{-0.06}$	$2.03^{+0.15}_{-0.15}$	$1.93^{+0.07}_{-0.05}$	$1.91^{+0.09}_{-0.07}$
	log ($N_{\rm H1}$/cm^{-2})	$22.91^{+0.09}_{-0.05}$	$22.95^{+0.12}_{-0.12}$	$22.83^{+0.11}_{-0.09}$	$22.76^{+0.12}_{-0.13}$	$22.79^{+0.06}_{-0.09}$	$22.78^{+0.08}_{-0.09}$
	log ($N_{\rm H2}$/cm^{-2})	$23.54^{+0.10}_{-0.11}$	$23.32^{+0.18}_{-0.15}$	$23.55^{+0.12}_{-0.15}$	$23.82^{+0.18}_{-0.16}$	$23.42^{+0.16}_{-0.15}$	$23.68^{+0.20}_{-0.22}$
	log ξ_2	$3.44^{+0.16}_{-0.24}$	$3.29^{+0.10}_{-0.10}$	$3.52^{+0.16}_{-0.12}$	$3.59^{+0.25}_{-0.17}$	$3.52^{+0.12}_{-0.25}$	$3.64^{+0.22}_{-0.27}$
	$v_{\rm min}/c$	$0.14^{+0.02}_{-0.02}$	$0.19^{+0.02}_{-0.02}$	$0.10^{+0.02}_{-0.02}$	$0.07^{+0.03}_{-0.06}$	$0.28^{+0.04}_{-0.07}$	$0.13^{+0.03}_{-0.06}$
	$v_{\rm max}/c$	$0.50^{+0.04}_{-0.02}$	$0.51^{+0.04}_{-0.04}$	$0.49^{+0.12}_{-0.08}$	$0.58^{+0.05}_{-0.05}$	$0.60^{+0.06}_{-0.07}$	$0.62^{+0.15}_{-0.10}$
	p	$1.6^{+0.4}_{-0.4}$	$1.8^{+0.8}_{-0.6}$	$2.3^{+1.0}_{-0.7}$	$1.4^{+0.6}_{-0.6}$	$2.8^{+2.2}_{-1.0}$	$2.6^{+2.0}_{-1.4}$
	χ^2/ν	60.5/67	68.8/60	70.2/65	56.1/65	89.6/60	43.8/65
	$P(\chi^2/\nu)$	0.70	0.21	0.32	0.78	0.01	0.98
MODEL2...	Γ	$1.98^{+0.05}_{-0.05}$	$2.03^{+0.04}_{-0.04}$	$1.95^{+0.05}_{-0.05}$	$2.00^{+0.10}_{-0.10}$	$1.92^{+0.05}_{-0.05}$	$1.91^{+0.07}_{-0.07}$
	log ($N_{\rm H1}$/cm^{-2})	$22.82^{+0.16}_{-0.20}$	$22.97^{+0.07}_{-0.07}$	$22.81^{+0.13}_{-0.11}$	$22.76^{+0.10}_{-0.15}$	$22.79^{+0.09}_{-0.09}$	$22.78^{+0.06}_{-0.08}$
	log ($N_{\rm H21}$/cm^{-2})	$23.23^{+0.15}_{-0.15}$	$23.10^{+0.20}_{-0.14}$	$23.08^{+0.18}_{-0.20}$	$23.50^{+0.15}_{-0.18}$	$23.42^{+0.20}_{-0.22}$	$23.48^{+0.20}_{-0.32}$
	log ($N_{\rm H22}$/cm^{-2})	$23.26^{+0.20}_{-0.18}$	$22.90^{+0.26}_{-0.22}$	$23.27^{+0.28}_{-0.20}$	$23.53^{+0.16}_{-0.17}$	< 23.5	$23.40^{+0.20}_{-0.36}$
	log ξ_2	$3.28^{+0.28}_{-0.18}$	$3.33^{+0.12}_{-0.16}$	$3.48^{+0.20}_{-0.26}$	$3.42^{+0.16}_{-0.17}$	$3.46^{+0.14}_{-0.13}$	$3.52^{+0.25}_{-0.30}$
	$v^{(1)}_{\rm min}/c$	$0.12^{+0.02}_{-0.02}$	$0.20^{+0.03}_{-0.03}$	$0.12^{+0.01}_{-0.01}$	$0.08^{+0.02}_{-0.03}$	$0.25^{+0.02}_{-0.02}$	$0.11^{+0.04}_{-0.03}$
	$v^{(1)}_{\rm max}/c$	$0.28^{+0.03}_{-0.03}$	$0.29^{+0.04}_{-0.04}$	$0.15^{+0.02}_{-0.02}$	$0.30^{+0.05}_{-0.05}$	$0.35^{+0.02}_{-0.02}$	$0.26^{+0.08}_{-0.08}$
	$v^{(2)}_{\rm min}/c$	$0.39^{+0.06}_{-0.06}$	$0.41^{+0.05}_{-0.05}$	$0.23^{+0.06}_{-0.06}$	$0.36^{+0.04}_{-0.04}$	$0.48^{+0.05}_{-0.05}$	$0.39^{+0.08}_{-0.08}$
	$v^{(2)}_{\rm max}/c$	$0.49^{+0.03}_{-0.02}$	$0.50^{+0.02}_{-0.02}$	$0.48^{+0.05}_{-0.05}$	$0.54^{+0.03}_{-0.03}$	$0.58^{+0.04}_{-0.06}$	$0.58^{+0.07}_{-0.07}$
	χ^2/ν	55.1/65	65.5/58	67.4/63	52.8/63	83.8/58	41.3/63
	$P(\chi^2/\nu)$	0.81	0.23	0.33	0.82	0.15	0.98

[a]MODEL1 is a power-law with Galactic, neutral, and a one component outflow absorption (XSPEC model WABS*ZWABS*MTABLE{WINDFULL.TAB}*POW); MODEL2 is a power-law with Galactic, neutral, and a two component outflow absorption (XSPEC model WABS*ZWABS*MTABLE{WINDVSLOW.TAB}*MTABLE{WINDVFAST.TAB}*POW).

[b]The spectra fitted are the added (with HEASOFT ftools routine ADDSPEC) spectra of the FI chips (XIS0, XIS2 and XIS3). For OBS 2 the XIS2 CCD was not operational, and only the XIS0 and XIS3 spectra were added for this observation. The BI spectra are taken with the XIS1 chip.

Table 4.4: Results from spectral fits of the *Chandra* and *XMM-Newton* observations of APM 08279+5255.

Model[a]	Parameter	Values Epoch 1	Values Epoch 2	Values Epoch 3	Values Epoch 4	Values Epoch 5
MODEL1...	Γ	$1.75^{+0.04}_{-0.03}$	$2.00^{+0.06}_{-0.05}$	$2.13^{+0.09}_{-0.05}$	$2.38^{+0.09}_{-0.08}$	$1.96^{+0.03}_{-0.03}$
	$\log\,(N_{\rm H1}/{\rm cm}^{-2})$	$22.67^{+0.04}_{-0.07}$	$22.72^{+0.04}_{-0.07}$	$22.71^{+0.02}_{-0.02}$	$22.68^{+0.02}_{-0.02}$	$23.02^{+0.03}_{-0.03}$
	$\log\,(N_{\rm H2}/{\rm cm}^{-2})$	$23.62^{+0.05}_{-0.06}$	$23.67^{+0.06}_{-0.06}$	$23.76^{+0.08}_{-0.05}$	$23.85^{+0.06}_{-0.05}$	$23.13^{+0.09}_{-0.11}$
	$\log\,\xi_2$	$3.56^{+0.08}_{-0.12}$	$3.35^{+0.09}_{-0.10}$	$3.47^{+0.10}_{-0.10}$	$3.36^{+0.05}_{-0.05}$	$3.28^{+0.12}_{-0.10}$
	$v_{\rm min}/c$	$0.15^{+0.01}_{-0.01}$	$0.13^{+0.01}_{-0.01}$	$0.08^{+0.02}_{-0.02}$	$0.05^{+0.01}_{-0.01}$	$0.13^{+0.03}_{-0.03}$
	$v_{\rm max}/c$	$0.43^{+0.03}_{-0.04}$	$0.64^{+0.07}_{-0.06}$	$0.69^{+0.03}_{-0.03}$	$0.73^{+0.03}_{-0.02}$	$0.31^{+0.02}_{-0.02}$
	p	$3.8^{+1.0}_{-1.0}$	$2.2^{+0.8}_{-0.5}$	$1.6^{+0.2}_{-0.2}$	$1.5^{+0.2}_{-0.1}$	$1.2^{+0.6}_{-0.4}$
	χ^2/ν	132.1/104	110.5/115	109.4/105	152.4/143	77.2/70
	$P(\chi^2/\nu)$	0.03	0.60	0.36	0.28	0.26
MODEL2...	Γ	$1.77^{+0.02}_{-0.02}$	$2.04^{+0.05}_{-0.05}$	$2.17^{+0.06}_{-0.07}$	$2.31^{+0.08}_{-0.05}$	$1.99^{+0.05}_{-0.04}$
	$\log\,(N_{\rm H1}/{\rm cm}^{-2})$	$22.61^{+0.05}_{-0.05}$	$22.63^{+0.05}_{-0.05}$	$22.67^{+0.04}_{-0.05}$	$22.63^{+0.03}_{-0.03}$	$23.01^{+0.04}_{-0.04}$
	$\log\,(N_{\rm H21}/{\rm cm}^{-2})$	$23.17^{+0.12}_{-0.13}$	$23.60^{+0.07}_{-0.08}$	$23.34^{+0.06}_{-0.10}$	$23.22^{+0.08}_{-0.10}$	
	$\log\,(N_{\rm H22}/{\rm cm}^{-2})$	$23.47^{+0.10}_{-0.13}$	$23.41^{+0.12}_{-0.12}$	$23.51^{+0.07}_{-0.07}$	$23.12^{+0.13}_{-0.22}$	
	$\log\,\xi_2$	$3.32^{+0.18}_{-0.19}$	$3.22^{+0.06}_{-0.06}$	$3.37^{+0.08}_{-0.08}$	$3.28^{+0.04}_{-0.04}$	$3.25^{+0.15}_{-0.11}$
	$v^{(1)}_{\rm min}/c$	$0.15^{+0.01}_{-0.01}$	$0.13^{+0.02}_{-0.02}$	$0.04^{+0.02}_{-0.02}$	$0.06^{+0.02}_{-0.03}$	$0.11^{+0.01}_{-0.01}$
	$v^{(1)}_{\rm max}/c$	$0.17^{+0.01}_{-0.01}$	$0.31^{+0.04}_{-0.04}$	$0.40^{+0.05}_{-0.05}$	$0.21^{+0.05}_{-0.05}$	$0.31^{+0.02}_{-0.02}$
	$v^{(2)}_{\rm min}/c$	$0.32^{+0.02}_{-0.02}$	< 0.12	$0.43^{+0.10}_{-0.10}$	$0.24^{+0.06}_{-0.06}$	$0.58^{+0.04}_{-0.04}$
	$v^{(2)}_{\rm max}/c$	$0.40^{+0.01}_{-0.01}$	$0.63^{+0.04}_{-0.03}$	$0.69^{+0.03}_{-0.03}$	$0.73^{+0.02}_{-0.02}$	$0.66^{+0.02}_{-0.03}$
	χ^2/ν	116.8/102	107.5/113	106.5/103	152.5/141	66.2/68
	$P(\chi^2/\nu)$	0.15	0.63	0.39	0.24	0.54

[a]MODEL1 is a power-law with Galactic, neutral, and a one component outflow absorption (XSPEC model WABS*ZWABS*MTABLE{WINDFULL.TAB}*POW); MODEL2 is a power-law with Galactic, neutral, and a two component outflow absorption (XSPEC model WABS*ZWABS*MTABLE{WINDVSLOW.TAB}*MTABLE{WINDVFAST.TAB}*POW).

We note that MODEL1 and MODEL2 use a neutral absorber to describe the intrinsic attenuation in the low energy range of 1−4 keV rest-frame. In this work we also tried fits with an ionized absorber to describe the attenuation at 1−4 keV; these fits did not result in a significant improvement over fits that used a neutral absorber. Additionally, as discussed in Saez, Chartas & Brandt (2009); Chartas et al. (2009a), the use of a neutral absorber to describe the absorption in the low energy range of 1−4 keV rest-frame did not improve with the use of more complex absorbers even for spectral fits performed to deep X-ray observations of APM 08279+5255. We also note that given the high redshift of APM 08279+5255, our fits to the spectra of this source cannot adequately constrain the low-energy intrinsic absorption at 1−4 keV rest-frame.
For MODEL2 the current data cannot adequately constrain the ionization parameters of both the slow and fast components of the outflow. We therefore set the ionization parameters of the slow and fast component to be equal in MODEL2.[18]

Table 4.5. Estimates of the improvement of fits to the spectra of APM 08279+5255 using MODEL2 over MODEL1.

OBSID	Instrument	F-statistic[a]	null probability	significance
OBS1	FI	2.59	4.8×10^{-2}	95.2%
OBS1	BI	3.05	1.5×10^{-1}	85.5%
OBS2	FI	5.32	2.4×10^{-1}	76.0%
OBS2	BI	7.15	1.4×10^{-1}	85.6%
OBS3	FI	1.31	2.8×10^{-1}	72.3%
OBS3	BI	1.91	1.6×10^{-1}	84.3%
Epoch 1	ACIS S3	6.68	1.8×10^{-3}	99.8%
Epoch 2	Epic pn	1.56	2.2×10^{-1}	78.4 %
Epoch 3	Epic pn	1.40	2.5×10^{-1}	74.9 %
Epoch 4	Epic pn	...	...	...
Epoch 5	Epic pn	5.66	5.32×10^{-3}	99.5%

[a]The value on the left of the slash is the F-statistic and is given by $F = \frac{\chi^2_{\nu_1} - \chi^2_{\nu_1}}{\Delta\nu} / \frac{\chi^2_{\nu_2}}{\nu_2}$. The value on the right of the slash represents the probability of exceeding the F-statistic based on the F-test.

The results of the fits of these models to the *Suzaku* spectra of APM 08279+5255 are presented in Table 4.3 and to the *Chandra* and *XMM-Newton* spectra in Table 4.4.

We note that in MODEL1 of Tables 4.3 and 4.4 $\log N_{\rm H_1}$ and $\log N_{\rm H_2}$ are the best fitted column densities of the intrinsic neutral absorber and the outflowing ionized

[18]Notice that in Saez, Chartas & Brandt (2009) we tried a similar model to MODEL2 (model XSTAR4, Table 5) and we fond that the ionization state of the slow component could not be distinguished for the ionization state of the fast component in the *Suzaku* observations. We have a similar case when we try MODEL2 on our eight X-ray observations without setting the ionization parameter of the slow and fast component as equal.

absorber, respectively. In MODEL2 of these same tables log $N_{\rm H1}$, log $N_{\rm H21}$, log $N_{\rm H22}$ are the best fitted column densities of the intrinsic neutral absorber, the slow and fast outflowing ionized absorber, respectively. In MODEL2 of these tables the velocity superscripts (1) and (2) represent the best-fitted velocity parameters of the slow and fast component, respectively.

In general the models that fit the high-energy outflowing absorber (see Tables 4.3 and 4.4) tend to have ionization parameters in the range $3.2 \lesssim \log \xi \lesssim 3.7$. With the exception of the *Chandra* observations, there is no improvement in the fits when using MODEL2 over MODEL1. In Table 4.5 we show the statistical improvements based on the F-test of fits using MODEL2 over those using MODEL1. For the *Chandra* observations the improvements are $\gtrsim 99.5\%$ when we use MODEL2 over MODEL1. There are also marginal improvements using MODEL2 over MODEL1 for the *Suzaku* observations especially in OBS1 (see Table 4.5). In general we will use MODEL2 to estimate the outflow parameters because this model provides better constrains of the maximum velocity of the outflow. However, in the case of the *XMM-Newton* observations we use MODEL1 to estimate the outflow parameters because these observations show the widest X-ray BALs and provide better constraints of the velocity profile parameter p.

Based on the spectral fits to the *Suzaku* observations (Table 4.3), we find possible variability ($\gtrsim 2\sigma$) in the minimum velocity of the outflow between OBS2 and OBS3 ($v_{\rm min}$ in MODEL1 and $v^{(1)}_{\rm min}$ in MODEL 2) for both the BI and FI spectra. The evidence of this variability in the *Suzaku* spectra of APM 08279+5255 was already analyzed in Saez, Chartas & Brandt (2009) and in this work we conclude that its significance is at the 99.9% and 98% significance levels in the FI and BI spectra, respectively. This variability is also confirmed to exist between the column density and velocity of the slow component when we compare epochs OBS2 and OBS3.

We confirm the dramatic change in the maximum velocity of the fast component of the *Chandra* observations as shown in Chartas et al. (2009a). We find a $\gtrsim 3\sigma$ change of $v^{(2)}_{\rm max}$ between Epoch 1 and Epoch 5 using either MODEL1 or MODEL2 (see Table 4.4). We also confirm this change in velocity when we plot the confidence contours of the column density (log $N_{\rm H22}$) versus the maximum velocity of the fast outflow component ($v^{(2)}_{\rm max}$) using MODEL2. In Figure 4.6 we present confidence contours of log $N_{\rm H22}$ versus $v^{(2)}_{\rm max}$ for Epoch 1 and Epoch 5. The significance of the change of log $N_{\rm H22}$ versus $v^{(2)}_{\rm max}$ between Epochs 1 and 5 is $\gtrsim 99.9\%$ with a null probability of $\lesssim 10^{-4}$.

Using either MODEL1 or MODEL2 we find a possible change in the maximum velocity of the outflow between the *XMM-Newton* observations of Epoch 2 and Epoch 4, however, the significance of this change is only at the $1-\sigma$ level (see Table 4.4). We do find however significant changes in the minimum velocity and total column density of the outflow (log $N_{\rm H2}$; Table 4.4) between Epochs 2 and 4. In Table 4.4 we show that this variability is significant at the $\gtrsim 2-\sigma$ level for fits using MODEL1. In Figure 4.7 we plot confidence contours of log $N_{\rm H2}$ versus $v_{\rm min}$ (left panel) and log $N_{\rm H2}$ versus $v_{\rm max}$ (right panel) for each *XMM-Newton* observation for fits using MODEL1. We find that the significance of the variability between Epoch 2 and Epoch 4 of log $N_{\rm H2}$ versus $v_{\rm min}$

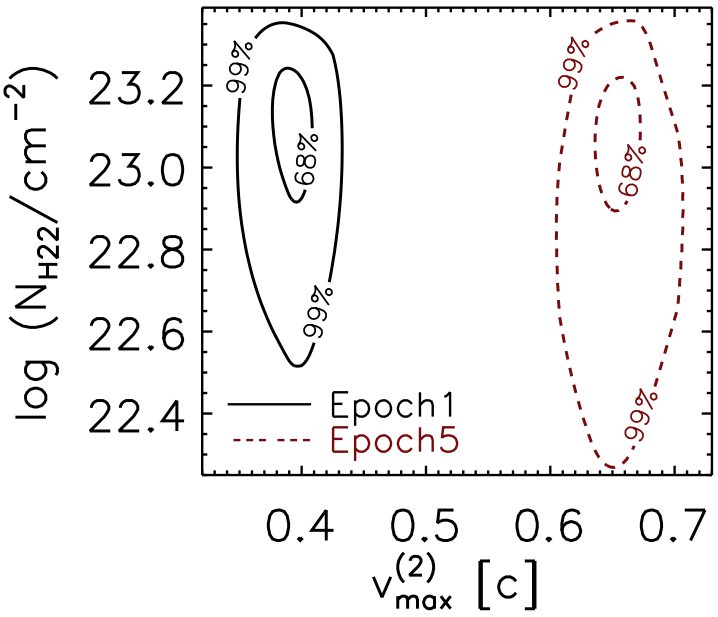

Fig. 4.6 Contour plots of the column density (log ($N_{\rm H22}$/cm^{-2})) versus maximum velocity ($v^{(2)}_{\rm max}$) of the fast component of the ionized outflow absorber. The contour plots have been calculated for the *Chandra* observations Epoch 1 (continuous line) and Epoch 5 (dashed line) at the 68% and 99% level of significance using MODEL2 of Table 4.4.

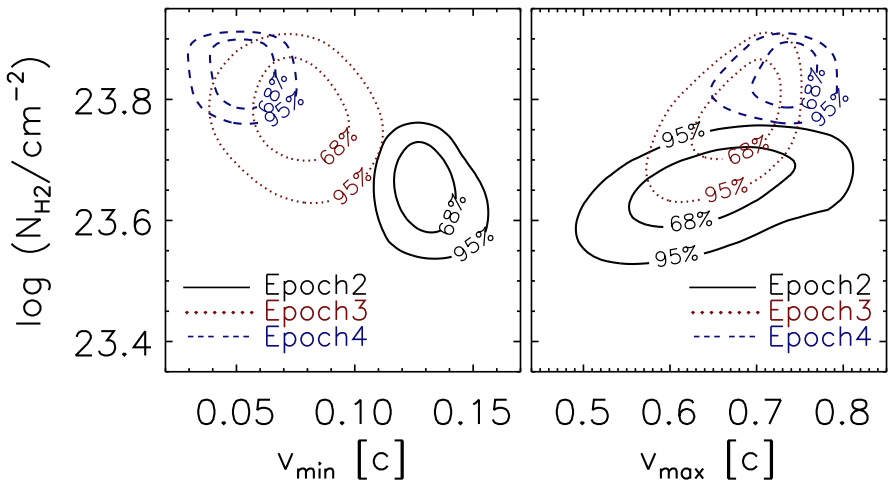

Fig. 4.7 Confidence contours of the total column density (log ($N_{\rm H2}$/cm^{-2})) versus minimum velocity ($v_{\rm min}$; left panel) and maximum velocity ($v_{\rm max}$; right panel) of the high-energy absorber. The contour plots have been calculated for the *XMM-Newton* observations Epoch 2 (solid line), Epoch 3 (dotted line) and Epoch 4 (dashed line) at the 68% and 95% level of significance using MODEL1 of Table 4.4.

is significant at the $\gtrsim 99.9\%$ level and of $\log N_{\rm H_2}$ versus $v_{\rm max}$ is significant at the $\gtrsim 99\%$ level. We also find variability in the minimum velocity of the outflow when we compare Epoch 2 and Epoch 3. This can be seen in Table 4.4 and the left panel of Figure 4.7. From the confidence contours (Figure 4.7, left panel), we estimate the significance of the variability on $\log N_{\rm H_2}$ versus $v_{\rm min}$ between Epoch 2 and Epoch 3 to be $\gtrsim 99\%$. It is worth mentioning that the fits using MODEL2 show an increase in the maximum velocity $\sim 2{-}\sigma$ of the slow outflow component ($v^{(1)}_{\rm max}$) between Epoch 3 and Epoch 4. This change is consistent with the change found in the first component energy of the two gaussian absorption line model of Chartas et al. (2009a). Finally we note that the spectral fits to the *XMM-Newton* observations show values of p that are greater than one. Although we find indications of variability of p, these changes are not significant given the poor constraints of this parameter.

4.3.3.3 Mass outflow rate and kinetic energy of outflow of APM 08279+5255

We use results from fits of our quasar outflow model to the spectra of APM 08279+5255 to constrain the mass outflow rate and kinetic energy injected by this outflow into the surrounding medium. In Saez, Chartas & Brandt (2009) and Chartas et al. (2009a) we also constrained these properties of the outflow, however, these estimates were based on less realistic models (see §4.2.2).

A trend between $v_{\rm max}$ and Γ based on the X-ray observations of APM 08279+5255 (Figure 4.8, upper panel) was recently found by Chartas et al. (2009a). Such a trend is consistent with models that predict that quasar winds are driven by radiation pressure. Our fits with a more realistic quasar outflow model confirm the trend between $v_{\rm max}$ and Γ. We also find a possible trend between the total column density of the outflowing ionized absorber ($\log N_{\rm H}$) and Γ. As the lower panel of Figure 4.8 shows, we find that $\log N_{\rm H}$ increases with Γ. The increase of the maximum velocity with Γ could be related to the fact that softer spectra have a stronger radiative effect on the wind (see §4.4 and §3.3 of Chartas et al. 2009a). On the other hand, a possible increase in column density with Γ could be indicating that APM 08279+5255 becomes a more effective radiative driving source as the spectrum of the ionizing source becomes softer. Additional X-ray observations of APM 08279+5255 will show if these trends are significant.

In order to calculate the mass outflow rate ($\dot{M}$) and the efficiency of the wind (ϵ_K) we have modified the formulas used in Saez, Chartas & Brandt (2009) and Chartas et al. (2009a) to include the modeled velocity gradient of the wind and include special relativistic corrections. The mass outflow rate is given by

$$\dot{M} = 4\pi f_c m_p \frac{R^2}{\Delta R} \int_0^{N_{\rm H}} v(\hat{N}_{\rm H}) d\hat{N}_{\rm H} = 4\pi f_c \frac{R^2}{\Delta R} N_{\rm H} m_p \left(v_{\rm min} + \frac{v_{\rm max} - v_{\rm min}}{p+1} \right), \quad (4.4)$$

and the wind efficiency, defined as the ratio of the rate of kinetic energy injected into the interstellar medium and IGM by the outflow to the quasars bolometric luminosity, is

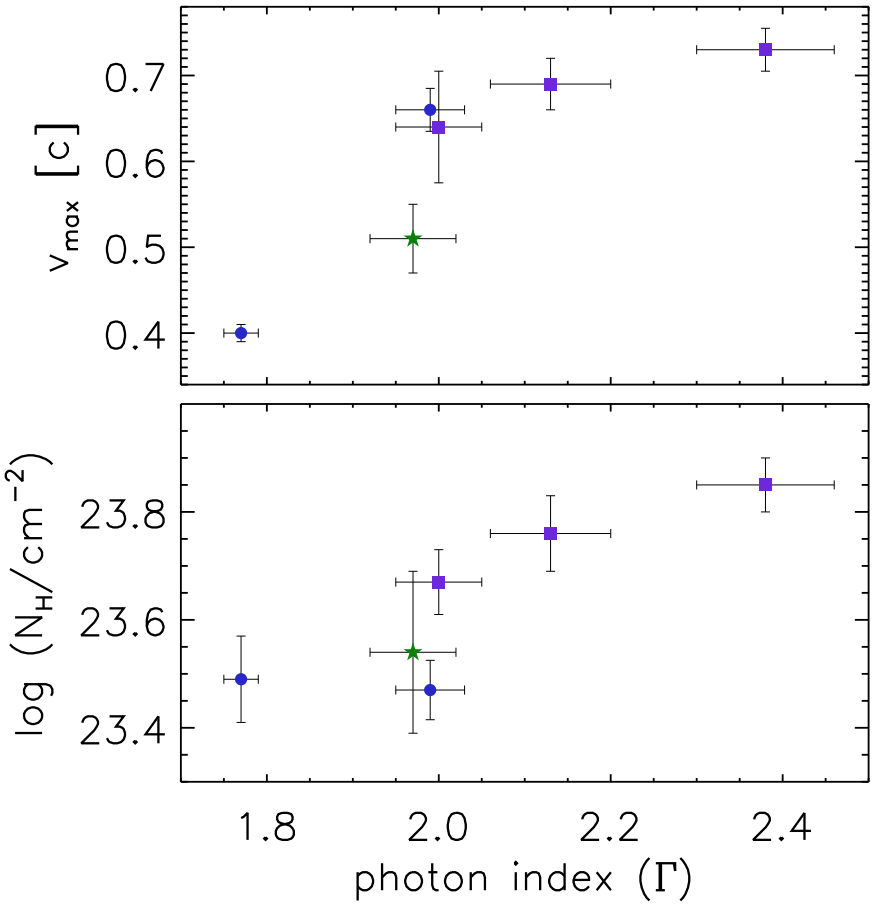

Fig. 4.8 Maximum velocity ($v_{\rm max}$; upper panel) and total column density of the outflow (log ($N_{\rm H}$/cm^{-2}); lower panel) versus photon index (Γ) for our eight deep observations. $v_{\rm max}$, log ($N_{\rm H}$/cm^{-2}) and Γ were derived from fits to the spectra of APM 08279+5255 with a model that included an absorbed power-law and two component outflow (MODEL2 of Tables 4.3 and 4.4) for the *Suzaku* and *Chandra* observations and a single component outflow for the *XMM-Newton* observations (MODEL1 of Table 4.4). Errors shown are at the 68% condence level. Data shown with circles, a star, and squares are obtained from *Chandra*, *Suzaku* and *XMM-Newton* observations respectively.

$$\epsilon_K = \frac{c^2}{L_{\rm bol}} \int (\gamma - 1) d\dot{M} = \frac{4\pi c^2 f_c m_p}{L_{\rm bol}} \frac{R^2}{\Delta R} \int_0^{N_{\rm H}} (\gamma - 1) v(\hat{N}_{\rm H}) d\hat{N}_{\rm H}. \quad (4.5)$$

In equations (4.4) and (4.5) f_c is the covering fraction, $N_{\rm H}$ is the column density, R is the radius, and ΔR is the thickness of the absorber. We note that for an absorber with constant non-relativistic speed ($v/c \ll 1$) equations (4.4) and (4.5) have the same form as the ones used in Saez, Chartas & Brandt (2009) and Chartas et al. (2009a) (see e.g., equation 4 of Saez, Chartas & Brandt 2009).[19] The velocity profile assumed in our models is given by equation (4.3), therefore equations (4.4) and (4.5) contain the dependence of the estimated outflow properties on the model parameters of the velocity profile. To obtain error bars for ϵ_K and $\dot{M}$, we performed a Monte Carlo simulation, assuming a uniform distribution of the parameters f_c, R, and $R/\Delta R$ around the expected values of these parameters, and a normal distribution for log $N_{\rm H}$, $v_{\rm min}$ and $v_{\rm max}$ (described by the parameters in Tables 4.3 and 4.4). Specifically, we assume a covering factor lying in the range $f_c = 0.1 - 0.3$, based on the observed fraction of BAL quasars (e.g., Hewett & Foltz 2003; Gibson et al. 2009) and a fraction $R/\Delta R$ ranging from 1 to 10 based on current theoretical models of quasar outflows (Proga et al. 2000, 2004). Based on our estimated maximum velocities ($v_{\rm max} \sim 0.7c$) (see e.g., Chartas et al. 2009a) and the fast variability of the outflow we expect that R will be close to the Schwarzschild radius (R_S). Therefore in the Monte Carlo simulation we allow R to vary between $3R_S$ and $15R_S$.

[19] For a constant velocity, i.e. a p-type profile (equation 4.3) with $p = 0$ and $v_{\rm min} = v$, then equation (4.4) reduces to $\dot{M} = 4\pi f_c (R^2/\Delta R) N_{\rm H} m_p v$. Also, since $\gamma \approx 1 + v^2/(2c^2)$ ($v/c \ll 1$) equation (4.5) becomes $\epsilon_K = \dot{M} v^2/(2L_{\rm bol})$.

Table 4.6: Mass-outflow rates and efficiencies of outflows in APM 08279+5255 [a].

OBS	Instr.	$\dot{M}$ (abs1) $[10^3 M_\odot \mu_L^{-1} \mathrm{yr}^{-1}]$	ϵ_K (abs1)	$\dot{M}$ (abs2) $[10^3 M_\odot \mu_L^{-1} \mathrm{yr}^{-1}]$	ϵ_K (abs2)	$\dot{M}$ (tot)[b] $[10^3 M_\odot \mu_L^{-1} \mathrm{yr}^{-1}]$	ϵ_K (tot)[b]
OBS1	XIS FI	$1.0^{+0.9}_{-0.6}$	$0.05^{+0.05}_{-0.03}$	$2.2^{+2.2}_{-1.5}$	$0.6^{+0.7}_{-0.4}$	$3.2^{+3.2}_{-2.1}/3.5^{+3.4}_{-2.3}$	$0.6^{+0.7}_{-0.4}/0.9^{+1.0}_{-0.6}$
OBS2	XIS FI	$0.9^{+0.8}_{-0.6}$	$0.06^{+0.07}_{-0.04}$	$1.0^{+1.0}_{-0.7}$	$0.3^{+0.3}_{-0.2}$	$1.9^{+1.9}_{-1.2}/2.0^{+2.0}_{-1.4}$	$0.3^{+0.4}_{-0.2}/0.5^{+0.5}_{-0.3}$
OBS3	XIS FI	$4.6^{+4.4}_{-3.0}$	$0.01^{+0.01}_{-0.01}$	$1.8^{+1.8}_{-1.2}$	$0.3^{+0.4}_{-0.2}$	$2.3^{+2.2}_{-1.5}/2.5^{+2.5}_{-1.7}$	$0.4^{+0.4}_{-0.2}/0.5^{+0.6}_{-0.3}$
OBS1	XIS BI	$1.7^{+1.7}_{-1.1}$	$0.11^{+0.13}_{-0.08}$	$4.2^{+4.1}_{-2.7}$	$1.1^{+1.2}_{-0.7}$	$5.9^{+5.8}_{-3.9}/6.5^{+6.4}_{-4.2}$	$1.2^{+1.3}_{-0.8}/1.7^{+1.8}_{-1.1}$
OBS2	XIS BI	$2.2^{+2.2}_{-1.5}$	$0.24^{+0.26}_{-0.16}$	$2.7^{+2.6}_{-1.9}$	$1.1^{+1.3}_{-0.7}$	$4.8^{+4.9}_{-3.3}/5.3^{+5.3}_{-3.7}$	$1.3^{+1.5}_{-0.9}/1.8^{+2.2}_{-1.3}$
OBS3	XIS BI	$1.6^{+1.6}_{-1.1}$	$0.09^{+0.14}_{-0.07}$	$3.4^{+3.3}_{-2.3}$	$1.2^{+1.5}_{-0.9}$	$5.0^{+5.0}_{-3.4}/5.4^{+5.4}_{-3.7}$	$1.3^{+1.6}_{-0.9}/1.9^{+2.4}_{-1.4}$
Epoch 1	ACIS S3	$0.8^{+0.8}_{-0.5}$	$0.02^{+0.02}_{-0.02}$	$1.2^{+1.1}_{-0.8}$	$0.2^{+0.2}_{-0.1}$	$2.1^{+1.9}_{-1.3}/2.2^{+2.1}_{-1.4}$	$0.2^{+0.2}_{-0.1}/0.3^{+0.3}_{-0.2}$
Epoch 2	EPIC pn	...	...	...	...	$3.9^{+3.6}_{-2.5}/4.3^{+4.0}_{-2.7}$	$0.9^{+1.0}_{-0.6}/1.4^{+1.6}_{-1.0}$
Epoch 3	EPIC pn	...	...	...	...	$5.2^{+4.9}_{-3.3}/5.8^{+5.4}_{-3.7}$	$1.6^{+1.5}_{-1.0}/2.5^{+2.5}_{-1.6}$
Epoch 4	EPIC pn	...	...	...	...	$6.5^{+5.8}_{-4.1}/7.4^{+6.6}_{-4.7}$	$2.3^{+2.1}_{-1.5}/4.0^{+3.7}_{-2.6}$
Epoch 5	ACIS S3	$0.9^{+0.8}_{-0.6}$	$0.05^{+0.05}_{-0.03}$	$2.3^{+2.3}_{-1.5}$	$1.4^{+1.4}_{-0.9}$	$3.2^{+3.1}_{-2.1}/3.5^{+3.4}_{-2.3}$	$1.5^{+1.4}_{-1.0}/2.3^{+2.3}_{-1.5}$

[a] Estimated values of the outflow properties of APM 08279+5255 based on a model that includes an absorbed power-law and a two component outflow (MODEL3 of Tables 4.3 and 4.4) for the *Suzaku* and *Chandra* observations and a single component outflow for the *XMM-Newton* observations (MODEL1 of Table 4.4). The values of $\dot{M}$ and ϵ_K are obtained from equations (4.4) and (4.5) assuming $M_{\rm BH} \sim 10^{12} \mu_L^{-1} M_\odot$ (see §4.2.1) and $L_{\rm bol} = 7 \times 10^{15} \mu_L^{-1} L_\odot$ (Irwin et al. 1998; Riechers et al. 2009).

[b] We provide two estimates of $\dot{M}$(tot) and ϵ_K(tot). The estimate on the left corresponds to the case where the angle between our line of sight and the outflow direction is zero while the one on the right corresponds to an angle of 10°.

In Table 4.6 we show the mass outflow rate ($\dot{M}$) and the efficiency (ϵ_K) of the wind in each observation. The parameters used in equations (4.4) and (4.5) to derive $\dot{M}$ and ϵ_K were obtained from spectral fits of MODEL2 to the *Suzaku* and *Chandra* observations, and through the use of MODEL1 for the *XMM-Newton* observations (see Tables 4.3 and 4.4). For the *Suzaku* and *Chandra* observations we estimate $\dot{M}$ and ϵ_K for the slow and fast component of the outflow. The total mass outflow rate and efficiency is obtained by summing the contributions of the slow and fast outflow component (MODEL2, § 4.3.3.2) when multiple components are required to fit the data. In the case of the *XMM-Newton* observations no summing is required since a one component wind model (MODEL1, § 4.3.3.2) provides better fits (in a statistical sense) to the spectra of APM 08279+5255 (see § 4.3.3.2). In Table 4.6, assuming that the outflow is viewed along our line of sight, we show that during the observations of APM 08279+5255 the total mass outflow rate varied between $21^{+19}_{-13} - 65^{+58}_{-41}\ M_{\odot}\mathrm{yr}^{-1}$ ($\mu_L = 100$) and the total efficiency varied between $0.2^{+0.2}_{-0.1} - 2.3^{+2.1}_{-1.5}$. However, the total values of $\dot{M}$ and ϵ_K are $\sim 10\%$ and $\sim 50\%$ higher respectively if we assume an outflow forming an angle of 10° with our line of sight (see Table 4.6). In Table 4.6 we also show that an important fraction ($> 10\%$) of the bolometric energy of APM 08279+5255 is injected into the surrounding galaxy through quasar winds.

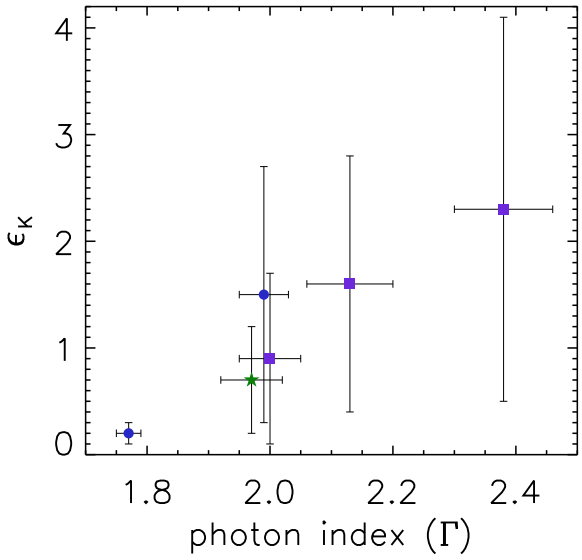

Fig. 4.9 Outflow efficiency (ϵ_K) of the outflow versus photon index (Γ) for our eight observations of APM 08279+5255. ϵ_K and Γ were derived from fits to the spectra of APM 08279+5255 with a model that included an absorbed power-law and two component outflow (MODEL3 of Tables 4.3 and 4.4) for the *Suzaku* and *Chandra* observations and a single component outflow for the *XMM-Newton* observations (MODEL1 of Table 4.4). Errors shown are at the 68% confidence level. Data shown with circles, a star, and squares are obtained from *Chandra*, *Suzaku* and *XMM-Newton* observations respectively.

As Figure 4.8 shows the softer spectra probably result in a faster and more massive (higher total column density) wind. This tendency can be seen more clearly in Figure 4.9 (upper panel) where we have plotted the total efficiency ($\epsilon_{_K}$) as a function of the photon index (Γ). In Figure 4.9 for the case of the *Suzaku* observations, we present one point with the weighted mean (the weights are the photon counts in Table 4.1) of Γ and $\epsilon_{_K}$. The latter is based on the fact that these observations do not present any variability either in Γ, $v_{_f}$ or the total column density (see Table 4.3). We note that a small contribution to the error bars ($\lesssim 20\%$) of $\epsilon_{_K}$ arises from errors in the fitted parameters (i.e., $v_{\rm min}$, $v_{\rm max}$ and $\log N_{\rm H}$) while most of the error in $\epsilon_{_K}$ is due to the uncertainty of R, $f_{_c}$, $R/\Delta R$.

4.4 Influence of the SED on the dynamics of the outflow

This section extends the analysis presented in §3.3 from Chartas et al. (2009a) by providing an analysis of force multipliers as a function of the spectral changes of a Mathews-Ferland SED, while, in the Chartas et al. paper we performed the same analysis but using a pure power-law SED. Parts of this section are therefore taken from Chartas et al. (2009a), however, we focus on the new results that are based on more realistic SEDs.

4.4.1 Background

One of the major unanswered questions in current theoretical and numerical models of quasar winds involves explaining how highly-ionized outflows of X-ray absorbing material become accelerated to near-relativistic velocities. The main problem is that for radiatively driven winds the magnitude of the force on an absorber is a function of its ionization state. As the ionization parameter of the absorber increases, fewer resonant transitions are available to absorb photons from the source, thus resulting in a weaker driving force. Chelouche & Netzer (2001) have explored the dependence of the radiation driving force on the ionization parameter of the outflowing gas and they conclude that for a highly ionized X-ray absorbing gas, the average force multipliers are close to 10.

Most current theoretical work on radiative acceleration in quasars has focused on interpreting the outflows of UV absorbers (e.g., Murray et al. 1995; Proga et al. 2000, 2004; Everett 2005), however; there are no self-consistent models that can explain the acceleration mechanism that leads to the near-relativistic outflows of X-ray absorbing material. A clue to understanding the acceleration process of the wind in APM 08279+5255 is perhaps provided by the large observed difference between the maximum velocities of the UV ($v_{\rm UV} \sim 0.04c$; e.g., Srianand & Petitjean 2000) and X-ray ($v_{\rm X-ray} \sim 0.4$–$0.7c$) absorbers. One possible explanation of the difference between the UV and X-ray outflow velocities is that the UV and X-ray BALs are produced by different absorbers, with UV emission from the accretion disk driving the UV absorbers and X-ray emission from the hot corona contributing to the acceleration of the X-ray absorbers. If the X-ray absorbers are partly driven by radiation from the hot corona we might expect to detect a correlation between the properties of the X-ray BALs and the properties of the X-ray spectrum. For example, we might expect the maximum outflow velocity of the X-ray absorbers to

depend on the shape of the X-ray spectrum that at first order can be represented with the X-ray photon index (Γ).

As we found in Chartas et al. (2009a) and shown in Figure 4.8, harder X-ray spectra in APM 08279+5255 appear to be associated with lower values of the maximum outflow velocities. One possible explanation is that flatter X-ray spectra over-ionize the X-ray absorber resulting in a decrease of the force multiplier and a lower outflow velocity. If this trend is confirmed with future observations it would imply that a significant acceleration mechanism responsible for the near-relativistic velocities of the X-ray outflowing gas in BAL quasars is radiation driving.

4.4.2 The dependence of the force multiplier on the photon index of the source spectrum.

We investigated our hypothesis of the origin of the possible $\Gamma - v_f$ correlation by calculating the force multiplier as a function of the incident spectral energy distribution (SED). The force multiplier represents the ratio by which the bound-bound (line) and bound-free (continuum) opacity increases the radiation force relative to that produced by Thomson scattering alone.

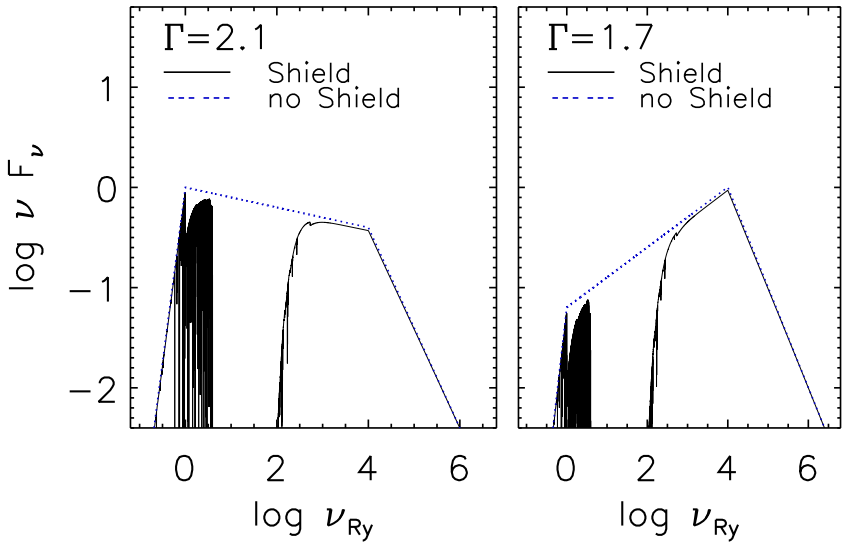

Fig. 4.10 Power law SEDs used to calculate force-multipliers in §4.4.2. The x-axis is the logarithm of frequency (in Ry units) and the y-axis is in units of the logarithm of the flux times the frequency (arbitrary units). The left and right panels correspond to the soft ($\Gamma = 2.1$) and hard SEDs ($\Gamma = 1.7$). In each panel the dotted line is the unabsorbed SED and the solid line is the shielded SED (with $\log \xi_{\rm sh} \sim 1.6$).

We performed calculations of force multipliers assuming a thin slab illuminated by an ionizing continuum using the CLOUDY code. We compared our results to those of Arav et al. (1994) and Everett (2005) who have used a similar approach to ours. In general

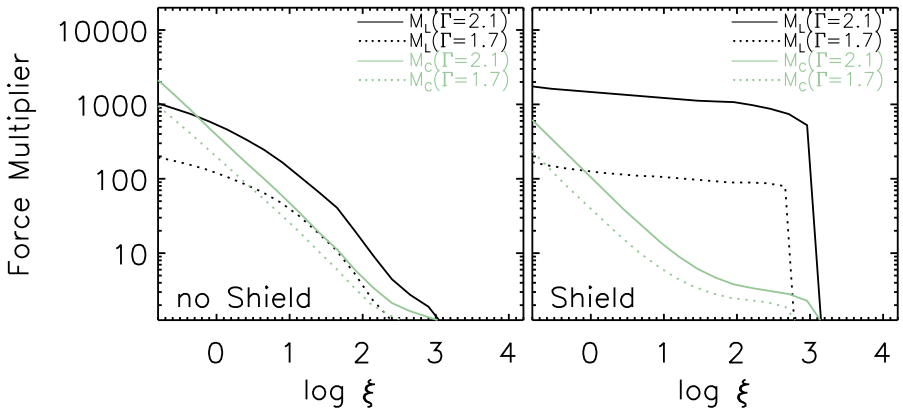

Fig. 4.11 The bound-free, $M_{\rm C}$, and bound-bound, $M_{\rm L}$, components of the force multiplier are shown as a function of the ionization parameter. Force multipliers are calculated for power-law SEDs with photon indices of $\Gamma = 2.1$ (solid lines) and $\Gamma = 1.7$ (dotted lines). In the left panel we have assumed no absorbing shield, whereas, in the right panel the soft and hard SEDs have been attenuated by a warm-absorber shield with log $(N_{\rm H}/{\rm cm}^{-2}) = 23$ and log $\xi_{\rm sh} = 1.6$ on its illuminated face (see Figure 4.10).

our computations are in good agreement (see Appendix C.5). We performed calculations assuming the SED is a power-law extending from the UV (or 1 Ryd ∼13.6 eV) to hard X-rays (or 10^4 Ryd ∼100 keV). For our calculations we assume SEDs with two different values of the power-law photon index. A "soft" ($\Gamma = 2.1$) and a "hard" ($\Gamma = 1.7$) SED (see Figure 4.10). For each SED we calculated the continuum ($M_{\rm C}$) and the line ($M_{\rm L}$) components of the force multiplier. M_L depends on an additional parameter, t, [20] which is commonly referred to as the "effective electron optical depth" and encodes the dynamical information of the wind in the radiative acceleration calculation (see Appendix C.5). For our calculations we have assumed log $t = -7$. In Figure 4.11 we show the $M_{\rm C}$ and $M_{\rm L}$ components of the force multiplier as a function of the ionization parameter for the soft and hard SED cases. Our simple ionized absorber model indicates that an increase of the photon-index from 1.7 to 2.1 of the incident spectrum will result in a large increase of the force multiplier. This result is consistent with the possible trend between Γ and v_f shown in Table 4.2 and Figure 4.8.

Theoretical models of AGN outflows (e.g., Murray et al. 1995; Chelouche & Netzer 2003) and our observations of APM 08279+5255 suggest that the UV BAL gas could be shielded from the driving radiation by an absorbing medium surrounding the central source. We included the effect of such a shield on our calculated values of the force multiplier by assuming that the soft and hard SEDs are attenuated by a shield with log $(N_{\rm H}/{\rm cm}^{-2}) = 23$ and ionization parameter on its illuminated face of log $\xi_{\rm sh} = 1.6$

[20] The dimensionless optical depth is $t = n_e \sigma_T v_{\rm th}/(dv/dr)$, where, $n_{\rm e}$ is the electron number density, $\sigma_{\rm T}$ is the Thomson cross section and $v_{\rm th}$ is the thermal velocity of the gas. The line force multiplier increases with decreasing t.

(see Figure 4.10). As shown in the left panel of Figure 4.11, $M_{\rm C}$ decreases for a shielded SED and for log $\xi \lesssim 2$, whereas, $M_{\rm L}$ increases for an absorbed SED. We find that $M_{\rm L}$ increases by almost an order of magnitude for absorbed SEDs and when the photon index increases from 1.7 to 2.1. In Figure 4.11 we show that in addition to the SED and t parameter, the force multiplier depends strongly on the ionization parameter. In Figure 4.11 (left panel) the force multiplier for a shielded outflow drops from about 1000 to 500 between log ξ of 2–2.8 and drops from about 500 to 1 between log ξ of 2.8–3, i.e., similar to the observed range of the ionization parameter of APM 08279+5255. We expect that we observe the ionized X-ray absorber of APM 08279+5255 while it has obtained its terminal velocity. The observed large value of the ionization parameter of APM 08279+5255 may therefore not be representative of the ionization parameter during the initial acceleration phase of the absorber.

4.4.3 The dependence of the force multiplier on the photon index and $\alpha_{\rm ox}$ for a Mathews-Ferland SED.

We note that our assumption that the driving force on the high-energy absorbers is produced primarily by X-rays is plausible since the short term variability time-scale of the X-ray BALs of APM 08279+5255 suggests a launching radius of $\lesssim 10R_{\rm S}$ (e.g, Chartas et al. 2002, 2009a; Saez et al. 2009; this work) and recent studies of AGN employing the microlensing technique indicate that the X-ray emission region of the hot corona in AGNs is compact with a half-light radius of a few $R_{\rm S}$ and their UV regions are roughly a factor of ten larger (e.g., Morgan et al. 2008; Chartas et al. 2009a). Therefore UV radiation is not expected to contribute initially at small radii to driving the X-ray absorbing outflow. However, as the outflowing absorber gets further away from the source the contribution of the UV photons to the driving force will increase relative to that of the X-ray photons. To investigate the driving mechanism of the wind we calculated the force multipliers for SEDs that extend to radio wavelengths and estimated the effect of changes in Γ. For our simulations we used a standard and a slightly modified version of the Mathews-Ferland SED (Mathews & Ferland 1987).

The standard Mathews-Ferland SED is characterized by $\alpha_{\rm ox} = -1.41$ and by a power-law spectral index of $\alpha_X = -0.7$ ($\Gamma = 1.7$) which extends from 27 Ry ($\sim$0.36 keV) to 7.4×10^3 Ry ($\sim$100 keV). The modified Mathews-Ferland SED is similar to the standard one but with $\alpha_X = -1.1$ and $\alpha_{\rm ox} = -1.52$ (see Figure 4.12 to see the different SEDs used).

In the left panel of Figure 4.13 we show that for low ionization parameters (log $\xi \lesssim$ 2) the UV dominates the driving of the wind, therefore in this regime there is no major change in the force multipliers when we compare the soft and hard Mathews-Ferland SEDs. However at log $\xi \gtrsim 2$, the line force multipliers for the soft Mathews-Ferland SED case are larger than those for the hard SED case. This effect is produced because in the case of a Mathews-Ferland SED with a soft X-ray spectrum ($\Gamma = 2.1$) the outflowing gas does not become very ionized at high levels of the ionization parameter compared to the case of a Mathews-Ferland SED with a hard X-ray spectrum ($\Gamma = 1.7$). We conclude that an ionizing source that is relatively soft in the X-ray band will result in a force multiplier that remains relatively large even at ionization levels of the outflowing

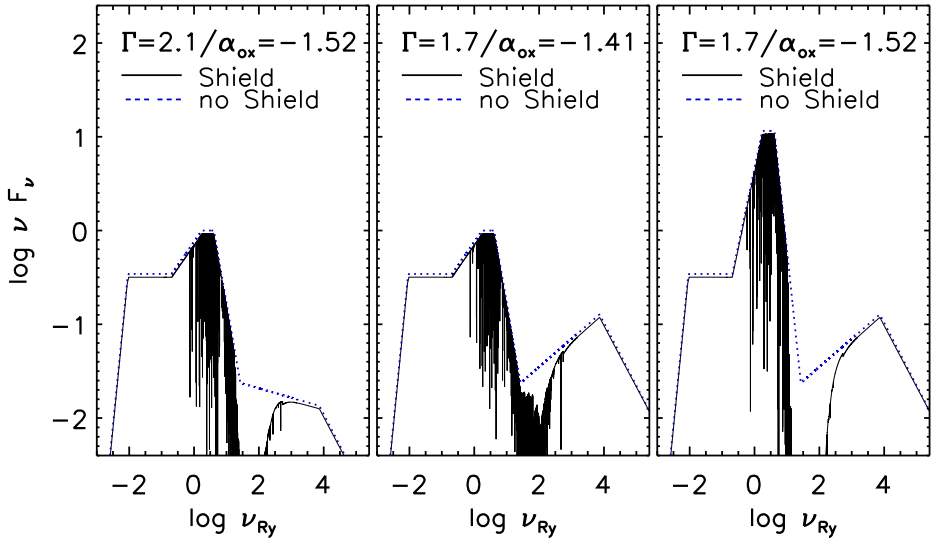

Fig. 4.12 Modified Mathews-Ferland SEDs used to calculate force-multipliers in §4.4.3. The x-axis is the logarithm of frequency (in Ry units) and the y-axis is in units of the logarithm of the flux times the frequency (arbitrary units). The left and right panels correspond to two modified versions of the Mathews-Ferland SED. In the left and right panels $\Gamma = 2.1$ and $\Gamma = 1.7$ with $\alpha_{ox} = -1.52$. The middle panel corresponds to the standard Mathews-Ferland SED, i.e. $\Gamma = 1.7$ with $\alpha_{ox} = -1.41$. In each panel the dotted line is the unabsorbed SED and the solid line is the shielded SED (with $\log \xi_{sh} \sim 2.9$).

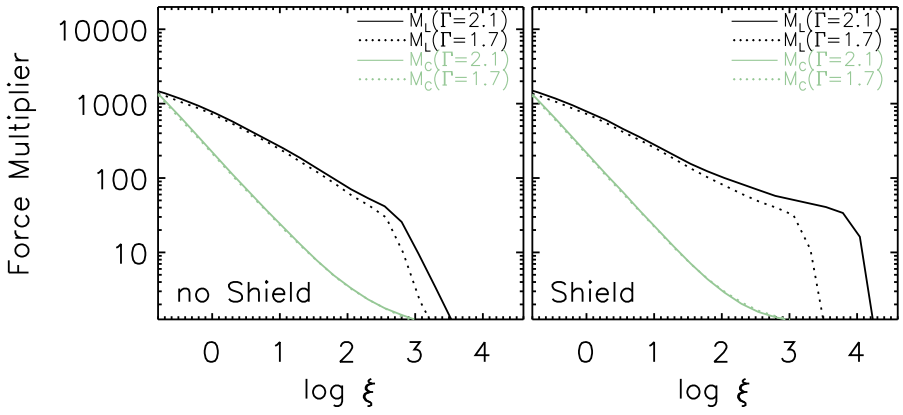

Fig. 4.13 The bound-free, M_C, and bound-bound, M_L, components of the force multiplier are shown as a function of the ionization parameter. Force multipliers are calculated for Mathews-Ferland SEDs with photon indices of $\Gamma = 2.1$ (solid lines) and $\Gamma = 1.7$ (dotted lines). In the left panel we have assumed no absorbing shield, whereas, in the right panel the soft and hard SEDs have been attenuated by a warm-absorber shield with $\log (N_H/\mathrm{cm}^{-2}) = 23$ and $\log \xi_{sh} = 2.9$ on its illuminated face. The SEDs used are described by the middle and right panels of Figure 4.12.

absorber of $\log \xi \gtrsim 3$. This prediction is consistent with the observed correlation of maximum outflow velocity with the X-ray photon index.

We modified the SEDs by including a warm-absorber shield with $\log (N_{\rm H}/{\rm cm}^{-2}) = 23$ and $\log \xi_{\rm sh} = 3.1$ (Figure 4.13 right panel; see also Figure 4.12 to see the shielded SED). The main effect of including a shield is a larger increase of the line force multipliers for the soft SED case ($\Gamma = 2.1$) compared to the increase produced by the hard SED case ($\Gamma = 1.7$) for $\log \xi \gtrsim 2$. We also find that by including a shield we obtain large line force multipliers at ionization levels that are larger than the ones possible with no shield present. This effect is especially important in the soft SED case.

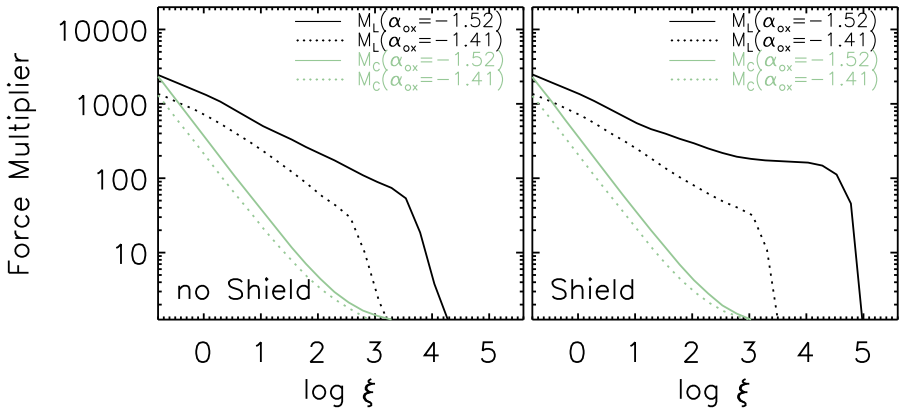

Fig. 4.14 The bound-free, $M_{\rm C}$, and bound-bound, $M_{\rm L}$, components of the force multiplier are shown as a function of the ionization parameter. Force multipliers are calculated for a Mathews-Ferland SED with $\alpha_{\rm ox} = -1.52$ (solid lines) and $\alpha_{\rm ox} = -1.41$ (dotted lines); in both SEDs $\Gamma = 1.7$. In the left panel we have assumed no absorbing shield, whereas, in the right panel the soft and hard SEDs have been attenuated by a warm-absorber shield with $\log (N_{\rm H}/{\rm cm}^{-2}) = 23$ and $\log \xi_{\rm sh} = 2.9$ on its illuminated face. The SEDs used are described by the middle and left panel of Figure 4.12.

In the process of changing the X-ray photon index from the default value of $\Gamma = 1.7$ (hard-spectrum) to $\Gamma = 2.1$ (soft spectrum) in the Mathews-Ferland SED, we also changed $\alpha_{\rm ox}$ from -1.41 to -1.52. To test the sensitivity of the force multiplier to changes of the $\alpha_{\rm ox}$ of the SED, we estimated the force multiplier for the case where $\alpha_{\rm ox}$ changed while the X-ray spectral slope remained constant. In order to produce this effect we increased the blue bump of the Mathews-Ferland SED by changing the default value of $\alpha_{\rm ox}$ from -1.41 to -1.52 (to see the SEDs used see Figure 4.12). As shown in the left panel of Figure 4.14 the force multiplier is more sensitive to $\alpha_{\rm ox}$ than Γ. This difference in sensitivity is associated with the fact that the UV covers the range where most of the absorption lines lie. We also modified the SEDs by including an absorbing shield with $\log (N_{\rm H}/{\rm cm}^{-2}) = 23$ and $\log \xi_{\rm sh} = 3.1$ (see Figure 4.12). In the right panel of Figure 4.14 we show that the effect of adding this warm-absorber shield is an increase of the force multiplier for soft SEDs even at high ionization levels.

We note that we used a moderate amount of shielding for the estimates shown in the left panels of Figures 4.11, 4.13 and 4.14. The combination of moderate attenuation and high force multipliers in this type of shield is expected to produce high velocity outflows (Chelouche & Netzer 2003). If we use an absorbing shield with a relatively low ionization level we find that the large absorption from the shield will attenuate a large fraction of the UV and X-ray photons, and therefore prevent the outflow from reaching high terminal velocities.

In general, the presence of an absorbing shield will increase the differences between the line force multipliers for the soft and hard SED cases. These differences will be important for shields with ionization parameters in the range of $1.0 \lesssim \log \xi_{\rm sh} \lesssim 1.8$ for the power-law SED case and will be important for shields with ionization parameters in the range of $1.2 \lesssim \log \xi_{\rm sh} \lesssim 3.1$ for the Mathews-Ferland SED case (see Appendix C.6). For values of the ionization parameter of the shield over these boundaries, the shield will be transparent to incident radiation and the force multipliers will be similar to ones with no shield present (left panels of Figures 4.11, 4.13 and 4.14). For values of $\log \xi_{\rm sh} \lesssim 1.0$ the large absorption produced by the shield will result in a weak outflow (see, Chelouche & Netzer 2003).

If the $\Gamma - v_f$ trend is confirmed with additional observations we plan to produce a more sophisticated model that will include more realistic kinematic, ionization and absorption properties of the outflow. If the $\Gamma - v_f$ relation is real we would also like to know if the changes in Γ are accompanied by changes of α_{ox}. Studies of correlations between outflow properties and the SED of the ionizing source will provide crucial information regarding the driving mechanism of the outflow. Simultaneous multiwavelength observations of sources such as APM 08279+5255 that show fast outflows will therefore be essential for the study of quasar outflows.

4.5 Conclusions

We have analyzed 8 long exposure X-ray observations of APM 08279+5255 (2 *Chandra*, 3 *XMM-Newton*, and 3 *Suzaku*), and in each observation we have found X-ray BALs that have been detected at a high level of significance. Our analysis of the X-ray observations of the BAL quasar APM 08279+5255 indicates strong and broad absorption at rest-frame energies of $1 - 4$ keV (low-energy) and $7 - 18$ keV (high-energy). The medium producing the low-energy absorption is a nearly neutral absorber with a column density of $\log (N_{\rm H}/{\rm cm}^{-2}) \sim 23$. The medium producing the high-energy absorption appears to be outflowing from the central source at relativistic velocities (between $0 - 0.7c$) and with a range of ionization parameters ($3 \lesssim \log \xi \lesssim 4$). The maximum detected projected outflow velocity of $\sim 0.7c$ constrains the angle between our line of sight and the wind direction to be $\lesssim 22^{\circ}$. The short time-scale variability ($\lesssim$ week in the rest-frame) of the high-energy absorption implies that X-ray absorbers are launched from distances of $\sim 10 R_S$ from the central source (where R_S is the Schwarzschild radius).

Simulations of highly-ionized near-relativistic winds indicate that the resulting X-ray broad absorption profile may have the apparent shape of an absorption edge, a notch, or a combination of absorption lines depending on the assumed dynamics and degree of ionization of the outflowing absorbers. We have used these simulations with

the photoionization code CLOUDY to generate XSPEC table models of near-relativistic quasar outflows. By fitting this quasar outflow model to several deep X-ray observations of APM 08279+5255 we recalculate the parameters describing the dynamics of the X-ray outflow, among them, its minimum velocity, maximum velocity, ionization level and column density. We confirm most of the results already found in Saez, Chartas & Brandt (2009) and Chartas et al. (2009a). We also confirm the trend between the photon index (Γ) and the maximum projected outflow velocity ($v_{\rm max}$); i.e. softer X-ray spectra generate larger outflow terminal velocities. We also find that the total column density ($N_{\rm H}$) of the outflow increases with Γ. The trends of $v_{\rm max}$ versus Γ and $N_{\rm H}$ with Γ suggest that the wind becomes more powerful as the incident spectrum becomes softer. This tendency is confirmed through estimates of the efficiency of the wind. Additionally, we estimate that a significant fraction (>10%) of the total bolometric energy over the quasar's lifetime is injected into the intergalactic medium of APM 08279+5255 in the form of kinetic energy.

In this work we modeled the spectrum of the central ionizing source with a power-law SED and with Mathews-Ferland SEDs and found that variations of the X-ray and UV parts of the SEDs will produce important changes in the strength of the radiative driving force. These results support the observed trend found between the outflow velocity and X-ray photon index in APM 08279+5255. In general we find as expected that the presence of a moderate absorbing shield results in more powerful outflows (Chelouche & Netzer 2003). Specifically, we find that shields with column densities of $\log\,(N_{\rm H}/{\rm cm}^{-2}) \sim 23$, covering an optically thin outflow, provide a significant increase in the driving force when their ionization parameters are in the range of $1.0 \lesssim \log\,\xi_{\rm sh} \lesssim 1.8$ for the case of a power-law SED and in the range of $1.2 \lesssim \log\,\xi_{\rm sh} \lesssim 3.1$ for the case of a Mathews-Ferland SED. Therefore the strength of the radiative driving force depends critically on both the column density of the shield and its ionization level. A confirmation of the results found in our simulations of quasar outflow will require new deeper X-ray multi-wavelegth observations of quasars that contain clear signs of fast outflow. Such observations will allow us to correlate the properties of the outflow with properties of the SED and thus test our predictions.

Chapter 5

Conclusions and future work.

5.1 Conclusions

In this work we took two different approaches to study AGN evolution. In the next two sections, I describe the most important conclusions of each one of these lines of study. In the last section of this chapter I present possible future projects that can be developed to follow up this work.

5.1.1 Main conclusions resulting from our X-ray spectral study of AGNs in the *Chandra* deep fields

In a sample of ~ 200 radio-quiet AGNs from the CDF surveys with moderate-to-high S/N we found strong evidence of a correlation between the X-ray spectral parameters Γ and $L_{\rm X}$. The slope and offset of a linear fit to the $\Gamma - L_{\rm X}$ relation possibly evolves for sources with $z > 0.1$. Analyzing this relation in three different redshift bins that contain a similar number of sources ($\sim$50) we conclude that this correlation is highly significant in two redshift bins, $0.3 \lesssim z \lesssim 0.96$, and $1.5 \lesssim z \lesssim 3.3$ and slightly less significant in the redshift bin $0.96 \lesssim z \lesssim 1.5$. The $\Gamma - L_{\rm X}$ correlations in $0.3 \lesssim z \lesssim 0.96$ and $1.5 \lesssim z \lesssim 3.3$ are significant at the >99.9% confidence level for fits performed in the 0.5–8 keV observed-frame and at the >99.5% confidence level in the 2–10 keV rest-frame. These correlations indicate a softening of the X-ray spectra of AGNs as their X-ray luminosity increases. The $\Gamma - L_{\rm X}$ correlation found in the redshift range of $1.5 \lesssim z \lesssim 3.3$ confirms a previous independent study of RQQ at $z > 1.5$ (Dai et al. 2004). The fact that this correlation is also present when we estimate the luminosities in the 2–10 keV rest-frame, and also holds for sources with low column densities, suggests that this correlation is not artificially driven by any un-modeled complexity in the intrinsic absorption ($N_{\rm H}$). We also conclude that a Compton-reflection component is unlikely driving the $\Gamma - L_{\rm X}$ correlation found in this study.
We presented two steady-corona models (Haardt et al. 1997; Merloni & Fabian 2001) that can explain the $\Gamma - L_{\rm X}$ correlation found in this work. Based on these models, we proposed two different interpretations to explain the correlation and its possible evolution with z. The first interpretation posits that this relation is driven by changes in the Eddington ratio for a population of AGNs of similar mass. The second interpretation posits that the relation is driven by changes in the black-hole mass of the AGNs. The evolution is probably driven by parameters that control the coronal emission; among them are the corona opacity, the black-hole mass and the accretion rate.

Since we have used the most sensitive X-rays surveys to date to determine the $\Gamma - L_{\rm X}$ correlation any future attempts to confirm and extend these results will require

the study of X-ray surveys of AGNs that are deeper and that cover a greater field of view than the ones currently available (see e.g. §5.2.1.1).

5.1.2 Main conclusions from the study of the X-ray BAL outflow of APM 08279+5255

We have analyzed 8 deep X-ray observations of APM 08279+5255 (2 *Chandra*, 3 *XMM-Newton*, and 3 *Suzaku*), and in each observation we have found X-ray BALs that have been detected at a high level of significance.[1] Our analysis of the X-ray observations of the BAL quasar APM 08279+5255 indicates strong and broad absorption at rest-frame energies of $1-4$ keV (low-energy) and $7-18$ keV (high-energy). The medium producing the low-energy absorption is a nearly neutral absorber with a column density of $\log\,(N_{\rm H}/{\rm cm}^{-2}) \sim 23$. The medium producing the high-energy absorption appears to be outflowing from the central source at relativistic velocities (between $0-0.7c$) and with a range of ionization parameters ($3 \lesssim \log\,\xi \lesssim 4$). The maximum detected projected outflow velocity of $\sim 0.7c$ constrains the angle between our line of sight and the wind direction to be $\lesssim 22^{\circ}$. The short time-scale variability ($\lesssim$ week in the rest-frame) of the high-energy absorption implies that X-ray absorbers are launched from distances of $\sim 10R_S$ from the central source (where R_S is the Schwarzschild radius).

In this thesis we have also generated a new outflow model with the photoionization code CLOUDY to generate absorption profiles of near-relativistic quasar outflows. By fitting this quasar outflow model to several deep X-ray observations of APM 08279+5255 we recalculate the parameters describing the dynamics of the X-ray outflow, among them, its minimum velocity, maximum velocity, ionization level and column density. Using this model we confirm the trend between the photon index (Γ) and the maximum projected outflow velocity ($v_{\rm max}$) found in Chartas et al. (2009a); i.e. softer X-ray spectra generate larger outflow terminal velocities. We find that the total column density ($N_{\rm H}$) of the outflow increases with Γ. The trends of $v_{\rm max}$ versus Γ and $N_{\rm H}$ with Γ suggest that the wind becomes more powerful as the incident spectrum becomes softer. This tendency is confirmed through estimates of the efficiency of the wind. We estimate that a significant fraction (>10%) of the total bolometric energy over the quasar's lifetime is injected into the intergalactic medium of APM 08279+5255 in the form of kinetic energy. We have also modeled the spectrum of the central ionizing source with a power-law SED and with Mathews-Ferland SEDs and found that variations of the X-ray and UV parts of the SEDs will produce important changes in the strength of the radiative driving force. These results support the observed trend found between the outflow velocity and X-ray photon index in APM 08279+5255.

In order to gain a better understanding of the driving mechanism controlling the dynamics of the wind of APM 08279+5255, additional deep X-ray observations of this source are required with simultaneous optical-UV observations. A description of future projects aimed at better discerning the driving mechanism of the fast outflow of APM 08279+5255 is provided in §5.2.2.

[1] Notice that in chapter 3 we provide a detailed analysis on the three *Suzaku* observations.

5.2 Future work

In this section we propose two studies aimed at extending the research presented in this thesis: §5.2.1.1 describes a study that will extend the work presented in chapter 2, and §5.2.2 presents a study to follow-up on work presented in chapters 3 and 4.

5.2.1 A study of the X-ray evolution of AGNs

The correlation found in chapter 2 is probably produced by changes in the physical parameters controlling the emission of the corona. Among one of the possible drivers controlling the X-ray spectral slope-luminosity correlation is the Eddington ratio, which is a measure of how quickly the black hole is growing. The study presented in chapter 2 provides tight constraints on moderate luminosity AGNs but provides limited information on the most luminous AGNs (the ones with the largest accretion-rates) and no constraints on the growth of black holes in over-dense regions. Black holes in over-dense regions of the Universe (galaxy clusters/protoclusters) are believed to have grown earlier in the Universe than the typical objects studied in chapter 2 (e.g., Lehmer et al. 2009; Martini, Sivakoff & Mulchaey 2009). Therefore we might expect a different X-ray spectral slope-luminosity relation for AGNs in galaxy cluster/protocluster environments than the one found in chapter 2. This project will address the following questions: Is the X-ray spectral slope-luminosity correlation applicable to all environments? What is the driving parameter of the correlation found?

5.2.1.1 Placing tighter constraints on the X-ray spectral shape vs luminosity correlation

The plan is to expand the distance-luminosity plane included in our AGN survey to include moderate-to-high S/N ratio X-ray spectra of AGNs in the wider-area C-COSMOS, the Extended CDF-S, the Groth Strip, the Extended Groth Strip, and Bootes deep-field surveys. A key extension will also be the utilization of the recently approved 4Ms CDF-S observations. The increase in the present sample size will allow us to test the correlation in narrower redshift bands and higher luminosities/black-hole mass than in our previous study. We will also seek to determine the driving parameter of the X-ray spectral slope-luminosity correlation by splitting the sample into bins of black-hole mass and Eddington ratio. We will estimate black-hole masses for a fraction of our sample using the virial method based on Hβ and/or MgII broad emission lines, and we will provide basic black-hole mass constraints using host-galaxy masses for the remainder of the sample.

5.2.1.2 Evolution of AGNs in dense environments

AGNs evolve differently in the field compared to galaxy clusters/protoclusters environments, indicating that the environment plays a significant role in the growth of black holes. We will explore the X-ray spectral slope-luminosity relationship in over-dense regions. The cluster sample will be extracted from the COSMOS and ChaMP surveys. In the first 36/55 pointings of the COSMOS survey there are 72 X-ray confirmed

clusters (Finoguenov et al. 2007). In the ChamP survey there are 100 optical clusters (Barkhouse et al. 2006). The protocluster sample will come from the SSA22 field (Lehmer et al. 2009) and the archived Chandra observations of the HS 1700+643 field (Steidel et al. 2005). Using several criteria to discriminate AGNs from other extragalactic sources (e.g., Bauer et al. 2004a) we will catalog the AGNs in the galaxy clusters and protoclusters. For sources with good spectral quality data we will constrain the X-ray spectral parameters and compare our results to those predicted by the X-ray slope-luminosity correlation.

5.2.2 The X-ray BAL outflows of APM08279+5255

APM08279+5255 is a distant (z=3.91) BAL AGN that is unusually bright due to gravitational lensing (appear ∼100 brighter than it normally would), providing the exceptional opportunity to study it with high-quality spectral data. High-energy absorption features in the X-ray spectra of APM 08279+5255 detected in past observations have been interpreted as arising from a near-relativistic outflow. The observations of this AGN are particularly important because they allow us to probe AGN outflows at an epoch when black holes were most active. From these features we extracted the ionization state, velocity and column density of the AGN wind. I propose to extend my work to answer the following question: what is the driving force of the observed X-ray fast winds? In Chartas et al. (2009a) and chapter 4, we found that flatter X-ray spectra appear to result in lower outflow velocities. If this trend is confirmed it would likely imply that the acceleration mechanism responsible for the near-relativistic velocities of the X-ray outflowing gas in BAL AGNs is radiative driving by the corona. However, it will be interesting to study whether changes in the X-ray spectral shape are also correlated with changes in the disk emission, which is strong in optical/UV. Currently there are 8 deep X-ray observations of APM08279+5255, 3 with *XMM-Newton*, 2 with Chandra and 3 with Suzaku. For one of the *XMM-Newton* and one of the *Chandra* observations I have simultaneous rest-frame UV (HET) observations that I will use to compare the maximum UV (C IV lines) and X-ray outflow velocities and search for flux variability and energy variability of the broad absorption lines. Also using the optical monitor data of the *XMM-Newton* observations I will explore possible correlations of the rest-frame UV with the X-ray spectral slope. I also plan to propose for additional X-ray deep observations of APM08279+5255 with simultaneous rest-frame optical/UV observations (e.g, HET, HST or VLT) to extend the variability baseline to longer durations. Finally, I will also search for evidence of AGN outflows in the high S/N observations compiled in §5.2.1.1.

Appendix A

Appendix to chapter 2

A.1 An example of a spectral fit for a source with absorption

In this appendix we present spectral fits using a PL (XSPEC notation WABS*POW) model and a APL (XSPEC notation WABS*ZWABS*POW) model for the CDF-N AGN CXOJ123719.86+620955.3. This source (at $z = 2.64$), which will be used in this appendix as an example, shows absorption and at the same time has ~ 440 counts in the 0.5–8 keV observed-frame which is close to the average of our sample. We performed spectral fits in the 0.5-8 keV observed-frame band using the χ^2-statistic, with a grouping of 10 counts per bin. From the best-fits using the PL and APL [1] we find that $\chi^2_{PL}/\nu = 66.3/43$ and $\chi^2_{APL}/\nu = 33.8/42$. Therefore the improvement of the APL model over the PL model in this source at the $> 99.99\%$ (null probability 1.2×10^{-7} when we use the F-test). In Figure A.1 we show the fits and residuals of the spectra of CXOJ123719.86+620955.3 using a PL and an APL model. The improvement on the fits when we use the APL over the PL model can be seen clearly in the residuals.

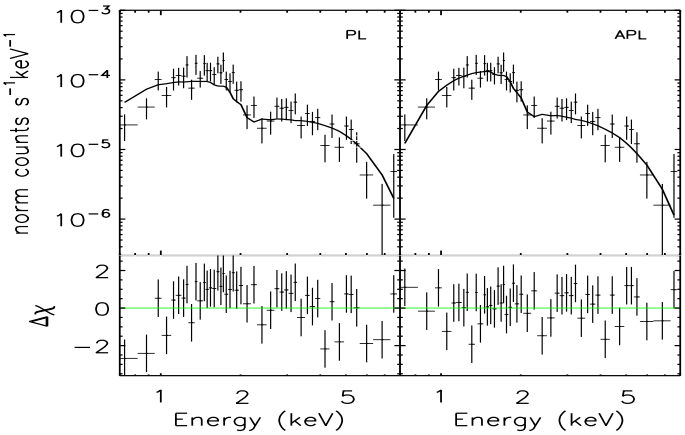

Fig. A.1 Spectra of the CDF-N source CXOJ123719.86+620955.3, fit with PL (upper left panel) and APL (upper right panel) model. In the lower panels, we show the $\Delta\chi$ residuals; the grouping is 10 counts per bin.

[1] Notice that the best-fitted parameters using a APL model are $\Gamma = 1.69^{+0.16}_{-0.12}$ and $N_{\rm H} = 13.8^{+4.2}_{-2.6}$ which is in agreement to the APL best-fitted parameters of this source using C-Statistics (see electronic version of Saez et al. 2008 for details).

Appendix B

Appendix to chapter 3.

B.1 Modified version of Figure 3.2

The equivalent width of a gaussian absorption (model ZGAUSS of XSPEC) line superposed on a power law continuum can be obtained from

$$W_A \approx \frac{N}{K}\left(\frac{E_L}{(1+z)\ \mathrm{keV}}\right)^{\Gamma} \tag{B.1}$$

were N and E_L are the total number of photons and energy of the gaussian line, K and Γ are the flux density of photons at 1 keV and the photon index of the power law spectrum, and z is the redshift of the source. Notice that N, K and E_L are directly obtained from the fits in the case of the APL+2AL model in §3.3 and therefore the contour plots in the W_A versus line energy of the line at $\sim$ 8 keV rest-frame can be obtained from the contour plots of Figure 3.2. In Figure B.1 we show the χ^2 confidence contours of the equivalent width of the first absorption line (line at $\sim$ 8 keV rest-frame in the APL + 2AL model) versus the best-fit energies in epoch OBS2 (solid line) and in epoch OBS3 (dotted line). The contour plots of Figure B.1 are analogous those found in Figure 3.2.

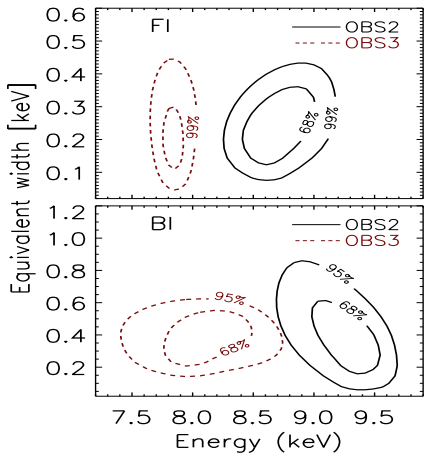

Fig. B.1 Confidence contours of absorption-line equivalent width versus absorption-line energies of the absorption line at rest-frame energies $\sim$ 8 keV (model 7, Table 3.3). The upper and lower panel contours correspond to fits performed to the FI and BI spectra, respectively. The contour plots are at the 68% and 99% level of significance in the upper panel and at the 68% and 95% level of significance in the lower panel. Solid and dotted lines are contours for epochs OBS2 and OBS3, respectively.

Appendix C

Appendix to chapter 4.

C.1 Ionization parameter.

There are two definitions of the ionization parameter that are broadly used in the scientific literature. The first definition, which will be mostly adopted in this work, is the ionization parameter of Tarter, Tucker & Salpeter (1969) given by

$$\xi = \frac{L_{\rm I}}{n_{_H} r^2} = \frac{4\pi}{n_{_H}} \int_{\rm 1Ry}^{\rm 1000Ry} F_{_\nu} d\nu = \frac{4\pi F_{_I}}{n_{_H}}, \tag{C.1}$$

where $L_{_I}$ is the ionizing luminosity, $F_{_I}$ is the ionizing flux, $F_{_\nu}$ is the incident flux, $n_{_H}$ is the hydrogen density, and r is the source-cloud separation. A second definition of the ionization (Davidson 1977) parameter is given by the ratio of photons that can ionize hydrogen to the number of hydrogen atoms in a spherical layer at a distance r from an illuminating point source, i.e.,

$$U = \frac{Q}{4\pi r^2 c n_{_H}} \quad , \text{where} \quad Q = \int_{\rm 1Ry}^{\infty} \frac{L_{_\nu}}{h\nu} d\nu. \tag{C.2}$$

We note that for a pure power law (i.e., $F_{_\nu} \propto \nu^{^\alpha}$), the analytic expressions to convert between ξ and U are,

$$\log \xi = \begin{cases} \log U + 1.754 & \alpha = -1 \\ \log U + 0.914 + \log\left(-(1000^{\alpha+1} - 1)\frac{\alpha}{\alpha+1}\right) & \alpha \neq -1 \end{cases} \tag{C.3}$$

C.2 When can an absorption slab be considered thin?

The fraction of flux absorbed in the rest-frame of a layer of gas depends on the ionization state of the absorber, its column density, and the SED of the illuminating source. Our quasar outflow code calculates the absorption profiles resulting from absorption of the central source spectrum by ionized gas in an accelerated outflow. One of the assumptions of our quasar outflow model is that the absorption layer producing the observed X-ray BALs has a plane-parallel geometry with a thickness that is much smaller than the distance from the central source[1]. We therefore expect any decrease in the ionization parameter across an absorbing layer to be predominantly due to the

[1] Let's assume a relatively faint AGN with $L_{_I} \sim 10^{42}$erg s^{-1} with an absorbing layer of log $(N_{\rm H}/{\rm cm}^{-2}) = 22$, $n_{_H} = 10^{8}{\rm cm}^{-3}$, and an ionization parameter of log $\xi = 3$ on the illuminated side of the layer. Since $\xi = L_{\rm I}/(nR^2)$,

absorption of the flux in the layer rather than to the $1/R^2$ decrease of the ionization parameter.

We will refer to a layer as optically thin if the change between the ionization parameter on the illuminated side and the dark side of the layer is less than 0.05 dex.[2]

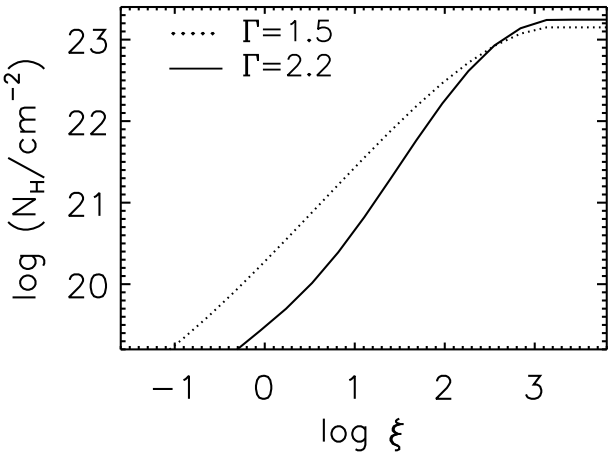

Fig. C.1 Limiting column density at which a layer will be considered thin. In this case we arbitrarily define a layer as thin when the ionization parameter decreases after crossing the layer less than 0.05 dex due to absorption. The solid and dotted lines represent a soft spectrum power-law ($\Gamma = 2.2$) and hard power-law spectrum ($\Gamma = 1.5$), respectively. Both spectra are defined between 1 Ry and 10^4 Ry

In Figure C.1 we show the column density of a thin layer that will produce a decrease of 0.05 dex of the ionization parameter across this layer as a function of the ionization parameter at the front surface of the layer. We plot this relation for power-law SEDs with a photon index of $\Gamma = 1.5$ (dotted line) and with $\Gamma = 2.2$ (solid line). The results show that the upper limit of the column density of an absorbing layer required for this layer to be considered thin, increases with ionization parameter. Soft spectra have lower thresholds than hard spectra, especially for low values of the ionization parameter ($\log \xi \lesssim 2$). However, for highly ionized media the threshold of the soft and hard spectra are similar, in particular for ($\log \xi \gtrsim 3$) the limiting column density is $\log (N_{\rm H}/{\rm cm}^{-2}) \sim 23$.

$R \sim 3{\times}10^{15} n_8^{-1/2}$ cm; therefore $\Delta R/R \sim 0.3\, n_8^{-3/2}$. Since this is an extreme case (faint AGN and highly ionizated layer), in general we expect $\Delta R/R \ll 0.1$.

[2] If we define ξ_i and ξ_f as the ionization parameters at the illuminated front and back sides of the layer, respectively, then our definition of a thin layer can be written as $\log (\xi_f/\xi_i) < -0.05$. In addition if we assume that the incident flux on layer is F_ν, we have that $\log (\xi_f/\xi_i) = \log(\int_{\nu_0}^{\nu_1} F_\nu e^{-\tau_\nu} d\nu / \int_{\nu_0}^{\nu_1} F_\nu d\nu) \sim \log(1 - \langle\tau\rangle) \sim -\langle\tau\rangle/\ln 10$, where $\nu_0 = 1$ Ry, $\nu_1 = 1000$ Ry and $\langle\tau\rangle$ is the average opacity through the layer between ν_0 and ν_1. Therefore, our definition of a thin layer is equivalent to a layer with an average opacity of $\langle\tau\rangle \lesssim 0.1$.

C.3 Near-relativistic quasar outflow code: assuming an outflow with a constant $\Delta v'$ between layers

Since our library of CLOUDY simulations was generated for a specific turbulent velocity we adjusted the relative speed between layers i and $i+1$ to be constant (i.e. $\Delta v_i^{'} = (v_{i+1} - v_i)/(1 - v_i v_{i+1}/c^2)$ constant). Assuming N_l layers, we initialize the parameters defining our profile by: 1) Deriving the velocity profile, which satisfies $v_0 = 0$; $v_{nl} = v_f$ ($\Delta v_i^{'} = \Delta v^{'}$). 2)Deriving $N_{\mathrm{H}i}$ (i=0,..,N_l) through the use of ${N_{\mathrm{H}}}_{i+1}^{p} - {N_{\mathrm{H}}}_{i}^{p} = \Delta v_i/k$; this result comes from $v(N_{\mathrm{H}}) = v_0 + k{N_{\mathrm{H}}}^{p}$ ($k = (v_f - v_0)/{N_{\mathrm{H}}}_{T}^{p}$ and $N_{\mathrm{H}T}$ is the total column density of the outflow). Using the last expression we calculate $N_{\mathrm{H}i}$ from $N_{\mathrm{H}i-1}$ starting from $N_{\mathrm{H}0} = 0$. 3) Calculating the average velocity $v_{mi} = (v(r_{i+1}) + v(r_i))/2$, the column density $\Delta N_{\mathrm{H}i} = N_{\mathrm{H}i+1} - N_{\mathrm{H}i}$, the density $n_i = n(v_{mi})$, (i=0,..,N_l-1) and the radial steps $\Delta r_i = \Delta N_{\mathrm{H}}/n_i$ of each layer.

We note that our assumptions are valid as long as $v_{turb} > \Delta v/\sqrt{12}$. In our simulations we chose $\Delta v_i \sim v_{\mathrm{turb}}$ and $v_{\mathrm{turb}} = 1500$ km s^{-1} $\sim 0.005c$. In the case of $v_{\mathrm{min}} = 0.1c$ and $v_{\mathrm{max}} = 0.7c$ we would have $N_l \sim 100$ layers.

C.4 Near-relativistic quasar outflow code: comparison with Schurch & Done (2007)

In this appendix we compare our quasar outflow code to a similar code presented in Schurch & Done (2007). The goal is to estimate the level of agreement between two independent quasar outflow codes and at the same time evaluate the limitations of each approach. We first generated absorption profiles for a linearly accelerated outflow ($p = 1$) with $v_{\mathrm{min}} = 0$, $v_{\mathrm{max}} = 0.3c$, $N_{\mathrm{H}} = 3 \times 10^{23}$ cm^{-2}, $n_0 = 10^{12}$ cm^{-3}, and values of log $\xi =$ 2.75, 3, 3.25, 3.5, 3.75 and 4. In order to make a fair comparison with the results of Schurch & Done (2007) we ran a large number of simulations using the photoionization code XSTAR and assumed a power-law model with $\alpha = -1.4$.

In each layer we subtract the absorption an add the emission. Since XSTAR does not include a "Compton scattered" component for the emission, we add this component in a similar way as the one described in Schurch & Done 2007. The Compton scattered emission component is obtained by calculating the Thompson scattered flux of each layer[3], where the incident spectrum is the output from the previous layer. Since in the case of Schurch & Done (2007) the calculations were made assuming spherical symmetry of the multilayer absorber, with covering fractions equal to one, we use similar assumptions to obtain the emission of each layer. We calculated the emission from a spherical shell by adding the spectral contribution from each solid angle of the layer. The emission from each solid angle of the shell is corrected for Doppler beaming of material outflowing at a projected velocity with respect to a fixed line of sight.

[3]The Thomson Scattered flux is the incident flux multiplied by $1 - e^{-\Delta N_{\mathrm{H}} \sigma_T}$ where ΔN_{H} is the column density of the layer σ_T is the Thomson cross section.

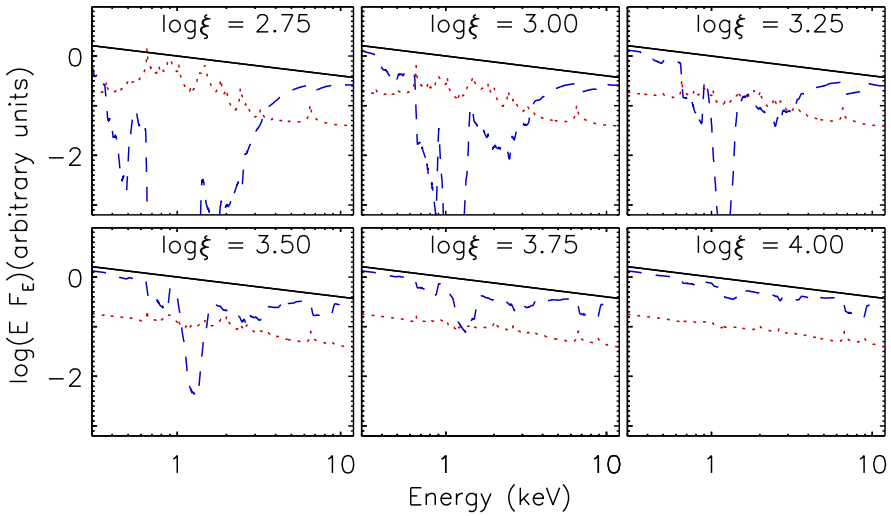

Fig. C.2 0.3-13 keV spectra of the incident (full-line), transmitted (dashed-line) and emitted (dotted-line) continua for different ionization levels of the outflowing material simulated with our quasar outflow code. In Panels 1-3 (Top, left to right) the ionization levels of the outflowing material are log ξ= 2.75, 3.0 & 3.25, respectively. In Panels 4-6 (Bottom, left to right) the ionization levels of the outflowing material are log ξ= 2.75, 3.0 & 3.25, respectively. For all these simulations the total number of layers is $N_l = 100$, the total column density of the outflowing material is $N_{\rm H} = 3 \times 10^{23}$ cm^{-2}, the initial gas density is 10^{12} cm^{-3} and the velocity of the outflow is assumed to vary linearly between 0 and 0.3 c. These results are in good agreement with those of Schurch & Done (2007) as evident from a comparison between this figure and their Figure 7.

The spectra of the incident, absorbed and emitted continua for each of the initial values of the ionization parameters used in these calculations of absorption line profiles are presented in the six panels of Figure C.2. We find a remarkable similarity of Figure C.2 with Figure 7 of Schurch & Done 2007. The small differences found in our results when compared to those of Schurch & Done (2007) are mainly associated with differences in the details of the calculations. Specifically, Schurch & Done 2007 pass the output flux from one layer to the other internally[4], while in our approach we perform separate photoionization runs from one layer to the next. Possibly an important factor that contributes to the discrepancies between the two codes is that in our calculations we approximate the incident flux on each layer as being the unabsorbed source SED. On the other hand, Schurch & Done (2007) use the absorbed SED to perform the photoionization calculations in each layer. We expect our approximation of using the unabsorbed source SED as incident on all layers to break down at low ionization levels where absorption through a layer may significantly change the SED. This explains why our results begin to noticeably differ from those of Schurch & Done (2007) at $\log \xi \lesssim 3$.

In Figure C.3 we plot the absorbed and emitted spectra in the energy range where we detect iron absorption ($\sim$7–9 keV) for three different values of the exponent of the p-type velocity profile, (see equation 4.3, §4.3) of $p = 5.0$, 1.0 and 0.2. For these comparison tests we set $v_{\rm min} = 0$, $v_{\rm max} = 0.3c$, $N_{\rm H} = 3 \times 10^{23}$ cm^{-2}, $n_0 = 10^{12}$ cm^{-3}, and $\log \xi = 3$. We find agreement between our code and that of Schurch & Done 2007 as shown in the comparison between the absorption and emission profiles presented in Figure C.3 and Figure 4 of Schurch & Done (2007). Our emission spectra for the case of a velocity profile with an exponent of $p = 5$ differs from those derived by Schurch & Done 2007 (see Figure 4 of Schurch & Done (2007)) mainly because in their simulations the turbulent velocity is set to be variable in order to model fine structures in the spectra. In our simulations we fix the turbulent velocity in the outflow, and therefore we are not able to reproduce fine details ($\lesssim 1500$ km s^{-1}) in the spectra. This is not a significant problem since we are mainly interested in simulating the broad absorption lines detected in the X-ray spectra of BAL quasars.[5]

We conclude that our quasar outflow code provides results that are very similar to those found in the independent code of Schurch & Done 2007 as long as the SED does not change significantly across the multilayer. For our study we have mostly selected quasar outflows of highly ionized material (i.e., $\xi \gtrsim 3.0$) and therefore expect the SED of the central source not to be significantly attenuated across the outflowing multilayer.

---

[4] In (Schurch & Done 2007) the authors use the same photon field XSTAR propagates internally, therefore their approach is consistent with a single, constant density, XSTAR run, in the absence of an external velocity field and constant gas density throughout the chain.

[5] A typical energy resolution of a X-ray telescope (at energies between 1−10 keV) is $\sim$ 100 keV, therefore for a Fe XXV Kα ($1s^2 - 1s2p$; 6.70 keV) line we will not be able to resolve features with Doppler broadenings $\lesssim 4000$ km s^{-1}.

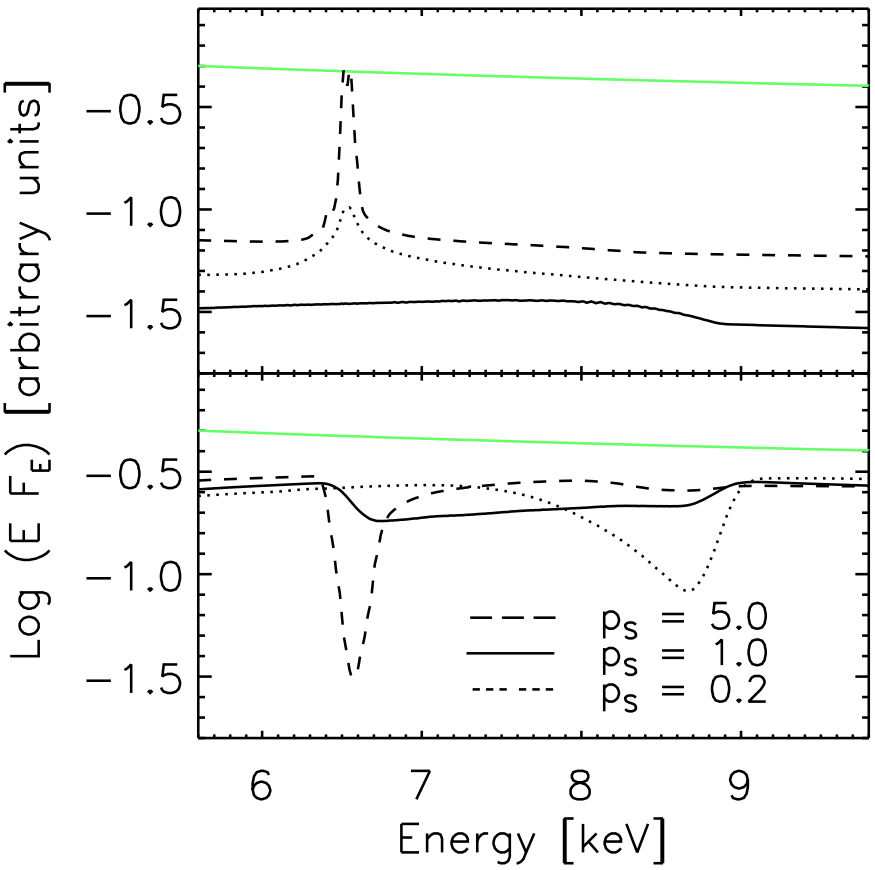

Fig. C.3 Emitted (upper panel) and absorbed (lower panel) spectra in the energy range where we detect iron absorption (∼7–9 keV) for three different values of the exponent of the p-type velocity profile, (see equation 4.3, §4.3) of $p = 5.0$, 1.0 and 0.2. For these comparison tests we set $v_{\rm min} = 0$, $v_{\rm max} = 0.3c$, $N_{\rm H} = 3 \times 10^{23}$ cm^{-2}, $n_0 = 10^{12}$ cm^{-3}, and log $\xi = 3$. We find agreement between our code and that of Schurch & Done 2007 as shown in the comparison between the absorption and emission profiles presented in Figure C.3 and Figure 4 of Schurch & Done (2007).

C.5 Force multiplier calculations

In this appendix we derive a formula for the force multiplier and compare our expression to ones reported in earlier studies (see e.g., Arav et al. 1994; Mihalas & Mihalas 1984).

C.5.1 Force multiplier calculation

For a medium that absorbs radiation, the force per unit volume on the medium is

$$f_v = \frac{1}{c}\int \alpha_\nu F_\nu d\nu, \tag{C.4}$$

where $\alpha_\nu(\mathrm{cm}^{-1})$ is the absorption coefficient and F_ν is the incident flux on the medium. Assuming that the flux originates from a point source with luminosity L_ν at $r = 0$ the acceleration is given by

$$\frac{dv(r)}{dt} = \frac{1}{4\pi r^2 \rho(r) c}\int \alpha_\nu L_\nu e^{-\tau_\nu} d\nu. \tag{C.5}$$

The factor $e^{-\tau_\nu}$ corresponds to the attenuation factor at radius r, ($\tau_\nu(r) = \int_0^r \alpha_\nu(r')dr'$). Assuming that the central source has a mass of M_s the force equation can be re-written as:

$$\frac{dv(r)}{dt} = \frac{n_e(r)\sigma_{\mathrm{T}} L_{\mathrm{bol}}}{4\pi r^2 \rho(r) c} M(r) - \frac{GM_s}{r^2} \quad \text{with} \quad M(r) = \frac{\int_0^\infty \alpha_\nu(r) L_\nu e^{-\tau_\nu(r)} d\nu}{n_e(r)\sigma_T L_{\mathrm{bol}}}, \tag{C.6}$$

where L_{bol} is the bolometric luminosity, σ_T is the Thomson cross section and $M(r)$ is the force multiplier. $M(r)$ can be interpreted as the ratio of energy absorbed by the medium to the energy absorbed by the electrons. As a simple example we assume that the medium is a spherical shell with inner and outer radii of R and $R+\Delta R$, respectively. For this case $\langle M(r)\rangle = \int M(r)dr/\Delta R$.

Assuming a mean force multiplier, the wind equation (C.6) is approximated as

$$\frac{dv(r)}{dt} = \frac{\sigma_{\mathrm{T}} L_{\mathrm{bol}}}{1.2 m_{\mathrm{p}} 4\pi r^2 c} \langle M(r)\rangle - \frac{GM_s}{r^2} \tag{C.7}$$

In this last stage we have assumed a high ionization state for the gas at solar metallicities and therefore $\rho_r/n_e(r) \sim 1.2m_{\mathrm{p}}$, where m_{p} is the mass of the proton. Assuming that $v(R_{\mathrm{min}}) = 0$ the solution of equation (C.7) is

$$v(r) = \sqrt{2GM_s \left(\frac{L_{\mathrm{bol}}}{1.2L_{\mathrm{Edd}}}\langle M\rangle - 1\right)\left(\frac{1}{r_{\mathrm{min}}} - \frac{1}{r}\right)} \tag{C.8}$$

where $L_{\rm Edd}$ is the Eddington Luminosity (i.e. $L_{\rm Edd} = \frac{4\pi c G \mu m_p M_s}{\sigma_T}$). To calculate the force multiplier of a line we start from equation (C.6). Let's assume that the absorption line has a constant opacity, frequency ν_l and a width $\Delta\nu_{\rm th} = \nu_l v_{\rm th}/c$ (where $v_{\rm th}$ is the thermal speed of the absorbing atoms[6]). The characteristic distances of radiative interactions are of the order of $l \sim v_{\rm th}/(\nabla v)$. Hence for radially streaming radiation in an expanding medium the optical thickness is,

$$\tau_l = \alpha_l v_{\rm th}/(dv/dr) \tag{C.9}$$

where α_l is the absorption coefficient of the line. We define $\eta_l = \frac{\alpha_l}{n_e \sigma_T}$ and introduce an equivalent electron optical depth scale

$$t = \tau_l/\eta_l = n_e \sigma_T v_{\rm th}/(dv/dr). \tag{C.10}$$

Therefore the mean force multiplier is $\langle M(r)\rangle = \int M(r)dr/l$, i.e.,

$$\langle M(r)\rangle = \frac{\int_r^{r+l} M(r)dr}{l} = \frac{L_{\nu_l}\Delta\nu_{th}(1-e^{-\tau_l})}{n_e\sigma_T l\ L_{\rm bol}}. \tag{C.11}$$

Summing up over all absorption lines we obtain

$$M(t) = \frac{1}{L_{\rm bol}}\sum_l \frac{L_{\nu_l}\Delta\nu_{th,l}(1-e^{-\eta_l t})}{t} \approx \frac{1}{L_{\rm bol}}\sum_l L_{\nu_l}\Delta\nu_{th,l}\ \min\left(\eta_l, \frac{1}{t}\right). \tag{C.12}$$

To obtain α_l we use equation 1.78 from Rybicki & Lightman (1985) i.e.,

$$\alpha_l = \frac{h\nu_l}{4\pi} n_l B_{lu}\left(1 - \frac{g_l n_u}{g_u n_l}\right)\phi(\nu). \tag{C.13}$$

Assuming that the absorption line has a square-topped profile of width $\Delta\nu_{\rm th,l}$, $\phi = \frac{1}{\Delta v_{\rm th,l}}$, and using $B_{lu} = \frac{4\pi^2 e^2}{h\nu_l mc} f_l$, where f_l is the oscillator strength we obtain

$$\alpha_l = \frac{\pi e^2}{m_e c} g_l f_l \frac{(n_l/g_l - n_u/g_u)}{\Delta\nu_{th,l}}. \tag{C.14}$$

Inserting equation C.14 into C.12 we reproduce the result of Arav et al. (1994), i.e.,

$$M(t) = \frac{1}{L_{\rm bol}}\sum_l L_{\nu_l}\Delta\nu_{th,l}\frac{1-e^{-\eta_l t}}{t} \qquad \text{with} \qquad \eta_l = \frac{\pi e^2}{m_e c} g f_l \frac{(n_l/g_l - n_u/g_u)}{n_e\sigma_T\Delta\nu_{th,l}}. \tag{C.15}$$

[6]Notice that we are using just thermal broadening in the force multiplier calculations. We are not using turbulent velocity in these calculations. The use of turbulent velocities in this work is to simulate the effect of the acceleration between layers in the obtention of absorption profiles using our multilayered nearly relativistic outflow model §4.3. Moreover, by using only thermal broadening in our calculations, we can directly compare our results to those of other authors.

C.5.2 Comparison with other results.

The force multiplier mainly depends on the SED of the source, the composition of the gas, and its ionization parameter. In general a soft spectrum irradiating a gas that is nearly neutral (i.e. low ionization parameter) will strongly accelerate the gas and the force multiplier will be relatively large.

When the gas is highly ionized it absorbs less radiation and is subject to a weaker radiative driving force (i.e., the force multiplier is relatively small).

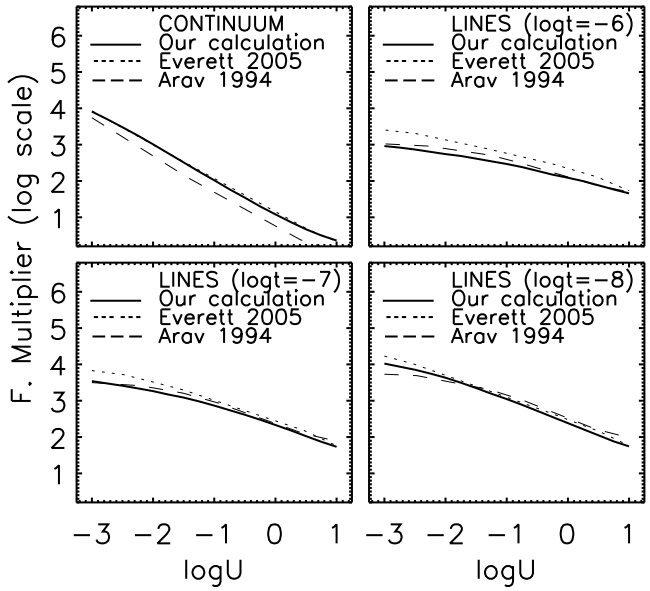

Fig. C.4 A comparison between our force multiplier calculations (solid lines) and those of Everett 2005 (dotted lines) and Arav et al. 1994 (dashed lines). The upper-left panel shows the continuum force multiplier as a function of the ionization parameter U. The other three panels show the line force multiplier as function of U for three different values of t.

Figure C.4 shows the estimated force multiplier assuming a Mathews-Ferland SED. Figure C.4 has four panels, the upper-left panel represents the continuum component of the force multiplier, mainly produced by bound-bound transitions. The other three panels in Figure C.4 show the contribution to the force multiplier from bound-free transitions for three different values of the dimensionless factor t; $\log\, t = -6$, -7 and -8. The line force multipliers increase as t decreases. This increase is noticeable when the medium is not highly ionized ($\log U \lesssim -1$; $\log \xi \lesssim 0.3$). Our calculations are in good agreement with those performed by Arav et al. (1994); Everett (2005).

C.6 Force multipliers calculations of material illuminated by absorbed power-laws and Mathews-Ferland SED

A warm absorber shielding the outflow may increase the effectiveness of radiation driving. In this appendix we use the same unabsorbed SEDs used in §4.4 to estimate the amount of shielding required to significantly increase the radiative driving force. Additionally, we estimate the differences between the radiative forces produced by a soft incident spectrum and a hard incident spectrum for different ionization levels of the absorbing outflow. As in §4.4 we assume that the warm absorber shielding the outflow has $\log\,(N_{\rm H}/{\rm cm}^{-2}) = 23$.

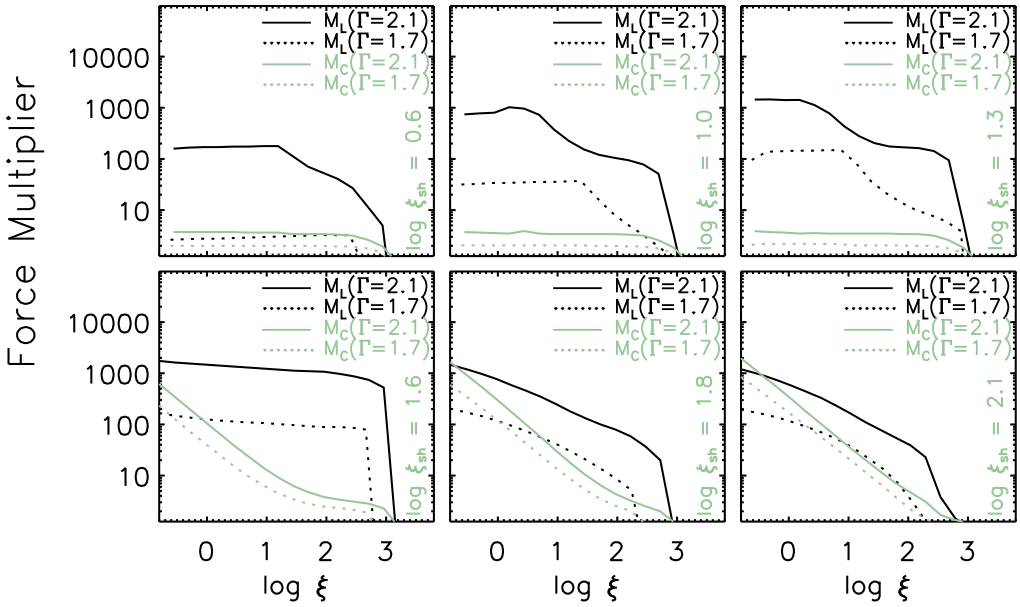

Fig. C.5 The bound-free, $M_{\rm C}$, and bound-bound, $M_{\rm L}$, components of the force multiplier are shown as a function of the ionization parameter. Force multipliers are calculated for a power-law SEDs with photon indices of $\Gamma = 2.1$ (solid lines) and $\Gamma = 1.7$ (dotted lines). In the upper-left, upper-right, lower-left and lower-right panel we have assumed absorbing shield where the soft and hard SEDs have been attenuated by a warm-absorber shield with $\log\,(N_{\rm H}/{\rm cm}^{-2}) = 23$ and $\log\,\xi_{\rm sh} = 0.6$, 1.0, 1.3, 1.6, 1.8 and 2.1 respectively.

In Figure C.5 we have plotted the bound-free, M_C, and the bound-bound, M_L, components of the force multiplier as a function of the ionization parameter for soft ($\Gamma = 2.1$) and hard ($\Gamma = 1.7$) absorbed power-law SEDs. In the upper-left, upper-right, lower-left and lower-right panel we have assumed absorbing shields with $\log\,(N_{\rm H}/{\rm cm}^{-2}) = 23$ and $\log\,\xi_{\rm sh} = 0.6$, 1.0, 1.3, 1.6, 1.8 and 2.1, respectively. In Figure C.5 we show that $M_{\rm L}$ is significantly larger for incident SEDs with soft spectra (i.e., $\Gamma = 2.1$) than for incident SEDs with hard spectra (i.e., $\Gamma = 1.7$) especially at low ionization levels of the shielding gas. For values of $\log\,\xi_{\rm sh} \lesssim 0.6$ we do not expect strong radiative driving given the

heavy attenuation of the continuum (see e.g., Chelouche & Netzer 2003). We also note that the force multipliers M_C and M_L are significantly reduced for low ionization levels of the shield as shown in Figure C.5. Additionally, when $\log \xi_{\rm sh} \gtrsim 2.0$ the shielding becomes transparent to the radiation and therefore the force multipliers are similar to the ones in the unabsorbed case. Finally from Figure C.5 we see that when the ionization parameter of the shield lies in the range of $1.0 \lesssim \log \xi_{\rm sh} \lesssim 1.8$ the line force multiplier of the outflowing material is greater with the presence of an absorbing shield than without one.

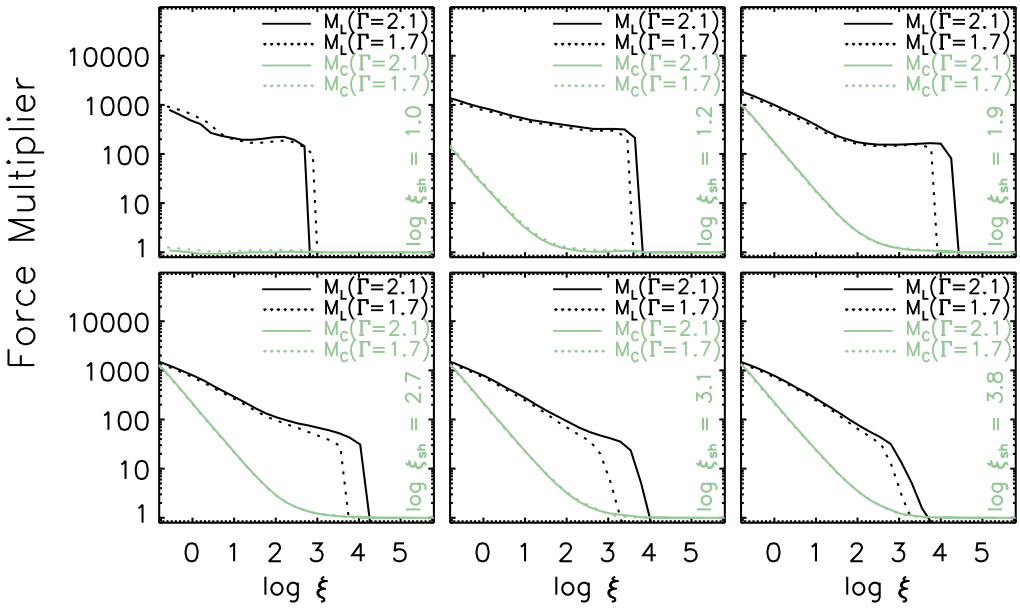

Fig. C.6 The bound-free, $M_{\rm C}$, and bound-bound, $M_{\rm L}$, components of the force multiplier are shown as a function of the ionization parameter. Force multipliers are calculated for Mathews-Ferland SEDs with X-ray photon indices of $\Gamma = 2.1$ ($\alpha_{\rm ox} = -1.52$; solid lines) and $\Gamma = 1.7$ ($\alpha_{\rm ox} = -1.41$ dotted lines). In the upper-left, upper-right, lower-left and lower-right panels we have assumed that the SEDs have been attenuated by shields with $\log (N_{\rm H}/{\rm cm}^{-2}) = 23$ and $\log \xi_{\rm sh} = 1.0$, 1.2, 1.9, 2.7, 3.1 and 3.8, respectively. The default parameters of a Mathews-Ferland SED are $\Gamma = 1.7$ and $\alpha_{\rm ox} = -1.41$.

In Figure C.6 we have plotted M_C, and M_L as a function of the ionization parameter for soft ($\Gamma = 2.1$; $\alpha_{\rm ox} = -1.51$) and hard ($\Gamma = 1.7$; $\alpha_{\rm ox} = -1.41$) absorbed Mathews-Ferland SEDs. In the upper-left, upper-right, lower-left and lower-right panels we assume shields that attenuate the SEDs with $\log (N_{\rm H}/{\rm cm}^{-2}) = 23$ and $\log \xi_{\rm sh} = 1.0$, 1.2, 1.9, 2.7, 3.1 and 3.8, respectively. In the case of a Mathews-Ferland SED incident on a shield with an ionization parameter in the range of $1.2 \lesssim \log \xi_{\rm sh} \lesssim 3.8$ we find that the line force multiplier M_L for soft SEDs (i.e., $\Gamma = 2.1$) extends to larger values of the ionization parameter of the outflowing material compared to hard SEDs (i.e., $\Gamma = 1.7$).

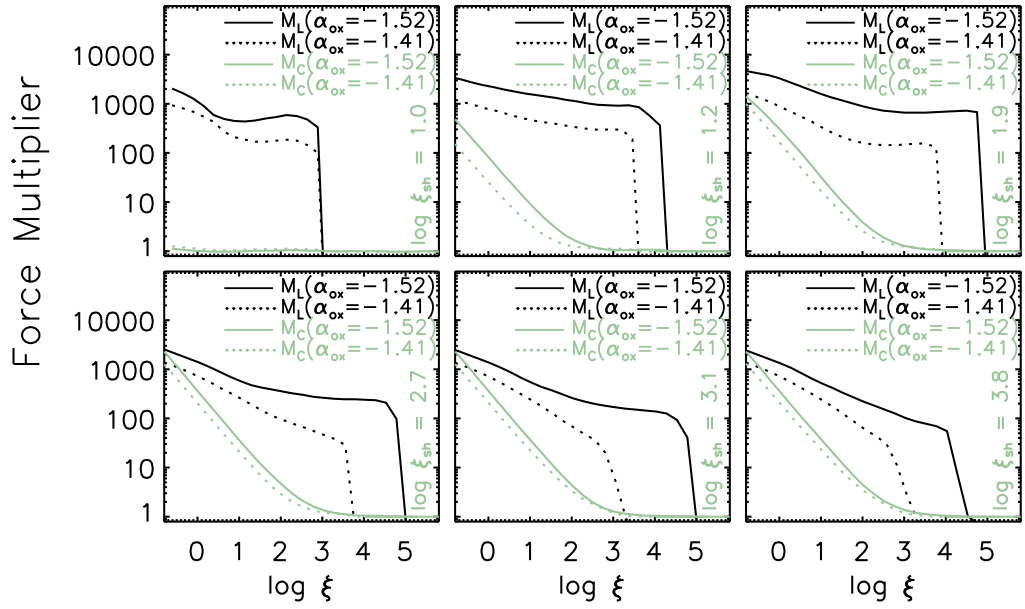

Fig. C.7 The bound-free, $M_{\rm C}$, and bound-bound, $M_{\rm L}$, components of the force multiplier are shown as a function of the ionization parameter. Force multipliers are calculated for Mathews-Ferland SEDs with X-ray photon indices of $\alpha_{\rm ox} = -1.52$ ($\Gamma = 1.7$; solid lines) and $\alpha_{\rm ox} = -1.41$ ($\Gamma = 1.7$; dotted lines). In the upper-left, upper-right, lower-left and lower-right panels we have assumed that the SEDs have been attenuated by absorbing shields with $\log (N_{\rm H}/{\rm cm}^{-2}) = 23$ and $\log \xi_{\rm sh} = 1.0$, 1.2, 1.9, 2.7, 3.1 and 3.8, respectively. The default parameters of a Mathews-Ferland SED are $\Gamma = 1.7$ and $\alpha_{\rm ox} = -1.41$.

In Figure C.7 we have plotted M_C, and M_L as a function of the ionization parameter of the outflow for soft ($\Gamma = 1.7$; $\alpha_{ox} = -1.51$) and hard ($\Gamma = 1.7$; $\alpha_{ox} = -1.41$) absorbed modified Mathews-Ferland SEDs. In the upper-left, upper-right, lower-left and lower-right panels we assume shields that attenuate the SEDs with $\log (N_H/\mathrm{cm}^{-2}) = 23$ and $\log \xi_{sh} = 1.0$, 1.2, 1.9, 2.7, 3.1 and 3.8, respectively. In the case of a modified Mathews-Ferland SED incident on a shield with an ionization parameter in the range of $1.0 \lesssim \log \xi_{sh} \lesssim 3.9$, we find that the line force multiplier M_L is significantly larger for soft SEDs (i.e., $\alpha_{ox} = -1.52$) than for hard SEDs (i.e., $\alpha_{ox} = -1.41$). We note that the line force multiplier for the case of a soft Mathews-Ferland SED incident on a shield with an ionization parameter of $\log \xi_{sh}$=1.9 has a value larger than ∼1000 for ionization parameters of the outflowing absorber in the range of $0 \lesssim \log \xi \lesssim 5$. For a shield with $\log \xi_{sh} \lesssim 1$ we predict that the continuum becomes too attenuated to allow effective radiative driving. When $\log \xi_{sh} \gtrsim 3.1$ the shield becomes transparent to the incident radiation and therefore the force multipliers are similar to the ones estimated for the unabsorbed case (see lower right panels of Figures C.6 and C.7).

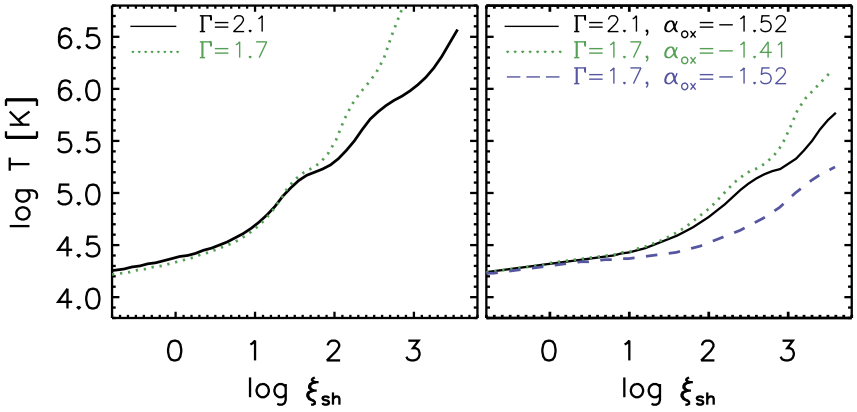

Fig. C.8 Temperature of a warm absorber (shield) as a function of its ionization parameter (illuminated side) for a warm absorber with $\log (N_H/\mathrm{cm}^{-2}) = 23$. In the left panel the illuminating source is a power law with $\Gamma = 2.1$ (solid line) and $\Gamma = 1.7$ (dotted line). In the right panel the illuminating source is a modified Mathews-Ferland SED with $\Gamma = 2.1$ and $\alpha_{ox} = -1.52$ (solid line), $\Gamma = 1.7$ and $\alpha_{ox} = -1.41$ (dotted line), and $\Gamma = 1.7$ and $\alpha_{ox} = -1.52$ (dashed line).

In Figure C.8 we plot the temperature of an absorbing shield as a function of its ionization parameter (on its illuminated side) for a shield with $\log (N_H/\mathrm{cm}^{-2}) = 23$. From the analysis in the last three paragraphs and from Figure C.8 we conclude that the most powerful winds are probably produced at temperatures in the range $4.5 \lesssim \log T \lesssim 5.2$. This occurs for power-law SEDs incident on shields with $1.0 \lesssim \log \xi_{sh} \lesssim 1.8$ and for Mathews-Ferland SEDs incident on shields with $1.2 \lesssim \log \xi_{sh} \lesssim 3.1$.

Bibliography

Afonso J., Mobasher, B., Koekemoer, A., Norris, R. P., & Cram, L. 2006, AJ, 131, 1216.

Akylas, A., Georgantopoulos, I., Georgakakis, A., Kitsionas, S., & Hatziminaoglou, E. 2006, A&A, 459, 693.

Alexander, D. M., Bauer, F. E., Brandt, W. N., Schneider, A. E., Hornschemeier, A. E., Vignaldi, C., Barger, A. J., Broos, P. S., Cowie, L. L., Garmire, G. P., Townsley, L. K., Bautz, M. W., Chartas, G. & Sargent, W. L. W. 2003, AJ, 126, 539.

Alexander, D. M., Bauer, F. E., Chapman, S. C., Smail, I., Blain, A. W., Brandt, W. N., & Ivison, R. J. 2005, ApJ, 632, 736.

Alexander, D. M., Swinbank, A. M., Smail, I., McDermid, R., & Nesvadba, N. P. H 2010, MNRAS, 402, 2211.

Arav, N., Li, Z.-Y., & Begelman, M. C. 1994, ApJ, 432, 62

Arnouts, S., Vandame, B., Benoist, C., Groenewegen, M. A. T., da Costa, L., Schirmer, M., Mignani, R. P., Slijkhuis, R., Hatziminaoglou, E., Hook, R., Madejsky, R., Rité, C., & Wicenec, A. 2001, A&A, 379, 740.

Bahcall, N. A., & Fan, X. 1998, ApJ, 504, 1.

Balbus, S. A., Hawley, J. F. 1991, ApJ, 376, 214.

Barger, A.J., Cowie, L. L., Capak, O., Alexander, D. M., Bauer, F. M., Fernandez, E., Brandt, W. N., Garmire, G. P., & Hornschemeier, A. E. 2003, AJ, 126, 632.

Barger, A. J., Cowie, L. L., Mushotzky, R. F., Yang, Y., Wang, W.-H., Steffen, A. T., & Capak, P. 2005, AJ, 129, 578.

Barkhouse, W. A., Green, P. J., Vikhlinin, A., Kim, D.-W., Perley, D., Cameron, R., Silverman, J., Mossman, A., Burenin, R., Jannuzi, B. T., Kim, M., Smith, M. G., Smith, R. C., Tananbaum, H., Wilkes, B. J. 2006, ApJ, 645, 955.

Bauer, F. E., Alexander, D. M., Brandt, W. N., Schneider, D. P., Treister, E., Hornschemeier, A. E., & Garmire, G. P. 2004a, AJ, 128, 2048.

Bauer, F. E., Vignali, C., Alexander, D. M., Brandt, W. N., Garmire, G. P., Hornschemeier, A. E., Broos, P. S., Townsley, L. K., & Schneider, D. P. 2004b, Adv. Space Res., 34, 2555.

Begelman, M. C., McKee, C. F., & Shields, G. A. 1983, ApJ, 271, 70.

Benitez, N., 2000, ApJ, 536, 571.

Bentz, M. C., Peterson, B. M., Netzer, H., Pogge, R. W., & Vestergaard, M. 2009, ApJ, 697, 160.

Best, P. N., Kauffmann, G., Heckman, T. M., Brinchmann, J., Charlot, S., Ivezić, Ž., & White, S. D. M. 2005, MNRAS, 362, 25.

Bianchi, S., Guainazzi, M., Matt, G., & Fonseca Bonilla, N. 2007, arXiv:astro-ph/0703433

Blandford, R. D., Payne, D. G. 1982, MNRAS, 199, 883.

Blundell, K. M., Beasley, A.J., Lacy, M., & Garrington, S.T. 1996, ApJ, 468, L91.

Boldt, E. 1987, IAUS, 124, 611.

Boyle, B.J., Fong, R, & Shanks, T. 1987, MNRAS, 227, 717.

Brandt, W.N. & Hasinger, G. 2005, ARAA, 43, 827.

Brandt, W. N., Laor, A., Wills, B. J. 2000, ApJ, 528, 637.

Brenneman, L. W., Reynolds, C. S., Wilms, J., & Kaiser, M. E. 2007, ApJ, 666, 817.

Bridle, A. H., & Perley, R. A. 1984, ARA&A, 22, 319.

Broos, P., Townsley, L., Getman, K., & Bauer, F. 2005, ACIS Extract, An ACIS Point Source Extraction Package, Pennsylvania State University, http://www.astro.psu.edu/xray/docs/TARA/ae_users_guide.html.

Bundy, K., Ellis, R. S., Conselice, C. J., Taylor, J. E., Cooper, M. C., Willmer, C. N. A., Weiner, B. J., Coil, A. L., Noeske, K. G., & Eisenhardt, P. R. M. 2006, ApJ, 651, 120.

Cash, W. 1979, ApJ, 228, 939.

Chartas, G. 2000, ApJ, 531, 81.

Chartas, G., Brandt, W. N., Gallagher, S. C., & Garmire, G. P. 2002, ApJ, 579, 169.

Chartas, G., Brandt, W. N., & Gallagher, S. C. 2003, ApJ, 595, 85.

Chartas, G., Brandt, W. N., Gallagher, S. C., & Proga, D. 2007a, AJ, 133, 1849

Chartas, G., Eracleous, M., Dai, X., Agol, E., & Gallagher, S. 2007b, ApJ, 661, 678

Chartas, G., Saez, C., Brandt, W. N., Giustini, M., & Garmire, G. P. 2009a, ApJ, 706, 644.

Chartas, G., Kochanek, C. S., Dai, X., Poindexter, S., & Garmire, G. P. 2009b, ApJ, 693, 174.

Chelouche, D. & Netzer, H. 2003, MNRAS 344, 233.

Chelouche, D., & Netzer, H. 2001, MNRAS, 326, 916.

Chiang, J., Reynolds, C. S., Blaes, O. M., Nowak, M. A., Murray, N., Madejski, G., Marshall, H. L., & Magdziarz, P. 2000, ApJ, 528, 292.

Cohen, J. G., Hogg, D. W., Blandford, R., Cowie, L. L., Hu, E., Songaila, A., Shopbell, P., & Richberg, K. 2000, ApJ, 538, 29.

Colbert, J.W., Teplitz, H.I., Yan, L., Malkan, M.A., & McCarthy, P.J., 2005, ApJ, 621, 587.

Cowie, L. L., & Barger, A. J. 2008, ApJ, 686, 72.

Cowie, L. L., Songaila, A., Hu, E. M. & Cohen, J. G. 1996, AJ, 112, 839.

Cowie, L.L., Barger, A.J., Hu, E.M., Capak, P., & Songaila, A. 2004, AJ, 127, 3137.

Croom, S. M., Richards, G. T., Shanks, T., Boyle, B. J., Strauss, M. A., Myers, A. D., Nichol, R. C., Pimbblet, K. A., Ross, N. P., Schneider, D. P., Sharp, R. G., & Wake, D. A. 2009, MNRAS, 399, 1755.

Croom, S. M., Warren, S. J., & Glazebrook, K. 2001, MNRAS, 328, 150.

Dadina, M. & Cappi, M. 2004, A&A, 413, 921.

Dai, X., Chartas, G., Eracleous, M., & Garmire, G. P. 2004, ApJ, 605, 45.

Dai, X., Shankar, F., & Sivakoff, G.R. 2008 ApJ, 672, 108.

Davidson, K. 1977, ApJ, 218, 20.

Degraf, C., Di Matteo, T., & Springel, V. 2010, MNRAS, 402, 1927.

Di Matteo, T., Springel, V., & Hernquist, L. 2005, Nature, 433, 604.

Di Matteo, T., Colberg, J., Springel, V., Hernquist, L., & Sijacki, D. 2008, ApJ, 676, 33.

Dickey, J. M., & Lockman, F. J. 1990, ARA&A, 28, 215.

Done, C., Mulchaey, J. S., Mushotzky, R. F., & Arnaud, K. A. 1992, ApJ, 395, 275.

Downes D., Neri R., Wiklind T., Wilner D. J., & Shaver P.A. 1999, ApJ 513, L1

Dwelly, T., & Page, M.J., 2006, MNRAS, 372, 1755.

Egami, E., Neugebauer, G., Soifer, B.T., Matthews, K., Ressler, M., Becklin, E. E., Murphy, T.W., Jr., & Dale, D.A. 2000, ApJ, 535, 561.

Elvis, M. 2000, ApJ, 545, 63.

Everett, J. E. 2005, ApJ, 631, 689.

Everett, J. E. 2007, Ap&SS ,311 , 269.

Fabian, A. C. 1999, MNRAS, 308, 39.

Fabian, A.C., Sanders, J.S., Ettori, S., Taylor, G.B., Allen, S.W., Crawford, C.S., Iwasawa, K., Johnstone, R.M., & Ogle, P.M. 2000, MNRAS, 318L, 65.

Fabian, A.C., Vasudevan, R.V., & Gandhi, P. 2008, MNRAS, 385, 43.

Ferland, G. J., Korista, K. T., Verner, D. A., Ferguson, J. W., Kingdon, J. B., & Verner, E. M. 1998, PASP, 110, 761.

Ferrarese, L., & Merritt, D. 2000, ApJ, 539, 9.

Finoguenov, A., Guzzo, L., Hasinger, G., Scoville, N. Z., Aussel, H., Böhringer, H., Brusa, M., Capak, P., Cappelluti, N., Comastri, A., Giodini, S., Griffiths, R. E., Impey, C., Koekemoer, A. M., Kneib, J.-P., Leauthaud, A., Le Fèvre, O., Lilly, S., Mainieri, V., Massey, R., McCracken, H. J., Mobasher, B., Murayama, T., Peacock, J. A., Sakelliou, I., Schinnerer, E., Silverman, J. D., Smolčić, V., Taniguchi, Y., Tasca, L., Taylor, J. E., Trump, J. R., Zamorani, G. 2007, ApJS, 172, 182.

Fukumura, K., Kazanas, D., Contopoulos, I., & Behar, E. 2010, ApJ, 715, 636.

Gallagher, S. C., Everett, J. E. 2007, ASPC, 373, 305.

Gallagher, S. C., Brandt, W. N., Sambruna, R. M., Mathur, S., & Yamasaki, N. 1999, ApJ, 519, 549.

Gallagher, S. C., Brandt, W.N., Chartas, G., & Garmire, G. P. 2002, ApJ, 567, 37.

Gallagher, S.C., Brandt, W.N., Chartas, G., Priddey, R., Garmire, G.P., & Sambruna, R.M. 2006, ApJ, 644, 709.

Gallimore, J.F., Axon, D.J., O'Dea, C.P., Baum, S.A., & Pedlar, A., 2006, AJ, 132, 546.

Gebhardt, K., Kormendy, J., Ho, L.C., Bender, R., Bower, G., Dressler, A., Faber, S.M., Filippenko, A.V., Green, R., Grillmair, C., Lauer, T.R., Magorrian, J., Pinkney, J., Richstone, D., & Tremaine, S. 2000, ApJ, 543, 5

George, I.M & Fabian, A.C. 1991, MNRAS, 249, 352.

George, I.M., Turner, T.J., Yaqoob, T., Netzer, H., Laor, A., Muchotzki, R.F., Nandra, K., & Takahashi, T. 2000, ApJ, 531, 52.

Ghisellini, G., Haardt, F., & Matt, G. 1994, MNRAS, 267, 743.

Giacconi, R., Zirm, A., Wamg, J., Rosati, P., Nonino, M., Tozzi, P., Gilli, R., Mainieri, V., Hasinger, G., Kewley, L., Bergeron, J., Borgani, S., Gilmozzi, R., Grogin, N., Koekemoer, A., Schreier, E., Zheng, W., & Collin, N. 2002, ApJS, 139, 369.

Giavalisco, M., Ferguson, H.C., Koekemoer, A.M., Dickinson, M., Alexander, D.M., Bauer, F. E., Bergeron, J., Biagetti, C., Brandt, W. N., Casertano, S., Cesarsky, C., Chatzichristou, E., Conselice, C., Cristiani, S., Da Costa, L., Dahlen, T., de Mello, D., Eisenhardt, P., Erben, T., Fall, S. M., Fassnacht, C., Fosbury, R., Fruchter, A., Gardner, J. P., Grogin, N., Hook, R. N., Hornschemeier, A. E., Idzi, R., Jogee, S.,

Kretchmer, C., Laidler, V., Lee, K. S., Livio, M., Lucas, R., Madau, P., Mobasher, B., Moustakas, L.A., Nonino, M., Padovani, P., Papovich, C., Park, Y., Ravindranath, S., Renzini, A., Richardson, M., Riess, A., Rosati, P., Schirmer, M., Schreier, E., Somerville, R.S., Spinrad, H., Stern, D., Stiavelli, M., Strolger, L., Urry, C.M., Vandame, B., Williams, R., & Wolf, C. 2004, ApJ, 600, 93.

Gibson, Robert R., Brandt, W. N., Schneider, Donald P., & Gallagher, S. C. 2008, ApJ, 675, 985.

Gibson, R. R., Jiang, L., Brandt, W. N., Hall, P. B., Shen, Y., Wu, J., Anderson, S. F., Schneider, D. P., Vanden Berk, D., Gallagher, S. C., & Fan, X. & York, D. G. 2009, ApJ, 692, 758.

Giustini, M., Cappi, M., Vignali, C. 2008, A&A, 491, 425

Granato, G.L., De Zotti, G., Silva, L., Bressan, A., & Danese, L. 2004, ApJ, 600 ,580.

Green, P. J. & Mathur, S. 1996, ApJ, 462, 637.

Green, P. J., Myers, A. D., Barkhouse, W. A., Mulchaey, J. S., Bennert, V. N., Cox, T. J., & Aldcroft, T. L. 2010, ApJ, 710, 1578.

Haardt, F., & Maraschi, L. 1991, ApJ, 380, L51.

Haardt, F., & Maraschi, L. 1993, ApJ, 413, 507.

Haardt, F., Marachi, L., & Ghisellini, G. 1997 ApJ, 476, 620.

Hamann, F., Kaplan, K. F., Rodríguez Hidalgo, P., Prochaska, J. X., & Herbert-Fort, S. 2008, MNRAS, 391, L39.

Hamann, F., Korista, K. T., Morris, S. L. 1993, ApJ, 415, 541.

Hasinger, G., Schartel, N., & Komossa, S. 2002, ApJ, 573, L77.

Hasinger, G., Miyaji, T., & Schmidt, M. 2005, A&A, 441, 417.

Heckman, T. M., Kauffmann, G., Brinchmann, J., Charlot, S., Tremonti, C., & White, S. D. M. 2004, ApJ, 613, 109.

Heinz, S., Choi, Y., Reynolds, C.S., & Begelman, M.C. 2002, ApJ, 569, L79.

Hewett, P. C. & Foltz, C. B. 2003, AJ, 125, 1784.

Hilton, M., Collins, C.A., Stanford, S.A., Lidman, C., Dawson, K.S., Davidson, M., Kay, S.T., Liddle, A.R., Mann, R.G., Miller, C.J., Nichol, R.C., Romer, A.K., Sabirli, K., Viana, P.T.P., & West, M.J. 2007, ApJ 670, 1000.

Hopkins, P. F., Hernquist, L., Cox, T. J., Di Matteo, T., Robertson, B. & Springuel, V. 2005a, ApJ, 625, L71.

Hopkins, P. F., Hernquist, L., Cox, T. J., Di Matteo, T., Robertson, B., & Springel, V. 2005b, ApJ, 632, 81.

Hopkins, P. F., Hernquist, L., Cox, T. J., Di Matteo, T., Robertson, B., & Springel, V. 2006, ApJS, 163, 1.

Irwin, M. J., Ibata, R. A., Lewis, G. F., & Totten, E. J. 1998, ApJ, 505, 529.

Isobe, T., Feigelson, E.D., Nelson, P.I., 1986, ApJ, 306, 490.

Ivezić, Ž., Menou, K., Knapp, G. R., Strauss, M. A., Lupton, R. H., Vanden Berk, D. E., Richards, G. T., Tremonti, C., Weinstein, M. A., Anderson, S., Bahcall, N. A., Becker, R. H., Bernardi, M., Blanton, M., Eisenstein, D., Fan, X., Finkbeiner, D., Finlator, K., Frieman, J., Gunn, J. E., Hall, P. B., Kim, R. S. J., Kinkhabwala, Ali, Narayanan, V. K., Rockosi, C. M., Schlegel, D., Schneider, D. P., Strateva, I., SubbaRao, M., Thakar, A. R., Voges, W., White, R. L., Yanny, B., Brinkmann, J., Doi, M., Fukugita, M., Hennessy, Gregory S., Munn, J. A., Nichol, R. C., & York, D. G. 2002, AJ, 124, 2364.

Iwasawa, K., Taniguchi, Yoshiaki 1993, ApJ, 413, 15L

Jiang, P., Wang, J. X., & Wang, T. G. 2006, ApJ, 644, 725.

Jiang, L., Fan, X., Ivezić, Ž., Richards, G. T., Schneider, D. P., Strauss, M. A., & Kelly, B. C. 2007, ApJ, 656, 680.

Kalberla, P. M. W., Burton, W. B., Hartmann, D., Arnal, E. M., Bajaja, E., Morras, R., & Pöppel, W. G. L. 2005, A&A, 440, 775.

Kallman, T., & Bautista, M. 2001, ApJS, 133, 221.

Kallman, T. R., Liedahl, D., Osterheld, A., Goldstein, & W., Kahn, S. 1996, ApJ, 465, 994.

Kato, Y., Mineshige, S., & Shibata, K. 2004, ApJ, 605, 307.

Kauffmann, G., & Haehnelt, M. 2000, MNRAS, 311, 576.

Kollmeier, J. A., Onken, C. A., Kochanek, C. S., Gould, A., Weinberg, D. H., Dietrich, M., Cool, R., Dey, A., Eisenstein, D. J., Jannuzi, B. T., Le Floc'h, E., & Stern, D. 2006, ApJ, 648, 128.

Konigl, A., & Kartje, J. F. 1994, ApJ, 434, 446.

Kormendy, J., & Richstone, D. 1995, ARA&A, 33, 581.

Krolik, J. H., & Begelman, M. C., 1986, ApJ, 308, L55.

La Franca, F., Gregorini, L., Cristiani, S., de Ruiter, H., & Owen, F. 1994, AJ, 108, 1548.

La Franca, F., Fiore, F., Comastri, A., Perola, G. C., Sacchi, N., Brusa, M., Cocchia, F., Feruglio, C., Matt, G., Vignali, C., Carangelo, N., Ciliegi, P., Lamastra, A., Maiolino, R., Mignoli, M., Molendi, S., Puccetti, S. 2005, ApJ, 635, 864L.

Laor, A., & Brandt, N. 2002, ApJ, 569, 641.

Le Fèvre, O., Vettolani, G., Garilli, B., Tresse, L., Bottini, D., Le Brun, V., Maccagni, D., Picat, J. P., Scaramella, R., Scodeggio, M., Zanichelli, A., Adami, C., Arnaboldi, M., Arnouts, S., Bardelli, S., Bolzonella, M., Cappi, A., Charlot, S., Ciliegi, P., Contini, T., Foucaud, S., Franzetti, P., Gavignaud, I., Guzzo, L., Ilbert, O., Iovino, A., McCracken, H. J., Marano, B., Marinoni, C., Mathez, G., Mazure, A., Meneux, B., Merighi, R., Paltani, S., Pellò, R., Pollo, A., Pozzetti, L., Radovich, M., Zamorani, G., Zucca, E., Bondi, M., Bongiorno, A., Busarello, G., Lamareille, F., Mellier, Y., Merluzzi, P., Ripepi, V., & Rizzo, D. 2005, A&A, 439, 845.

Lee, J. C., Fabian, A. C., Reynolds, C. S., Brandt, W. N., Iwasawa, K. 2000, MNRAS, 318, 857.

Lehmer, B. D., Alexander, D. M., Chapman, S. C., Smail, I., Bauer, F. E., Brandt, W. N., Geach, J. E., Matsuda, Y., Mullaney, J. R., & Swinbank, A. M. 2009, MNRAS, 400, 299.

Lightman, A. P., & White, T. R. 1988, ApJ, 335, 57.

Lockman 2004, Soft X-Ray Emission from Clusters of Galaxies and Related Phonomena, ed. R. Lieu (Dordrecht: Kluwer), 111.

Lynden-Bell, D. 1996, MNRAS, 279, 389.

Magdziarz, P., & Zdziarski, A. A., 1995, MNRAS, 273, 837.

Magdziarz, P., Blaes, O.M., Zdziarski, A.A., Johnson, W.N., & Smith, D.A., 1998, MNRAS, 301, 179.

Marconi, A., Risaliti, G., Gilli, R., Hunt, L.K., Maiolino, R., & Salvati, M., 2004, MNRAS, 351, 169.

Martini, P., Sivakoff, G. R., & Mulchaey, J. S. 2009, ApJ, 701, 66.

Mathews, W. G., & Ferland, G. J. 1987, ApJ, 323, 456.

McNamara, B. R., & Nulsen, P. E. J. 2007, ARA&A, 45, 117.

McNamara, B. R., Wise, M., Nulsen, P. E. J., David, L. P., Sarazin, C. L., Bautz, M., Markevitch, M., Vikhlinin, A., Forman, W. R., Jones, C., & Harris, D. E. 2000, ApJ, 534L, 135.

Merloni, A., & Fabian, A.C., 2001, MNRAS, 328, 958.

Merloni, A., & Fabian, A.C., 2002, MNRAS, 332, 165.

Mihalas, D., & Mihalas, B. W., "Foundations of radiation hydrodynamics", New York, Oxford University Press, 1984.

Mizuno, T, Takahashi, H., Uehara, Y., Nakazawa, K., Bamba, A., Fukasawa, Y., Kokubun, M., & Watanabe, S. 2007, JX-ISAS-SUZAKU-MEMO-2007-09.

Mobasher, B., Idzi, R., Benítez, N., Cimatti, A., Cristiani, S., Daddi, E., Dahlen, T., Dickinson, M., Erben, T., Ferguson, H. C., Giavalisco, M., Grogin, N. A., Koekemoer, A. M., Mignoli, M., Moustakas, L. A., Nonino, M., Rosati, P., Schirmer, M., Stern, D., Vanzella, E., Wolf, C., & Zamorani, G. 2004, ApJ, 600, 167.

Morgan, C. W., Kochanek, C. S., Dai, X., Morgan, N. D., & Falco, E. E. 2008, ApJ, 689, 755.

Morrison, R., & McCammon, D. 1983, ApJ, 270, 119.

Muñoz, J. A., Kochanek, C. S., & Keeton, C. R. 2001, ApJ, 558, 657.

Murray, N., Chiang, J., Grossman, S. A., & Voit, G. M. 1995, ApJ, 451, 498.

Muxlow, T.W.B., Richards, A.M.S., Garrington, S.T., Wilkinson, P.N., Anderson, B., Richards, E.A., Axon, D.J., Fomalont, E.B., Kellermann, K.I., Partridge, R.B., & Windhorst, R.A. 2005, MNRAS, 358, 1159.

Nandra, K., Fabian, A. C., Brandt, W. N., Kunieda, H., Matsuoka, M., Mihara, T., Ogasaka, Y., & Terashima, Y. 1995, MNRAS, 276, 1.

Nandra, K., George, I. M., Mushotzky, R. F., Turner, T. J., & Yaqoob, T. 1997 ApJ, 488, 91.

Norris, R.P., Afonso, J., Appleton, P.N., Boyle, B.J., Ciliegi, P., Croom, S.M., Huynh, M.T., Jackson, C.A., Koekemoer, A.M., Lonsdale, C.J., Middelberg, E., Mobasher, B., Oliver, S.J., Polletta, M., Siana, B.D., Smail, I., & Voronkov, M.A. 2006, AJ, 132, 2409.

Nousek, J.A., & Shue, D.R., 1989, ApJ, 342, 1207.

Page, K.L., Turner, M.J.L., Reeves, J.N., O'Brien, P.T., & Sembay, S., 2002, MNRAS, 338, 1004.

Page, K. L., O'Brien, P. T., Reeves, J. N., & Turner, M. J. L. 2004a, MNRAS, 347, 316.

Page, K. L., Reeves, J. N., O'Brien, P. T., Turner, M. J. L., & Worrall, D. M. 2004b, MNRAS, 353, 133.

Page, K. L., Reeves, J. N., O'Brien, P. T., & Turner, M. J. L. 2005, MNRAS, 364, 195.

Paolillo, M., Schreier, E. J., Giacconi, R., Koekemoer, A. M., Grogin, N. A., 2004, AJ, 611, 93.

Peacock, J.A., Miller, L., & Longair, M. S. 1986, MNRAS, 218, 265

Peterson, B. M., 1997. An Introduction to Active Galactic Nuclei. Cambridge University Press.

Pounds, K. A., King, A. R., Page, K. L., & O'Brien, P. T. 2003, MNRAS, 346, 1025.

Proga, D., Stone, J. M., & Kallman, T. R. 2000, ApJ, 543, 686.

Proga, D., & Kallman, T. R. 2004, ApJ, 616, 688.

Proga, D. 2005, ApJ, 630, L9.

Protassov, R., van Dyk, D. A., Connors, A., Kashyap, V. L., Siemiginowska, A. 2002, ApJ, 571, 545.

Ramírez, J. M. 2008, A&A, 489, 57.

Reeves, J.N., & Turner, M.J.L. 2000, MNRAS, 316, 234.

Reeves, J.N., Turner, M.J.L., Ohashi, T., & Kii, T. 1997, MNRAS, 292, 468.

Reeves, J. N., Wynn, G., O'Brien, P. T., & Pounds, K. A. 2002, MNRAS, 336, L56.

Reeves, J. N., O'Brien, P. T., & Ward, M. J. 2003, ApJ, 593, L65.

Reeves, J. N., O'Brien, P. T., Braito, V., Behar, E., Miller, L., Turner, T. J., Fabian, A. C., Kaspi, S., Mushotzky R., & Ward, M. 2009, ApJ, 701, 493.

Richards, E.A. 2000, ApJ, 533, 611.

Richards, E.A., Kellermann, K.I., Fomalont, E.B., Windhorst, R.A., & Partridge, R.B. 1998, AJ, 116, 1039.

Riechers, D. A., Walter, F., Carilli, C. L., & Lewis, G. F. 2009, ApJ, 690, 463.

Rodriguez-Hidalgo, P., Hamann, F., Nestor, D., & Shields, J. 2007, ASPC, 373, 287.

Rybicki, G. B., & Lightman, A. P. "Radiative processes in astrophysics". John Wiley & Sons, New York, 1985.

Saez, C., Chartas, G., Brandt, W. N., Lehmer, B. D., Bauer, F. E., Dai, X., & Garmire, G. P. 2008, AJ, 135, 1505.

Saez, C., Chartas, G., Brandt, W. N. 2009, ApJ, 697, 194.

Salpeter, E. E. 1964, ApJ, 140, 796.

Schindler, S., Castillo-Morales, A., De Filippis, E., Schwope, A. & Wambsganss, J. 2001, A&A, 376, L27.

Schmidt, M., Green, R. F., 1983, ApJ, 269, 352.

Schmidt, M. 1968, AJ, 151, 393.

Schneider, D. P., van Gorkom, J. H., Schmidt, M., & Gunn, J. E. 1992, AJ, 103, 1451.

Schurch, N. J., & Done, C. 2007, MNRAS, 381, 1413.

Shemmer, O., Brandt, W. N., Netzer, H., Maiolino, R., & Kaspi, S. 2006, ApJ, 646, L29.

Shemmer, O., Brandt, W. N., Netzer, H., Maiolino, R., & Kaspi, S. 2008, ApJ, 682, 81.

Shields, G. A. 1977, BAAS, 9, 608.

Silverman, J. D., Mainieri, V., Lehmer, B. D., Alexander, D. M., Bauer, F. E., Bergeron, J., Brandt, W. N., Gilli, R., Hasinger, G., Schneider, D. P., Tozzi, P., Vignali, C., Koekemoer, A. M., Miyaji, T., Popesso, P., Rosati, P., Szokoly, G. 2008, ApJ, 675, 1025.

Soltan, A. 1982, MNRAS, 200, 115.

Springel, V., Di Matteo, T., & Hernquist, L. 2005, ApJ, 620, L79.

Srianand, R. & Petitjean, P. 2000, A&A, 357, 414.

Stark et al. 1992, ApJS, 79, 77.

Steffen, A. T., Barger, A. J., Cowie, L. L., Mushotzky, R. F., & Yang, Y. 2003, ApJL, 596, L23.

Steffen, A. T., Strateva, I., Brandt, W. N., Alexander, D. M., Koekemoer, A. M., Lehmer, B. D., Schneider, D. P., & Vignali, C. 2006, AJ, 131, 2826.

Steidel, C. C., Adelberger, K. L., Shapley, A. E., Pettini, M., Dickinson, M., & Giavalisco, M. 2003, ApJ, 592, 728.

Steidel, C. C., Adelberger, K. L., Shapley, A. E., Erb, D. K., Reddy, N. A., & Pettini, M. 2005, ApJ, 626, 44.

Strateva, I. V., Brandt, W. N., Schneider, D. P., Vanden Berk, D. G., & Vignali, C. 2005, AJ, 130, 387.

Szokoly, G.P., Bergeron, J., Hasinger, G., Lehmann, I., Kewley, L., Mainieri, V., Nonino, M., Rosati, P., Giacconi, R., Gilli, R., Gilmozzi, R., Norman, C., Romaniello, M., Schreier, E., Tozzi, P., Wang, J. X., Zheng, W., & Zirm, A. 2004, ApJS, 155, 271.

Tananbaum, H., Avni, Y., Branduardi, G., Elvis, M., Fabbiano, G., Feigelson, E., Giacconi, R., Henry, J. P., Pye, J. P., Soltan, A., & Zamorani, G. 1979, ApJ, 234, L9.

Tarter, C. B., Tucker, W. H., & Salpeter, E. E. 1969, ApJ, 156, 943.

Thorne, K. S. 1974, ApJ, 191, 507.

Townsley, L. K., Feigelson, E. D., Montmerle, T., Broos, P. S., Chu, Y. H., & Garmire, G. P. 2003, ApJ, 593, 874.

Tozzi, P., Gilli, R., Mainieri, V., Norman, C., Risaliti, G., Rosati, P., Bergeron, J., Borgani, S., Giacconi, R., Hasinger, G., Nonino, M., Streblyanska, A., Szokoly, G., Wang, J.X., & Zheng, W. 2006, A&A, 451, 457.

Triester, E., & Urry, C. M. 2006, ApJ652, L79-L82.

Ueda, Y., Akiyama, M., Ohta, K., & Miyaji, T. 2003, ApJ, 598, 886.

Vestergaard, M., & Peterson, B. M. 2006, ApJ, 641, 689.

Vanzella, E., Cristiani, S., Dickinson, M., Kuntschner, H., Nonino, M., Rettura, A., Rosati, P., Vernet, J., Cesarsky, C., Ferguson, H. C., Fosbury, R. A. E., Giavalisco, M., Grazian, A., Haase, J., Moustakas, L. A., Popesso, P., Renzini, A., & Stern, D. 2006, A&A, 454, 423.

Vaughan S., & Uttley P. 2008, MNRAS, 390, 421.

Vignali, C., Comastri, A., Capi, M., Palumbo, G.G.C., Matsuoka, M., & Kubo, H. 1999, ApJ, 516, 582.

Wadadekar, Y. 2004, A&A, 416, 35.

Wang, J., Watarai, K., & Mineshige, S., 2004, ApJ, 607, L107.

Wang, J., Jiang, P., Zhou, H., Wang, T., Dong, X., & Wang, H. 2008, ApJ, 676, L97.

Warren, S.J., Hewett, P.C., & Osmer, P.S. 1994, ApJ, 421, 412.

Weymann, R. J., Morris, S. L., Foltz, C. B., & Hewett, P. C. 1991, ApJ, 373, 23.

Wilkes, B. J., & Elvis, M. 1987, ApJ, 323, 243.

Wirth, G. D., Willmer, C.N.A., Amico, P., Chaffee, F. H., Goodrich, R. W., Kwok, S., Lyke, J. E., Mader, J. A., Tran, H. D., Barger, A. J., Cowie, L. L., Capak, P. C., Alison L., Cooper, M. C., Conrad, A., Davis, M., Faber, S. M., Hu, E. M., Koo, David C., Le Mignant, D., Newman, J. A., & Songaila, A., 2004, AJ, 127, 3121.

Wolf, C., Meisenheimer, K., Kleinheinrich, M., Borch, A., Dye, S., Gray, M., Wisotzki, L., Bell, E. F., Rix, H.-W., Cimatti, A., Hasinger, G., & Szokoly, G. 2004, A&A, 421, 913.

Younger, J. D., Bahcall, N. A., & Bode, P. 2005, ApJ, 622, 1

Yu, Q., & Tremaine, S. 2002, MNRAS, 335, 965.

Zdziarski, A. A., Lubinski, P., Gilfanov, M., & Revnivtsev, M., 2003, MNRAS, 342, 355.

Zheng, Z. Y., & Wang, J. X. 2008, ApJ, 688, 116.

Zheng, W., Mikles, V. J., Mainieri, V., Hasinger, G., Rosati, P., Wolf, C., Norman, C., Szokoli, G., Gilli, R., & Tozzi, P. 2004, ApJS, 155, 73.

Zhou, H., Wang, T., Wang, H., Wang, J., Yuan, W., & Lu, Y. 2006, ApJ, 639, 716.

Vita
Cristian Saez

Education

The Pennsylvania State University State College, Pennsylvania 2003–Present

Ph.D. in Astronomy & Astrophysics, expected in August 2010
Area of Specialization: X-ray studies of AGNs

Universidad de Chile Santiago, Chile 2000–2002

B.S. in Astronomy, *cum laude* with distinction.

Awards and Honors

US National Science Foundation supplemental funds to attend "Cosmology at the Beach". 2009
Zaccheus Daniel Foundation for Astronomical Science Grant 2007–2009
Ecos-Sud Supplemental funds to visit Institut d'Astrophysique de Paris. 2002

Research Experience

Doctoral Research The Pennsylvania State University 2005–Present
Thesis Advisor: Dr. George Chartas

My research centers on the study of galaxies that host Active Galactic Nuclei (AGN), which are the sites of rapidly growing black holes. I study AGNs mainly through X-ray observations, which probe the hottest and innermost region of the gas surrounding the black hole.

Graduate Research The Pennsylvania State University 2003–2005
Research Advisor: Prof. Pablo Laguna

Study of trajectories of star-like bodies in the vicinity of an intermediate mass Kerr Black-hole.

Undergraduate Research Universidad de Chile 2001–2003
Research Advisor: Prof. Luis Campusano

Studies of strong gravitational lenses in galaxy clusters.

Teaching Experience

Teaching Assistant The Pennsylvania State University 2003–2005

I taught Astro011 "Elementary Astronomy Laboratory".

Teaching Assistant Universidad de Chile, Santiago, Chile 2002–2003

I was assistant instructor of "Extragalactic Astronomy" .